ROLE OF YTTRIUM IN THE HIGH TEMPERATURE OXIDATION OF Ni-25wt%Cr ALLOYS

Sanjay B. Shendye
B.Tech., Indian Institute of Technology, Bombay 1983
M.S., Oregon Graduate Center, 1985

A thesis submitted to the faculty
of the Oregon Graduate Institute of Science & Technology
in partial fulfillment of the
requirements for the degree
Doctor of Philosophy
in
Materials Science and Engineering

October 1994

The dissertation "Role of Yttrium in the High Temperature Oxidation of Ni-25wt%Cr Alloys" by Sanjay B. Shendye has been examined and approved by the following Examination Committee:

David A. Downham, Thesis Advisor
Assistant Professor

David G. Atteridge
Professor

Margaret Ziomek-Moroz
Assistant Professor

Carl D. Palmer
Associate Professor

ACKNOWLEDGEMENT

I wish to express my appreciation and sincere thanks to Dr. David A. Downham for his guidance and encouragement throughout this work. I am grateful to Drs. David G. Atteridge, Margaret Ziomek-Moroz and Carl D. Palmer, for examining my thesis. I would also like to acknowledge the Electric Power Research Institute for sponsoring this study.

My sincere thanks to Dr. James T. Stanley, for helping me in using the Desktop Microscopist™. Sincere thanks are also due to Dr. Yvon LePage of the Canadian National Research Council, Ottawa, for allowing me to use their transmission electron microscope. I express my gratitude to Jack McCarthy, Shary McIntee, Robert Turpin, Ken Burns, Steve Brooks and Curtis Bernard and all the faculty, staff and students from the department of Materials Science and Engineering for helping me during the experimental part of my thesis.

Finally, I would like to thank my wife, Sharmila, who always provided encouragement to me during this study. And very special thanks to my son, Sumant. Without their support this work would never have been completed.

TABLE OF CONTENTS

LIST OF TABLES

LIST OF FIGURES

ABSTRACT

Role of Yttrium in the High Temperature Oxidation of Ni-25wt%Cr Alloys

Sanjay B. Shendye, Ph. D

Supervising Professor : David A. Downham

Yttrium when added as an alloying addition (< 1 wt%) to the high temperature alloys, is known to dramatically reduce the oxide scale growth rate, and improve the adherence of the oxide scale. A potential explanation of this phenomenon is that yttrium getters the impurities in the alloy such as sulfur, which is believed to degrade the oxidation resistance. The objective of this study was to investigate the role of yttrium in imparting its beneficial effect on the oxidation resistance.

Ni-25wt%Cr alloys containing 0 - 0.62wt% yttrium and 4.8 ppm - 220 ppm sulfur, were prepared by arc melting nickel, chromium and yttrium metal, followed by homogenization at 1100°C. The sulfur content of the nickel and chromium metal was approximately 50 ppmw and 30 ppmw, respectively. Oxidation kinetics at 900°C in air, and thermal cycling of the alloys oxidized at 900°C, was studied. Oxidation experiments were also carried out at 1000°C in air. Microstructure of both the as-homogenized and the oxidized alloys was characterized using transmission electron microscopy and scanning electron microscopy.

Yttrium containing alloys exhibited a lower oxide scale growth rate compared to the yttrium free alloys. Thermal cycling of the oxidized alloys containing both low (4.8 ppm) and high (220 ppm) sulfur, led to the spallation of the oxide scale, except in the Ni-22Cr-0.62Y alloy. In the yttrium containing alloys, several yttrium containing compounds including yttrium oxysulfide, Y_2O_2S, were found in the as-homogenized alloys and in the oxide scale grown on the alloys.

Spallation of the oxide scale from the yttrium free alloy containing 4.8 ppm sulfur, indicated that a mere reduction in the alloy sulfur content, may not result in improving its oxidation resistance. Observation of Y_2O_2S in the as-homogenized yttrium containing alloys and in the oxide scales grown on them, clearly demonstrated the form in which the reactive elements tie up the sulfur. The observation of other yttrium containing compounds such as Ni_5Y in the as-homogenized yttrium containing alloys, and yttrium oxysulfate, $Y_2O_2SO_4$, and yttrium orthochromite, $YCrO_3$, in the oxide scales grown on these alloys, may explain how the reactive elements continue to impart their beneficial effects on the high temperature oxidation resistance, in the event of spallation of the oxide scale.

OBJECTIVE OF THIS STUDY

Recent studies on the reactive element effect have been directed towards the role of surface active impurities such as sulfur in the alloy. Trace quantities of sulfur in the alloy, are believed to be responsible for the degradation of the high temperature oxidation resistance of heat resisting alloys. It was suggested that addition of the reactive elements to the heat resisting alloys, was effective in gettering the sulfur in the alloy in the form of a sulfide, and prevent it from segregating to the oxide/alloy interface, resulting in the improved oxide scale adherence.

However, no substantial evidence is reported in the literature so far on the nature of the reactive element-sulfur species which may be responsible in tying up sulfur in the alloy, and which may lead to the improved oxide scale adherence. It has also been reported that the oxide/alloy interface was inherently strong and the removal of indigenous sulfur from the alloy would result in the improved spalling resistance of the oxide.

The objective of this study was to investigate the role of ytrium in improving the oxidation resistance of high temperature alloys. Accordingly Ni-25wt%Cr alloys containing high and low yttrium content were prepared. Since sulfur is considered to degrade the oxidation resistance, two Ni-25wt%Cr alloys containing very low sulfur (4.8 ppm) and high sulfur (140 ppm) were also made. The oxidation kinetics of both the yttrium free and yttrium containing alloys was studied, and the alloys and the oxide scales grown on them at 900°C and 1000°C, were characterized by scanning electron microscopy and transmission electron microscopy. Adherence of the oxide scales was studied by thermal cycling of the oxidized alloys. Scanning electron microscopy was carried out on the thermally cycled alloys to observe the spallation of the oxide.

A literature survey was conducted before conducting experimental studies to obtain information on the oxidation behavior of heat resistant alloys. The theory of oxidation of metals and alloys along with the mechanisms pertaining to the reactive element effect as described in the

literature, are covered in Chapter 1. Chapter 2 consists of the experimental work that was carried out in this study. Results of this study and the discussion of the results obtained are included in Chapters 3 and 4, respectively. Finally the conclusions from this study are included in Chapter 5. References are given at the end of Chapter 5.

CHAPTER 1

LITERATURE REVIEW

A. BACKGROUND

Heat resistant alloys are used for many critical applications in several industries, including steam turbine power generation, aircraft gas turbine, chemical and petrochemical, waste incineration, heat treating and metal processing[1]. Most high temperature alloys used presently are nickel, iron or cobalt based, mainly due to their favorable properties such as strength, formability, fatigue strength, creep resistance and oxidation resistance[1,2]. With ever increasing demand for improved efficiency, there is a trend towards developing materials suitable for higher service temperatures in a variety of environments. Since air or oxygen rich environments are very common, high temperature exposure of alloys to such environments results in the oxidation of the alloys, leading to excessive loss of metal. Oxidation resistance, therefore, is an important parameter in high temperature alloy design.

An alloy derives resistance to oxidation from the protective oxide scale which forms on its surface at elevated temperature. An oxide scale may be termed protective if it has a combination of the following favorable properties[3-10]:

1) it is thermodynamically stable
2) it grows at a slow rate
3) it forms a continuous layer at high temperature, and
4) it is adherent to the alloy surface under all conditions including thermal cycling.

High temperature alloys rely on the formation of chromia (Cr_2O_3) or alumina (Al_2O_3) scales since these oxides satisfy most of the criteria required for an oxide scale to be protective[3-12]. The applicability of the chromia forming alloys is however limited to the operating temperature of 1000°C, since Cr_2O_3 evaporates above this temperature[12-14].

B. THERMODYNAMIC STABILITY OF THE OXIDES

Thermodynamic stability of an oxide may be determined on the basis of an Ellingham diagram[15], which is a plot of the Gibb's standard free energy change of oxide formation (per mole of oxygen), ΔG°, as a function of temperature, T. This is illustrated in Figure 1[5]. For most metals, oxidation is spontaneous because the free energy change for such a reaction is large and negative, and a large negative value of ΔG° signifies a more stable oxide. CaO and MgO are significantly more stable oxides than Cr_2O_3. However, they are not suitable candidates for high temperature protection since they are highly sensitive to water and CO_2 contamination. Thermodynamic stability alone is thus not the deciding factor in choosing the appropriate oxide for high temperature protection.

For many reactions, kinetics rather than thermodynamics determine whether a reaction would proceed or not. A similar situation exists in the case of high temperature oxidation. Chromium has a greater affinity for oxygen than Ni, Co or Fe and hence when a Ni-Cr binary alloy is oxidized, Cr_2O_3 rather than NiO is favored thermodynamically[9,16]; whether it develops a steady state continuous scale is determined by factors such as alloy Cr content, temperature of the reaction, oxygen partial pressure, solubility and diffusion of oxygen, the flow rate of the oxidizing gas and temperature fluctuations. The Ellingham diagram[15] is not useful in predicting the rate of oxidation, since kinetics rather than thermodynamics are critical in controlling the oxide scale thickening[9].

C. OXIDATION KINETICS

Since a metal or an alloy gains weight when it reacts with oxygen, the growth rate of an oxide is commonly determined by thermogravimetric methods[3,5,7]. The weight gain, Δw, is measured by means of a continuously recording microbalance. The weight gain per unit area of the alloy specimen, $\Delta w/A$, when plotted as a function of time follows one or a combination of the three kinetic laws of oxidation - parabolic, linear and logarithmic. These laws are illustrated in Figure 2[5]. If the oxides evaporate during oxidation (as in the case of Cr_2O_3 above approximately 1000°C)[12-14], or if they spall, the weight gain measurements require careful interpretation.

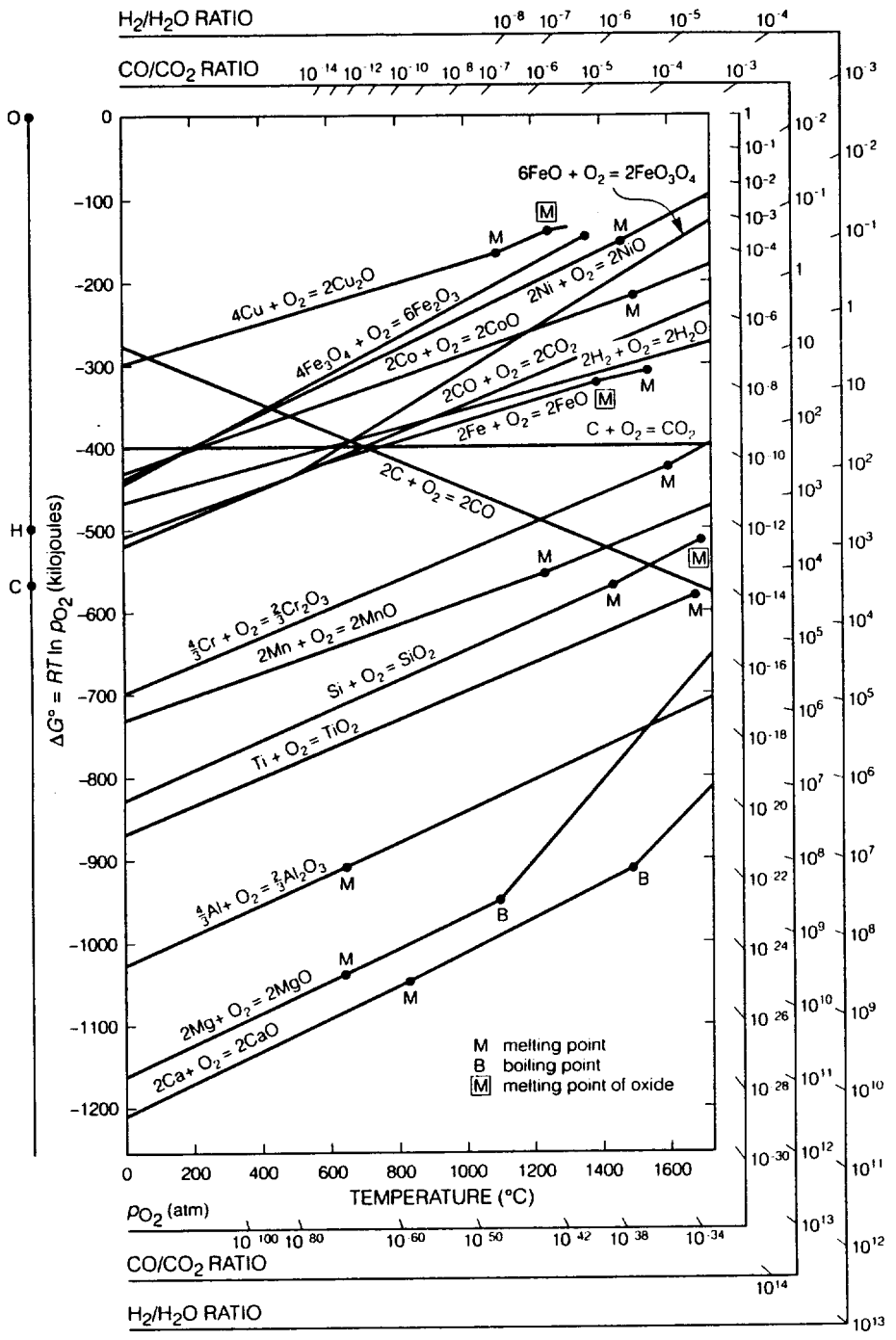

Figure 1

Ellingham diagram for oxides : Plot of Gibb's standard free energy change of oxide formation (per mole of oxygen) as a function of temperature (Reference Jones[5])

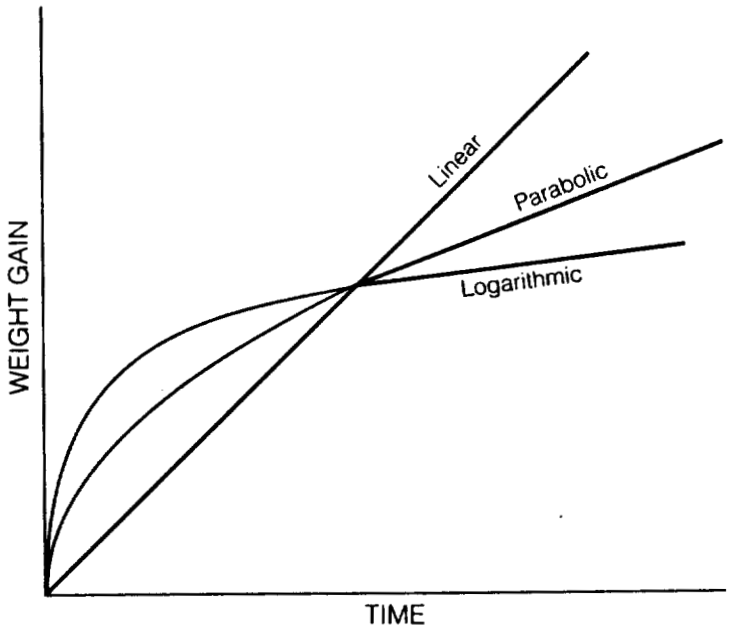

Figure 2

Kinetic rate laws for oxidation of metals (Reference Jones[5])

The following equations describe the parabolic, linear and the logarithmic rate laws of oxidation :

$x^2 = k_p t$ ---------- parabolic (1)

$x = k_L t$ ---------- linear (2)

$x = k_e \log (at + 1)$ ---------- logarithmic (3)

where x = oxide scale thickness, k_p = parabolic rate constant, k_L = linear rate constant, k_e = logarithmic rate constant, and a = constant, t = time.

Since weight gain Δw is proportional to the scale thickness[5,17], it can be substituted for x in all the three equations, with appropriate changes in the value of the constants. When an oxide layer develops relatively uniformly in thickness, its growth may be represented by one of the three kinetic laws, typically parabolic or logarithmic for protective behavior, and linear for non-protective behavior[5-8].

During oxidation of the alloys used for high temperature service, parabolic behavior is often observed[5-9]. The parabolic rate law may however be invalid in the early stages of oxidation before the oxide scale develops sufficient continuity and thickness[5,16]. Also when the oxide scale undergoes physical or chemical transformations that allow enhanced diffusion, the parabolic rate law may abruptly transform to linear kinetics. Furthermore, short circuit diffusion paths such as fissures, and grain boundaries can cause deviations from the parabolic rate law[5]. Since components of alloys have different affinities for oxygen, they seldom diffuse at the same rate in the alloy or the oxide. Consequently simple kinetic rate equations may not be valid.

The parabolic rate constant K_p is dependent on the temperature T and follows an Arrhenius type of relationship given by the equation[5-8],

$$K_p = K_o \exp(-Q/RT) \qquad \text{---- (4)}$$

where K_o is a constant, Q is the activation energy, R is the gas constant and T is in K. From this equation it can be seen that the parabolic rate constant increases with increasing temperature.

D. OXIDE STRUCTURE

Apart from the thermodynamic and kinetic considerations, the oxide structure also affects the oxidation behavior of an alloy. Oxides formed on alloy surfaces at elevated temperatures have certain unique structural features and are often non-stoichiometric[5,8,18]. TiO_2 is thermodynamically more stable than Cr_2O_3; however it is a highly non-stoichiometric oxide leading to a fast diffusion of oxygen anions resulting in a high oxide growth rate[12]. Thus TiO_2 can not be considered as a potential candidate for providing oxidation resistance to an alloy.

Oxides usually have either an excess or deficit of metal, equivalent to a deficit or excess of oxygen, respectively. In metal deficit oxides such as NiO, electron 'holes' carry current by exchanging electrons with neighboring normally charged cations. Since the electrons are carried by electron 'holes' of positive charge, the metal deficit oxides are termed as p-type semiconductors[5,16,18,19]. Cr_2O_3 is an example of a p-type semiconductor and its growth is believed to be due to the predominant outward diffusion of Cr^{3+} ions i.e. towards the oxide/gas interface compared with any inward oxygen transport[7-9].

A metal excess oxide carries the excess metal ions as either interstitial cations, or as oxygen anion vacancies. In either case, excess electrons are responsible for electrical conductivity and both the types of metal excess oxides are termed as n-type semiconductors[5-8,18,19]. Alumina is an example of a n-type semiconductor oxide[6,7,16].

In a p-type oxide, doping the oxide with cations of lower charge than the cation of the oxide, reduces the cation vacancy concentration, and thus the oxidation rate[18,19]. However, when the oxide is doped with a cation with a higher positive charge than the cation of the oxide, the concentration of the cation vacancies increases, and so does the oxidation rate[18,19]. When a n-type oxide is doped with a cation with a higher positive charge than that of the cation of the oxide, the concentration of the cation vacancies decreases and so does the oxidation rate. An opposite effect is produced when a n-type oxide is doped with a cation with a lower positive charge than

that of the cation of the oxide[18,19].

Although it is sometimes possible to reduce the ionic diffusivity by doping the oxide lattice, doping effects are not strong enough to provide the basis for oxidation resistant alloys[5,19]. Usually the base metal composition is changed by alloying with Cr or Al, so that an inherently more protective compound such as chromia or alumina is formed as the scale[4,5,9].

E. OXIDE SCALE GROWTH

Development of a surface healing layer of the thermodynamically more stable and kinetically more protective oxide such as Cr_2O_3 on binary Ni-Cr alloys requires a critical concentration of chromium, typically 20wt%[4,20-22]. Parameters such as alloy Cr concentration, and solubility and diffusivity of oxygen in the alloy, determine whether preferential oxidation of Cr results in the development of a healing layer, or in the formation of the internal oxide precipitates in the alloy[16,20].

The supply of Cr from the bulk alloy to the surface can play a crucial role in the oxide growth process. Since the diffusion coefficient for Cr in Ni-Cr alloys is relatively low[20], the defects in the alloy, such as the grain boundaries, may provide enhanced diffusion paths for this element, facilitating establishment of the healing layer[16].

F. OXIDE SCALE ADHERENCE

In one of the earliest studies on the oxidation of metals, Pilling and Bedworth[23] proposed that the ratio of the oxide scale volume to metal volume was a predictor of protectiveness of the oxide. Volume ratio less than 1 was thought to be unprotective, since the oxide scale would be insufficient to cover the metal. A volume ratio much greater than 1 was thought to introduce large compressive stresses in the oxide causing poor scale adherence, and consequently resulting in the poor oxidation resistance due to the cracking and spallation of the oxide scale.

The volume ratio however did not take in to account factors such as plasticity of the oxide scale at higher temperatures, oxide scale porosity, and volatilization of some oxides at higher

temperature. Thus, oxide scales predicted to be protective on the basis of the volume ratio are in practice not found to be protective, and vice-versa.

Spallation of an oxide layer could result from the stresses arising from the oxide scale growth process itself, or from strains arising from mechanical flexing of the component in service[4,8]. Very often though, thermal cycling is a major cause for poor adherence of many oxide scales[4,5,8]. The coefficient of thermal expansion of most metal oxides is lower than that of the substrate[10], resulting in the generation of stresses in the oxide scale. Excessive build up of such stresses may lead to the spallation of the scale. In the spalled areas, an Al or Cr depleted metallic surface may be in direct contact with the environment resulting in an accelerated oxidation. Repeated spallation may eventually lead to the formation of less protective scale as the substrate composition changes.

G. REACTIVE ELEMENT EFFECT

Over 50 years ago, it was discovered that addition of small amounts of yttrium and metals from the lanthanide series of elements as a melt deoxidant, produced substantial improvement in the oxidation resistance of Nichrome (Ni-20%Cr) heating elements[3,4]. This "rare earth effect" as it was then called, was later on observed even with additions of other reactive metals such as hafnium and zirconium.

Comparatively recent studies on chromia forming alloys have shown that metallic alloying additions of reactive elements such as yttrium[4,24-39], cerium[27,32,38,40-42], lanthanum[26,27,31,38], gadolinium[26,31,32,36] and zirconium[26,31,35,39] or reactive element oxide dispersions[31,39,41,43-53], improved the oxidation resistance of high temperature alloys. The same effect was also observed when the alloys were implanted[24,54-64] with ions of reactive metals or when the alloy surface was coated[31,38,65-70] with reactive metal oxides. Since the "rare earth effect" is also produced by elements other than the rare earth elements, this phenomenon of improvement in the oxidation resistance is now called the " reactive element effect" (REE or RE effect)[4,11].

Several beneficial effects of the RE additions in the case of chromia forming alloys have been reported; they are :

1) the oxide scale growth rate is reduced[24,31-33,35,41,42,46,48,49,56,65,67]

2) the oxide scale adherence is improved substantially[25,28,29,31,32,38,45,50,55-69]

3) the oxidation mechanism is changed from predominant cation transport out to predominant anion transport in[38,45,50,55-69]

4) the grain size of the oxide scale is reduced significantly [24,38,44,50,56,60-62] and,

5) the amount of chromium required to form the protective chromia scale is reduced[30,40,41,56]

Each of these beneficial effects along with the suggested mechanisms are presented in the following sections.

1. REDUCTION IN THE OXIDE SCALE GROWTH RATE

Significant reduction in the oxide scale growth rate of chromia forming alloys containing small quantities of reactive element have been reported in the literature. In the Ni-20wt%Cr alloys containing alloying additions of 0.7 wt% Zr, Gd, La and Y, Nagai[31] reported a reduction of 3 to 9 times in the weight gain at 1000°C, and 2 to 2.5 times reduction at 1100°C, after oxidation for approximately 19 hours in air (Figures 3a and 3b). A reduction in the weight gain by more than 10 times was reported by Rhys-Jones and Grabke[41] in the Fe-10wt%Cr-1wt%Ce alloy and the Fe-20wt%Cr-1wt%Ce alloy, when these alloys were oxidized at 1000°C in 13.33 kPa O_2 for 70 hours.

It may be noted that the oxidation rate may be dependent on the type of reactive element added and on the temperature of reaction. Nagai[31] reported that when 0.7wt% Al, Si, Ti, Zr, Y, La and Gd were added to Ni-20wt%Cr alloys, La and Y showed best improving effect on the oxidation rate at 1000°C in air. However, the oxidation rate of the alloys with Y and La additions

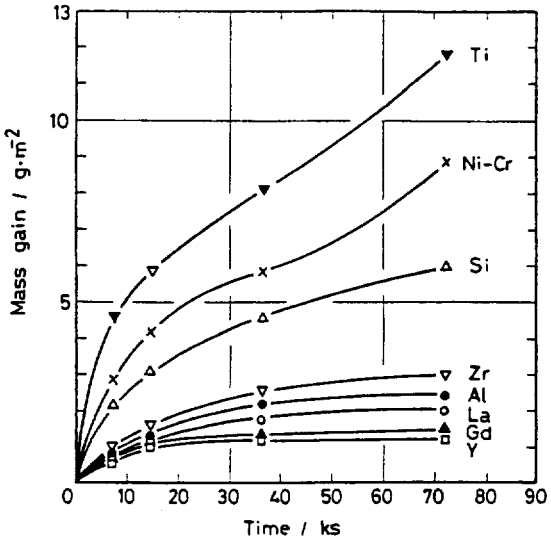

a) 1000°C in air

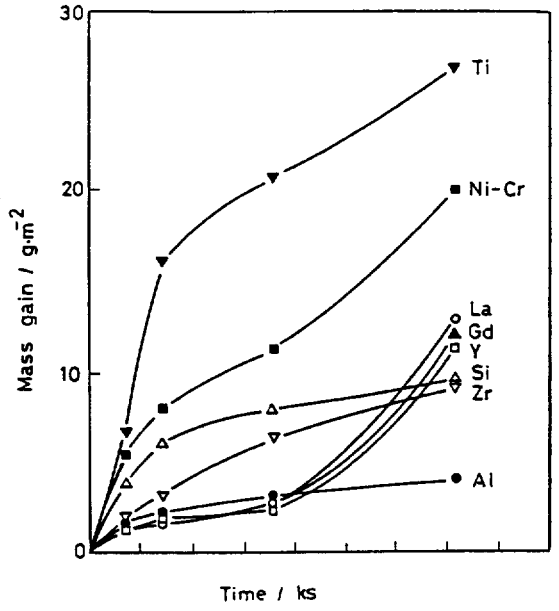

b) 1100°C in air

Figure 3

Weight gain per unit area for Ni-20Cr alloy containing 0.7 wt% alloying additions of Zr, Gd, La and Y at a) 1000°C in air, and b) 1100°C in air. (Reference Nagai[31])

increased rapidly after 10 hours at 1100°C, whereas alloys containing Si and Al showed the best improving effect at 1100°C.

There also have been some apparent inconsistencies in the results reported. For instance, Tsuzi[29] had reported that addition of 0.063wt% and 0.87wt% Y to Fe-24Cr alloy did not show any significant difference in the oxidation rates at both 1000° and 1100°C, although oxidation rate was higher at 1100°C than at 1000°C. Strafford and Harrison[35] had reported that the addition of 0.5wt% Y and Zr to a Ni-15Cr alloy decreased the oxidation rate, while addition of elements such as Ce, La and Th to the alloy increased the oxidation rate when the alloys were oxidized in oxygen at 900°C. This result however, may not be strictly valid for the chromia forming alloys, since 20 wt% or more of Cr is required for the formation of chromia[4,20-22].

Alloys containing a fine dispersion of the reactive element oxide, typically 1-2 vol.%, also exhibit reduction in the oxide growth rate. The first observation of this effect was for an alloy of Ni-20wt%Cr containing thoria (ThO_2) dispersion which was primarily intended to improve the high temperature creep strength[3]. Subsequently, both Ni-Cr and Fe-Cr alloys containing dispersed oxides have been studied in much detail. These include Y_2O_3[31,39,43-47,49-51], TiO_2[31,46], CeO_2[31,38,41,50], ThO_2[48-50] and La_2O_3[31,46,49].

More recently, ion-implantation of a reactive element on the alloy surface has been a topic of extensive investigation[56-58]. Ion-implantation is a process which permits incorporation of reactive metal ions into the surface of the alloys[24]. An attractive feature of ion-implantation is that it can provide the reactive element effect through a surface layer while maintaining the mechanical integrity of the alloy. Most of the ion-implantation studies have been made with Y[24,55-57,59-63] and Ce[4,58] implants, but La, Zr and Hf implants[4,54,55] were also found to be equally effective in reducing the oxide scale growth rate.

One of the claims made in the early literature was that in the case of chromia formers the RE effect could be developed by a surface deposit of the reactive element oxides on the alloy[4]. Several methods of depositing reactive metal oxides have been reviewed in the literature[66]. Surface coating of oxides offers potential commercial advantages of low cost and of relative ease of application. In addition, it avoids problems associated with adding metallic or oxide dispersoid

components to bulk substrates.

a. Mechanisms to Explain the Phenomenon of Reduction in the Oxide Scale Growth Rate

The main mechanisms which have been proposed to explain the reduction in the scale growth rate are (a) doping of the oxide, (b) formation of a partial or complete blocking layer in the scale, (c) short circuit diffusion, and (d) change in the mechanism of oxidation.

The oxide doping mechanism proposed that when the reactive elements are doped into Cr_2O_3 the concentration of Cr cation vacancies would be reduced. A reduction in the Cr cation vacancies would reduce the mobility of the Cr cations and consequently the oxidation rate[25]. However, substitution of an element such as cerium and thorium (which can attain a valency of +4) in Cr_2O_3 may increase the concentration of the cation vacancies and thus increase the oxidation rate. It is known from the literature that when an oxide is doped with a cation with a higher positive charge than the cation of the oxide, the concentration of the cation vacancies increases and so does the oxidation rate[18,19]. However, additions of Ce and Th have been reported to improve the oxidation resistance.

By the same oxide doping argument, since Y is trivalent no doping effect would be expected if this element dissolved in Cr_2O_3, as it would only substitute for the Cr cation vacancies, and the net charge of the oxide would be unchanged[71]. However, Y additions do improve the oxidation resistance. The main weakness of the oxide doping mechanism thus lies in the apparently equal efficacy of a wide range of elements with the valence state 3^+ as Cr.

Giggins and Pettit[48] had proposed a model in which they suggested that, incorporation of the dispersoid oxide particles in the oxide scale, reduced its growth rate by partially blocking the outward (towards gas/metal interface) chromium ion transport through Cr_2O_3, thereby reducing the oxidation rate. Ikeda et al.[72] had also proposed a similar mechanism in the case of Al_2O_3 forming alloys containing dispersions of Y_2O_3. Ramanarayanan and Petkovic-Luton[44] had however shown using transmission electron microscopy, that the volume fraction of the yttria particles in the oxide scale grown on a Ni-20%Cr-0.5%Ti-0.6%Y_2O_3 at 1000°C, 1050°C and

1100°C in CO_2-CO gas mixture, was much smaller than the volume fraction of yttria in the alloy. The oxide particle blocking mechanism thus seemed untenable.

The third school of thought believes that growth of chromia films at high temperatures was controlled mainly by transport of chromium cations along the short circuit diffusion paths such as grain boundaries and/or dislocations. Evidence has been presented in the literature[45,56-59,61,62,65-67] using scanning electron microscopy, analytical electron microscopy and energy dispersive x-ray (EDX) spectroscopy that, reactive element ions segregate to grain boundaries in the Cr_2O_3 scale, and they are thought to decrease the rate of transport of chromium cations along the grain boundaries, thereby reducing the rate of oxidation.

Change in the mode of oxide growth is also put forth as a mechanism for the observed reduction in the oxide growth rate. By using $^{18}O_2$ isotope of oxygen in the secondary ion mass spectroscopy (SIMS) analysis of oxide scales grown on CeO_2 sputter coated Fe-26Cr alloy at 900°C, Downham et al.[64] demonstrated that Ce found within the scale changed the mechanism of Cr_2O_3 growth from predominantly cation to predominantly anion diffusion. It was found that Ce segregated to form particles of $CeCrO_3$ which likely retard grain boundary diffusion of Cr cations, while allowing diffusion of oxygen anions to continue. Analogous results were observed on Y-implanted alloys by Pryzybylski and Yurek[56].

2. IMPROVEMENT IN THE OXIDE SCALE ADHERENCE

Improvement in the oxide scale adhesion as one of the RE effects is not only a beneficial effect, it is usually the most dramatic, and therefore has been studied in greater detail. A number of hypotheses have been put forward to account for this observation[3].

The mechanisms explaining the phenomenon of improved scale adherence are :

1) oxide pegging or ' keying '
2) vacancy sink model
3) gettering of surface active impurities, such as sulphur by the reactive element
4) modification of growth process, and
5) enhanced scale plasticity

a. Oxide Pegging or 'Keying'

Mechanical keying of the oxide to the alloy substrate as a result of internal oxidation of active element alloying addition, or dispersoid particles growing in size to form 'oxide stringers' of thin elongated oxide intrusions extending into the alloy substrate, is the principle premise of this mechanism. Earlier models had suggested that the oxide pegs consisted of the active element oxide itself, or a compound between active element oxide and the main scale forming constituent. However, it was later shown using EDX analysis[73] that the pegs consisted primarily of Al_2O_3, at least on alumina forming alloys.

Although some researchers[25,28,31,38] suggested the 'keying' effect as the mechanism for improved scale adherence in Cr_2O_3 forming alloys, in many of such alloys oxide pegs are seldom, if ever, observed[4]. It should be noted that in a number of studies, pegs protruding from the oxide scale into the substrate were not observed[27,29,32,57,69,74].

b. Vacancy Sink Model

When the surface scale is removed from the alloy, in many cases unintentionally, during cooling from the oxidation temperature, the exposed alloy shows a number of concave craters having a smooth, sometimes thermally etched appearance, and representing areas where oxide and metal are not in intimate contact during oxidation[47]. Elsewhere, the surface exhibits oxide grain imprints, where the scale had maintained alloy contact. The presence of these voids between scale and substrate does not seemingly affect the growth rate of the surface scale. The voids can, however, have a relatively dramatic effect on the adhesion of the scale to the substrate, and may result in the spallation of the oxide scale.

Evidence has been presented using SEM and optical microscopy techniques, that the presence of an active metal or an oxide dispersion in chromia forming alloys minimizes the development of voids at the scale/alloy interface[29,31,60]. In some other studies[25,32,50] on chromia forming alloys, the evidence of minimization of voids was not very clear. It may be noted that, the presence of voids approximately 50μm in diameter in Fe-28Cr-1.3Gd alloy did not result in the spallation of the oxide[32].

It was proposed that the voids may arise from the condensation of vacancies at the alloy/scale interface[34] although the source of the vacancies leading to void formation is not clearly understood. Vacancies are believed to be created due to outward diffusion of cations in metal deficit oxides such as NiO[8]. Another source of vacancies invokes a Kirkendall effect[75] in the alloy, in which surplus vacancies result from a difference in diffusion rates of metal elements to and from the scale/metal interface.

c. Gettering of Surface Active Impurities by the Reactive Elements

It was recently suggested that the scale adhesion was related to the segregation of impurities in the alloy and their subsequent migration to the scale-metal interface, and that the reactive elements in some way inhibit the segregation. Some studies had indicated that the role of the reactive elements was to interact with indigenous sulphur present in the alloy to prevent the preferential segregation of sulphur to the scale-metal interface[4,20,56,72,76-92]. It was also suggested by some researchers[77,78,80] that the bond between the chromia or the alumina scale and the alloy, was inherently strong, and the presence of impurities such as sulfur weakened it.

Smeggil et al.[93] had reported that reduction in the sulfur levels from ~50 ppm down to 1-2 ppm in a NiCrAl Al_2O_3 forming alloy, strongly increased the oxide scale adherence without requiring additions of reactive elements such as yttrium. In another study Smeggil[94] reported that reduction in the sulfur content of Ni-40wt%Cr alloy to < 2 ppm improved the oxide adherence while the normally prepared alloy containing ~ 50 ppm S resulted in poor oxide scale adherence. Furthermore, yttrium additions to the normally prepared alloy, containing ~ 50 ppm S, also resulted in poor oxide scale adherence[94].

In the case of Cr_2O_3 forming alloy, Fox et al.[80] found that the oxide-metal interface adhesion was very poor when the alloy had sulfur content of 165 ppm. Melas and Lees[78] in their study of oxidation of Cr metal found that, annealing of the Cr metal in hydrogen at 1100°C for 16 hours prior to oxidation, greatly improved the adhesion of the Cr_2O_3 scale. They attributed the improved adhesion to the reduction in the indigenous sulfur in the Cr metal due to annealing in hydrogen, although they did not report the sulfur content of the Cr metal after annealing.

Rhys-Jones and Grabke[41] had also observed that increasing alloy sulfur impurity content of Fe-20Cr-S alloy from 0.0055% to 0.02% caused a marked loss in scale adhesion. They conducted hot stage Auger Electron Spectroscopy (AES) to investigate the presence of sulfur at the oxide/alloy boundary. Addition of cerium as an alloying element was found to markedly reduce the deleterious effects of sulfur contamination, possibly as a result of Ce-sulfide or Ce-oxysulfide formation, which would reduce the amount of sulfur reaching the alloy/oxide interface during oxidation.

Papaiacovou et al.[95] studied the oxidation behavior of Fe-20Cr, Fe-20Cr-0.78Ce and Fe-20Cr alloy containing 0.055wt% S, coated with 4 nm CeO_2, at 900°C. They used SIMS to detect sulfur. In all the three cases, segregation of sulfur was observed at the oxide/metal interface, although, in the case of base alloy and cerium containing alloy, sulfur was distributed more evenly through the scale. CeO_2 coating did not affect the segregation of sulfur, though oxide scale adhesion was better for the CeO_2 coated alloy. Hussey et al.[67] had also reported that segregation of sulfur to the oxide/metal interface was not affected, as might be expected, in the presence of CeO_2 coatings. Moreover, in their experiments on the Fe-20Cr alloys, segregation of sulfur did not adversely affect oxide adhesion[67].

Ikeda et al.[72] had studied the oxidation behavior of two sets of alloys: oxide dispersion strengthened (ODS) alloys with different amounts of Y_2O_3 and commercial or modified stainless steels. They observed that the dispersed oxide suppressed the spalling of the Al_2O_3 scale by trapping the sulfur present in the alloy. The quantity of sulfur in the alloys ranged between 10 ppm and 350 ppm. They were however unable to identify the Y-S species which may have been responsible for the improved spalling resistance.

d. Modification of Oxide Scale Growth Process

As mentioned above, addition of reactive elements to chromia forming alloys substantially reduces the growth rate of the oxide scale when the alloys are exposed to elevated temperatures. This would be expected to reduce the growth stresses associated with the growth of oxide scale; however, probably of more significance is the actual mechanism responsible for the growth of Cr_2O_3. It is now abundantly clear from the reported results on chromia forming alloys, that

reactive element additions promote a contribution from oxygen transport to scale growth and may even make this predominant[38,45,50,55-69]. Thus, due to the reduction in the transport of Cr^{3+} ions to the scale/metal interface, growth rate of Cr_2O_3 is consequently reduced.

e. Enhanced Scale Plasticity

In a high temperature oxidation situation, stresses developed during the growth of the oxide scale, may be accommodated by deformation of the scale, rather than scale spalling. Thus, modification of the deformation characteristics of the scale may improve scale adherence during isothermal oxidation. Several researchers[33,41,55,66,96] had proposed that reactive elements change the microstructure of Cr_2O_3, thereby facilitating plastic deformation and stress relief in the scale/alloy system, thus reducing the driving force for spallation.

3. CHANGE IN THE MECHANISM OF OXIDATION

Several researchers[38,45,50,55-69] had reported that reactive element additions to chromia forming alloys promote oxidation by diffusion of oxygen to the alloy/scale interface, by suppressing the outward diffusion of chromium to the scale/gas interface. The oxide scale growth location thus changes from scale/gas interface to the scale/alloy interface. This is believed to help reduce the oxide scale growth rate. This is schematically shown in Figure 4.

Several methods involving platinum markers[48], platinum ink markers[44], gold markers[44,55], painted Engelhard platinum strips[50], and sequential oxidation in $^{18}O_2$ and $^{16}O_2$ followed by SIMS analysis[57,59,63-68,95] were used to determine the mechanism of scale growth. Location of the markers at the oxide/gas interface in alloys containing reactive elements, as opposed to markers found at the metal/oxide interface for alloys not containing reactive elements, indicated that oxide growth was predominantly due to inward diffusion of oxygen in alloys containing reactive elements. Sequential oxidation of yttrium implanted chromium in $^{16}O_2$ and then in $^{18}O_2$ resulted in the higher concentration of $^{18}O_2$ at the metal/scale interface, as determined by SIMS sputter-depth profiling[57,59], suggested that the mechanism of oxide growth had changed from predominant outward chromium diffusion to predominant inward oxygen transport. Similar results were reported by other authors for Ni-base[58,63] and Fe-base[64,65,67,68,95] chromia forming alloys.

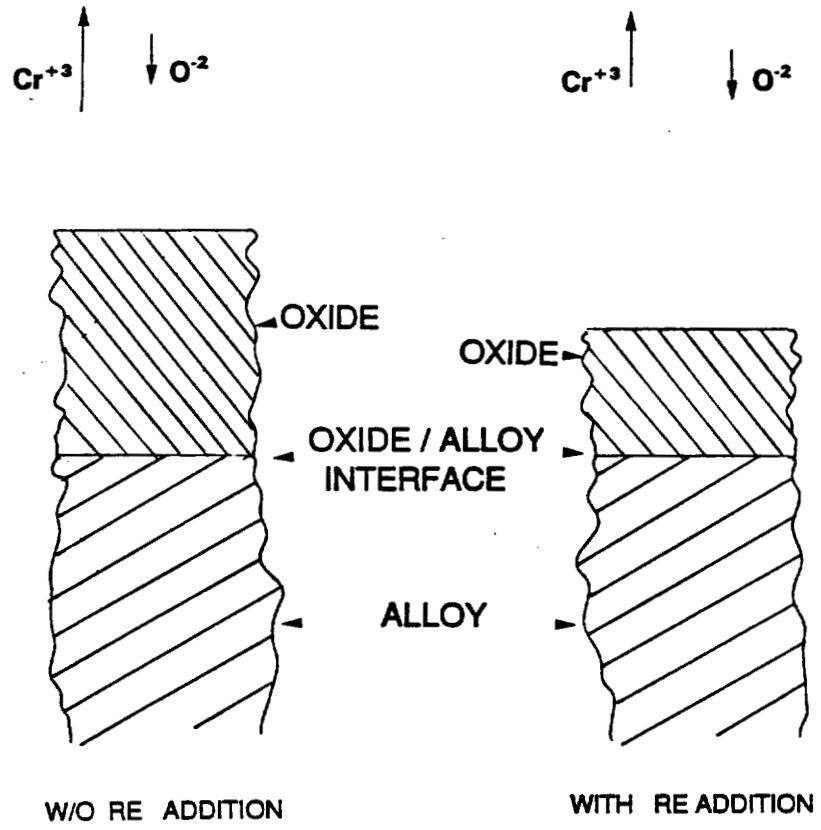

SCHEMATIC ILLUSTRATION OF CHANGE IN THE MECHANISM OF OXIDE GROWTH

Figure 4

Schematic illustration of the change in the mechanism of oxidation from predominant cation transport out to predominant anion transport in

4. REDUCTION IN THE OXIDE SCALE GRAIN SIZE

One of the reported reactive element effects in chromia forming alloys is the reduction in the oxide scale grain size due to the addition of reactive elements. Several investigators[24,38,44,50,56,60-62] had suggested reduction in the grain size of the oxide scale as a possible reason for the improved oxidation resistance of high temperature alloys, as this may improve the plasticity of the scale and thereby improve scale adherence. Results reported in the literature[56,61,62] suggest that reactive element additions to high temperature alloys do not cause a decrease in the grain size of chromia scale through its entire thickness, but it just causes a decrease in the grain size of the oxide scale at the scale/gas interface i. e. the first formed oxide. The grains away from the scale/gas interface and near to the alloy/scale interface were found to be more elongated and columnar in shape[56,61].

5. REDUCTION IN THE AMOUNT OF CHROMIUM REQUIRED FOR PROTECTIVE SCALE FORMATION

In the case of chromia formers, the reactive element addition reduced the amount of chromium required in the alloy to form a protective chromia scale[4,30,40,41,56]. Rhys-Jones and Grabke[41] showed by thermogravimetric analysis that, additions of Ce and dispersion of CeO_2 in Fe-Cr alloys reduced the oxidation rates, and the amount of Cr required to produce a continuous layer of Cr_2O_3. The oxidation rate for the Fe-10Cr-0.9Ce alloy was found to be lower than that for Fe-20Cr alloy after 70 hours at 1273 K in 13.33 kPa O_2 and the same was the case with Fe-20Cr-0.9CeO_2 and Fe-20Cr alloy.

Although reduction in the amount of Cr required for protective scale formation is claimed to be one of the beneficial effects as a result of RE additions, this aspect has not been studied in greater detail for binary chromia forming alloys with ternary additions of reactive elements.

H. SUMMARY OF LITERATURE

Following is a summary of the results reported in the literature on the RE effects in chromia forming high temperature alloys.

a) RE additions in any form such as metallic additions, ion-implantation, oxide dispersion or surface coating, in general improve the oxidation resistance

b) The ability of the reactive elements to improve the oxidation resistance differs from one element to another, and the reasons for this phenomenon are not clearly understood

c) No single mechanism has been found so far, which may be able to explain all the beneficial RE effects, irrespective of the method of adding the reactive elements

d) Minor quantities (ppm) of sulfur drastically reduce the oxidation resistance of chromia forming alloys. Simultaneous addition of reactive elements seem to negate the deleterious effect of sulfur. The compounds which may be formed when the reactive elements tie up the sulfur have not been conclusively determined. Furthermore, it is not clearly understood, whether the absence of sulfur, or whether the RE additions improve the oxidation resistance.

A substantial amount of work has been done on the RE effect on the chromia forming alloys, and it is clear that a wide variety of reactive element additions result in the reduction in the oxide growth rate and an improvement in the adherence of the oxide scale. However, several questions have remained unanswered.

What happens to the reactive elements when they are added to the alloy during alloy preparation? There is no data in the literature on the reactive element effect, regarding the form in which the reactive elements may be present in the alloy, when they were added as metallic alloying additions. Do they form a substitutional solid solution with the elements of the alloy matrix, or do they form any intermetallic compounds? How are they distributed in the alloy, prior to oxidation? If the reactive elements do form compounds with the elements of the alloy, do these

compounds remain stable at the temperature of oxidation? Do these compounds react with the chromium oxide? Does sulfur have any role in the oxidation kinetics of the alloys? In what form do the reactive elements tie up the sulfur? Do the reactive elements segregate preferentially to the oxide/alloy interface during oxidation? Why do different reactive elements show a variation in their effectiveness in imparting their beneficial influence on the oxidation resistance?

The beneficial effects of reactive element additions have been questioned recently by some researchers. It was shown by some investigators that sulfur when present as an impurity in the alloy was detrimental to the oxidation resistance and merely reducing the sulfur content improved the oxidation resistance of the alloy. Here again it is not clear whether 1-2 ppm S was a threshold limit above which, sulfur would start imparting its deleterious effect on the oxide scale adherence. In some instances removal of sulfur from the alloy was achieved by annealing the alloy specimens in hydrogen. The effect of hydrogen on the alloy itself was not answered.

In some studies reduction in the sulfur content in the alumina forming alloys was achieved by repeatedly oxidizing and grinding the oxidized alloy surface, untill the sulfur level had reduced significantly. It was not clear whether by grinding away the oxide repeatedly, the Al concentration on the alloy surface had been depleted, and whether this may affect the final result. It may be noted that the effect of sulfur when present as an impurity, has been studied for chromia forming alloys such as Fe-Cr and pure Cr; Ni-Cr system has not been studied in greater detail.

With regard to the tools used to study the reactive element effect, significant work was done using SIMS and Auger Electron Spectroscopy (AES), among other techniques, to determine the distribution of the reactive elements and sulfur, in the oxide scale. Very little seems to have been done using transmission electron microscopy, to characterize the base alloy and the oxide scales grown on them. The purpose of this work was to use transmission electron microscopy as a tool to study the reactive element effect. Availability of the database for the crystal structure of various compounds, and the computer program Desktop Microscopist™, was expected to facilitate the rapid identification of phases.

CHAPTER 2

EXPERIMENTAL WORK

The experimental work involved: the preparation of alloys, preparation of specimens for oxidation experiments and electron microscopy, setting up of the equipment for continuously recording oxidation kinetics data, simulation of the reactions which may be taking place in the oxide scales and at the oxide/metal interface, scanning electron microscopy, transmission electron microscopy and electron diffraction analysis.

A. PREPARATION OF THE ALLOYS

Approximately 150 g of high purity nickel pellets, chromium flakes and yttrium metal were weighed in appropriate proportions and melted in a conventional arc melting furnace (Figure 5) under argon atmosphere using a non-consumable water cooled tungsten electrode. The starting materials Ni and Cr were analyzed for sulfur content, which was found to be approximately 50 ppmw and 30 ppmw, respectively. The sulfur content of the starting materials Ni and Cr was determined using a Leco CS-244 carbon and sulfur analyzer. Approximately 0.5 g of the sample was combusted in an oxygen stream. The infrared absorption of the SO_2 in the resultant gas was measured and converted to concentration of sulfur using calibration curves.

Alloys of the nominal composition Ni-25wt%Cr and varying yttrium content were prepared. A water cooled copper crucible was used to melt the alloys. The alloy buttons were remelted 3 times to ensure that the ingredients of the alloy did not remain segregated. The solidified alloy buttons were removed from the crucible between every remelting operation and cleaned ultrasonically in acetone followed by cleaning with ethanol. Approximately twice the amount of desired yttrium level in the final alloy, was added to the Ni pellets and the Cr flakes before melting.

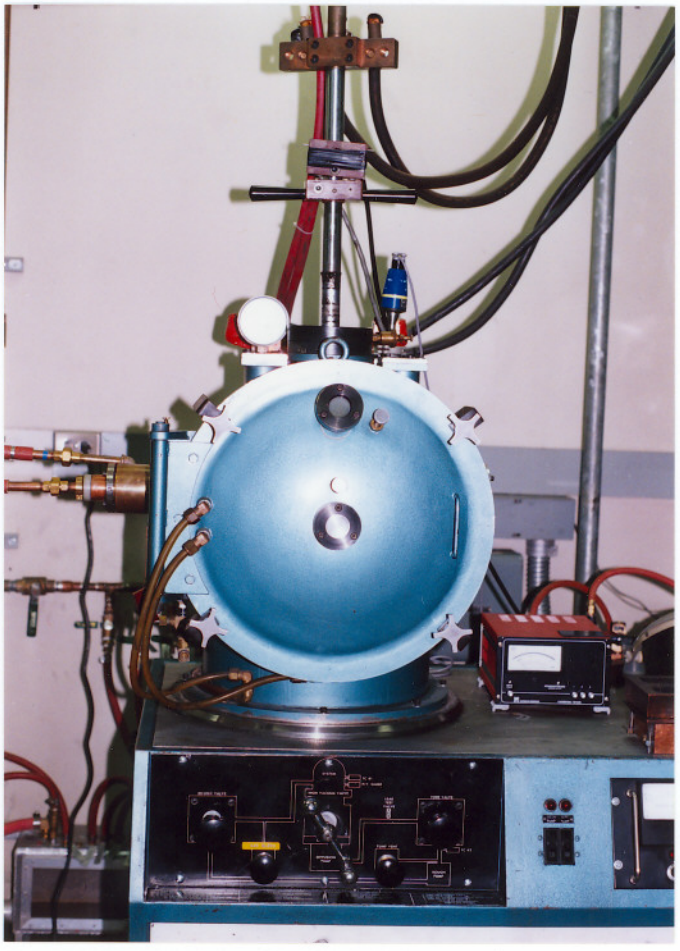

Figure 5

Arc melting furnace used for the preparation of the alloys

The remelted alloy buttons were placed in nickel crucibles and the crucibles were then kept in the tungsten Brew furnace. The furnace was then heated to a temperature of 1100°C and the homogenization treatment was carried out in vacuum (2.667×10^{-3} Pa or 2×10^{-5} torr) for a period of 48 hours. Use of the nickel crucibles eliminated any possibility of the contamination of the alloy. One specimen of the size 2x2x20 mm was cut from each alloy and sent for chemical analysis, by the glow discharge mass spectroscopy (GDMS) technique, to Charles Evans & Associates, California. Compared to the other techniques of analyzing the alloys for chemical composition, GDMS was reported to be more reliable, and the results were found to be reproducible with significant accuracy[94]. A few comments about the analytical techniques used to analyze sulfur are relevant and appropriate.

Traditionally, fusion techniques have been used to analyze bulk sulfur in alloys. Although widely succesful in support of the ferrous metals industry, fusion techniques have yielded unsatisfactory results in the sulfur analysis of metal matrices, such as those investigated in this study[94]. After many experimental studies, sulfur analysis based on Auger surface techniques were discounted as being unable to yield reliable or reproducible bulk sulfur contents in multiphase alloys containing reactive metals[94]. The sulfur analysis was found to be highly dependent on the phase being analyzed by the Auger spectrometer; accordingly, the alloy microstructure became an important variable[94].

As a result of several analyses on many different specimens, GDMS was found to have adequate precision to measure the sulfur contents below 50 ppm, and as low as 1-2 ppm by weight[94]. Since alloys containing sulfur levels of ~ 100 ppmw and ~ 5 ppmw were to be made for this study, it was thought necessary to analyze the alloys for chemical composition by GDMS.

B. OXIDATION EXPERIMENTS

1. SPECIMEN PREPARATION

Coupons measuring approximately 5x5x1 mm from each alloy, were cut using a high speed saw and then polished using 600, 800 and 1200 grit SiC polishing paper. The specimens were then polished using 9 μm, 5 μm and 1μm SiC lapping paper. All the polished specimens

were ultrasonically cleaned in acetone followed by cleaning in ethanol and then dried using a blower.

2. SHORT TERM OXIDATION

A Lucifer furnace was used for these experiments. The furnace was brought up to the required temperature before inserting the specimens in it. From each alloy, 2-3 specimens were oxidized in air at 900°C and 1000°C for a period ranging from 2 minutes to 2 hours. The specimens were placed vertically in a platinum crucible and the crucible was then placed in the furnace. This eliminated any possibility of contamination of the alloy surface prior to oxidation. The contamination by Pt was also kept minimal by placing the coupons vertically in the crucible. The oxidized specimens were saved for further analysis.

3. LONG TERM OXIDATION

Oxidation kinetics of all the alloys was measured at a temperature of 900°C in air for a period of 24 hours. A SATEC split type furnace capable of operating at a maximum temperature of 1150°C was used for these experiments. The furnace was mounted vertically on a vertically moving fixture powered by an electric motor. The dimensions of two coupons from each alloy were measured with a vernier guage prior to carrying out the oxidation kinetics experiments on them. The total surface area of each of the specimens was calculated, including the area on the thin edges of the specimens. A CAHN D-200 microbalance (Figure 6) capable of continuously measuring weight changes as small as 0.1 μg was used to acquire the weight change data at an interval of 10-30 seconds, and the data was recorded using an IBM PC compatible computer.

Schematic illustration of the principles of operation and the weighing unit of the microbalance is shown in the Figures 7a and 7b. The software required to record the weight change data was supplied by CAHN Instruments, Inc. along with the microbalance.

The microbalance (Figure 7a) may be described as a force-to-current convertor. Weights or forces to be measured are applied to the sample (left) side of the beam which produces a force about the axis of rotation. An electric current flowing in the torque motor also produces a force

Figure 6

Setup of the furnace and the microbalance

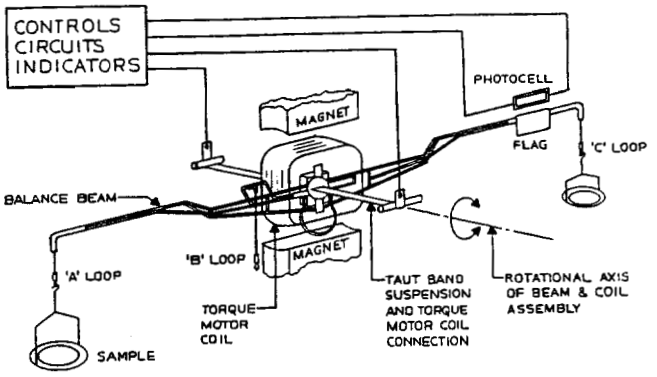

a) Principles of operation

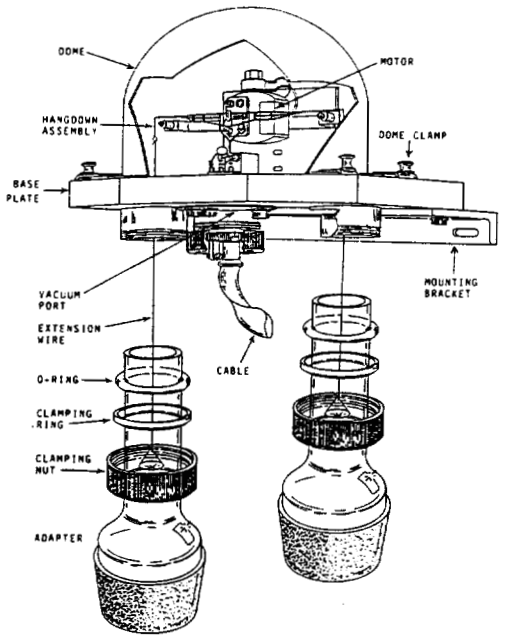

b) Weighing unit

Figure 7

Schematic illustration of the microbalance. a) Principles of operation, and b) Weighing unit

about the same axis which is equal and opposite to the force from the beam if the beam is at the beam reference position. This reference position is detected by the beam position sensing system. A greater force on the beam will require a greater opposite force from the torque motor in order to maintain the beam at its reference position. Therefore the current necessary to produce the required torque motor force is a direct measure of the force on the beam. The process of calibration allows this current to be measured in units of weight (grams) or force (dynes).

A quartz tube 25 mm in diameter and about 2 m long with a 40 mm opening at one end and 5 mm opening at the other end, was attached to the adapter assembly on the microbalance. The adapter assembly was aligned with the 'A' arm on the balance (Figure 7b). The tube was then aligned vertically and fixed to a support. The microbalance was calibrated in accordance with the procedure laid out in the instruction manual for the balance.

One coupon at a time from each of the alloys was kept horizontally in a quartz bowl 12 mm in diameter, and the bowl was attached to one end of an oxidation resistant wire supplied by CAHN Instruments. The bowl was then introduced into the quartz tube through the 'A' port of the balance and hung on to the 'A' arm of the balance. Care was taken to ensure that the bowl did not touch the quartz tube. The furnace was brought up to the required temperature and then moved vertically in order to position the specimen at the center of the hot zone of the furnace. The weight gain data at 900°C in air was then recorded at an interval of 10-30 seconds for a period up to 24 hours. The oxidized coupons were saved for further analysis.

The oxidation kinetics data was saved on a diskette and converted in to a format suitable for analyzing on the Macintosh personal computer using the software program Soft PC available for the Macintosh computers. The kinetics data was then analyzed and plotted using the software program Kaleidagraph available on the Macintosh computer. The average weight gain per unit area (mg/cm^2) was calculated from the 2 sets of data points recorded for each alloy, and was plotted as a function of time in seconds.

The weight gain/area data points were then fitted to a parabolic curve with an equation of the type $y = a + b(x^{½})$. The equation which gave the value of the regression coefficient, R, very close to 1, was accepted as the best fit. The parabolic rate constant was then calculated by

calculating the slope of the parabolic curve at t = 86400 s (24 hours). The weight gain data for each of the alloys at the end of 24 hours was also calculated using the equation which best fitted the weight gain/area data for each alloy.

4. THERMAL CYCLING OF THE OXIDIZED ALLOYS

The coupons of yttrium free alloys spalled upon cooling to room temperature after exposure at 900°C in air for 24 hours, and hence they were not cycled thermally. The coupons of the yttrium containing alloys oxidized at 900°C in air for 24 hours were thermally cycled in the following manner.

An oxidized alloy coupon was placed in the 12 mm diameter quartz bowl, and the bowl was tied to a heat resistant wire. The wire was then hung in the 'A' arm of the microbalance, and the alloy coupon was positioned in the center of the hot zone of the furnace. The furnace was brought up to a temperature of 900°C, before inserting the specimen in the furnace. The specimen was held in the furnace for a period of 15 minutes and then removed from the furnace, and brought to room temperature and held at room temperature for 5 minutes. The surface of the specimen was then observed in the scanning electron microscope. After observation of the specimen in the scanning electron microscope, the specimen was then again inserted into the furnace by the procedure described above. This procedure was followed ten times.

C. SCANNING ELECTRON MICROSCOPY

A Zeiss digital scanning electron microscope (SEM) model DSM 960 fitted with a LINK windowless detector for EDX analysis, was used (Figure 8). Alloy specimens ground and polished to 1 μm finish using 1 μm SiC lapping film, oxidized specimens, and thermally cycled specimens were observed in the SEM. Cross section specimens of the yttrium containing alloys oxidized at 900°C for 24 hours were also prepared and observed in the SEM. Some specimens prepared for transmission electron microscopy were also observed in the SEM. An operating voltage of 10-20 kV was used. Spot EDX analysis and x-ray mapping techniques were used. The procedure used to prepare cross section specimens for observation in the SEM is described below.

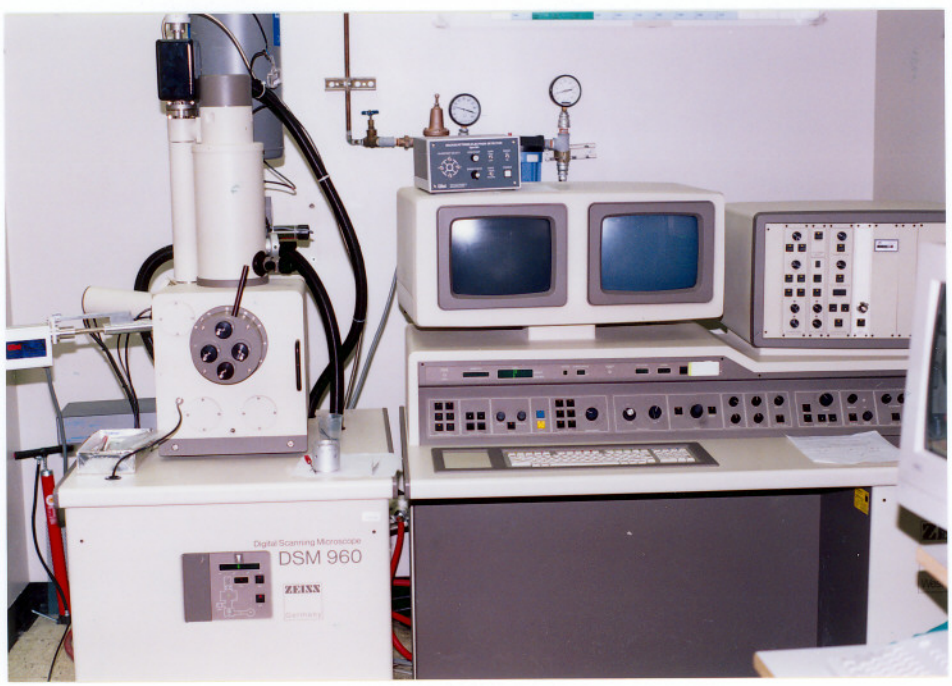

Figure 8

Zeiss DSM 960 scanning electron microscope used in this study

Oxidized coupon of the alloy was cut into 2 pieces using the slow speed saw. The cut pieces were thoroughly cleaned ultrasonically in acetone and then in ethanol, and dried. The oxidized surfaces of both the cut pieces were glued to each other by means of a thermosetting wax. The cut pieces were then glued on to a grinding stub by means of wax so that the oxide surfaces were perpendicular to the flat surface of the grinding stub. The stub was then placed in a stub holder and the specimen was ground using 9 μm, 5 μm and 1 μm SiC lapping film. The polished surface of the specimen was then observed in the SEM.

D. TRANSMISSION ELECTRON MICROSCOPY

A Hitachi H-800 transmission electron microscope (TEM) fitted with a Tracor Northern EDX detector capable of detecting sodium and elements higher in atomic number than sodium, was used (Figure 9). A Philips CM20 TEM fitted with a LINK windowless EDX detector was also used. This microscope was made available by the Canadian National Research Council, Ottawa, Canada. The specimens were observed in the TEM in the imaging mode and in the scanning transmission electron microscope (STEM) mode, and SEM mode. Diffraction patterns and the EDX spectra obtained from several specimens were recorded. An operating voltage of 200 kV and a C2 condenser aperture with a diameter of 150-30 μm was used. Beam diameter varying between 3 μm and 0.1 μm was used for recording the electron diffraction patterns and for acquiring the EDX spectra. Semi-quantitative analysis of the EDX spectra was also carried out using the standardless metal thin film (SMTF) analysis software available on the Tracor Northern system.

The calibration of the Hitachi H-800 microscope was carried out using pure aluminum specimen. The objective lens current of 4.041 amperes used during the calibration of the Hitachi H-800 microscope was used later on for recording the diffraction patterns from the various specimens observed. Similarly the objective lens current used for the calibration of the Philips CM20 microscope was used for recording the diffraction patterns.

Diffraction patterns were taken from several poles, typically 3-5 poles, from each particle observed in the TEM. This was the limit imposed by the limited tilt available on the microscope. The diffraction patterns were analyzed using the computer program Desktop Microscopist™. The

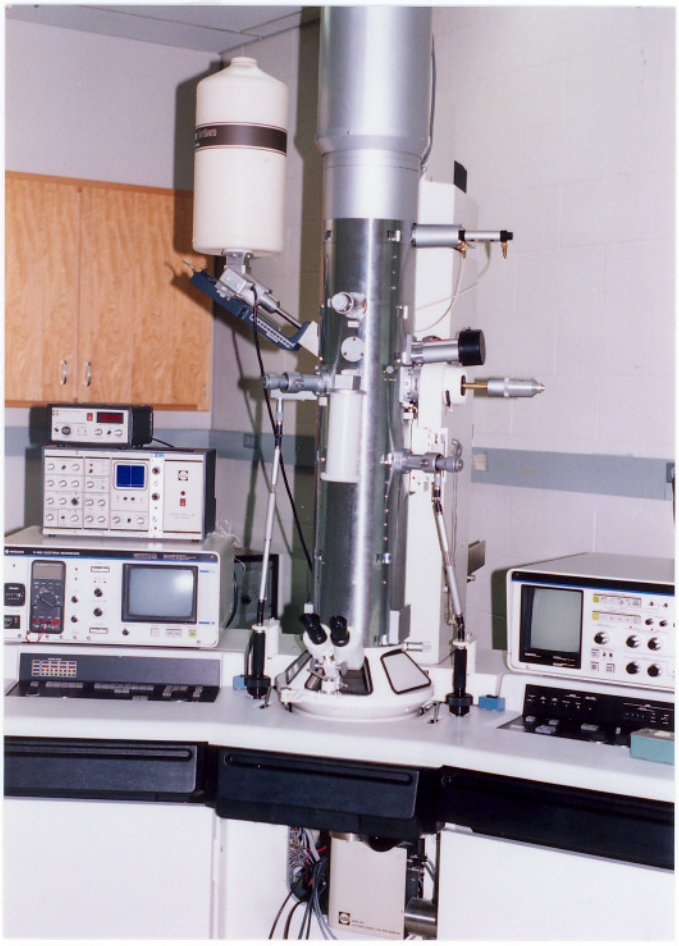

Figure 9

Hitachi H-800 transmission electron microscope used in this study

reduced unit cell volume calculations[97] were also made using the program Desktop Microscopist™, from the diffraction patterns where the higher order laue zones could be obtained. The EDX analysis was also performed on each of the particles from which the diffraction patterns were taken. No attempt was made to carry out convergent beam electron diffraction (CBED) analysis.

The various compounds identified in this study were identified on the basis of the best match found in the published literature for the d-spacings and the reduced unit cell volume of crystals. A list of potential compounds which best fitted the experimentally calculated d-spacings and the reduced unit cell volume, was assembled by searching the database for the crystals, using the computer program Desktop Microscopist™. The information from the EDX analysis was used to narrow down the list of possible compounds. The lattice parameters and the Wyckoff positions of the atoms in the crystal whose d-spacings and the reduced unit cell volume best fitted the experimental data, were fed into the program, and the electron diffraction patterns were generated. The experimentally recorded zero order laue zone (zolz), and higher order laue zone (holz) diffraction patterns and the angles between the different zones along which the diffraction patterns were taken, were then matched with the computer generated diffraction patterns and the angles between the zones calculated by the program.

The nomenclature used to describe the various crystal systems and the various space groups which are used to describe the crystal symmetry are described in detail in the literature[98,99]. The formulae used to calculate the reduced unit cell volume and the distance between the planes for different crystal systems may be found in the literature[98,99].

1. PREPARATION OF SPECIMENS

One of the methods used for preparation of the specimens from the oxidized alloys was to scrape the oxidized surface, and collect the powder on to a carbon coated copper grid. The other two methods of specimen preparation were : ion-milling in argon atmosphere and the dissolution of alloy in the iodine-methanol solution.

a. Ion-milling

An Ion Tech Teddington U.K Ltd. ion-milling machine (Figure 10) was used to make the electron thin specimens from the homogenized alloys. The procedure followed for the preparation of electron thin specimens using ion-milling technique is described below. Prior to thinning the specimens in the ion-milling machine, the alloy coupons were ground from both the sides to a thickness of approximatly 100 μm. 3 mm discs were then punched from the thin foils for further thinning.

A 3 mm specimen disc was glued on to the stub of the grinding jig by means of a low melting wax, and then ground using 9 μm, 5 μm and 1 μm silicon carbide lapping film, in that order. The surface of the ground specimen was cleaned with ethanol. A 3 mm diameter molybdenum washer, 0.15 mm in thickness with a 1 mm diameter central hole, was then glued on to the 3 mm specimen disc, by means of superglue. Care was taken to ensure that the washer exactly fitted on to the specimen, so that the entire specimen surface was covered by the washer.

The washer with the specimen side up, was then glued on to the stub of the grinding jig. The specimen thus mounted on the stub was then ground using 9 μm, 5 μm and 1 μm silicon carbide lapping film, in that order. The specimen was ground till its thickness was approximately 30 μm. The stub was then heated in order to melt the wax which held the washer. The washer with the specimen glued on one of its sides was removed from the stub. The washer-specimen composite was cleaned in acetone and then in ethanol. Another washer was then glued on to the ground and polished specimen surface, by means of superglue. Care was taken to ensure that the washer covered the entire surface area of the specimen.

This washer-specimen-washer composite was then thinned in the ion-milling machine from both the sides of the specimen, using research grade argon gas. Both the ion guns were tilted at an angle of 15-20 degrees to ensure a gradual thinning of the specimens. The voltage used varied from 4 to 6 kV and the ion current varied from 0.08 to 0.1 mA. The specimens had to be ion-milled for a period ranging from 10 hours to 15 hours, to obtain a sufficient thin area in the specimen for TEM investigation.

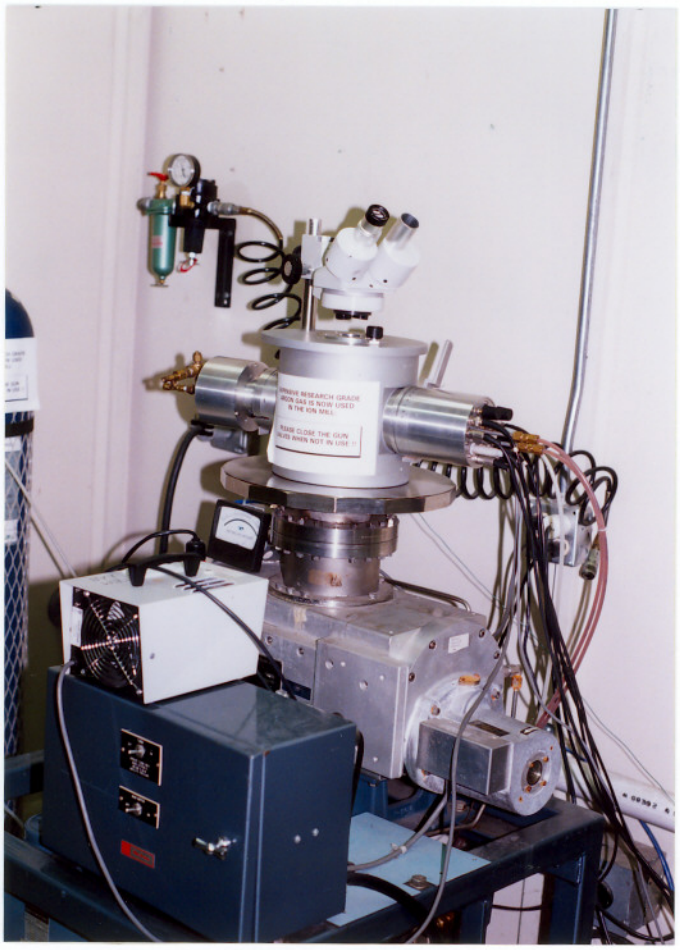

Figure 10

The Ion-Tech Teddington ion-milling machine used in this study

b. Alloy Dissolution

One specimen at a time from each of the homogenized alloys was kept in a Pt cage (made from Pt gauze) and the cage was dipped in the iodine-methanol (100 g iodine in 1000 ml anhydrous methanol) solution in a stripping apparatus (Figure 11). The specimen was left in the solution for a period of 24 to 48 hours for the dissolution of the alloy. The residue left in the Pt cage after the dissolution of the specimen was flushed with anhydrous methanol in a dish and collected on a carbon coated copper grid. The copper grids used were purchased from Ernest M. Fullam, Inc. This method has been used by other researchers[64,100-105] for the separation of the oxides from the alloy and for stripping the oxide films from the alloy substrate. The copper grids were then subsequently observed in the SEM and the TEM.

Procedure as described above was also used for stripping the oxide films from the substrate of the oxidized specimens. The oxide films were collected on folding type copper grids which were also purchased from Ernest M. Fullam, Inc. The grids were then observed in the TEM.

E. SIMULATION EXPERIMENTS

Since yttrium oxysulfide, Y_2O_2S, was found in both the homogenized yttrium alloys, as well as in the oxide scales grown on these alloys, it was thought necessary that the stability of this species at temperature be determined, and the reactions of this species with Cr_2O_3 and Cr at higher temperature be studied. This would help in understanding the possible reactions which may be occurring in the oxide scale and at the alloy/oxide interface.

Since Y_2O_2S was not commercially available, powders of cerium oxysulfide (- 200 mesh) and lanthanum oxysulfide (- 200 mesh) which were commercially available, were used instead. It is known from the literature that the oxysulfides of yttrium, lanthanum and cerium are isostructural and have many identical properties[106-114]. Hence the observations made with the oxysulfides of cerium and lanthanum would be expected to be applicable to yttrium oxysulfide. All the powders used in this study were purchased from CERAC, Inc., except for Cr_2O_3 which was purchased from Plasma-Technik AG.

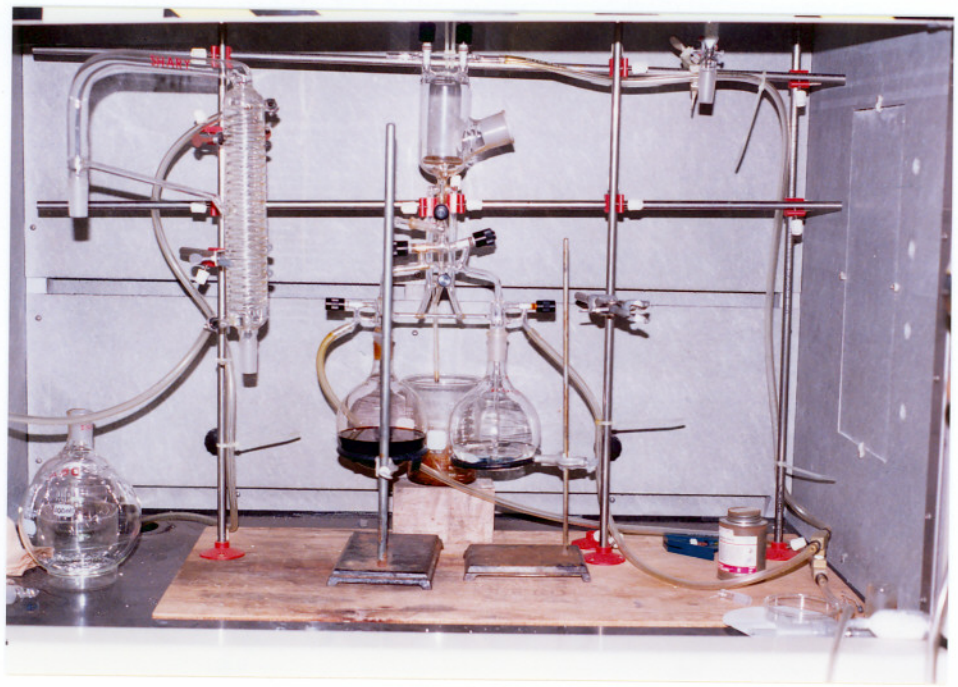

Figure 11

Oxide stripping apparatus used in this study

Each of the mixtures of Cr_2O_3 + 1wt% Ce_2O_2S, Cr + 1wt% Ce_2O_2S, Cr_2O_3 + 10wt% Cr + 1wt% Ce_2O_2S and Cr_2O_3 + 1wt% La_2O_2S, Cr + 1wt% La_2O_2S and Cr_2O_3 + 10wt% Cr + 1wt% La_2O_2S powders were mixed in heptane wax and a slurry was made. The size of Cr powder was - 325 mesh and that of the Cr_2O_3 was -45 +22 μm. The slurry was then compacted into 3 mm rods using a stainless steel mold with a 3 mm diameter hole in the center.

Heating the Cr_2O_3 + 1wt% Ce_2O_2S (or La_2O_2S) and the Cr + 1wt% Ce_2O_2S (or La_2O_2S) mixtures were expected to simulate the reactions of Y_2O_2S with chromia and the base alloy respectively. Heating the Cr_2O_3 + 10wt% Cr + 1wt% Ce_2O_2S (or La_2O_2S) mixture was expected to simulate the reactions which may be occuring at the alloy/scale interface.

The 3 mm diameter rods were then placed in a Pt crucible and the crucible heated in vacuum (2.667×10^{-3} Pa or 2×10^{-5} torr) in the tungsten Brew furnace at a temperature of 900°C and 1000°C, and also in air in the Lucifer furnace at 900°C and 1000°C, for a period of 1 hour. Heating the 3 mm rods in vacuum resulted in the crumbling of the rod into powder. A soild rod was obtained after heating the compacted rods in air. The powder formed by heating the 3 mm rods in vacuum was collected on copper grids coated with graphite on one side. Thin slices were cut from the rods which had remained as solid rods after heating them in air. Electron thin specimens were prepared from the thin slices, using the ion-milling procedure described above.

The thinned specimens were subsequently observed in the TEM. EDX analysis was performed on the thin areas of the specimen and electron diffraction patterns were taken from those thin areas of the specimen. Specimens for observation in the TEM and the STEM mode were also prepared by collecting fine particles from the air heated mixtures, on carbon coated copper grids.

Small amount (1 gm) of lanthanum oxysulfide powder was also heated in air in the SATEC furnace at 900°C in a Pt crucible for 30 minutes and 2 hours, and fine particles from the heated powder were collected on a carbon coated copper grid. This experiment was carried out to simulate the stability of yttrium oxysulfide at higher temperature. The copper grid was then observed in the TEM. EDX analysis was performed on the thin areas of the specimens. Electron diffraction patterns were also taken from the same thin areas of the observed specimens.

CHAPTER 3

RESULTS

A. CHEMICAL COMPOSITION OF THE ALLOYS

Table 1 shows the chemical composition of the homogenized alloys prepared and used in this investigation. Two yttrium free alloys, one with a very low sulfur content and the other with a high sulfur content were chosen. In addition to these alloys, three yttrium containing alloys with varying yttrium and sulfur content, were used in this study. The sulfur found in all the alloys was a result of several factors. The starting materials Ni and Cr had approximately 50 and 30 ppmw sulfur, which may have ended up in the final alloy. The other factors include the remelting of the alloys and the homogenizing treatment, both of which may introduce sulfur into the alloy. Other elements found in the alloys were also a result of the impurities present in the starting materials and/or a result of the remelting and homogenizing of the alloys.

B. OXIDATION KINETICS

1. YTTRIUM FREE ALLOYS

No significant difference was found in the weight gain/area of the Ni-25Cr-4.8 ppm S alloy and the Ni-29Cr-140 ppm S alloy at the end of 24 hours at 900°C (Figure 12). Both the alloys followed the parabolic rate law of oxidation (Table 2).

2. YTTRIUM CONTAINING ALLOYS

The Ni-22Cr-6200 ppm Y alloy had a lower weight gain/area compared to the Ni-31Cr-900 ppm Y and the Ni-23Cr-650 ppm Y alloy, at the end of 24 hours at the temperature of 900°C (Figure 13). All of the 3 alloys followed the parabolic rate law of oxidation. Table 2 gives the calculated parabolic rate constant for the yttrium containing alloys. While the difference in the

Table 1

Chemical composition of the alloys used in this study. All figures are in ppmw except for Ni and Cr which are in weight%

Element ---> / Alloy	C	O	S	Al	Si	Fe	Co	Cu	Ni	Cr	Y
Ni-25Cr	2.4	150	4.8	6	4.9	9.8	0.01	1.9	75%	25%	0
Ni-29Cr	51	57	140	4.5	200	87	490	6.3	79%	29%	0
Ni-23Cr-650 ppm Y	30	68	47	11	69	34	150	3.8	77%	23%	650
Ni-31Cr- 900 ppm Y	55	71	220	15	170	120	430	23	69%	31%	900
Ni-22Cr- 6200 ppm Y	210	200	29	11	440	55	420	20	78%	22%	6200

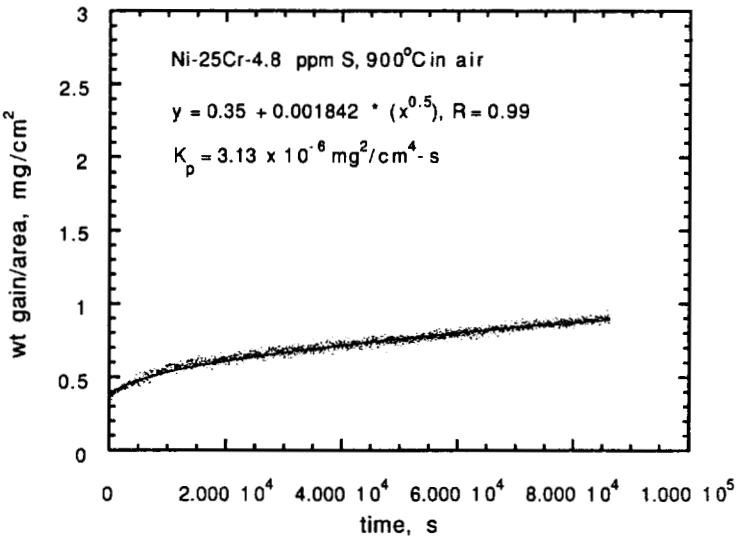

a)

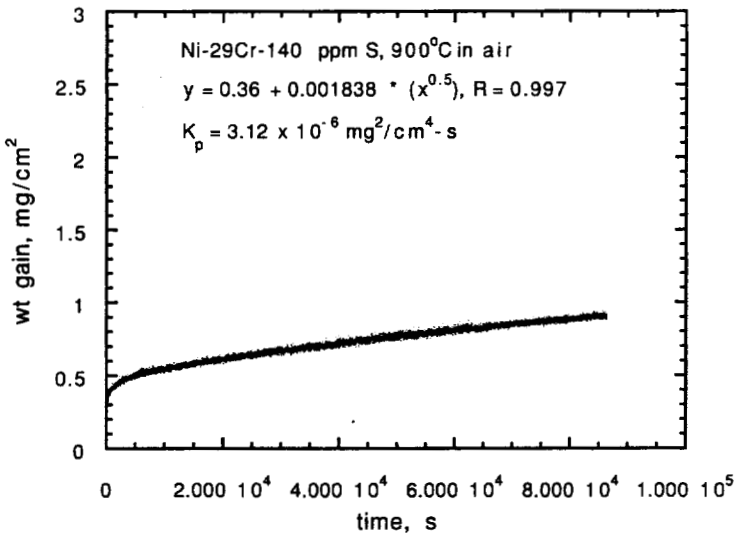

b)

Figure 12

Weight gain/area as a function of time for the a) Ni-25Cr-4.8 ppm S alloy, and b) Ni-29Cr-140 ppm S alloy oxidized at 900°C in air

Table 2

Parabolic rate constant at the end of 24 hours for the yttrium free and yttrium containing alloys oxidized at 900°C in air for 24 hours

Alloy Composition	Parabolic Rate Constant, K_p, mg^2/cm^4-s
Ni-25Cr-4.8 ppm S	3.13×10^{-6}
Ni-29Cr-140 ppm S	3.12×10^{-6}
Ni-23Cr-650 ppm Y	1.94×10^{-6}
Ni-31Cr-900 ppm Y	1.70×10^{-6}
Ni-22Cr-6200 ppm Y	7.74×10^{-7}

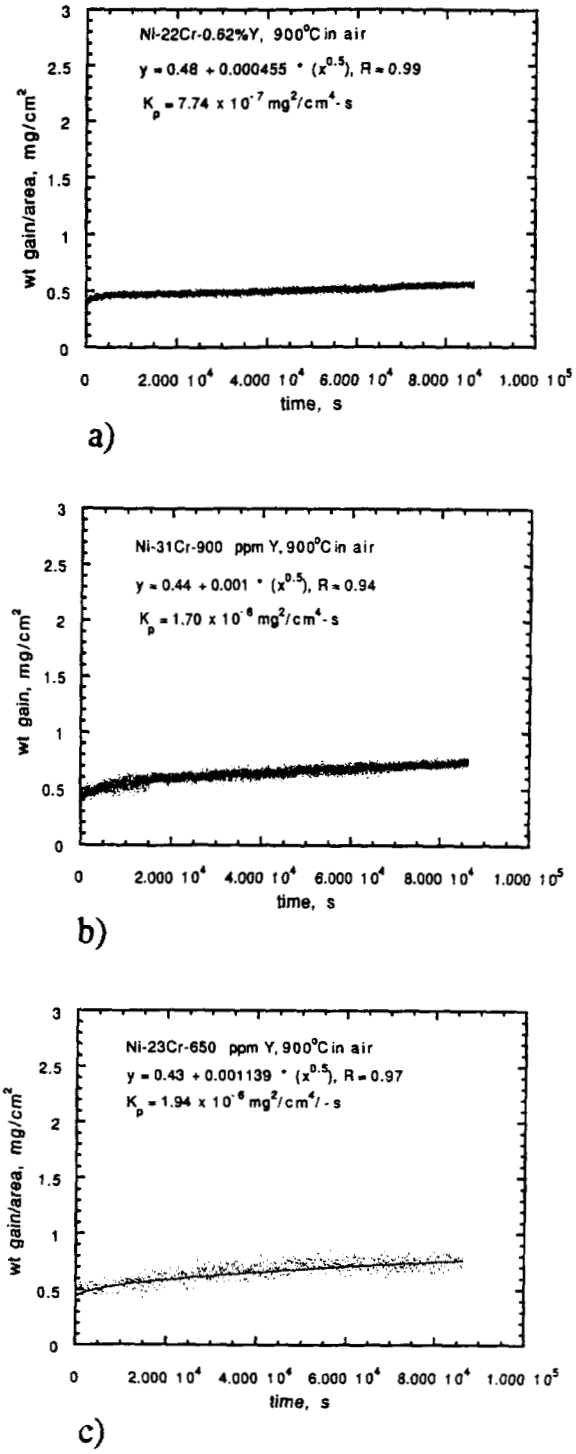

Figure 13

Weight gain/area as a function of time for the a) Ni-22Cr-6200 ppm Y alloy, b) Ni-31Cr-900 ppm Y alloy, and c) Ni-23Cr-650 ppm Y alloy oxidized at 900°C in air

rate constant for the alloys containing 650 ppm Y and 900 ppm Y was insignificant, the rate constant for the alloy containing 0.62%Y (6200 ppm Y) was lower by more than 50% compared with the former two alloys.

3. COMPARISON BETWEEN THE YTTRIUM FREE AND YTTRIUM CONTAINING ALLOYS

The weight gain/area for the yttrium containing alloys was lower than that for the yttrium free alloys at 900°C, at the end of 24 hour exposure (Figure 14). A comparison of the parabolic rate constant for all the alloys is shown in Figure 15. The parabolic rate constant for the yttrium containing alloys was lower than the yttrium free alloys. The parabolic rate constant for the 0.62% Y containing alloy was the lowest of all the alloys investigated.

C. THERMAL CYCLING OF THE OXIDIZED ALLOYS

1. YTTRIUM FREE ALLOYS

Both the yttrium free alloys exhibited spallation of the oxide scale at the end of the short and long durations of exposure at 900°C in air. The spalled regions on the oxide scale were visible with the naked eye. The oxidized specimens were thus not thermally cycled after they were removed from the furnace and cooled to room temperature. The specimens were then examined in the SEM.

2. YTTRIUM CONTAINING ALLOYS

The Ni-23Cr-650 ppm Y and Ni-31Cr-900 ppm Y alloys did not exhibit spallation of the oxide scale even at the end of 24 hours of exposure at 900°C in air. However, oxide spallation was observed when the specimens from these two alloys were thermally cycled twice at 900°C in air and then observed in the SEM. The spalled regions on the oxide scale were not visible with the naked eye. The SEM micrographs of the spalled regions from these two alloys are shown in the section on scanning electron microscopy. The Ni-22Cr-0.62Y alloy however did not exhibit oxide spallation even at the end of 10 thermal cycles at 900°C in air.

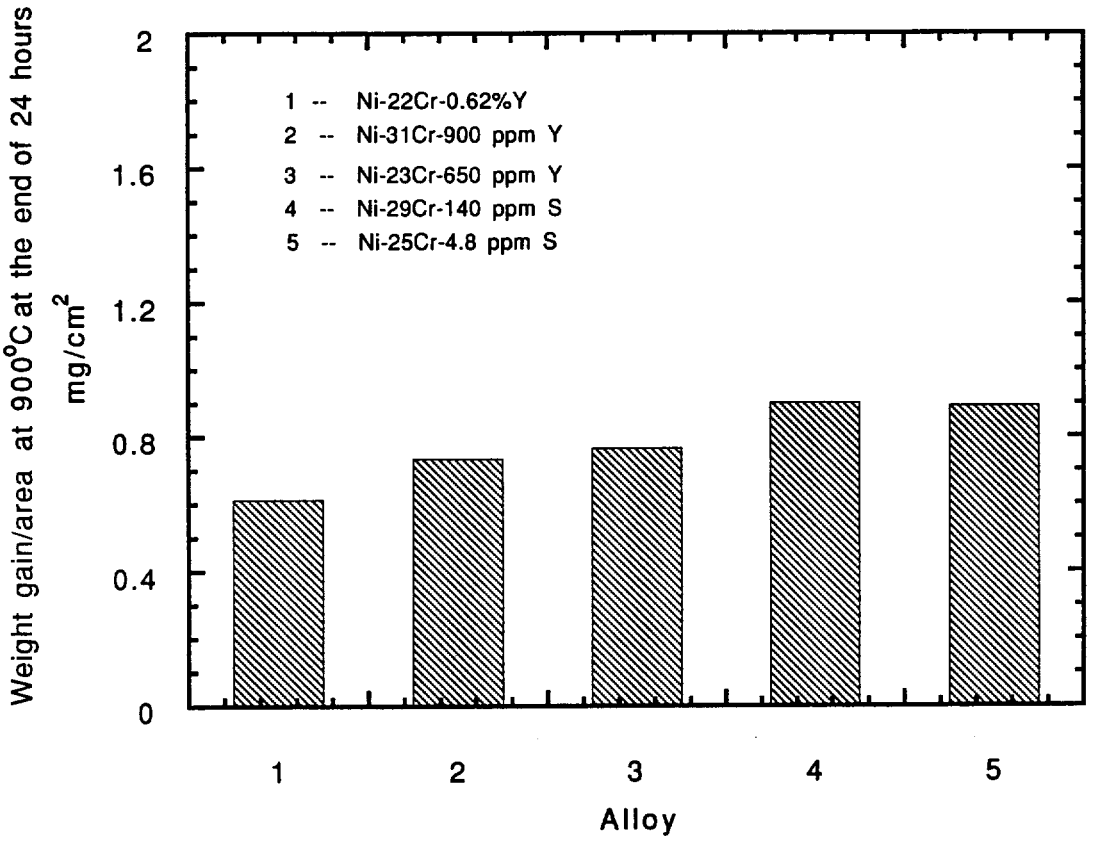

Figure 14

Weight gain/area at the end of 24 hours at 900°C in air for all the alloys investigated

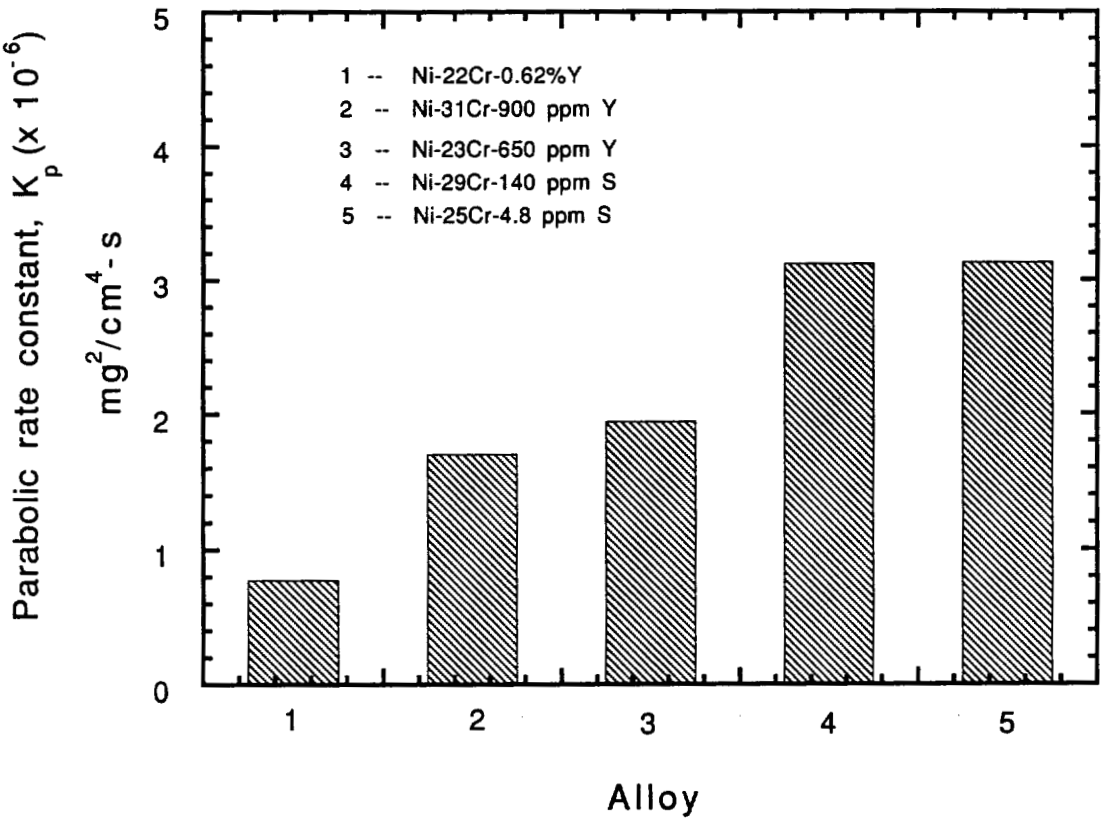

Figure 15

Comparison of the parabolic rate constant at the end of 24 hours for all the alloys oxidized at 900°C in air for 24 hours

D. SCANNING ELECTRON MICROSCOPY

1. HOMOGENIZED YTTRIUM FREE ALLOYS

The as-homogenized yttrium free alloys exhibited only a one phase structure consisting of Ni and Cr. Similar structure was observed in the Ni-29Cr-140 ppm S alloy. No elements other than Ni and Cr were observed along the grain/dendrite boundaries of both the alloys.

2. HOMOGENIZED YTTRIUM CONTAINING ALLOYS

The polished specimens of the yttrium containing alloys were observed in the SEM (Figure 16a). In all the three yttrium containing alloys investigated, yttrium and nickel rich regions were observed along the alloy grain boundaries and the interdendritic regions (Figure 16b). A similar microstructure and the EDX spectrum was observed in the case of the Ni-31Cr-900 ppm Y alloy.

SEM micrograph (Figure 16c) and the EDX spectrum (Figure 16d) showed that yttrium had segregated along the grain/dendrite boundaries in the as-homogenized and polished Ni-22Cr-0.62Y alloy. SEM micrograph (Figure 17a) and the x-ray map of yttrium (Figure 17b) also showed that yttrium had segregated along the alloy grain/dendrite boundaries.

Particles rich in sulfur and oxygen, in association with yttrium were also found in all the yttrium containing alloys. Figures 18a and 18b show the micrograph and the EDX spectrum obtained from a Y-S-O rich particle found in the as-homogenized ion-milled Ni-23Cr-650 ppm Y alloy.

a. Alloy Dissolution

The specimens prepared for TEM analysis from the residue collected by dissolving the as-homogenized yttrium containing alloys in the iodine-methanol solution, were observed in the SEM. Particles globular in morphology and rich in oxygen, sulfur and yttrium, were identified using EDX analysis. Shown in the Figures 19a and 19b are the micrographs of a Y-S-O rich

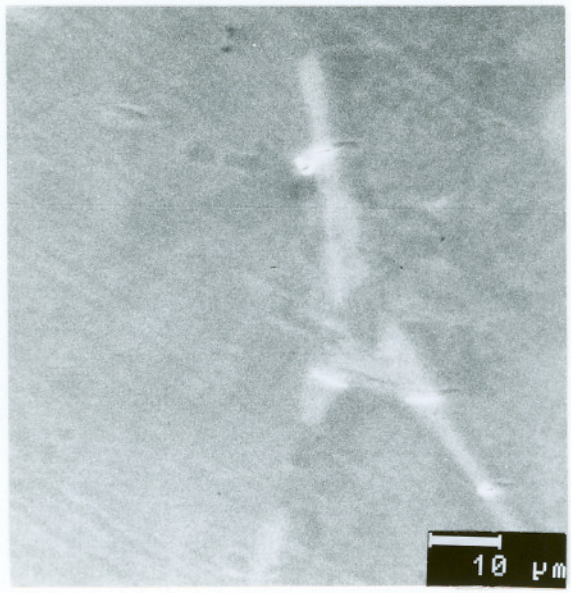

a)

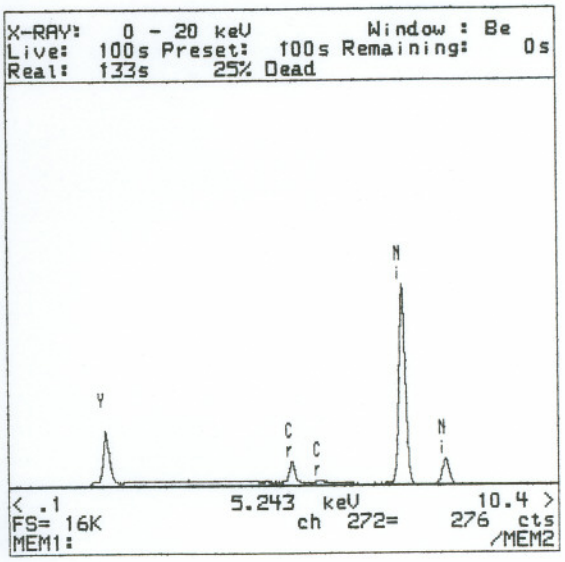

b)

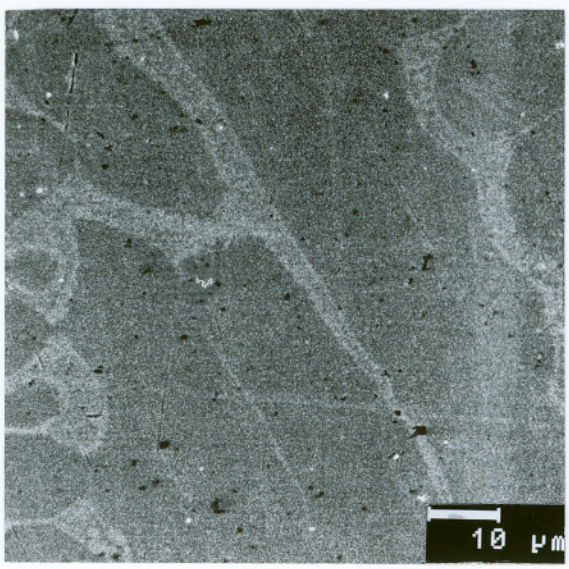

c)

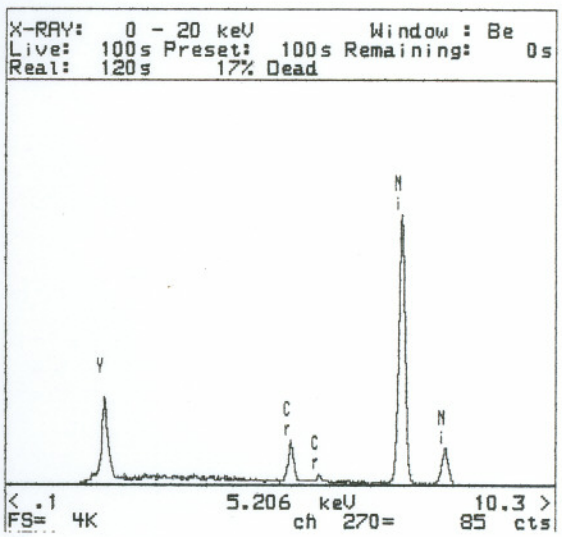

d)

Figure 16

a) SEM micrograph of the as-homogenized and polished Ni-23Cr-650 ppm Y alloy, and b) EDX spectrum obtained from the grain/dendrite boundary area, c) SEM micrograph of the as-homogenized and polished Ni-22Cr-0.62Y alloy, and d) EDX spectrum obtained from the grain/dendrite boundary area

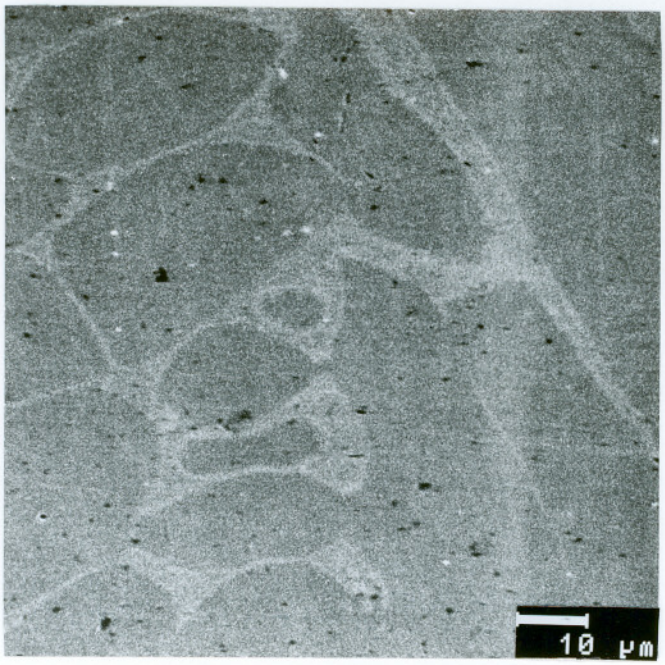

a)

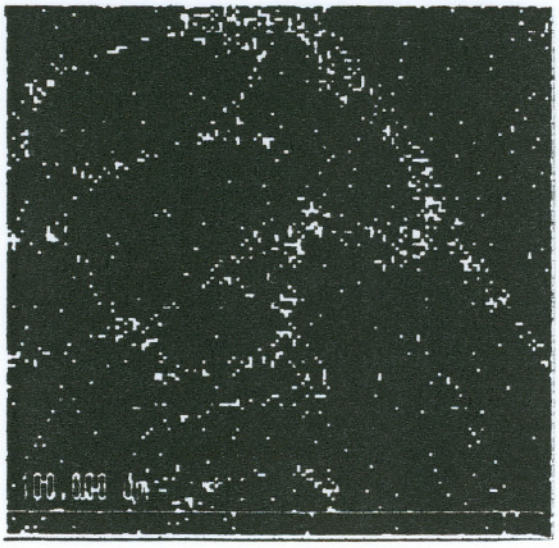

b)

Figure 17

a) SEM micrograph and, b) x-ray map of Y taken from the as-homogenized and polished Ni-22Cr-0.62Y alloy

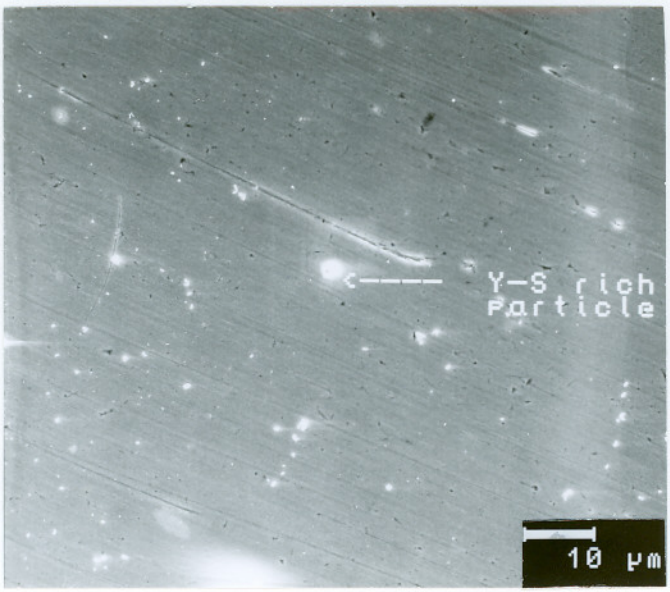

a)

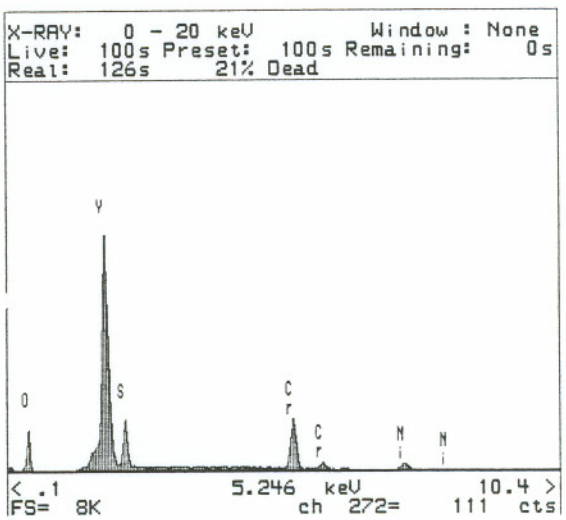

b)

Figure 18

a) SEM micrograph, and b) EDX spectrum obtained from the Y-S-O rich particle found in the ion-milled as-homogenized Ni-23Cr-650 ppm Y alloy

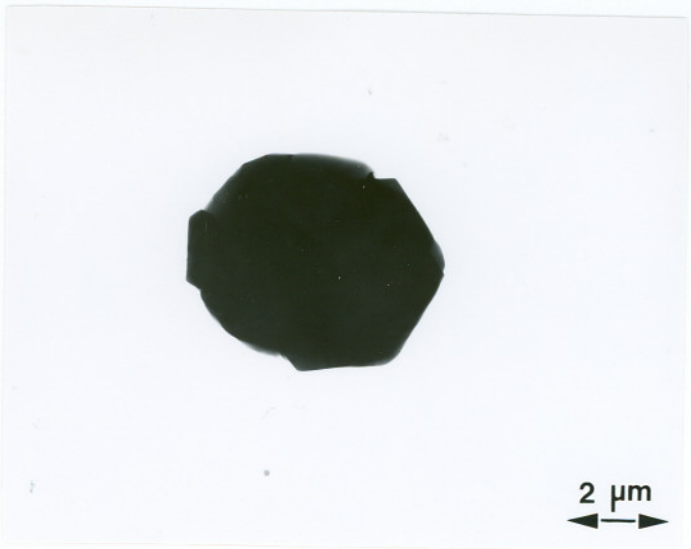

a)

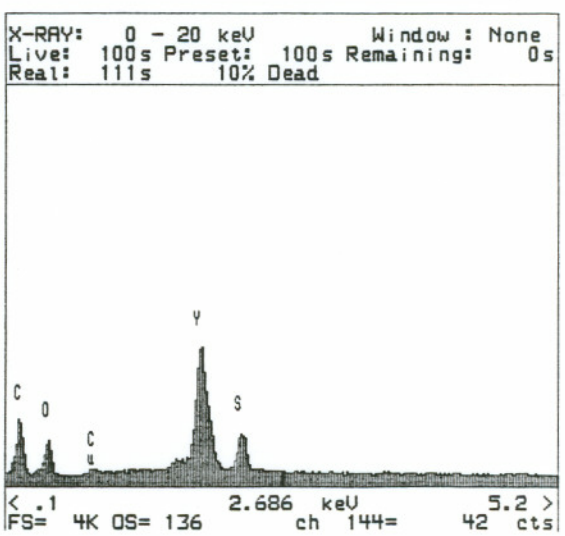

b)

Figure 19

a) SEM micrograph of a Y-S-O rich particle and b) the EDX spectrum obtained from this particle found in the as-homogenized Ni-23Cr-650 ppm Y alloy, dissolved in the iodine-methanol solution

particle and the EDX spectrum obtained from this particle, respectively, which was found in the Ni-23Cr-650 ppm Y alloy. Several such Y-S-O rich particles were observed in all the yttrium containing alloys.

3. OXIDIZED YTTRIUM FREE ALLOYS

Figures 20a-d show the typical microstructure of the oxide scale formed on the Ni-25Cr-4.8 ppm S alloy at 900°C in air for 5 minutes. Similar microstructure was observed at the end of 2 hour exposure at 900°C and also in the case of the Ni-29Cr-140 ppm S alloy. The EDX spectra obtained from the bulk of the oxide layer and from the flowerlike oxides, are shown in the Figures 20e and 20f respectively. The flowerlike oxides were found to be Ni-Cr-O rich particles.

The SEM micrographs of the oxide surface at the end of 24 hours of exposure at 900°C in air for Ni-25Cr-4.8 ppm S alloy, are shown in the Figures 21a-d. Similar oxide structure was observed in the Ni-29Cr-140 ppm S alloy. The EDX spectra taken from the bulk of the oxide layer and from the alloy grain/dendrite boundary oxide (Figures 21a-d), are shown in the Figures 21e and 21f.

A large region of the oxide formed on these alloys at 900°C for a period of 24 hours, had Ni-Cr-O rich areas (Figures 21a-d). Similar observations were also made for the Ni-29Cr-140 ppm S alloy. The Ni-Cr-O rich oxide formed on the oxide scale had a flowerlike morphology, (Figures 21b and 21c). Occasionally such florets were also observed within the substrate alloy grains.

The oxide formed after exposure at 1000°C in air for 2 minutes to 2 hours (Figures 22a-d) for both the alloys had a morphology similar to that which was observed after exposure of the alloys at 900°C in air for 5 minutes. Figures 22e and 22f show the EDX spectra obtained from the bulk oxide layer and the Ni-Cr-O rich flowerlike oxide, respectively. A similar microstructure and EDX spectrum was also observed in the case of Ni-29Cr-140 ppm S alloy.

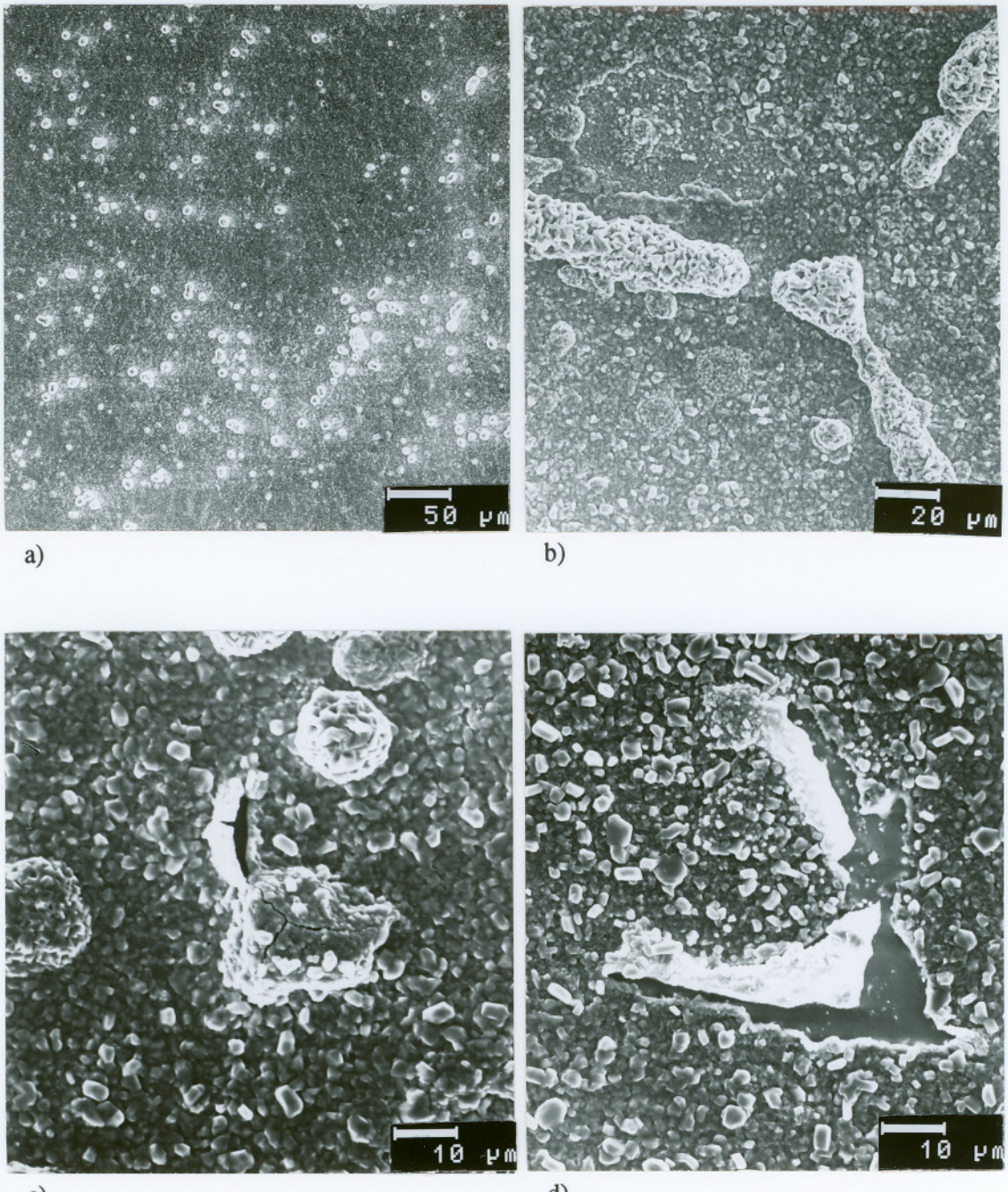

a) b)

c) d)

Figure 20

a) - d) SEM micrographs of the oxide grown on the Ni-23Cr-4.8 ppm S alloy after exposure at 900°C in air for 5 minutes

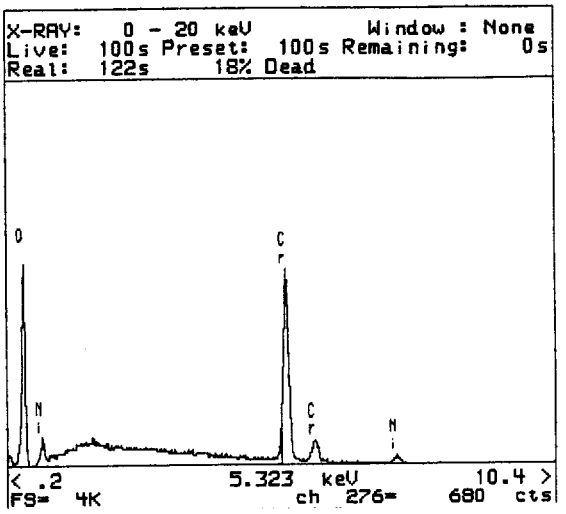

e)

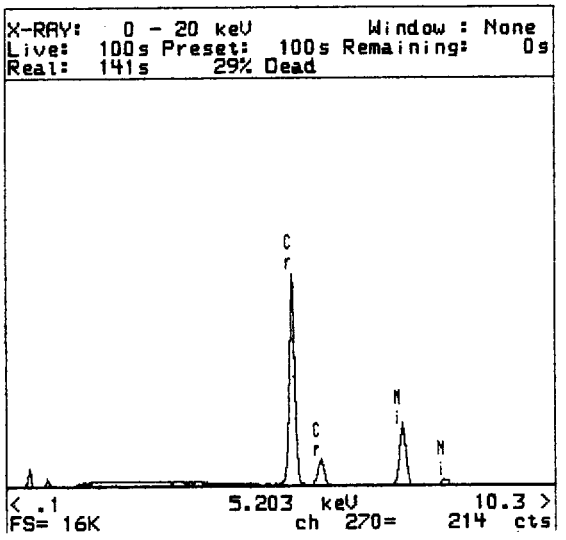

f)

Figure 20 (cont.)

e) the EDX spectrum obtained from the oxide surface, and f) the EDX spectrum obtained from the flowerlike oxides

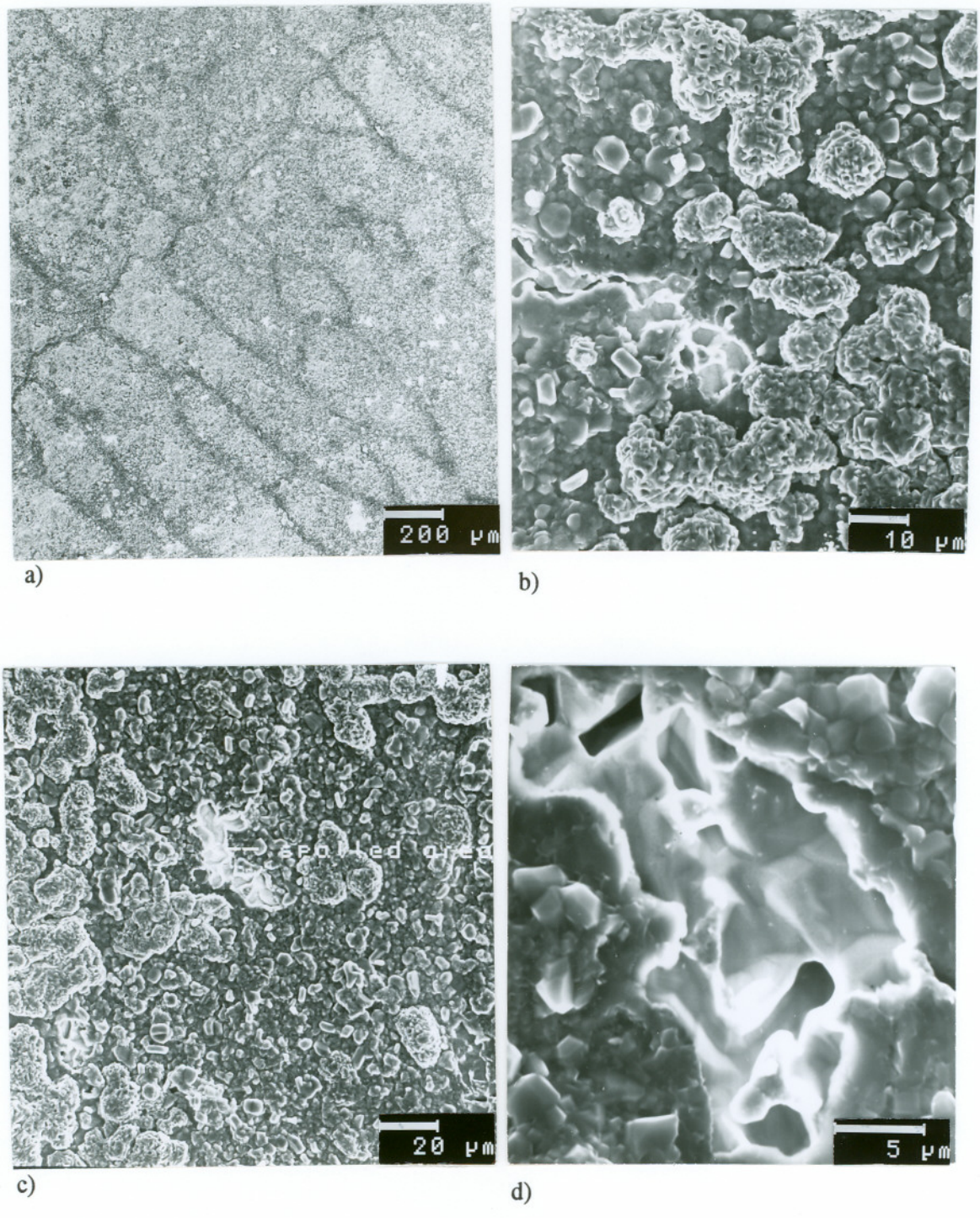

Figure 21

a) - d) SEM micrographs of the oxide grown on the Ni-25Cr-4.8 ppm S alloy at 900°C in air for 24 hours

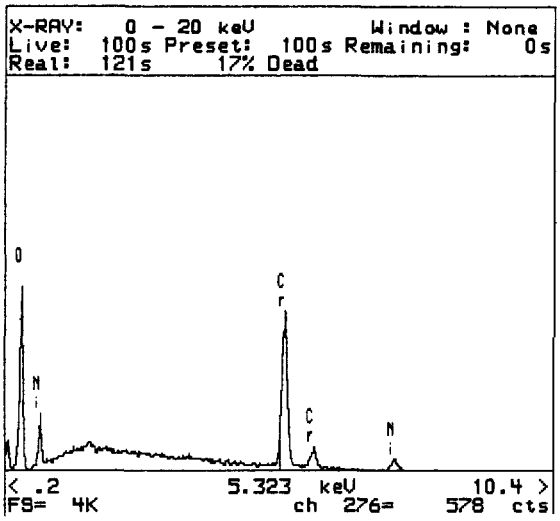

e)

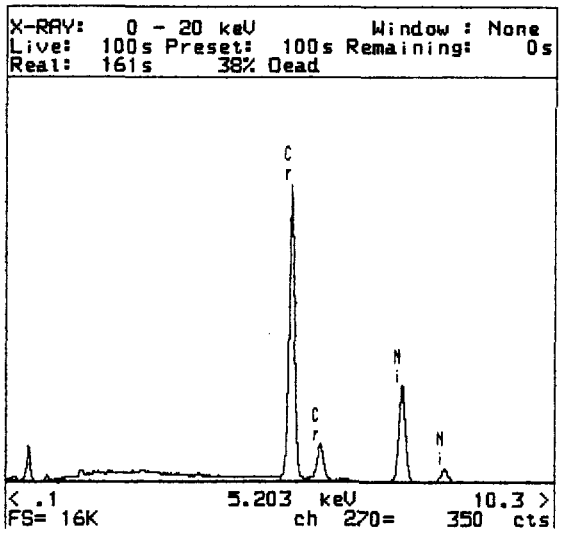

f)

Figure 21 (cont.)

e) the EDX spectrum obtained from the oxide surface, and f) the EDX spectrum obtained from the grain/dendrite boundary area

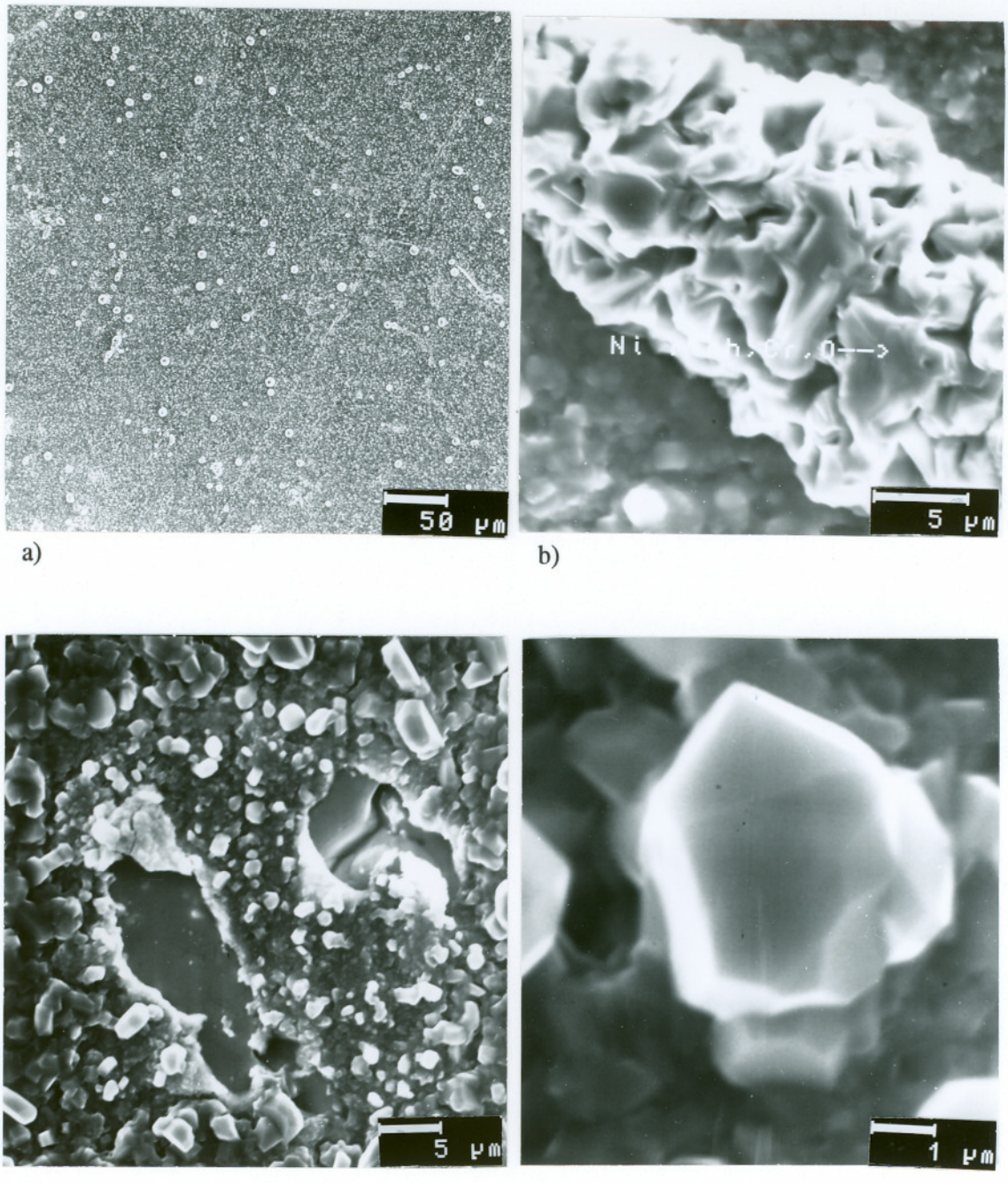

a) b)

c) d)

Figure 22

a) - d) SEM micrographs of the oxide scale grown on the Ni-25Cr-4.8 ppm S alloy after exposure at 1000°C in air for 5 minutes

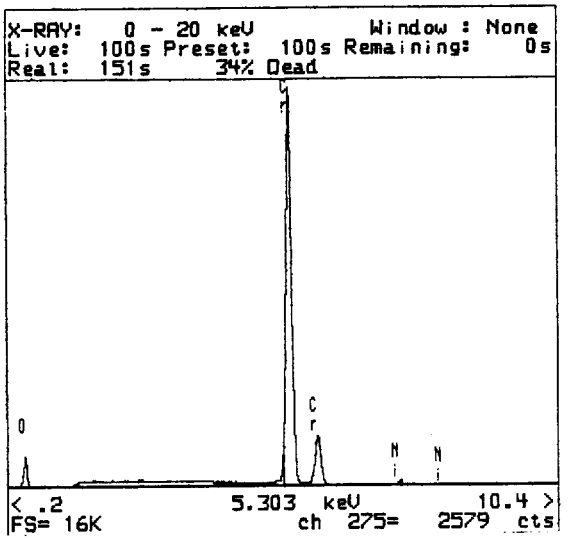

e)

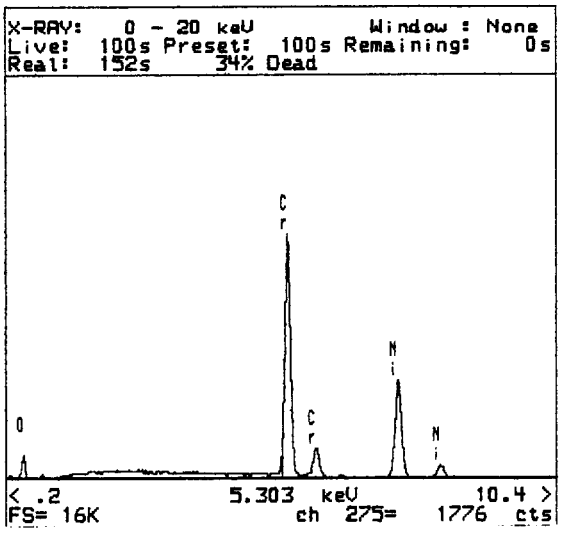

f)

Figure 22 (cont.)

e) the EDX spectrum obtained from the oxide surface and, f) the EDX spectrum obtained from the oxide shown in b)

The oxide scale formed on the surface of both the yttrium free alloys spalled after exposure at 900°C and 1000°C in air for a short time such as 5 minutes, and also at longer exposure time such as 24 hours, at 900°C. Shown in the Figures 23a and 23b are the SEM micrograph of the spalled oxide and the EDX spectrum obtained from the spalled area, for the Ni-25Cr-4.8 ppm S alloy exposed at 900°C in air for 5 minutes. The spalled oxide on the surface of the Ni-29Cr-140 ppm S alloy exposed at 900°C in air for 5 minutes, and the EDX spectrum obtained from the spalled region are shown in Figures 23c and 23d, respectively. No element other than Ni and Cr was detected in the EDX spectrum obtained from the spalled oxide region. The spalled region of the oxide scale had a thermally etched appearance (Figures 23a and 23c). Some voids were also seen at the grain boundaries in the spalled regions of the oxide scale (Figures 23a and 23c).

Figures 24a and 24b show the SEM micrograph of the spalled oxide and the EDX spectrum taken from the spalled region, after exposure of the Ni-25Cr-4.8 ppm S alloy at 900°C in air for 24 hours. Figures 24c and 24d show the SEM micrograph of the spalled area and the EDX spectrum taken from the spalled area, after exposure of the Ni-29Cr-140 ppm S alloy at 900°C in air for 24 hours. In this case too, no element other than Ni and Cr was detected in the EDX spectrum taken from the spalled oxide layer.

The spalled region of the oxide had a thermally etched appearance (Figures 24a and 24c). Some voids were also seen at the grain boundaries in the spalled regions of the oxide scale (Figures 24a and 24c).

4. OXIDIZED YTTRIUM CONTAINING ALLOYS

Figures 25a-d show the typical microstructure of the oxide surface layer formed after exposure at 900°C in air for 5 minutes, for all the three yttrium containing alloys investigated. The microstructure was found to be similar for a period of exposure varying between 2 minutes and 2 hours. The EDX spectra obtained from the bulk of the oxide layer and from the floret type oxide shown in the Figure 25d, are shown in the Figures 25e and 25f respectively. Yttrium was detected along the alloy grain/dendrite boundaries.

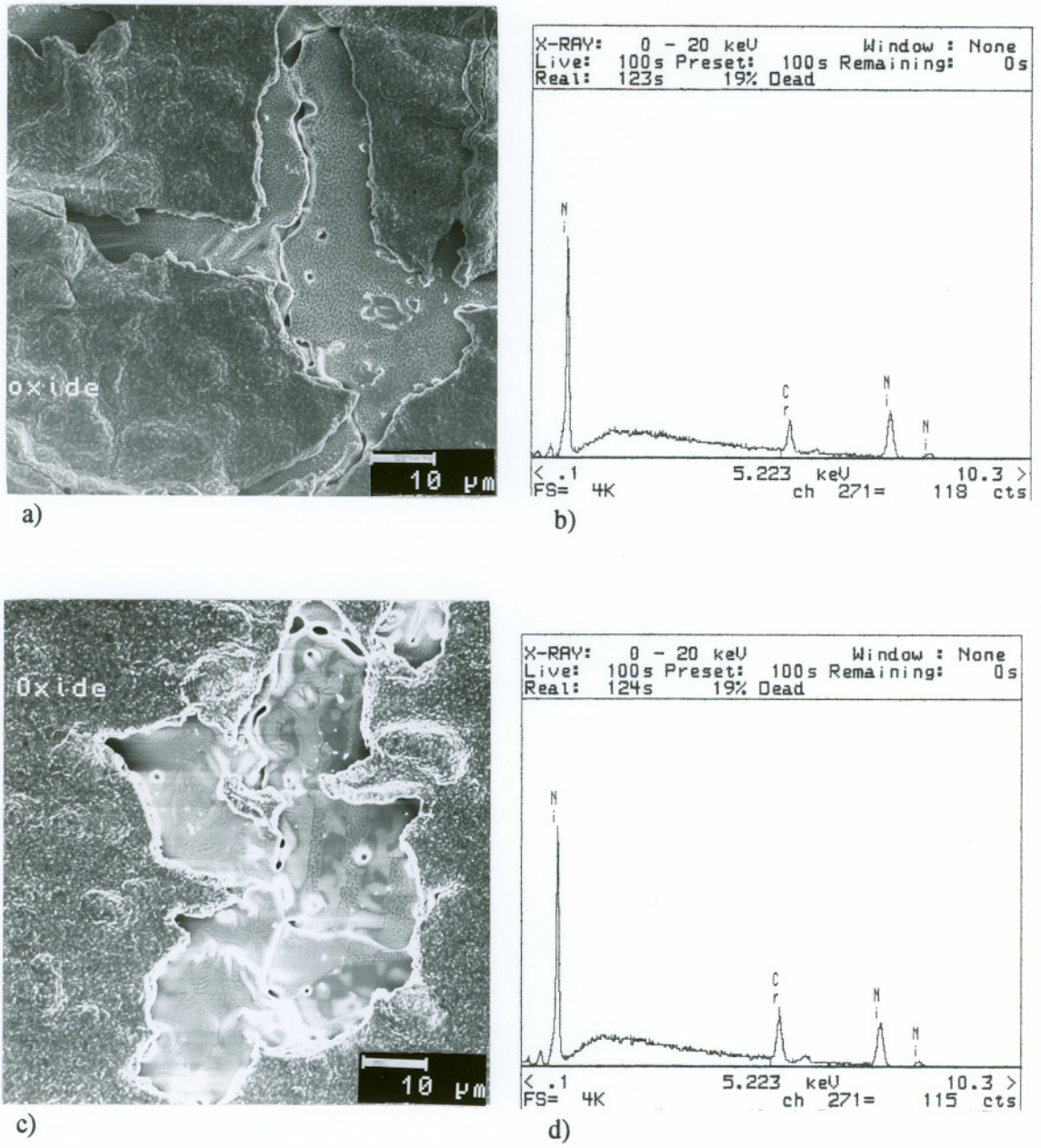

Figure 23

SEM micrographs of the spalled oxide scale. Oxide grown at 900°C in air for 5 minutes. a) Ni-25Cr-4.8 ppm S alloy, b) EDX spectrum obtained from the spalled region shown in a), c) Ni-29Cr-140 ppm S alloy, d) EDX spectrum obtained from the spalled region of the oxide shown in c)

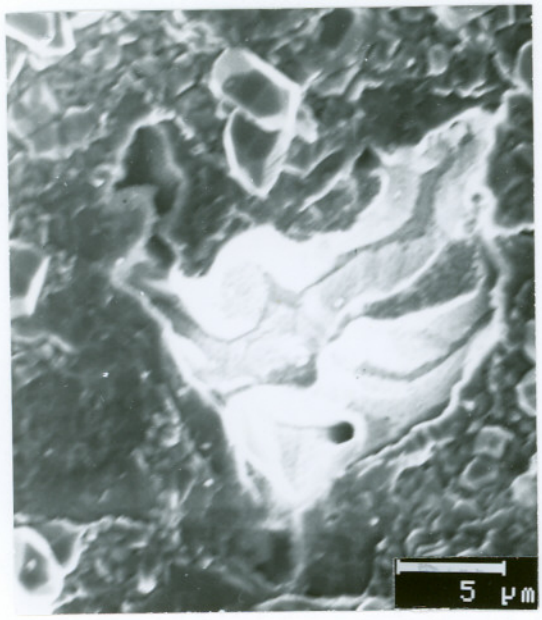

a)

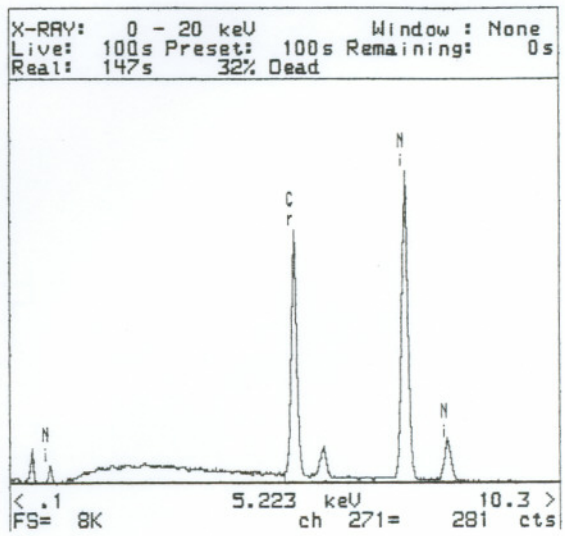

b)

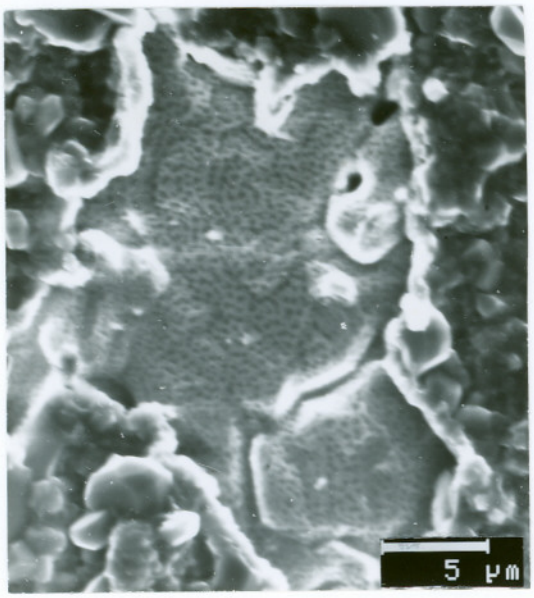

c)

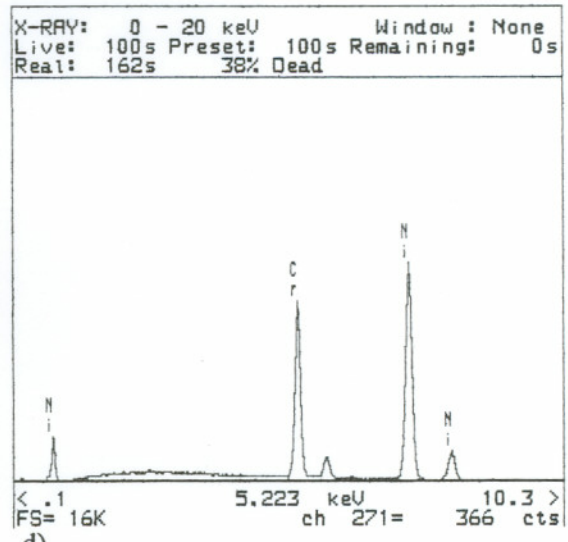

d)

Figure 24

SEM micrographs of the spalled area of the oxide scale grown at 900°C in air for 24 hours. a) Ni-25Cr-4.8 ppm S alloy, b) EDX spectrum obtained from the spalled region of the oxide scale shown in a), c) Ni-29Cr-140 ppm S alloy, d) EDX spectrum obtained from the spalled region of the oxide scale shown in c)

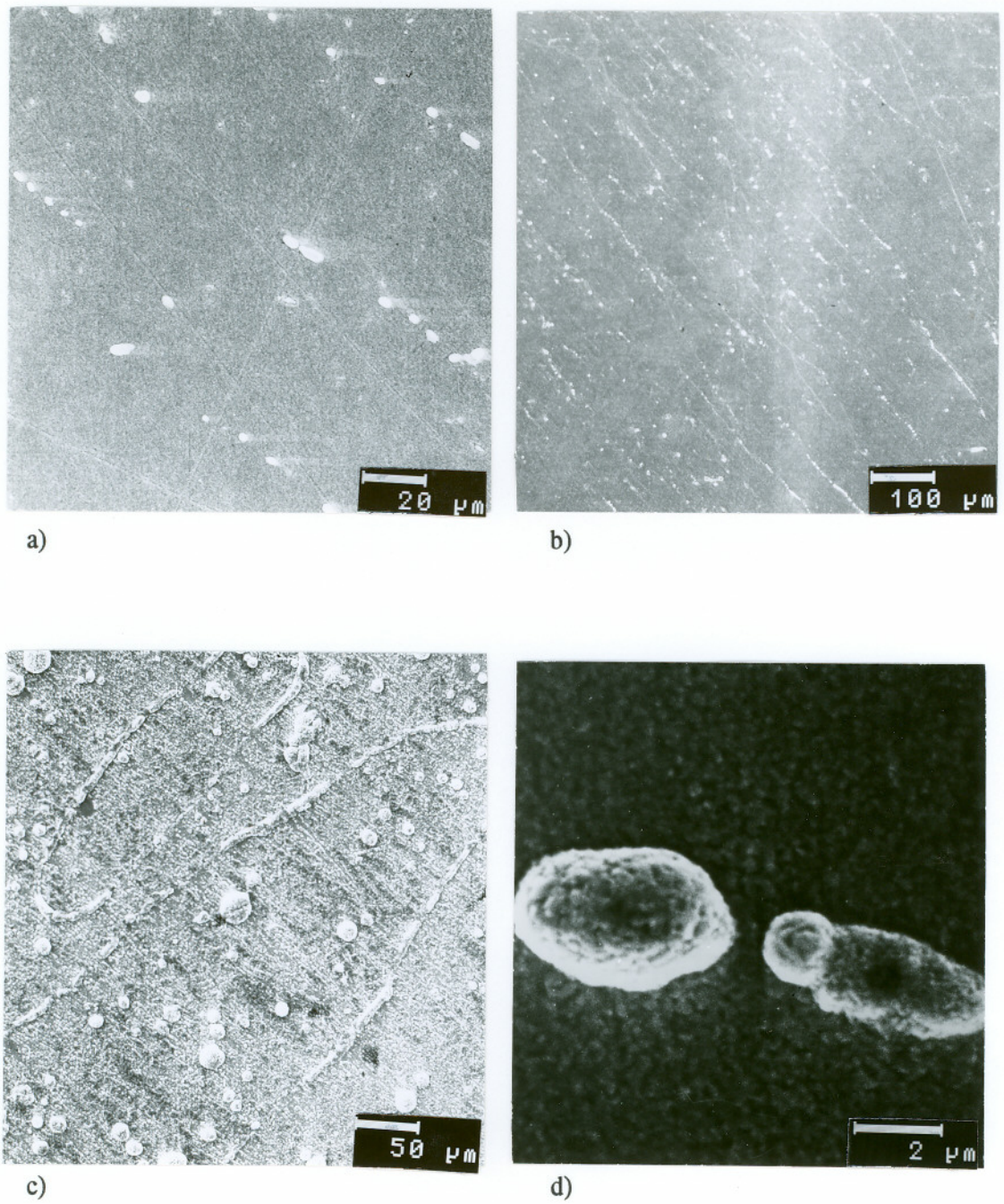

Figure 25

SEM micrographs of the oxide scale grown on a) Ni-23Cr-650 ppm Y alloy, b) Ni-31Cr-900 ppm Y alloy, c) Ni-22Cr-0.62Y alloy after exposure at 900°C in air for 5 minutes. d) floret type oxide formed in the oxide scale

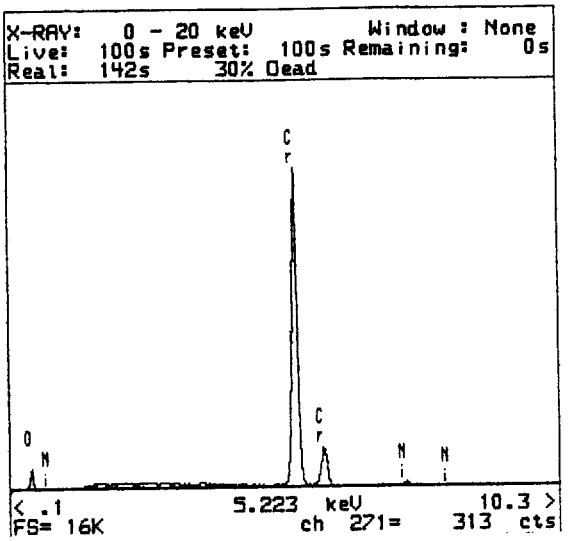

e)

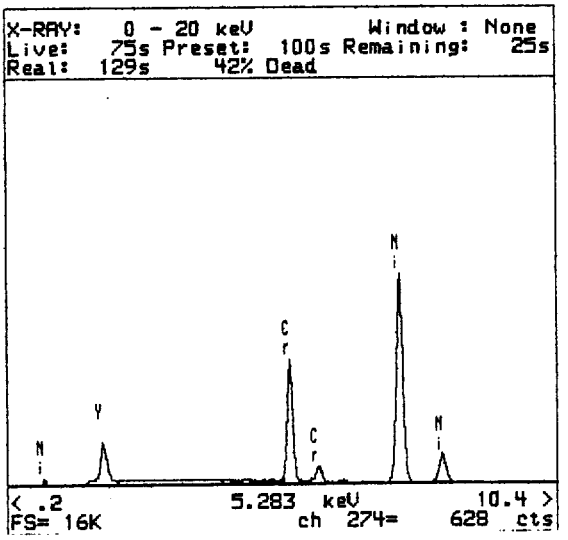

f)

Figure 25 (cont.)

e) EDX spectrum obtained from the oxide scale and f) EDX spectrum obtained from the grain/dendrite boundary oxide shown in d)

Sulfur in association with yttrium and oxygen was also detected at some locations along the alloy grain/dendrite boundary, in all the three yttrium containing alloys studied. The SEM micrograph and the EDX analysis of the grain/dendrite boundary region of the Ni-23Cr-650 ppm Y alloy oxidized at 900°C in air for 5 minutes, are shown in the Figures 26a and 26b.

The microstructure of the oxide scale, for all the three yttrium containing alloys, at the end of 24 hours of exposure at 900°C in air is shown in the Figures 27a-d. A typical EDX analysis of the oxide scale shown in the Figures 27a-d, is shown in the Figure 27e. The oxide formed at the alloy grain/dendrite boundary had a flowerlike morphology, and was found to be rich in Ni-Cr and O. Occasionally such florets were also observed within the substrate alloy grains as shown in the micrographs. A similar microstructure and EDX spectrum was also observed in the other two yttrium alloys.

The oxide formed after exposure at 1000°C in air for 2 minutes and 2 hours in all the three yttrium containing alloys, had a morphology similar to that which was observed on the specimen exposed at 900°C in air for 5 minutes. Figures 28a-d show the micrographs of the oxide scale formed at the end of 5 minute exposure at 1000°C in air for all the three alloys. Figures 28e and 28f show the EDX analysis of the oxide scale and the flowerlike oxide.

Figure 29a shows the SEM micrograph as seen in the cross section, of the Ni-22Cr-0.62Y alloy, oxidized at 900°C in air for 24 hours. The x-ray map taken for yttrium from the microstructure shown in the Figure 29a, is shown in the Figure 29b and 29d. No evidence of segregation of yttrium at the oxide/alloy interface was found. Similarly observations were made in the case of the other two yttrium containing alloys.

5. THERMALLY CYCLED ALLOYS

The oxide formed on the yttrium free alloys had spalled when the specimens oxidized at 900°C and 1000°C in air, were cooled to room temperature (Figures 23 and 24). Since the spallation of the oxide scale was observed even without thermal cycling, the yttrium free alloys were not thermally cycled.

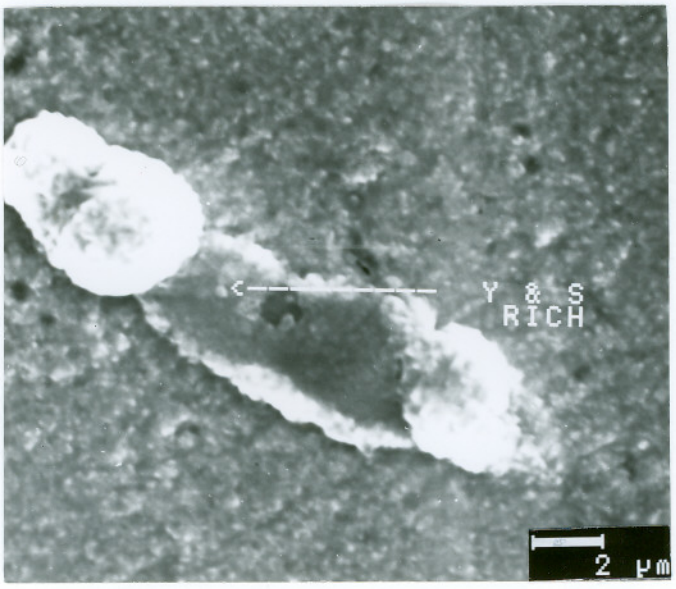

a)

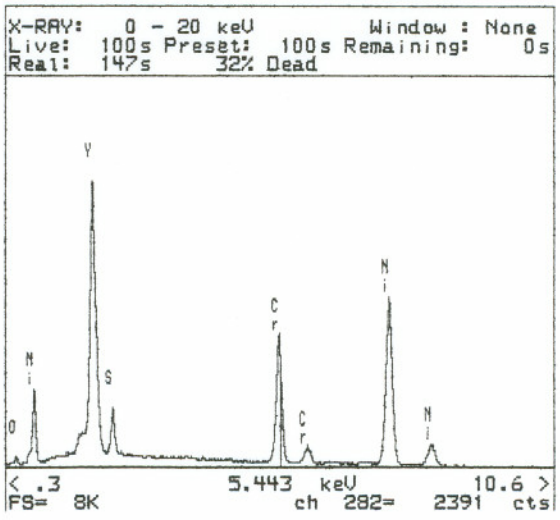

b)

Figure 26

a) SEM micrograph of the Ni-23Cr-650 ppm Y alloy oxidized at 900°C in air for 5 minutes, showing the Y, S and O rich particles at the alloy grain/dendrite boundary, b) the EDX spectrum obtained from this particle

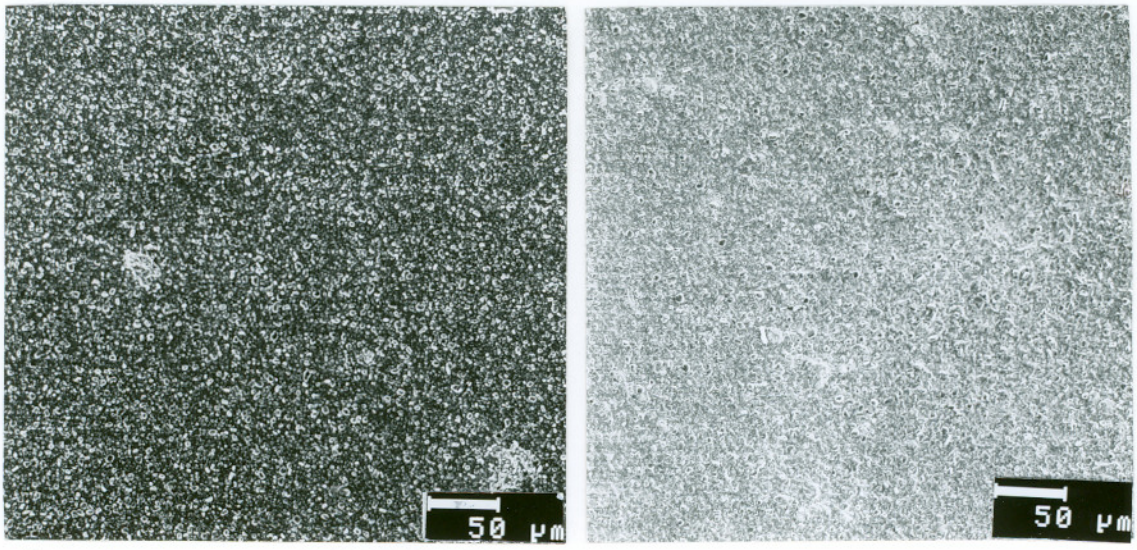

a) b)

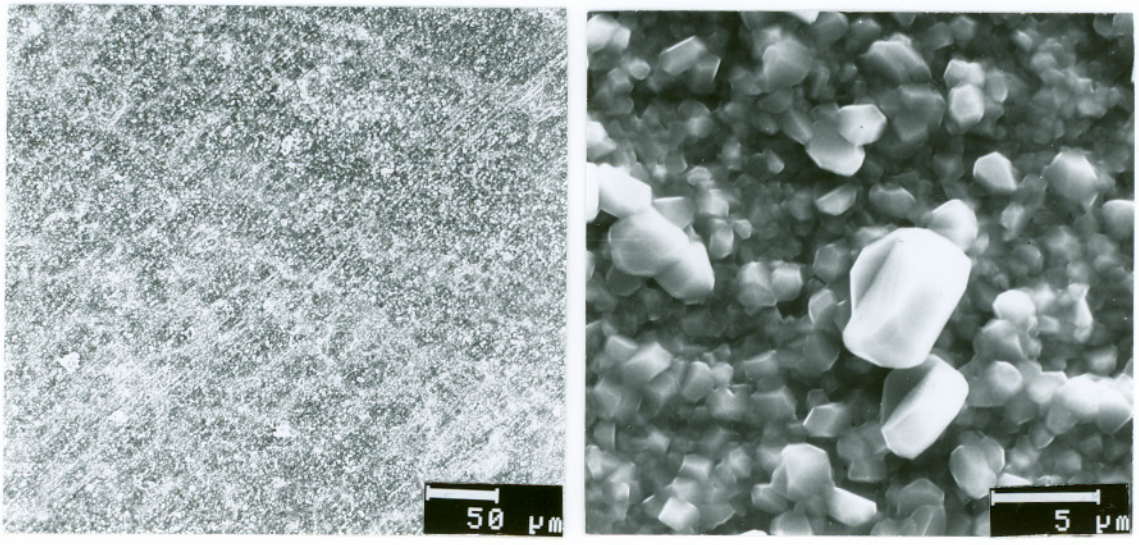

c) d)

Figure 27

SEM micrographs of the oxide scale grown on the a) Ni-23Cr-650 ppm Y alloy b)Ni-31Cr-900 ppm Y alloy, c) Ni-22Cr-0.62Y alloy, after exposure at 900°C in air for 24 hours. d) floret type oxide

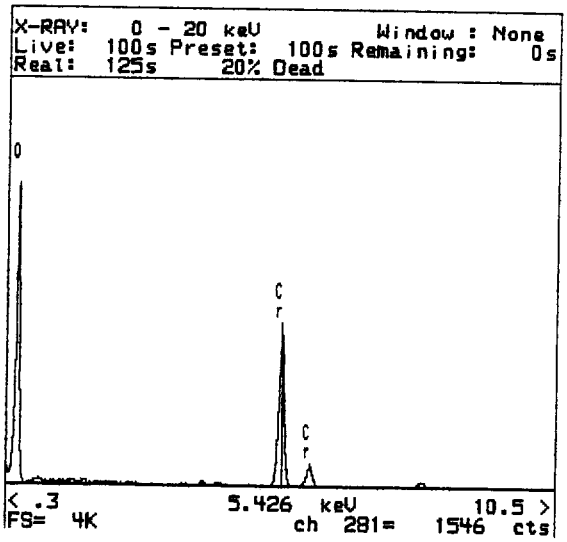

e)

Figure 27 (cont.)

e) EDX spectrum obtained from the oxide scale

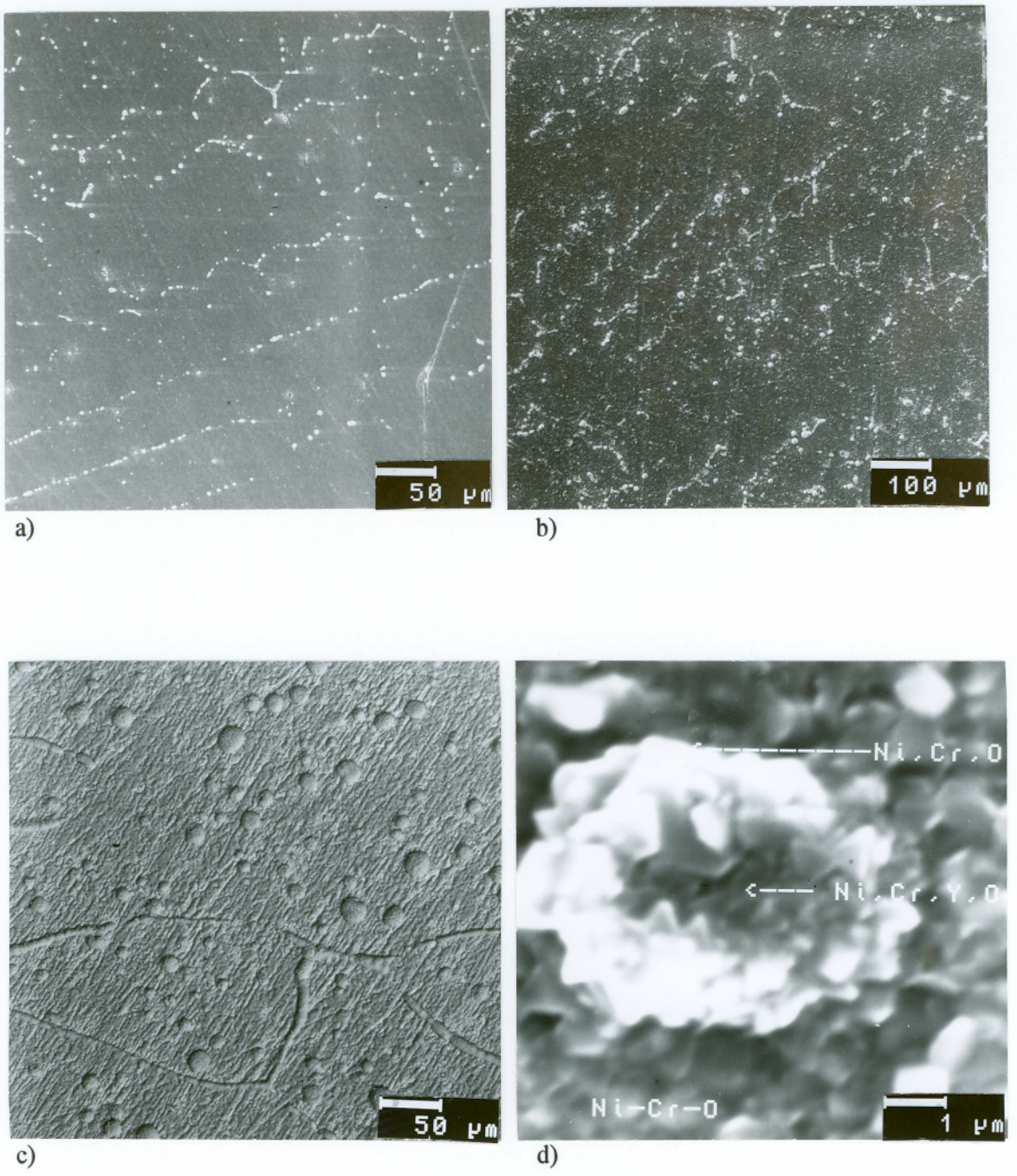

Figure 28

SEM micrographs of the oxide scale grown on the a) Ni-23Cr-650 ppm Y alloy, b) Ni-31Cr-900 ppm Y alloy, c) Ni-22Cr-0.62Y alloy, after exposure at 1000°C in air for 5 minutes. d) grain/dendrite boundary oxide

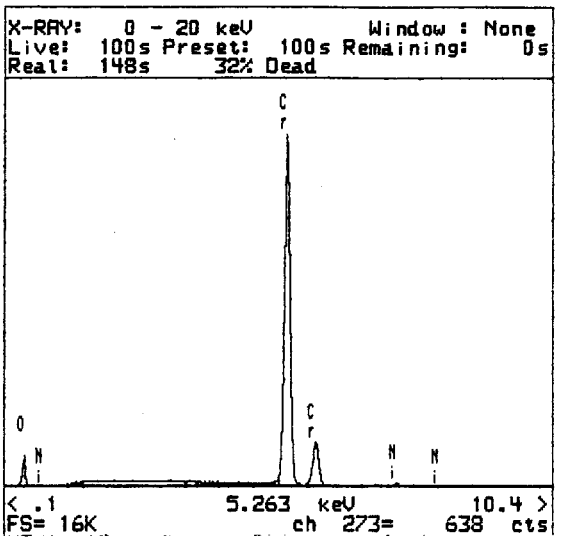

e)

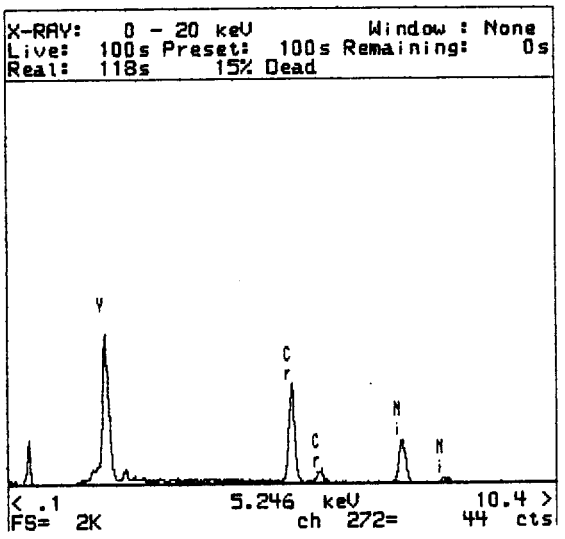

f)

Figure 28 (cont.)

e) EDX spectrum obtained from oxide scale and f) EDX spectra obtained from the grain/dendrite boundary oxide shown in d)

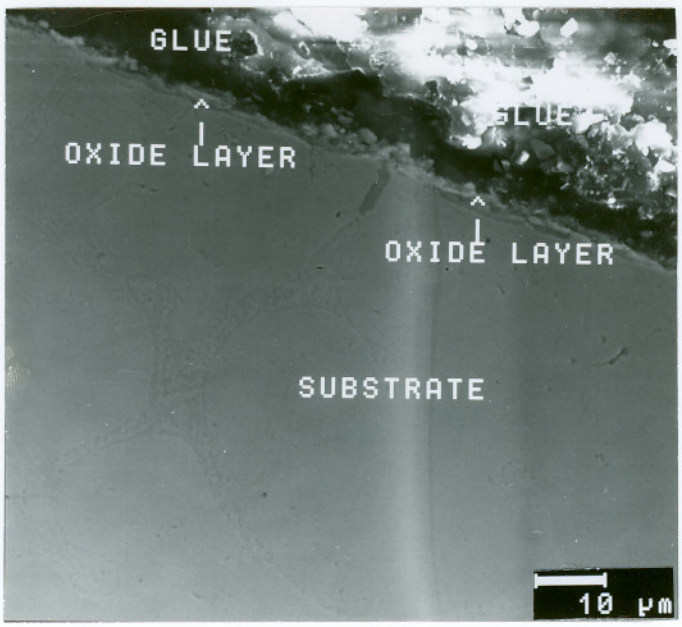

a)

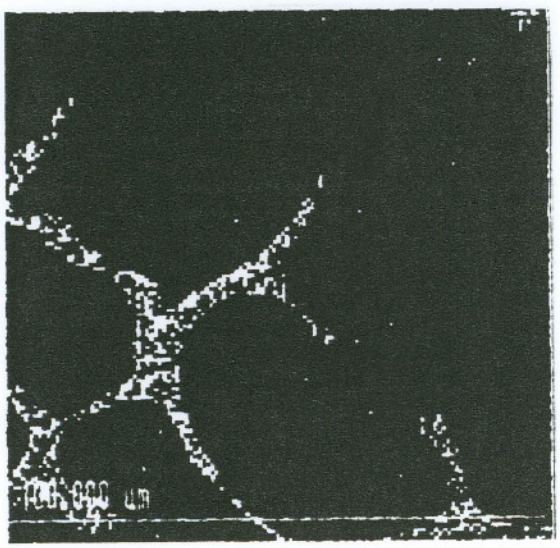

b)

Figure 29

a) SEM micrograph of the cross section of the Ni-22Cr-0.62Y alloy oxidized at 900°C in air for 24 hours, b) x-ray map of Y taken from the microstrcture shown in a)

The yttrium containing alloys did not exhibit oxide spallation when exposed at 900° C in air for 24 hours and cooled to room temperature. However, when the Ni-23Cr-650 ppm Y alloy and the Ni-31Cr-900 ppm Y alloy oxidized at 900°C in air for 24 hours, were thermally cycled at 900°C in air for 2 times, they exhibited oxide spallation. Figures 30a and 30b show the SEM micrograph and the EDX spectrum obtained from the spalled oxide scale area on the Ni-23Cr-650 ppm Y alloy, respectively. No element other than Ni and Cr was detected in the spalled region.

The Ni-22Cr-0.62% Y alloy oxidized at 900°C in air for 24 hours, however, did not exhibit oxide spalling even after thermally cycling the alloy 10 times at 900°C in air. The SEM micrographs of the oxide scale, after thermally cycling the alloy 2, 5, and 10 times at 900°C in air, are shown in the Figures 31a-c.

E. TRANSMISSION ELECTRON MICROSCOPY

1. HOMOGENIZED YTTRIUM FREE ALLOYS

There was no evidence of any precipitates along the grain/dendrite boundaries or in the grains of the Ni-Cr matrix, in the ion-milled yttrium free alloys. Hence further TEM observation was not carried out on the as-homogenized yttrium free alloys.

a. CrS Phase

Particles rich in Cr and S were identified by the EDX analysis in the Ni-29Cr-140 ppm S alloy, dissolved in the iodine-methanol solution (Figures 32a and 32b). These particles had a platelike morphology. Dissolution of the specimens from the Ni-25Cr-4.8 ppm S alloy did not leave any residue and hence TEM analysis could not be carried out. The electron diffraction patterns taken from the particle are shown in Figures 33a-33c. The diffraction patterns were matched with the phase CrS, whose crystal structure has been reported[115] to be hexagonal space group 194 $P6_3/mmc$. Higher order laue zones (HOLZ) could not be obtained, and hence only the zero order laue zones (ZOLZ) are reported here. Thus, the reduced unit cell volume calculations could not be carried out.

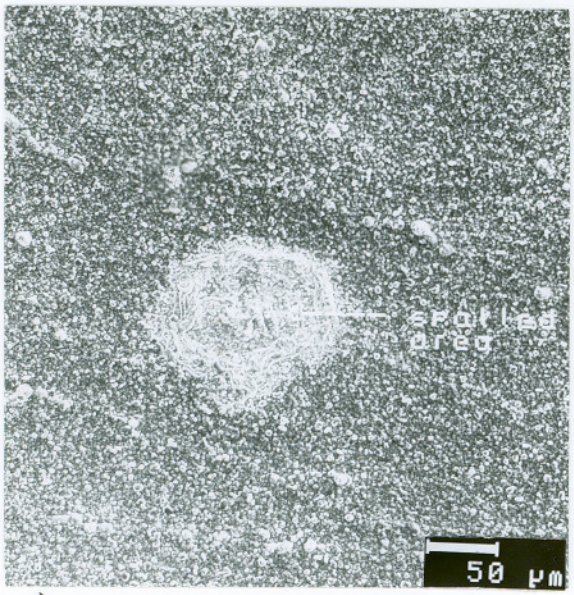

a)

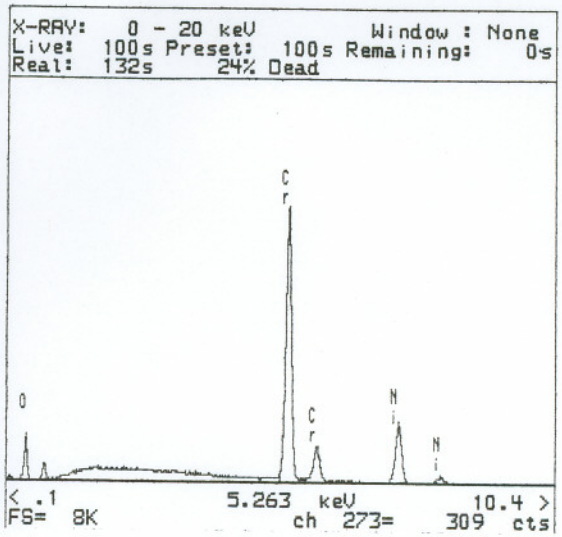

b)

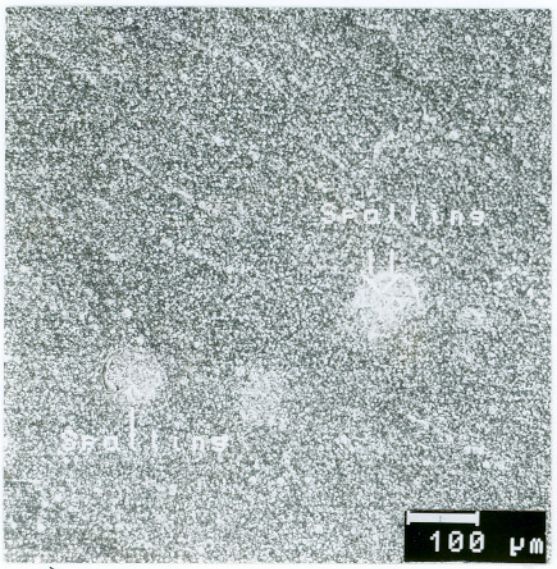

c)

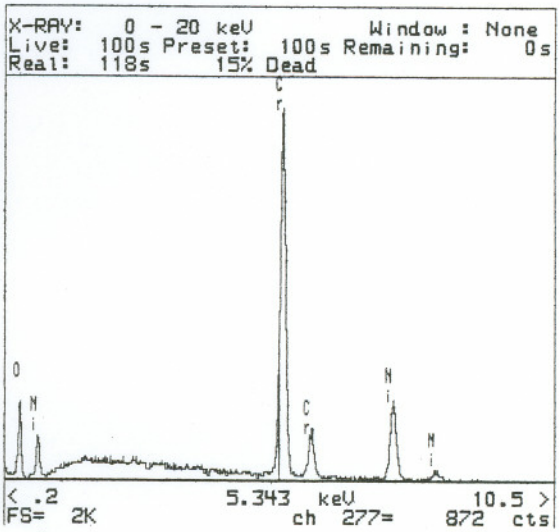

d)

Figure 30

a) SEM micrograph of the Ni-23Cr-650 ppm Y alloy oxidized at 900°C in air for 24 hours, and thermally cycled at 900°C in air 2 times, b) EDX spectrum obtained from the spalled region, c) SEM micrograph of the Ni-31Cr-900 ppm Y alloy oxidized at 900°C in air for 24 hours, and thermally cycled at 900°C in air 2 times, d) EDX spectrum obtained from the spalled region

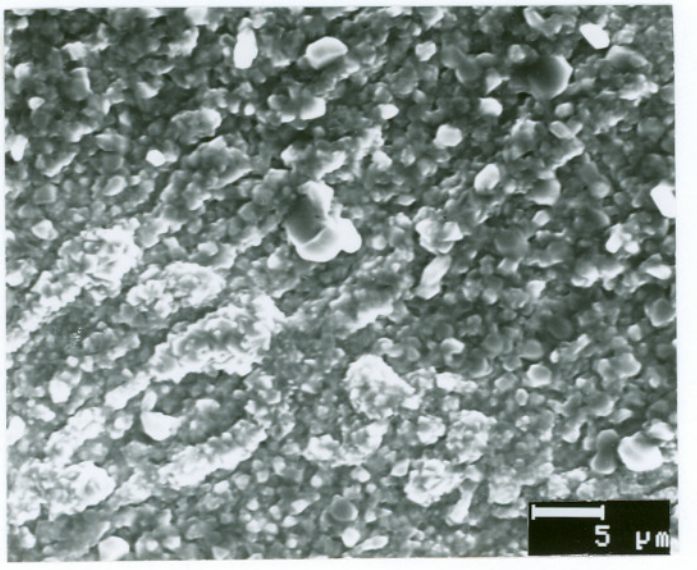

a)

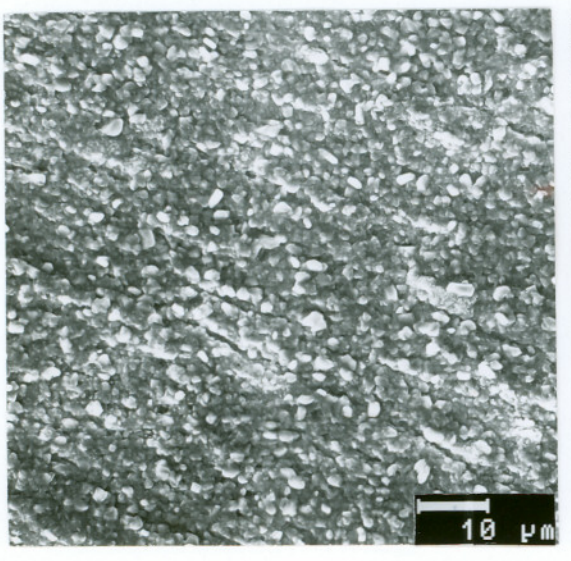

b)

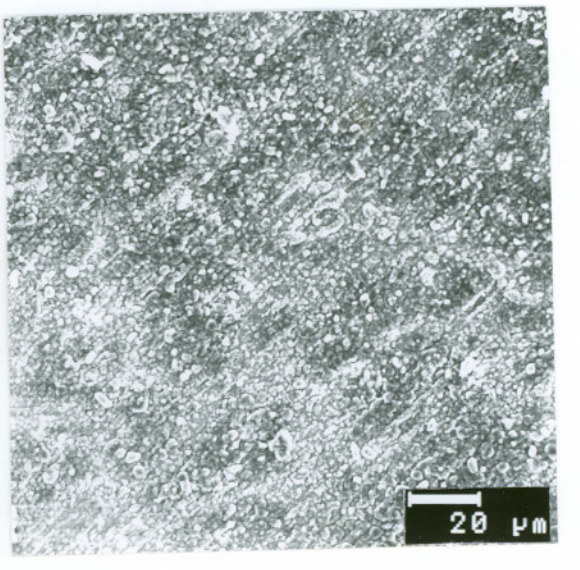

c)

Figure 31

a) SEM micrographs of the oxide scale grown on the Ni-22Cr-0.62Y alloy at 900°C in air for 24 hours, and thermally cycled at 900°C in air for a) 2 times, b) 5 times, c) 10 times

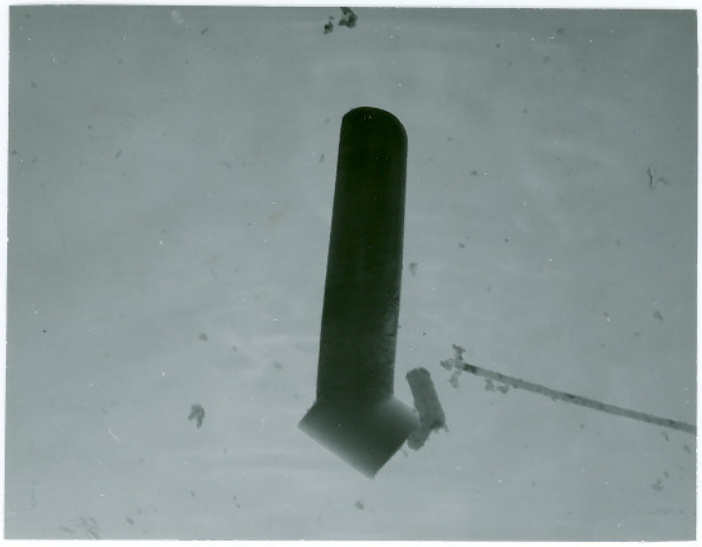

a)

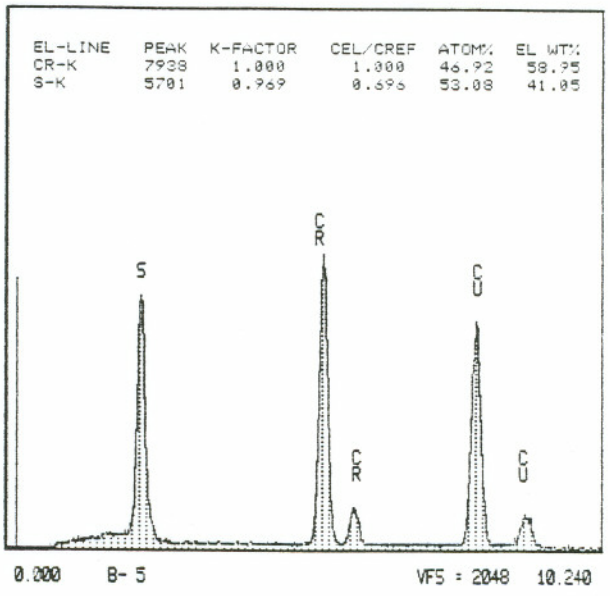

b)

Figure 32

a) Bright field image and b) EDX spectrum obtained from a Cr and S rich particle found in the as-homogenized Ni-29Cr-140 ppm S alloy dissolved in the iodine-methanol solution

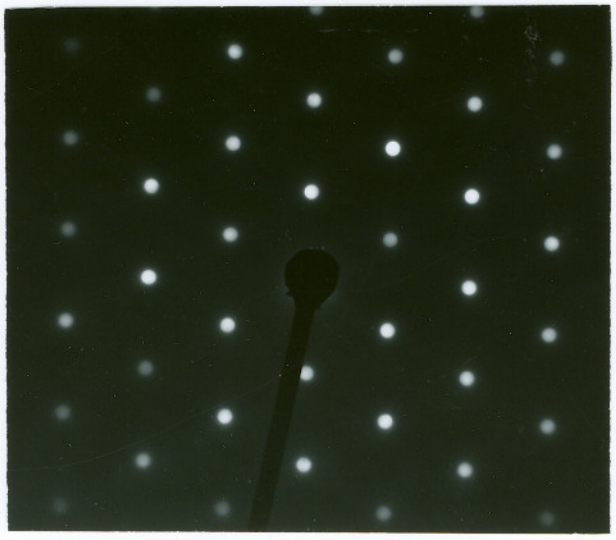

a)

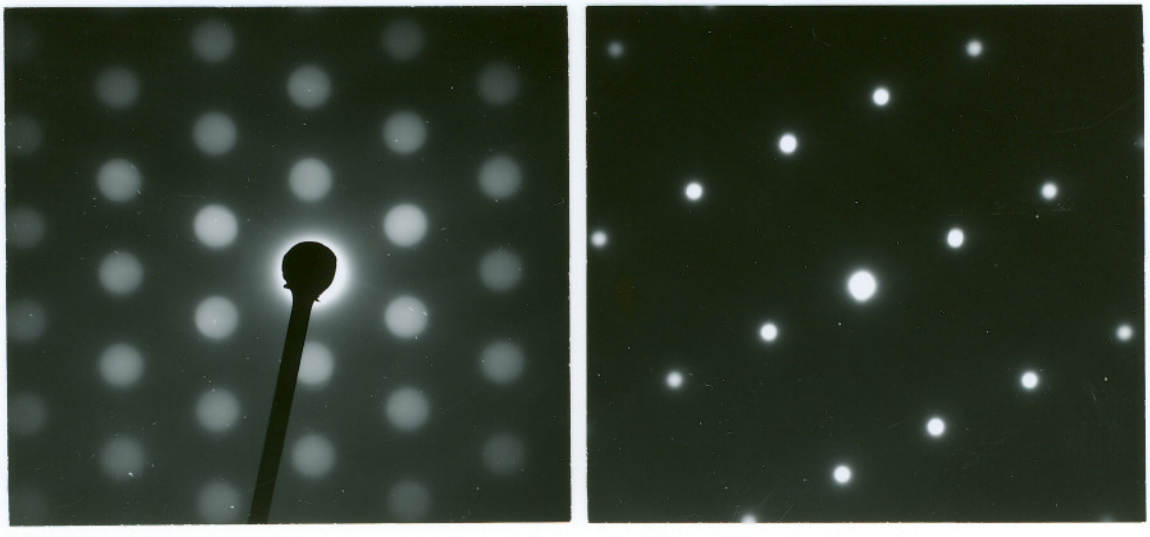

b) c)

Figure 33

Diffraction patterns obtained from a CrS particle found in the as-homogenized Ni-29Cr-140 ppm S alloy, dissolved in the iodine-methanol solution. a) [0001] zolz pattern, b) [11$\bar{2}$3] zolz pattern, c) [10$\bar{1}$2] zolz pattern

The Wyckoff positions of the atoms in the CrS crystal (2 Cr on a sites at (0, 0, 0) and 2 S on c sites at (1/3, 2/3, 1/4))[115] and the lattice parameters, required for simulating the crystal, the diffraction patterns, and for calculating the d-spacings and the angle between the axes, using Desktop Microscopist™, were obtained from the Pearsons Handbook of Crystallographic Data for Intermetallic Phases, Volume 2[115]. The unit cell dimensions of the CrS phase found in the alloy matched with the reported lattice parameters of a = 3.46 Å and c = 5.78 Å. The experimentally measured and theoretically calculated d-spacings are given in Table 3a, and the angles between the zone axes are shown in Table 3b. These figures match well with each other.

3. OXIDIZED YTTRIUM FREE ALLOYS

The oxide scales stripped from the specimens oxidized for a period of 2-10 minutes at 900°C and 1000°C in air were observed in the TEM. The oxide scales stripped from specimens exposed to these temperatures for a period longer than 10 minutes were too thick for observation in the TEM. The oxide scales were stripped by dissolving the substrate alloy in the iodine-methanol solution.

a) $NiCr_2O_4$ Phase

Among large grains rich in Cr, florets rich in Ni and Cr were observed in the oxide scales grown on both the yttrium free alloys at both the temperatures. Shown in the Figures 34a and 34b are the micrographs of the Ni-Cr rich floret found in the oxide scale, grown on the Ni-29Cr-140 ppm S alloy oxidized in air at 900°C for 5 minutes. These micrographs are the bright field image and the image as seen in the SEM mode in the TEM. Similar floret type morpholgy was observed in the oxide scale grown on the other yttrium free alloy. The EDX spectrum obtained from the floret structure shown in the Figure 34a and 34b, is shown in Figure 34c. In the analysis of the EDX spectrum of the floret structure, Ni and Cr content were found to be 63.38 weight% and 36.62 weight% respectively.

The bright field image of the Ni-Cr rich floret is shown in Figure 34d. The EDX spectrum, along with the semi-quantitative analysis of the EDX spectrum (Figure 34e), obtained from the edge of a Ni-Cr rich floret found in the oxide scale grown on the Ni-29Cr-140 ppm S

Table 3a

Experimentally measured and theoretically calculated d-spacings for the phase CrS found in the as-homogenized Ni-29Cr-140 ppm S alloy, dissolved in the iodine-methanol solution

zone axis	measured (theoretical) d-spacing, Å
[0001]	a) 2.99 (2.99) b) 2.99 (2.99) c) 1.74 (1.73)
$[11\bar{2}3]$	a) 2.94 (2.99) b) 2.63 (2.66) c) 1.47 (1.48)
$[10\bar{1}2]$	a) 1.72 (1.73) b) 1.44 (1.45) c) 2.65 (2.66)

Table 3b

Experimentally measured and theoretically calculated angles between the zone axes for the phase CrS found in the as-homogenized Ni-29Cr-140 ppm S alloy, dissolved in the iodine-methanol solution. Figures in brackets are the theoretical values

zone axis	[0001]	$[11\bar{2}3]$	$[10\bar{1}2]$
[0001]	0.0 (0.0)	30.75 (30.99)	28.7 (27.4)
$[11\bar{2}3]$	30.75 (30.99)	0.0 (0.0)	14.5 (14.88)
$[10\bar{1}2]$	28.7 (27.4)	14.5 (14.88)	0.0 (0.0)

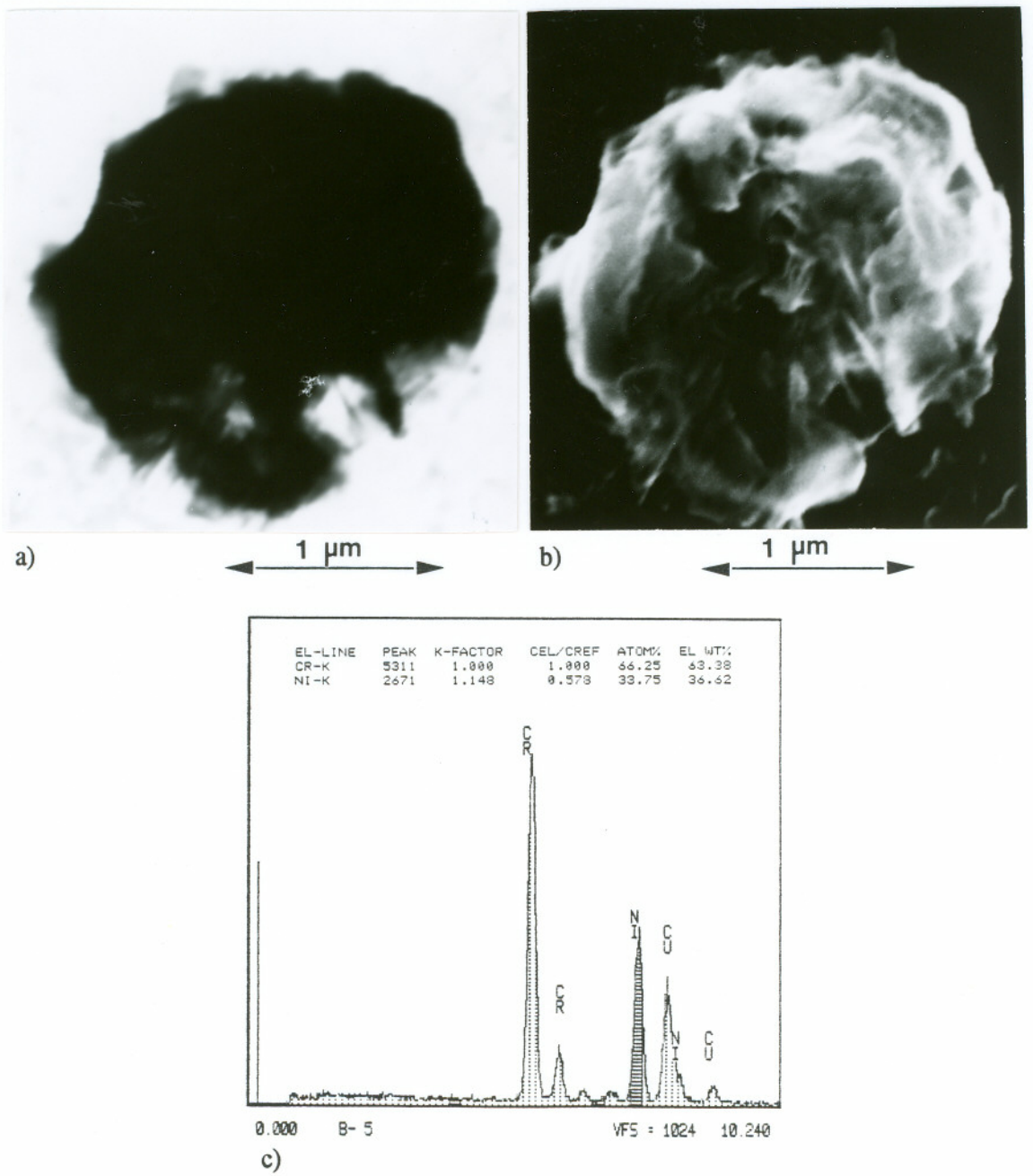

Figure 34

a) Bright field image of a floret rich in Ni and Cr, b) micrograph of the floret shown in a) taken in the SEM mode in the TEM, c) EDX spectrum obtained from the Ni-Cr rich floret. The Cu peaks are from the Cu grid

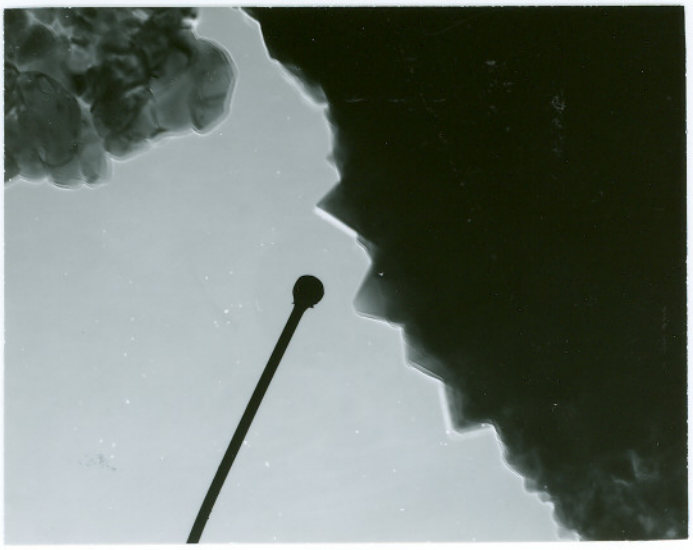

d) 200 nm

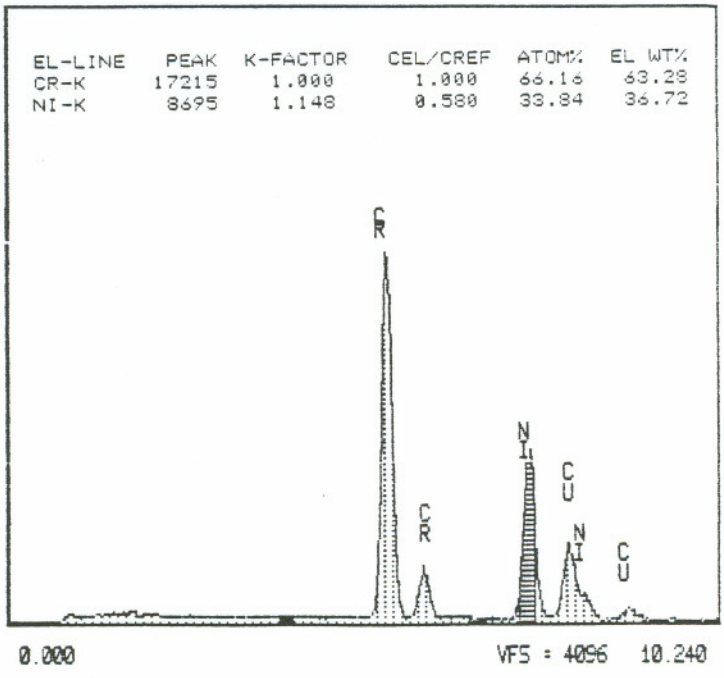

e)

Figure 34 (cont.)

d) Bright field image and e) the EDX spectrum obtained from the $NiCr_2O_4$ particles found in the oxide scale grown on the Ni-29Cr-140 ppm S alloy at 900°C in air for 5 minutes. The Cu peaks are from the Cu grid

alloy oxidized at 900°C in air for 5 minutes, yielded 63.28 wt% Ni and 36.72 wt%Cr content.

Diffraction patterns (Figure 35a-j) were obtained from the Ni-Cr rich particles shown in the Figure 34d and they matched with those for $NiCr_2O_4$ which is reported[116] to have a cubic crystal structure space group 227 $Fd\bar{3}m$, lattice parameter a = 8.32 Å. Tables 4a and 4b show the experimentally determined and theoretically calculated values of the d-spacings, the reduced unit cell volume and the angle between the zone axes .

The Wyckoff positions (16 Cr on d sites at (1/2, 1/2, 1/2), 8 Ni atoms on a sites at (1/8, 1/8, 1/8) and 32 O on e sites at (0.251, 0.251, 0.251))[115] of the atoms in the $NiCr_2O_4$ crystal (isostructural with $MgAl_2O_4$) and the lattice parameters of the crystal, required for simulating the crystal, the diffraction patterns, and for calculating the d-spacings, the reduced unit cell volume and the angle between the axes, using Desktop Microscopist™, were obtained from the data published in the literature[115,116]. The experimentally determined d-spacings, the reduced unit cell volume and the angles between the zone axes matched well with their theoretical values, as shown in Table 4a and 4b.

The oxide grown on the yttrium free alloys at 900°C in air for 24 hours was lightly scraped and the particles collected on a carbon coated Cu grid, and observed in the TEM. Shown in the Figures 36a and 36b are the bright field image and the EDX spectra taken from such a particle. The analysis of the EDX spectrum shown in the Figure 36b, yielded 62.49 wt% Ni and 37.51 wt% Cr.

The diffraction patterns obtained from the particle shown in the Figure 36a, are shown in the Figures 37a-37f. These diffraction patterns matched with the computer simulated patterns for the compound $NiCr_2O_4$. The crystal structure of $NiCr_2O_4$ was found to be cubic space group 225, $Fm\bar{3}m$, with the lattice parameters of a = b = c = 8.32 Å, as reported in the literature[115,116].

The experimentally measured and theoretically calculated d-spacings, the reduced unit cell volume, and the angles between the zone axes are given in Table 5a and 5b, and they match very well with each other.

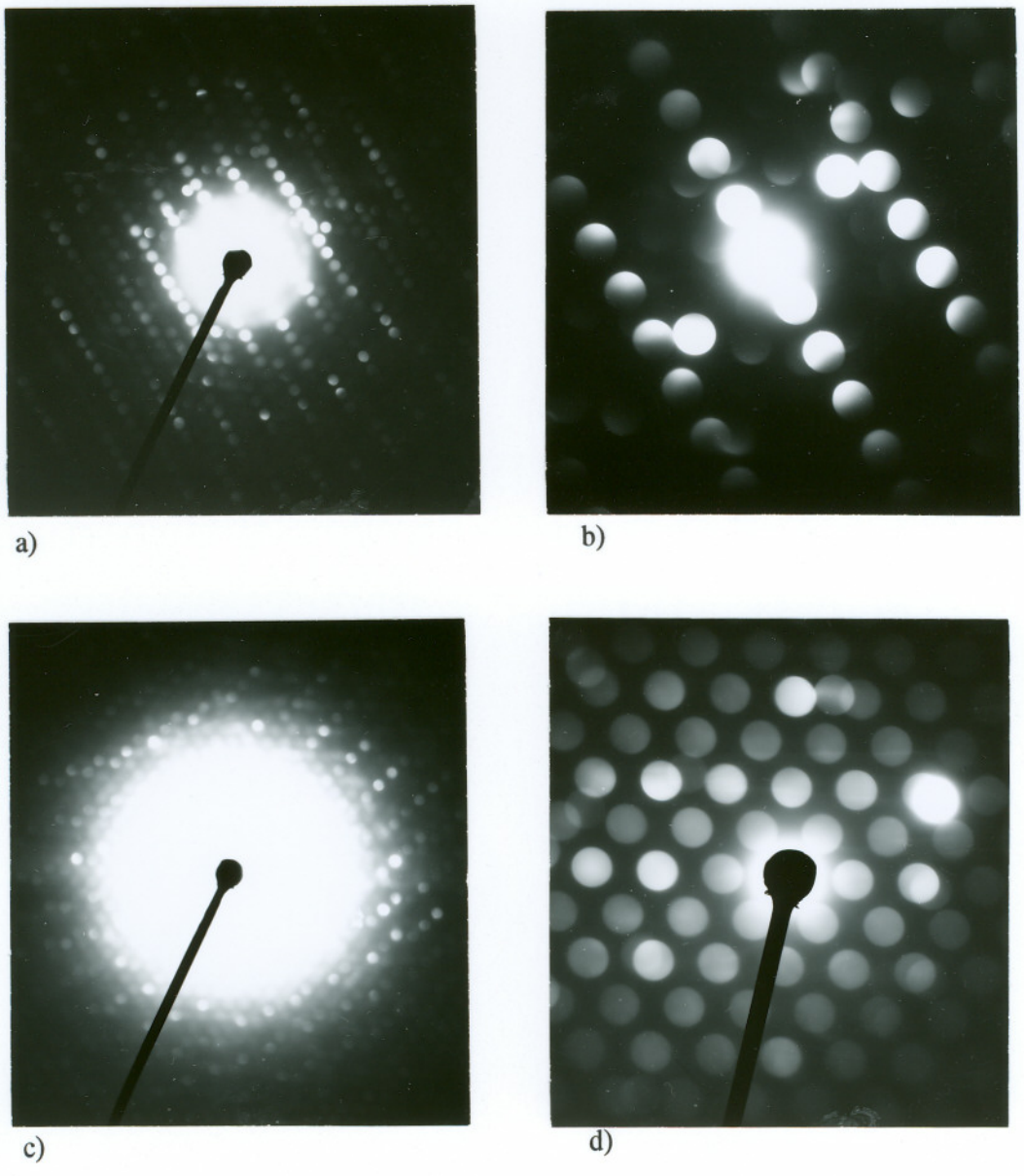

Figure 35

Diffraction patterns obtained from a $NiCr_2O_4$ particle found in the oxide scale grown on the Ni-29Cr-140 ppm S alloy at 900°C in air for 5 minutes. a) $[\bar{2}\bar{1}3]$ holz pattern, b) $[\bar{2}\bar{1}3]$ zolz pattern, c) $[\bar{1}01]$ holz pattern, d) $[\bar{1}01]$ zolz pattern

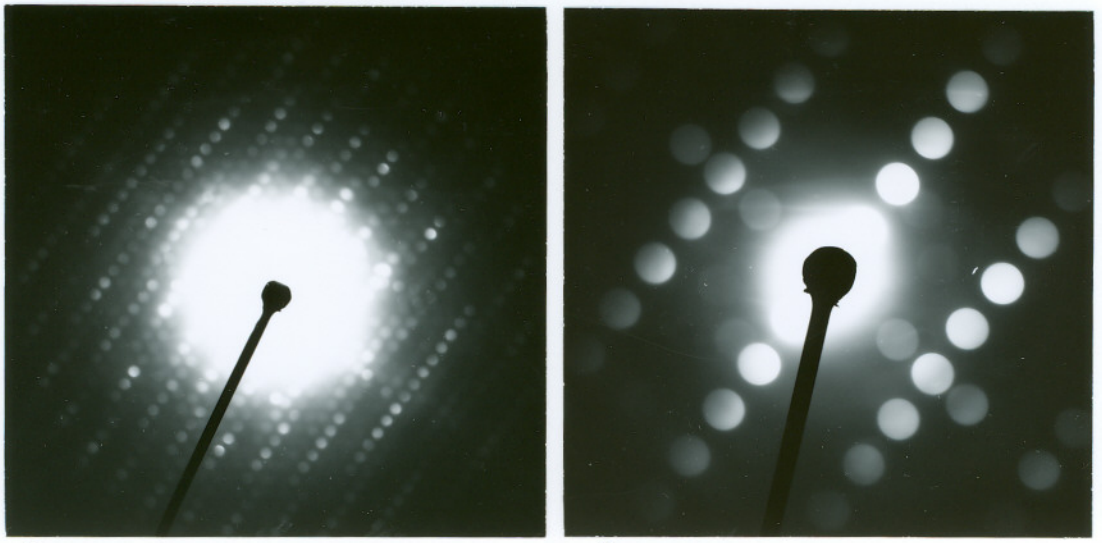

e) f)

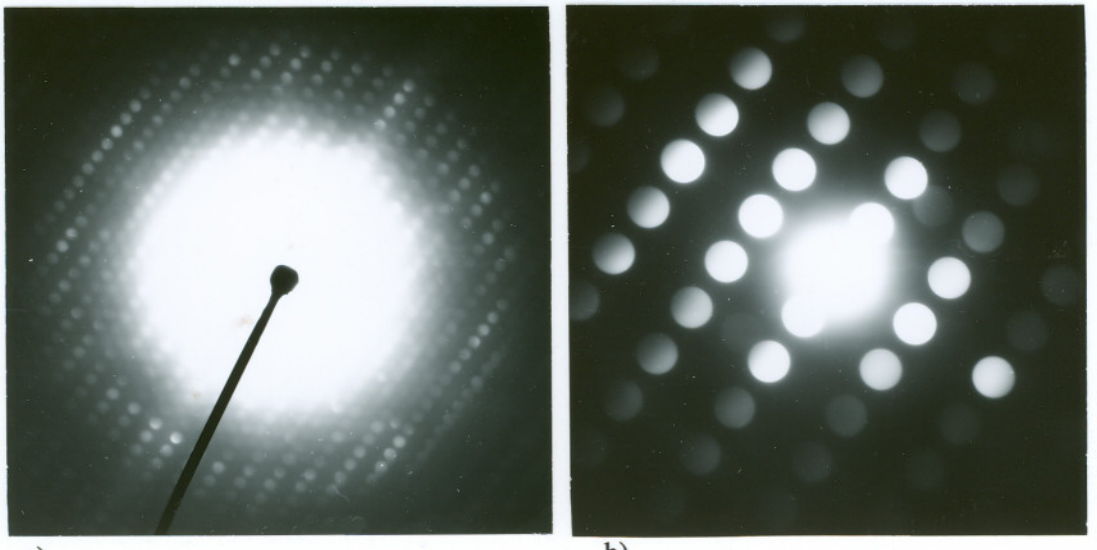

g) h)

Figure 35 (cont.)

Diffraction patterns obtained from a $NiCr_2O_4$ particle found in the oxide scale grown on the Ni-29Cr-140 ppm S alloy at 900°C in air for 5 minutes. e) $[\bar{3}\bar{1}2]$ holz pattern, f) $[\bar{3}\bar{1}2]$ zolz pattern, g) $[\bar{2}\bar{1}1]$ holz pattern, h) $[\bar{2}\bar{1}1]$ zolz pattern

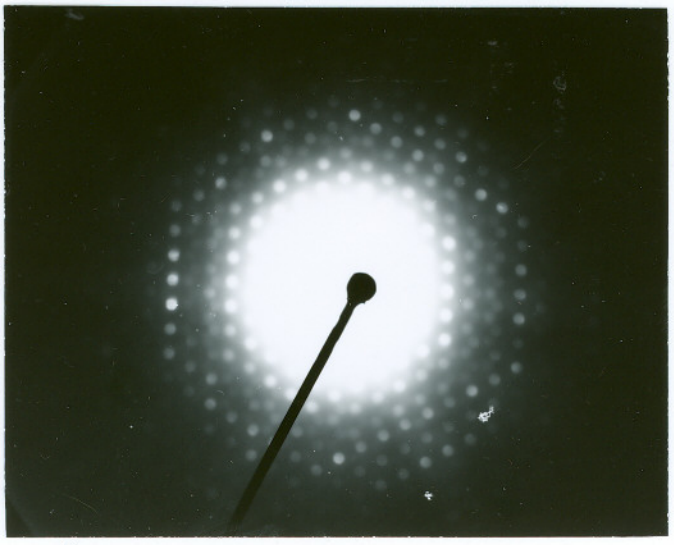

i)

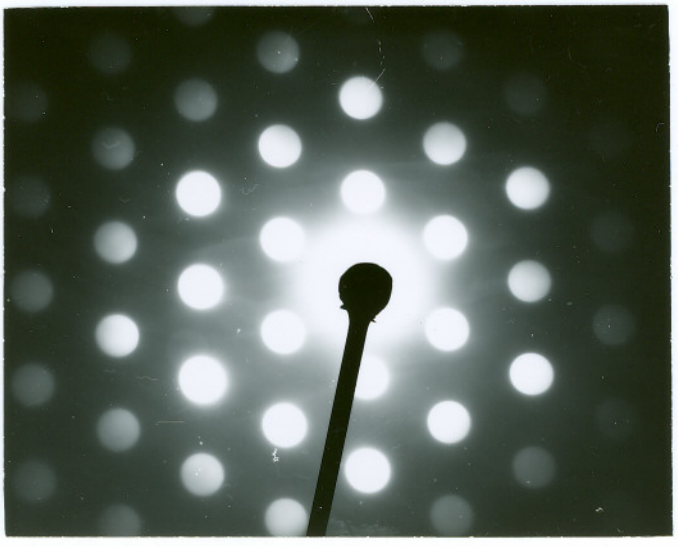

j)

Figure 35 (cont.)

Diffraction patterns obtained from a $NiCr_2O_4$ particle found in the oxide scale grown on the Ni-29Cr-140 ppm S alloy at 900°C in air for 5 minutes. i) $[\bar{1}\bar{1}1]$ holz pattern, j) $[\bar{1}\bar{1}1]$ zolz pattern

Table 4a

Experimentally measured and theoretically calculated d-spacings and the reduced unit cell volume for a $NiCr_2O_4$ particle found in the oxide scale grown on the Ni-29Cr-140 ppm S alloy at 900°C in air for 5 minutes

zone axis	$[\bar{2}\bar{1}3]$	$[\bar{1}01]$	$[\bar{3}\bar{1}2]$	$[\bar{2}\bar{1}1]$	$[\bar{1}\bar{1}1]$
measured (theoretical) d-spacing, Å	a) 4.75 (4.80) b) 1.90 (1.91) c) 1.7 (1.70)	a) 4.79 (4.80) b) 2.94 (2.94) c) 4.79 (4.80)	a) 4.77 (4.80) b) 1.69 (1.70) c) 1.9 (1.91)	a) 4.81 (4.80) b) 2.51 (2.51) c) 2.92 (2.94)	a) 2.94 (2.94) b) 2.93 (2.94) c) 1.69 (1.70)
measured (theoretical) reduced unit cell volume, $Å^3$	133 (144)	(144)	136 (144)	137 (144)	144 (144)

Table 4b

Experimentally measured and theoretically calculated angles between the zone axes for a $NiCr_2O_4$ particle found in the oxide scale grown on the Ni-29Cr-140 ppm S alloy at 900°C in air for 5 minutes. Figures in brackets are the theoretical values

zone axis	$[\bar{2}\bar{1}3]$	$[\bar{1}01]$	$[\bar{3}\bar{1}2]$	$[\bar{2}\bar{1}1]$	$[\bar{1}\bar{1}1]$
$[\bar{2}\bar{1}3]$	0.0 (0.0)	21.02 (19.11)	21.94 (21.79)	29.39 (29.21)	23.02 (22.21)
$[\bar{1}01]$	21.02 (19.11)	0.0 (0.0)	13.68 (19.11)	26.27 (30.00)	35.54 (35.26)
$[\bar{3}\bar{1}2]$	21.94 (21.79)	13.68 (19.11)	0.0 (0.0)	12.60 (10.89)	25.68 (22.21)
$[\bar{2}\bar{1}1]$	29.39 (29.21)	26.27 (30.00)	12.60 (10.89)	0.0 (0.0)	21.20 (19.47)
$[\bar{1}\bar{1}1]$	23.02 (22.21)	35.54 (35.26)	25.68 (22.21)	21.20 (19.47)	0.0

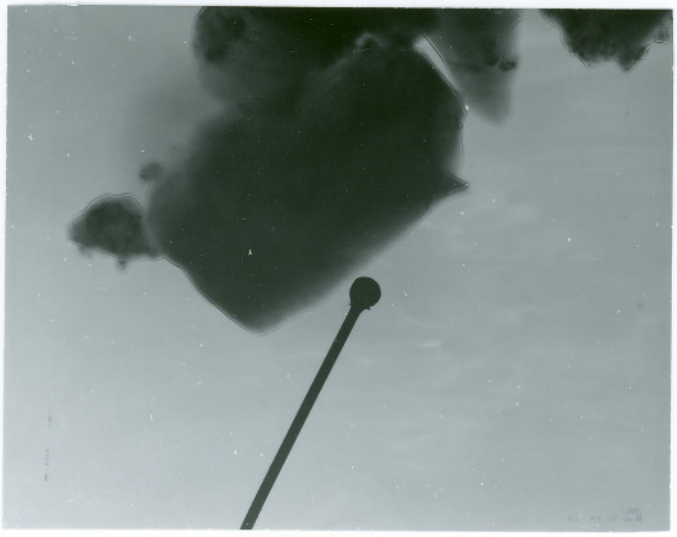

a)

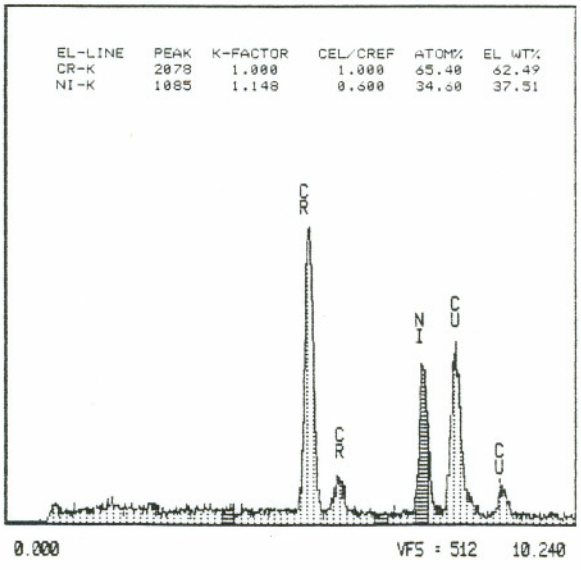

b)

Figure 36

a) Bright field image and b) EDX spectrum obtained from a $NiCr_2O_4$ particle found in the oxide scale grown on the Ni-25Cr-4.8 ppm S alloy at 900°C in air for 24 hours. The Cu peaks are from the Cu grid

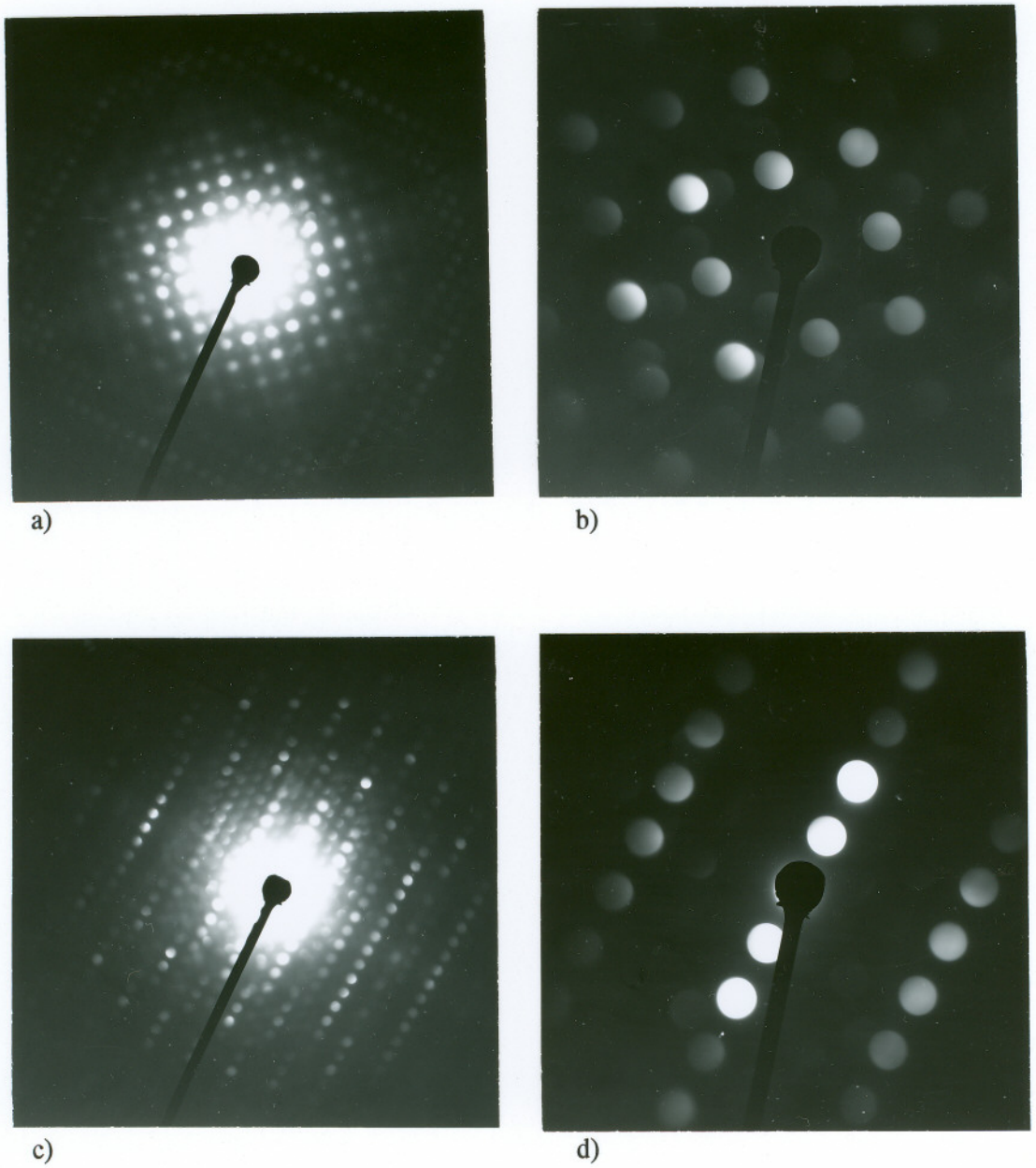

Figure 37

Electron diffraction patterns obtained from a $NiCr_2O_4$ particle found in the oxide scale grown on the Ni-25Cr-4.8 ppm S alloy at 900°C in air for 24 hours. a) [001] holz pattern, b) [001] zolz pattern, c) [015] holz pattern, d) [015] zolz pattern

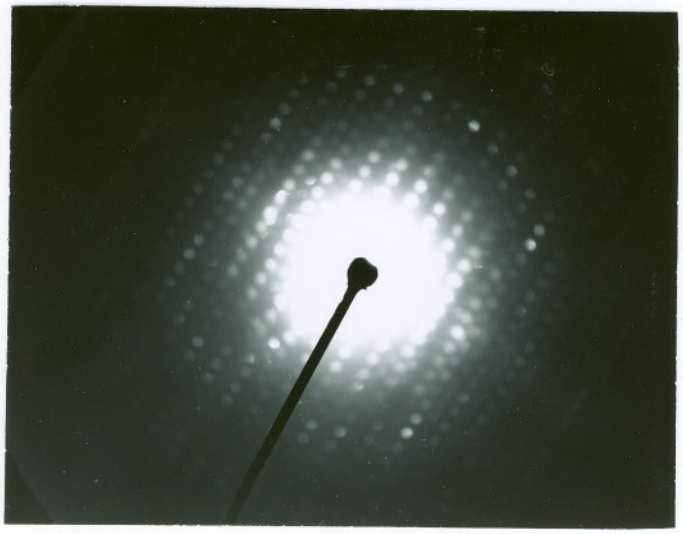

e)

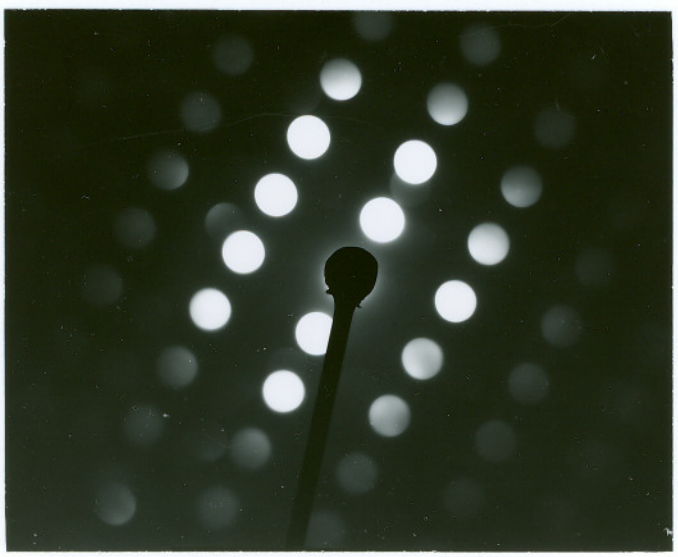

f)

Figure 37 (cont.)

Electron diffraction patterns obtained from a $NiCr_2O_4$ particle found in the oxide scale grown on the Ni-25Cr-4.8 ppm S alloy at 900°C in air for 24 hours. e) [013] holz pattern, f) [013] zolz pattern

Table 5a

Experimentally measured and theoretically calculated d-spacings and the reduced unit cell volume for a $NiCr_2O_4$ particle found in the oxide scale grown on the Ni-25Cr-4.8 ppm S alloy at 900°C in air for 24 hours

zone axis	[001]	[015]	[013]
measured (theoretical) d-spacing, Å	a) 2.95 (2.94) b) 2.06 (2.08) c) 2.93 (2.94)	a) 1.60 (1.60) b) 1.39 (1.41) c) 2.06 (2.08)	a) 1.31 (1.31) b) 2.50 (2.51) c) 2.07 (2.08)
measured (theoretical) reduced unit cell volume, $Å^3$	134 (144)	136 (144)	142 (144)

Table 5b

Experimentally measured and theoretically calculated angles between the zone axes for a $NiCr_2O_4$ particle found in the oxide scale grown on the Ni-25Cr-4.8 ppm S alloy at 900°C in air for 24 hours. Figures in brackets are the theoretical values

zone axis	[001]	[015]	[013]
[001]	0.0 (0.0)	11.54 (11.31)	18.53 (18.43)
[015]	11.54 (11.31)	0.0 (0.0)	7.0 (7.13)
[013]	18.53 (18.43)	7.0 (7.13)	0.0 (0.0)

b. Cr_2O_3 Phase

The diffraction patterns obtained from the Cr rich regions of the oxide scale matched with those for the compound Cr_2O_3 which is reported[115] to have a rhombohedral crystal structure space group 167, $R\bar{3}c$. The lattice parameters matched with the lattice parameters reported in the literature for Cr_2O_3; a = 4.96 Å and c = 13.59 Å, as represented in the hexagonal form.

The bright field image and the EDX spectrum obtained from the Cr_2O_3 particles found in the oxide scale grown on Ni-25Cr-4.8 ppm S alloy at 900°C in air for 5 minutes, are shown in the Figures 38a and 38b respectively. The diffraction patterns taken from a Cr_2O_3 particle are shown in the Figures 39a to 39h. The experimentally measured and theoretically calculated d-spacings, the reduced unit cell volume and the angles between the zone axes are given in Table 6a and 6b.

The Wyckoff positions of the atoms in the Cr_2O_3 crystal (12 Cr on c sites at (0, 0, 0.3475) and 18 O on e sites at (0.36, 0, 0.25)[115] and the lattice parameters of the crystal, required for simulating the crystal, were obtained from the data published in the literature[115]. The diffraction patterns, the d-spacings, the reduced unit cell volume and the angles between the axes, were then calculated using Desktop Microscopist™. The experimentally measured d-spacings, the reduced unit cell volume, and the angles between the zone axes compared well with the theoretically calculated values, as shown in the Table 6a and 6b.

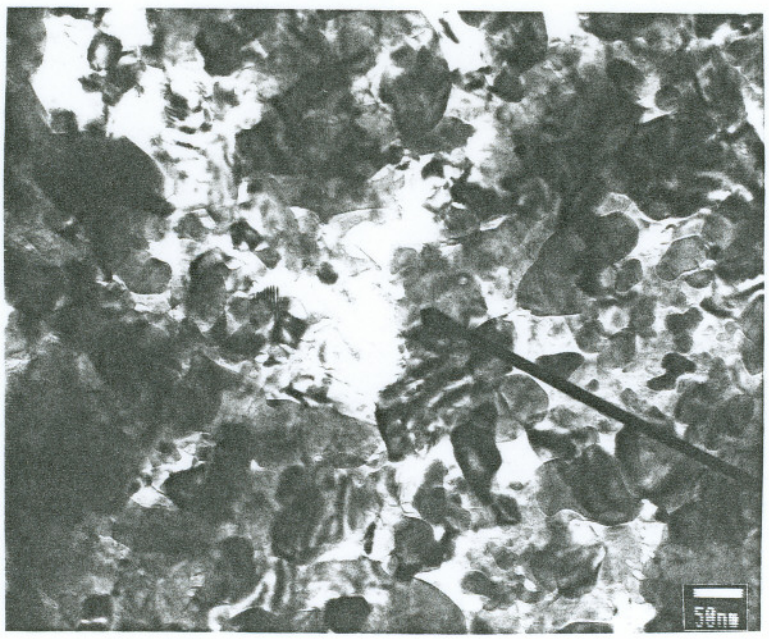

a)

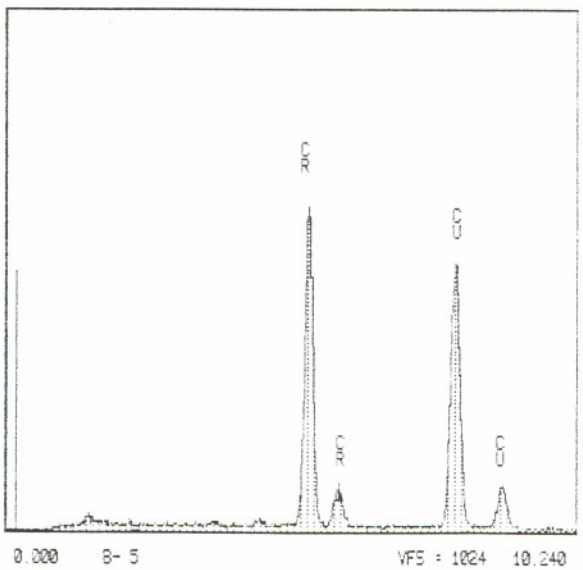

b)

Figure 38

a) Bright field image and b) the EDX spectrum obtained from the Cr_2O_3 grains found in the oxide scale grown on the Ni-25Cr-4.8 ppm S alloy at 900°C in air for 5 minutes. The Cu peaks are from the Cu grid

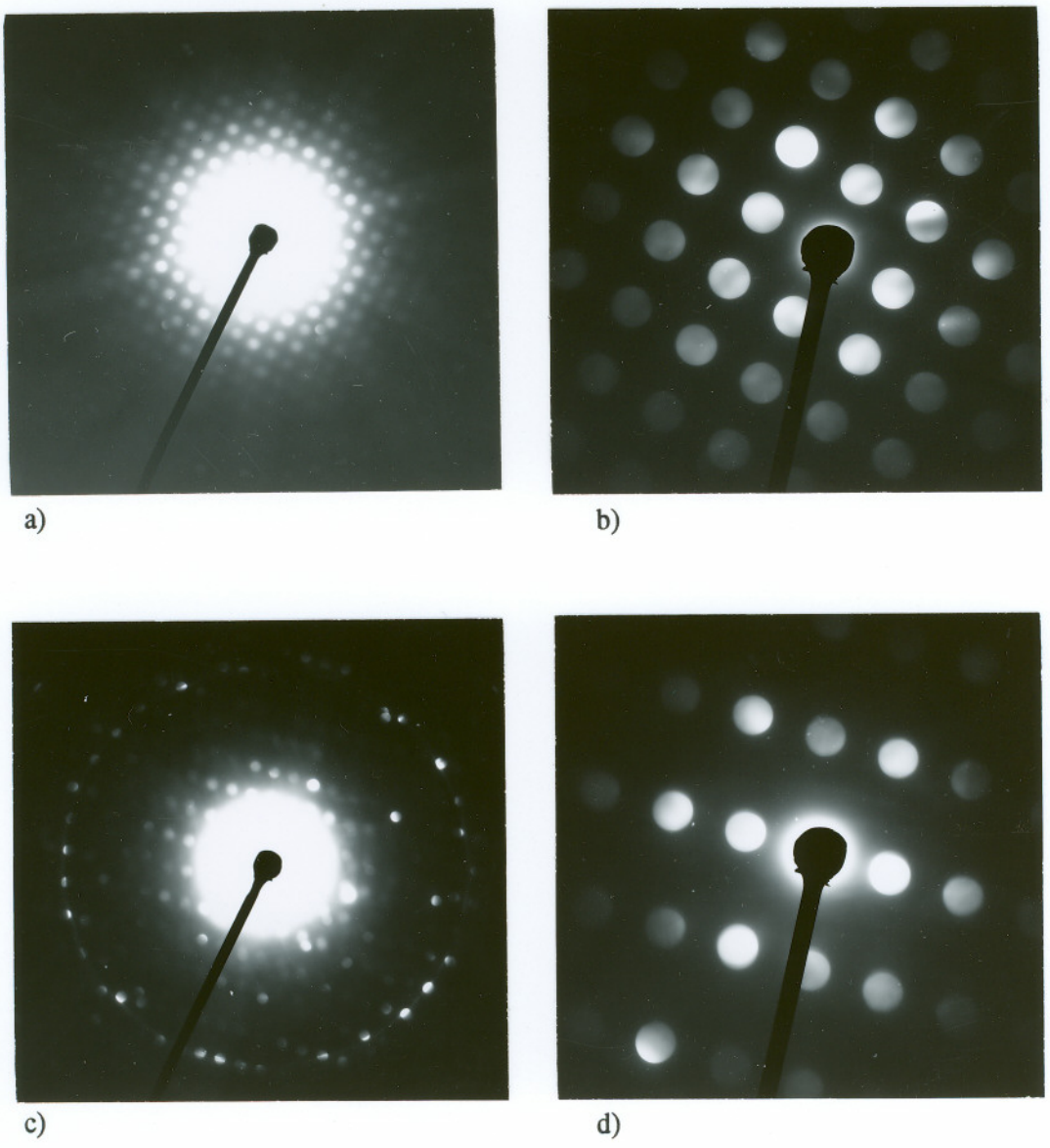

Figure 39

Diffraction patterns obtained from the Cr_2O_3 grains found in the oxide scale grown on the Ni-25Cr-4.8 ppm S alloy at 900°C in air for 5 minutes. a) [$\bar{2}$021] holz pattern, b) [$\bar{2}$021] zolz pattern, c) [$\bar{4}$131] holz pattern, d) [$\bar{4}$131] zolz pattern

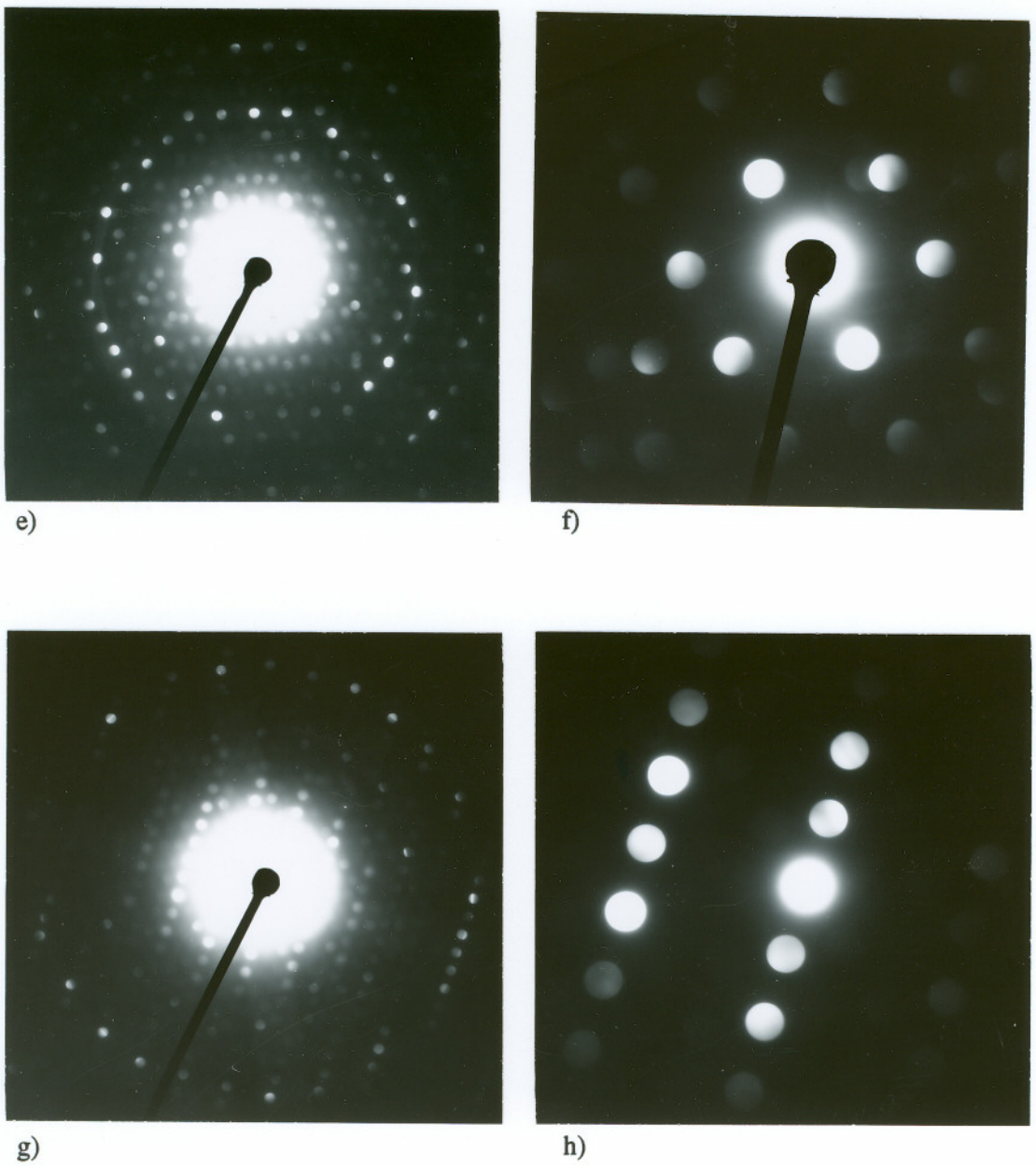

Figure 39 (cont.)

Diffraction patterns obtained from the Cr_2O_3 grains found in the oxide scale grown on the Ni-25Cr-4.8 ppm S alloy at 900°C in air for 5 minutes. e) [$\bar{5}$232] holz pattern, f) [$\bar{5}$232] zolz pattern, g) [$\bar{4}$223] holz pattern, h) [$\bar{4}$223] zolz pattern

Table 6a

Experimentally measured and theoretically calculated d-spacings and the reduced unit cell volume for a Cr_2O_3 particle found in the oxide scale grown on the Ni-25Cr-4.8 ppm S alloy at 900°C in air for 5 minutes

zone axis	[$\bar{2}$021]	[$\bar{4}$131]	[$\bar{5}$232]	[$\bar{4}$223]
measured (theoretical) d-spacing, Å	a) 2.45 (2.48) b) 3.57 (3.63) c) 2.64 (2.66)	a) 2.26 (2.26) b) 2.17 (2.18) c) 3.61 (3.63)	a) 2.59 (2.66) b) 2.12 (2.17) c) 2.08 (2.05)	a) 1.56 (1.58) b) 1.44 (1.43) c) 3.59 (3.63)
measured (theoretical) reduced unit cell volume, $Å^3$	92 (96)	93 (96)	95 (96)	90 (96)

Table 6b

Experimentally measured and theoretically calculated angles between the zone axes for a Cr_2O_3 particle found in the oxide scale grown on the Ni-25Cr-4.8 ppm S alloy at 900°C in air for 5 minutes. Figures in brackets are the theoretical values

zone axis	[$\bar{2}$021]	[$\bar{4}$131]	[$\bar{5}$232]	[$\bar{4}$223]
[$\bar{2}$021]	0.0 (0.0)	20.83 (19.81)	18.03 (18.76)	25.86 (25.64)
[$\bar{4}$131]	20.83 (19.81)	0.0 (0.0)	14.11 (14.78)	33.74 (32.51)
[$\bar{5}$232]	18.03 (18.76)	14.11 (14.78)	0.0 (0.0)	19.83 (18.48)
[$\bar{4}$223]	25.86 (25.64)	33.74 (32.51)	19.83 (18.48)	0.0 (0.0)

2. HOMOGENIZED YTTRIUM CONTAINING ALLOYS

a. Ion-milling

i. Ni_5Y Phase

The phase Ni_5Y was found in all the ion-milled yttrium containing alloys, along the grain/dendrite boundaries and in the interdendritic regions. The bright field image and the EDX spectrum, along with the semi-quantitative analysis of the EDX spectrum, obtained from the Ni_5Y particle found in the Ni-23Cr-650 ppm Y alloy, are shown in the Figures 40a and 40b respectively. The bright field image and the EDX spectrum along with the semi-quantitative analysis of the EDX spectrum obtained from the grain/dendrite boundary of the Ni-22Cr-0.62Y alloy are shown in the Figures 40c and 40d. The diffraction patterns taken from the particle shown in Figure 40a and their attendant indexing, are shown in the Figures 41a to 41j.

The semi-quantitative analysis of the EDX spectra (Figures 40b and 40d) yielded 75.76 weight% Ni and 24.24 weight% Y, and 75.30 weight% Ni and 24.70 weight% Y, respectively. The theoretical values for Ni and Y weight% in Ni_5Y are 76.75% and 23.25%, respectively. Thus the experimentally and theoretically calculated Ni and Y content in Ni_5Y (76.75% Ni, 23.25% Y) match very well.

The crystal structure of the Ni_5Y particle was found to be hexagonal space group 191, P6/mmm, as reported in the literature[117]. The lattice parameters were found to be a = 4.89 Å, and c = 3.96 Å. The experimentally determined and theoretically calculated values of the d-spacings, reduced unit cell volume, and the angles between the zone axes for the Ni_5Y phase are given in Table 7a and Table 7b.

The Wyckoff positions of the atoms in the Ni_5Y crystal (2 Ni on c sites at (1/3, 2/3, 0), 3 Ni on g sites at (1/2, 0, 1/2) and i Y on a site at (0, 0, 0))[117] and the lattice parameters of the crystal required for simulating the crystal, the diffraction patterns, and for calculating the d-spacings, the reduced unit cell volume and the angle between the axes, using Desktop Microscopist™, were obtained from the data published in the literature[117]. It can be seen from

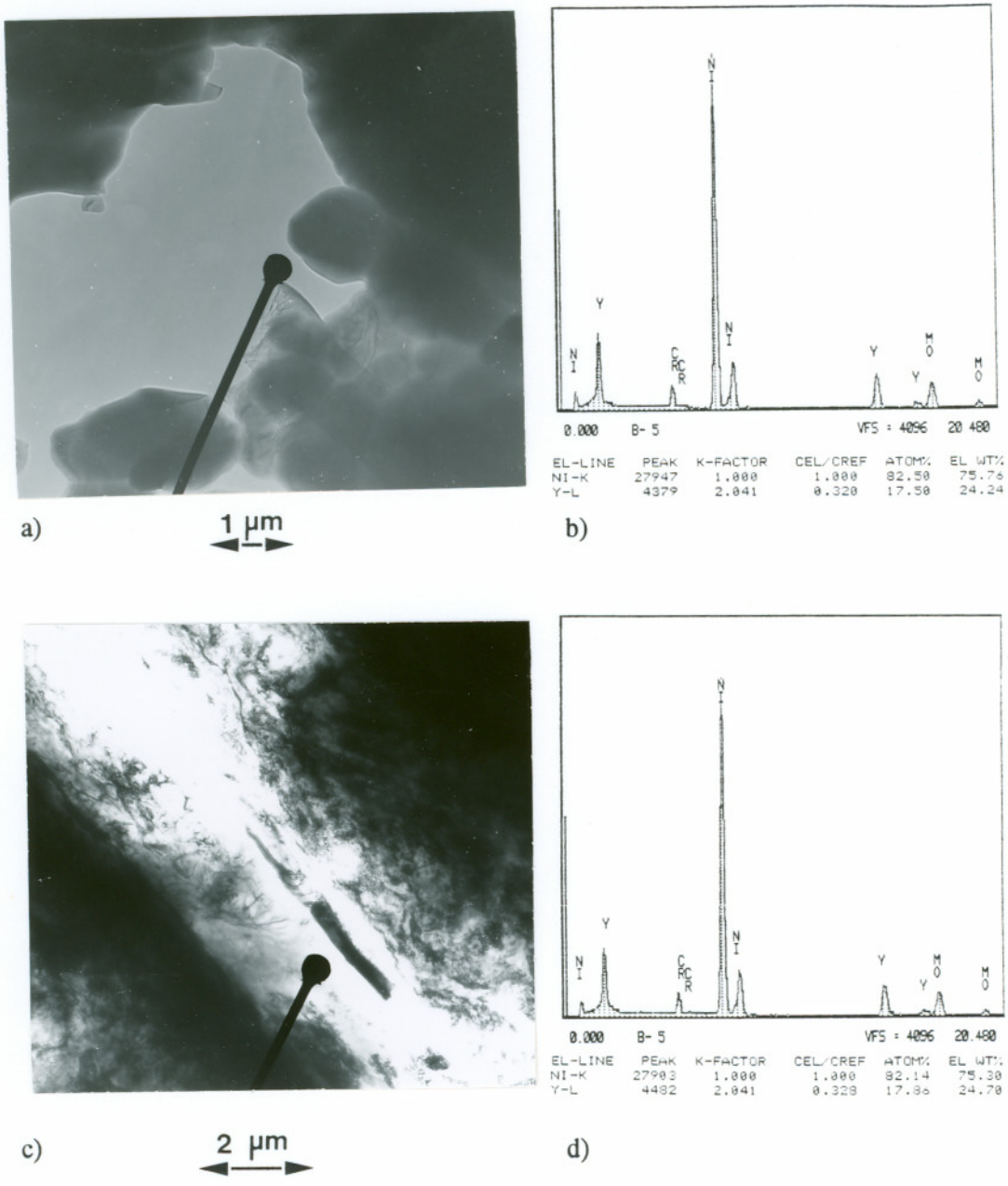

Figure 40

a) Bright field image and b) the EDX spectrum obtained from the Ni_5Y particle found in the ion-milled as-homogenized Ni-23Cr-650 ppm Y alloy, c) bright field image, and d) EDX spectrum of the Ni-Y rich grain/dendrite boundary in the ion-milled as-homogenized Ni-22Cr-0.62Y alloy. The Mo peaks seen in the EDX spectra are from the Mo washer

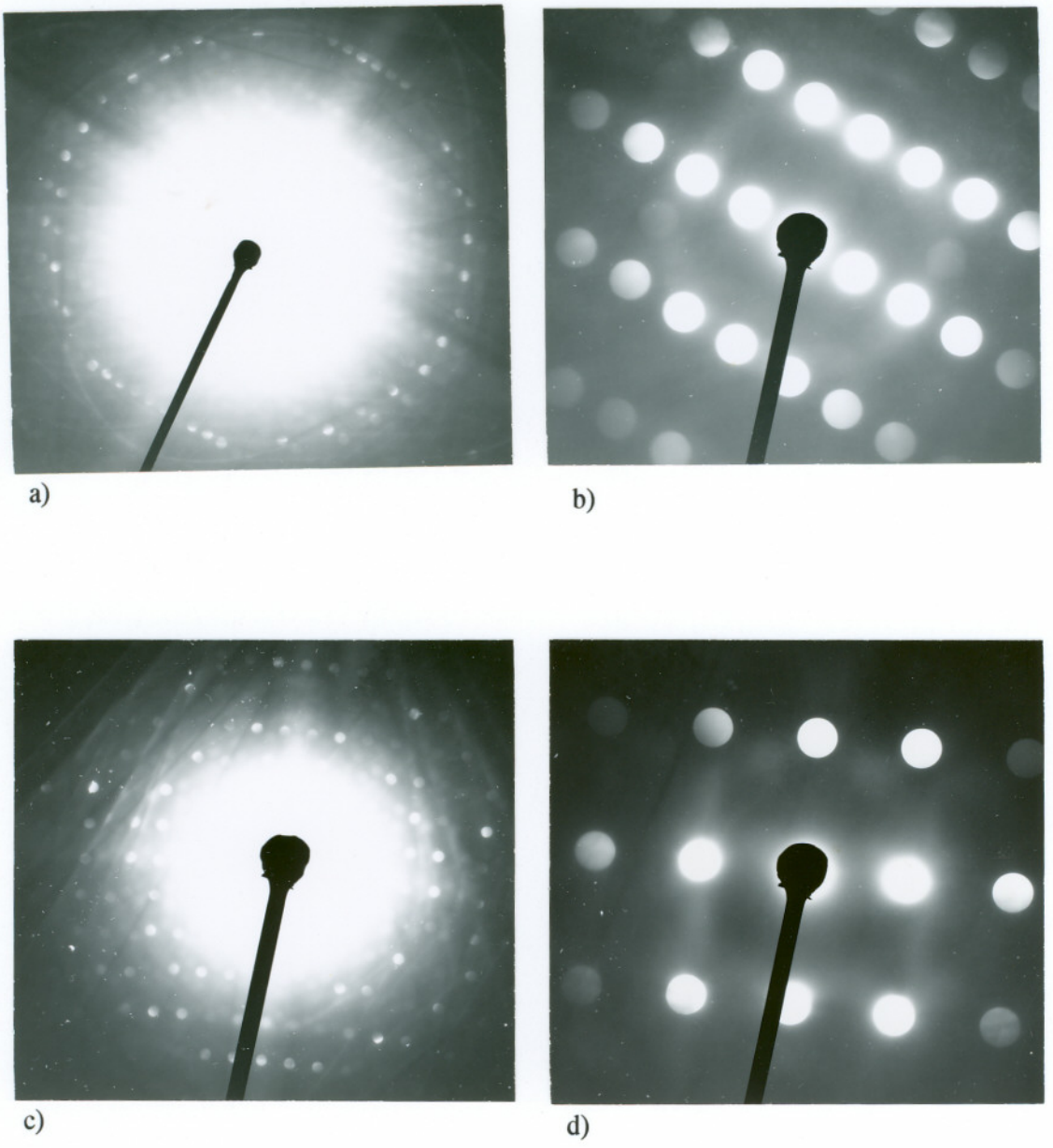

Figure 41

Electron Diffraction patterns obtained from the Ni_5Y particle found in the ion-milled as-homogenized Ni-23Cr-650 ppm Y alloy. a) $[\bar{1}\bar{1}26]$ holz pattern, b) $[\bar{1}\bar{1}26]$ zolz pattern, c) $[\bar{1}014]$ holz pattern, d) $[\bar{1}014]$ zolz pattern

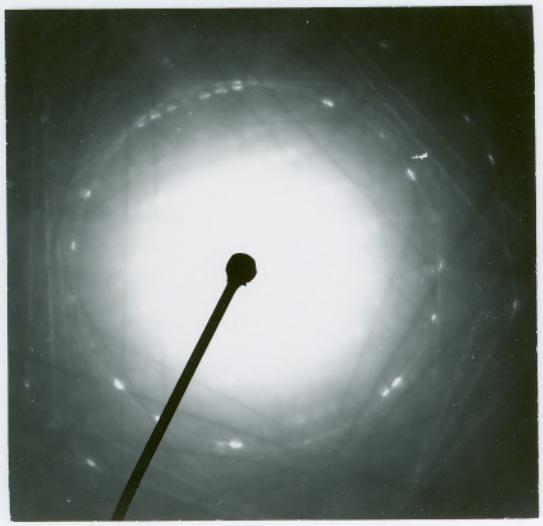

e)

f)

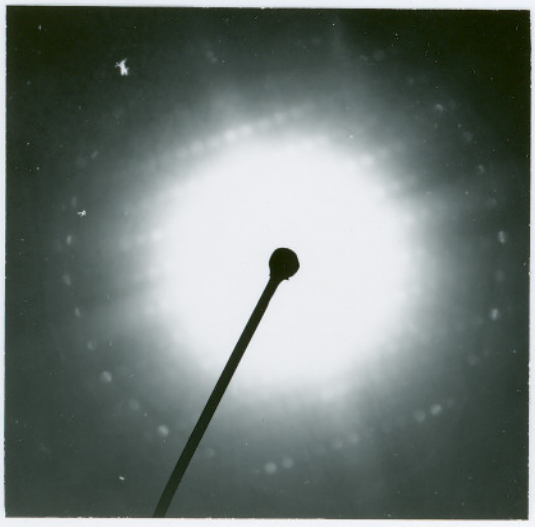

g)

h)

Figure 41 (cont.)

Electron Diffraction patterns obtained from the Ni_5Y particle found in the ion-milled as-homogenized Ni-23Cr-650 ppm Y alloy. e) [$\bar{2}$119] holz pattern, f) [$\bar{2}$119] zolz pattern, g) [$\bar{2}$116] holz pattern, h) [$\bar{2}$116] zolz pattern

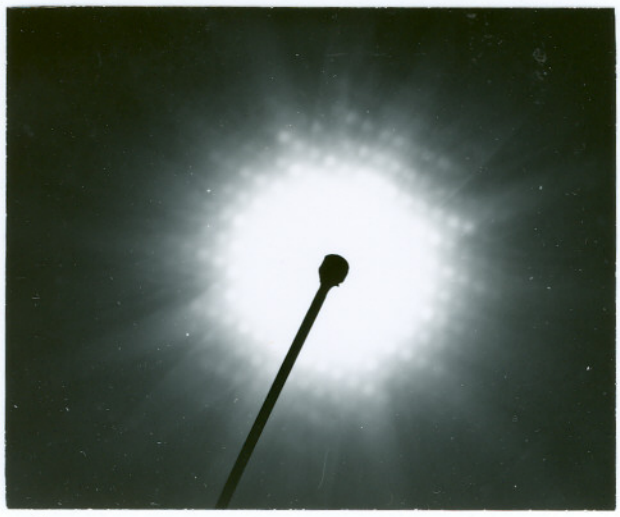

i)

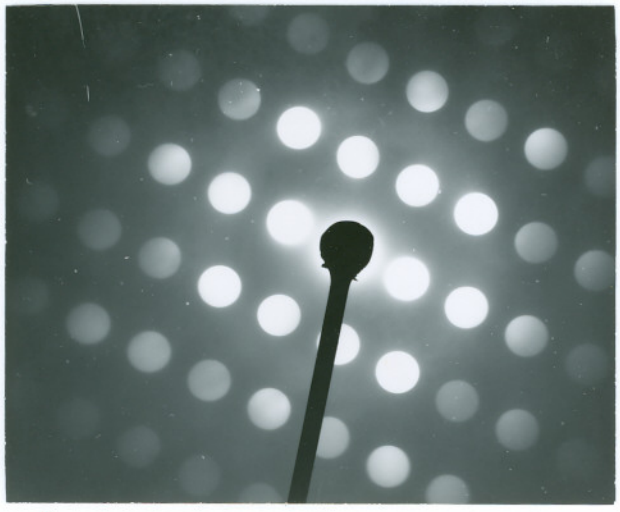

j)

Figure 41 (cont.)

Electron diffraction patterns obtained from the Ni_5Y particle found in the ion-milled as-homogenized Ni-23Cr-650 ppm Y alloy. i) $[\bar{1}\bar{1}23]$ holz pattern, j) $[\bar{1}\bar{1}23]$ zolz pattern

Table 7a

Experimentally measured and theoretically calculated d-spacings and the reduced unit cell volume for a Ni_5Y particle , found in the ion-milled as-homogenized Ni-23Cr-650 ppm Y alloy

zone axis	$[\bar{1}\bar{1}26]$	$[\bar{1}014]$	$[\bar{2}119]$	$[\bar{2}116]$	$[\bar{1}\bar{1}23]$
measured (theoretical) d-spacing, Å	a) 4.18 (4.23) b) 1.85 (1.87) c) 2.07 (2.08)	a) 1.9 (1.87) b) 1.52 (1.48) c) 2.49 (2.44)	a) 1.47 (1.48) b) 1.32 (1.33) c) 4.23 (4.23)	a) 2.08 (2.08) b) 1.86 (1.87) c) 4.24 (4.23)	a) 1.47 (1.48) b) 1.32 (1.33) c) 4.20 (4.23)
measured (theoretical) reduced unit cell volume, $Å^3$	78 (81.9)	79 (81.9)	82 (81.9)	81 (81.9)	77 (81.9)

Table 7b

Experimentally measured and theoretically calculated angles between the zone axes for a Ni_5Y, particle found in the ion-milled as-homogenized Ni-23Cr-650 ppm Y alloy. Figures in brackets are the theoretical values

zone axis	$[\bar{1}\bar{1}26]$	$[\bar{1}014]$	$[\bar{2}119]$	$[\bar{2}116]$	$[\bar{1}\bar{1}23]$
$[\bar{1}\bar{1}26]$	0.0 (0.0)	15.13 (15.23)	27.78 (27.52)	29.94 (30.46)	21.02 (19.31)
$[\bar{1}014]$	15.13 (15.23)	0.0 (0.0)	15.12 (13.19)	14.87 (15.23)	29.9 (29.27)
$[\bar{2}119]$	27.78 (27.52)	15.12 (13.19)	0.0 (0.0)	9.91 (9.32)	45 (43.12)
$[\bar{2}116]$	29.94 (30.46)	14.87 (15.23)	9.91 (9.32)	0.0 (0.0)	42.87 (42.3)
$[\bar{1}\bar{1}23]$	21.02 (19.31)	29.9 (29.27)	45 (43.12)	42.87 (42.83)	0.0 (0.0)

Table 7a and 7b that the experimentally measured and theoretically calculated values of the d-spacings, the reduced unit cell volume, and the angles between the zones match very well.

ii. Y_2O_2S Phase

The yttrium oxysulfide, Y_2O_2S, phase with a trigonal crystal structure space group 164, $P\bar{3}m1$ with the reported[113,118] lattice parameters a = b = 3.79 Å and c = 6.59 Å was found in the as-homogenized Ni-22Cr-0.62% Y alloy. This phase was found at the alloy grain/dendrite boundaries. The bright field image and the EDX spectrum obtained from a Y_2O_2S particle found in the Ni-22Cr-0.62Y alloy at the grain/dendrite boundary, are shown in the Figures 42a and 42b respectively. The Y_2O_2S particle had a globular morphology, as shown in the Figure 42a. The analysis of the EDX spectrum yielded 85.91 weight% Y and 14.09 weight% S in the Y_2O_2S phase, as shown in the Figure 42b.

The diffraction patterns taken from the Y_2O_2S particle are shown in the Figures 43a-h. Tables 8a and 8b show the experimentally measured and theoretically calculated values of the d-spacings, the reduced unit cell volume and the angles between the zone axes, using the crystal structure data reported in the literature[113,118].

The Wyckoff positions of the atoms in the Y_2O_2S crystal (2 Y on d sites at (1/3, 2/3, 0.29), 1 S on a site at (0, 0, 0) and 2 O on d sites at (1/3, 2/3, 0.64))[113] and the lattice parameters of the crystal, required for simulating the crystal, the diffraction patterns, and for calculating the d-spacings, the reduced unit cell volume and the angles between the zone axes, using Desktop Microscopist™, were obtained from the data published in the literature[113,118].

From the Table 8a and 8b it can be seen that the experimentally determined d-spacings, the reduced unit cell volume and the angles between the zone axes, match very well.

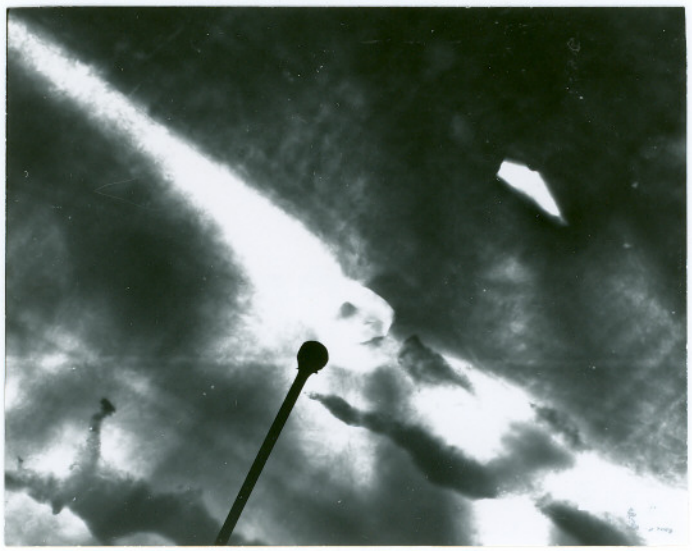

a) 3 μm

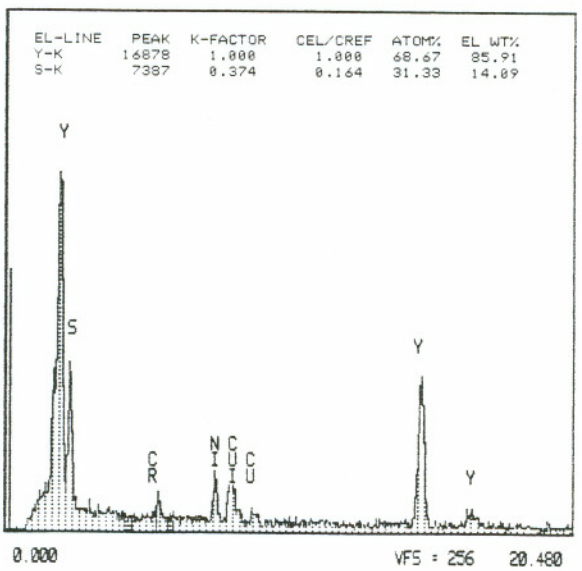

b)

Figure 42

a) Bright field image and b) EDX spectrum obtained from the Y_2O_2S particle found in the ion-milled as-homogenized Ni-22Cr-0.62Y alloy. The Mo peaks are from the Mo washer

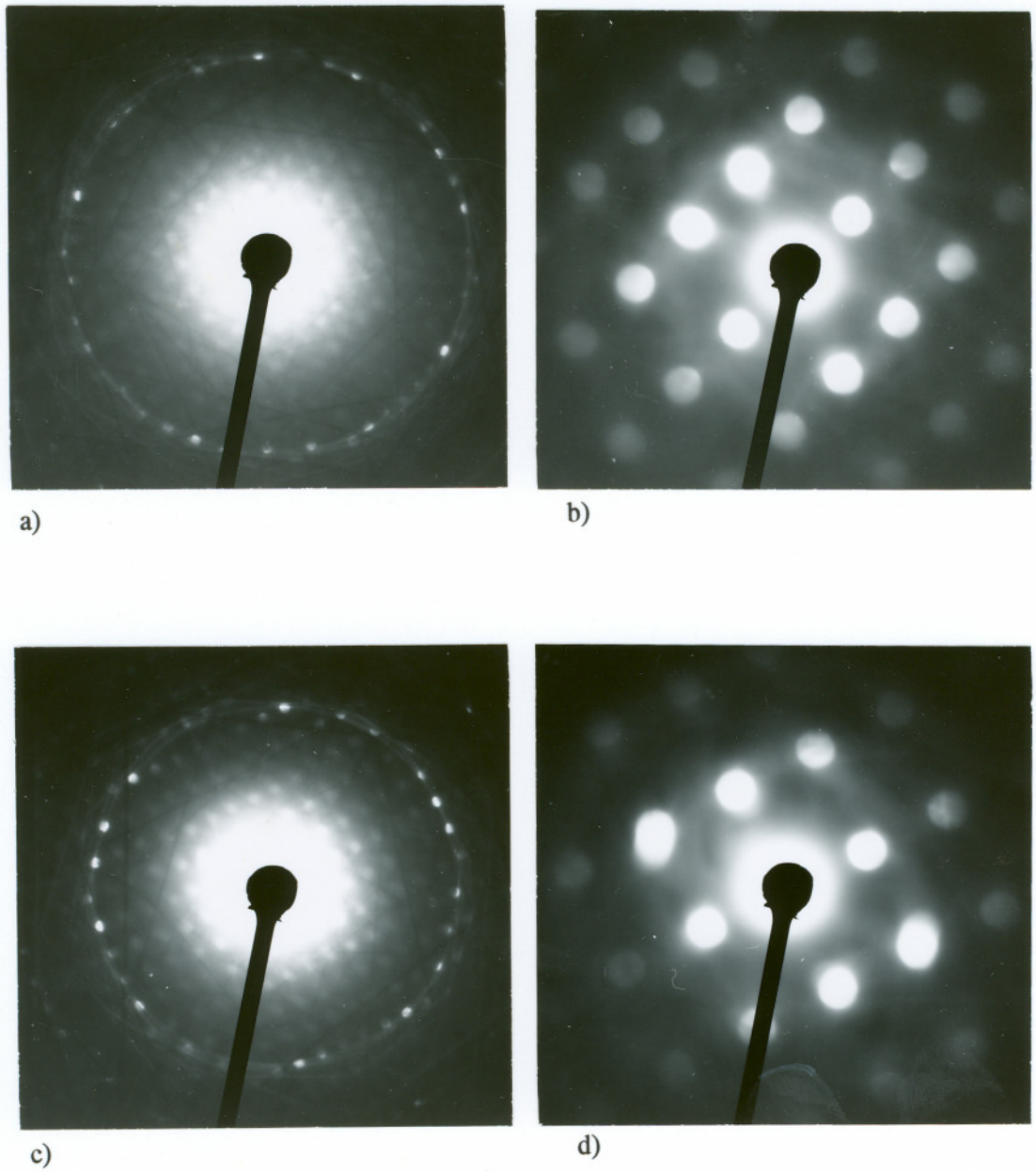

Figure 43

Electron diffraction patterns obtained from the Y_2O_2S particle found in the ion-milled as-homogenized Ni-22Cr-0.62Y alloy. a) [$4\bar{2}\bar{2}3$] holz pattern, b) [$4\bar{2}\bar{2}3$] zolz pattern, c) [$5\bar{4}\bar{1}3$] holz pattern, d) [$5\bar{4}\bar{1}3$] zolz pattern

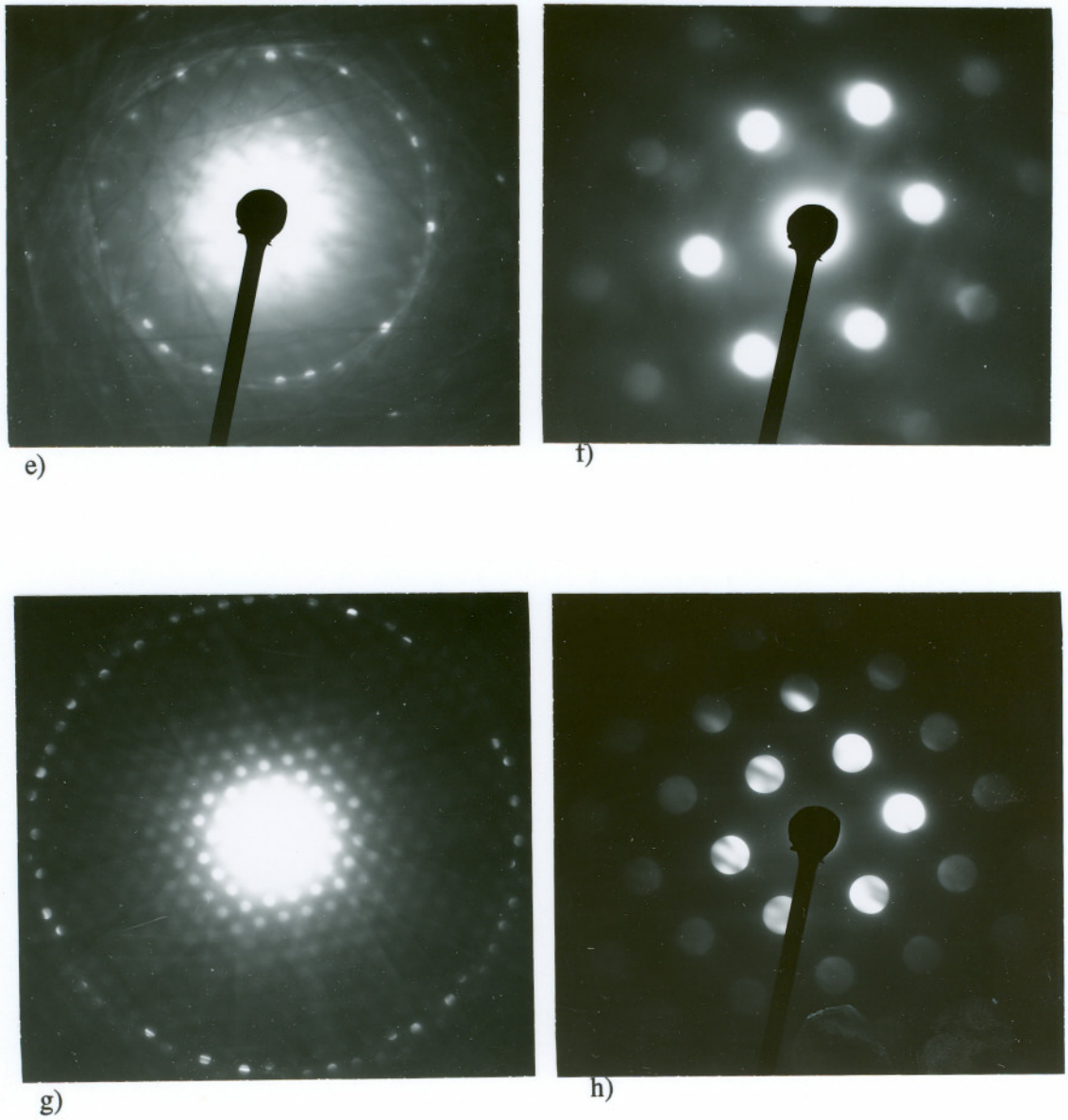

Figure 43 (cont.)

Electron diffraction patterns obtained from the Y_2O_2S particle found in the ion-milled as-homogenized Ni-22Cr-0.62Y alloy. e) $[2\bar{2}01]$ holz pattern, f) $[2\bar{2}01]$ zolz pattern, g) $[2\bar{1}\bar{1}3]$ holz pattern, h) $[2\bar{1}\bar{1}3]$ zolz pattern

Table 8a

Experimentally measured and theoretically calculated d-spacings and the reduced unit cell volume for the phase Y_2O_2S, found in the ion-milled as-homogenized Ni-22Cr-0.62Y alloy

zone axis	$[4\bar{2}\bar{2}3]$	$[5\bar{4}\bar{1}3]$	$[2\bar{2}01]$	$[2\bar{1}\bar{1}3]$
measured (theoretical) d-spacing, Å	a) 2.30 (2.32) b) 2.28 (2.32) c) 3.28 (3.27)	a) 2.30 (2.32) b) 1.81 (1.82) c) 2.92 (2.92)	a) 2.29 (2.32) b) 1.88 (1.89) c) 2.32 (2.32)	a) 2.92 (2.93) b) 2.92 (2.93) c) 3.27 (3.27)
measured (theoretical) reduced unit cell volume, $Å^3$	79 (81.55)	79 (81.55)	76 (81.55)	80 (81.55)

Table 8b

Experimentally measured and theoretically calculated angles between the zone axes for the phase Y_2O_2S, found in the ion-milled as-homogenized Ni-22Cr-0.62Y alloy. Figures in brackets are the theoretical values

zone axis	$[4\bar{2}\bar{2}3]$	$[5\bar{4}\bar{1}3]$	$[2\bar{2}01]$	$[2\bar{1}\bar{1}3]$
$[4\bar{2}\bar{2}3]$	0.0 (0.0)	18.43 (17.00)	31.65 (28.53)	20.23 (19.08)
$[5\bar{4}\bar{1}3]$	18.43 (17.00)	0.0 (0.0)	13.31 (11.54)	30.23 (29.56)
$[2\bar{2}01]$	31.65 (28.53)	13.31 (11.54)	0.0 (0.0)	39.10 (39.21)
$[2\bar{1}\bar{1}3]$	20.23 (19.08)	30.23 (29.56)	39.10 (39.21)	0.0 (0.0)

b. Alloy Dissolution

i. Y_2O_2S Phase

Globular particles rich in yttrium and sulfur were detected in all the yttrium containing alloys (Figures 44a and 44b), dissolved in the iodine-methanol solution. They were identified as yttrium oxysulfide particles by matching the electron diffraction patterns with the computer simulated diffraction patterns for Y_2O_2S (Figures 45a to 45h).

The bright field image and the EDX spectrum obtained from a Y_2O_2S particle found in the Ni-23Cr-650 ppm Y alloy dissolved in the iodine-methanol solution, are shown in Figures 44a and 44b. The electron diffraction patterns taken from this particle along with their attendant indexing, are shown in the Figures 45a to 45h. Given in the Tables 9a and 9b are the experimentally determined and theoretically calculated d-spacings, the reduced unit cell volume and the angles between the zone axes. The experimentally determined d-spacings, the reduced unit cell volume, and the angles between the zones, compare well with the theoretically calculated figures. The analysis of the EDX spectrum shown in Figure 44b, yielded 85.30 weight% Y and 14.70 weight% S, also shown in Figure 44b.

The Wyckoff positions of the atoms in the Y_2O_2S crystal and the lattice parameters of the crystal, required for simulating the crystal, the diffraction patterns, and for calculating the d-spacings, the reduced unit cell volume and the angles between the zone axes, using Desktop Microscopist™, were obtained from the data published in the literature [113,118].

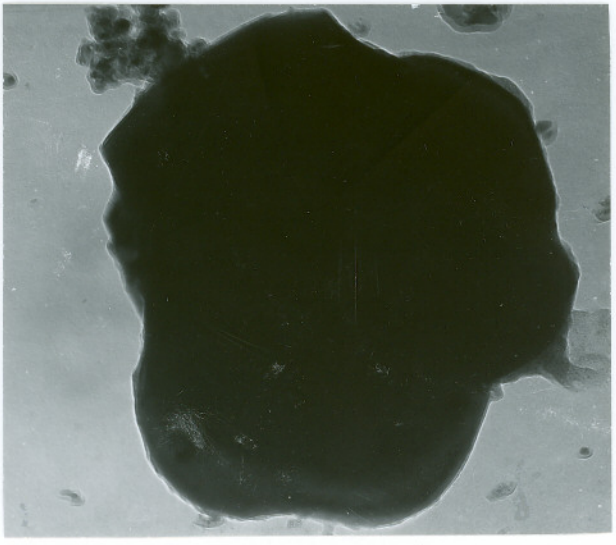

a) 125 nm

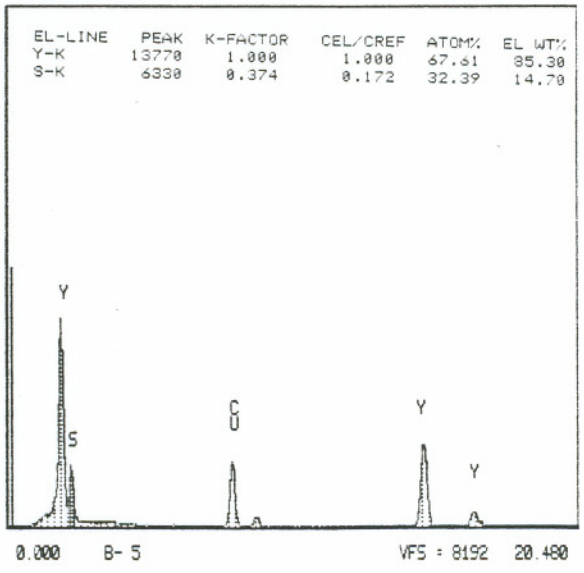

b)

Figure 44

a) Bright field image and b) EDX spectrum obtained from a Y_2O_2S particle found in the as-homogenized Ni-23Cr-650 ppm Y alloy dissolved in the iodine-methanol solution

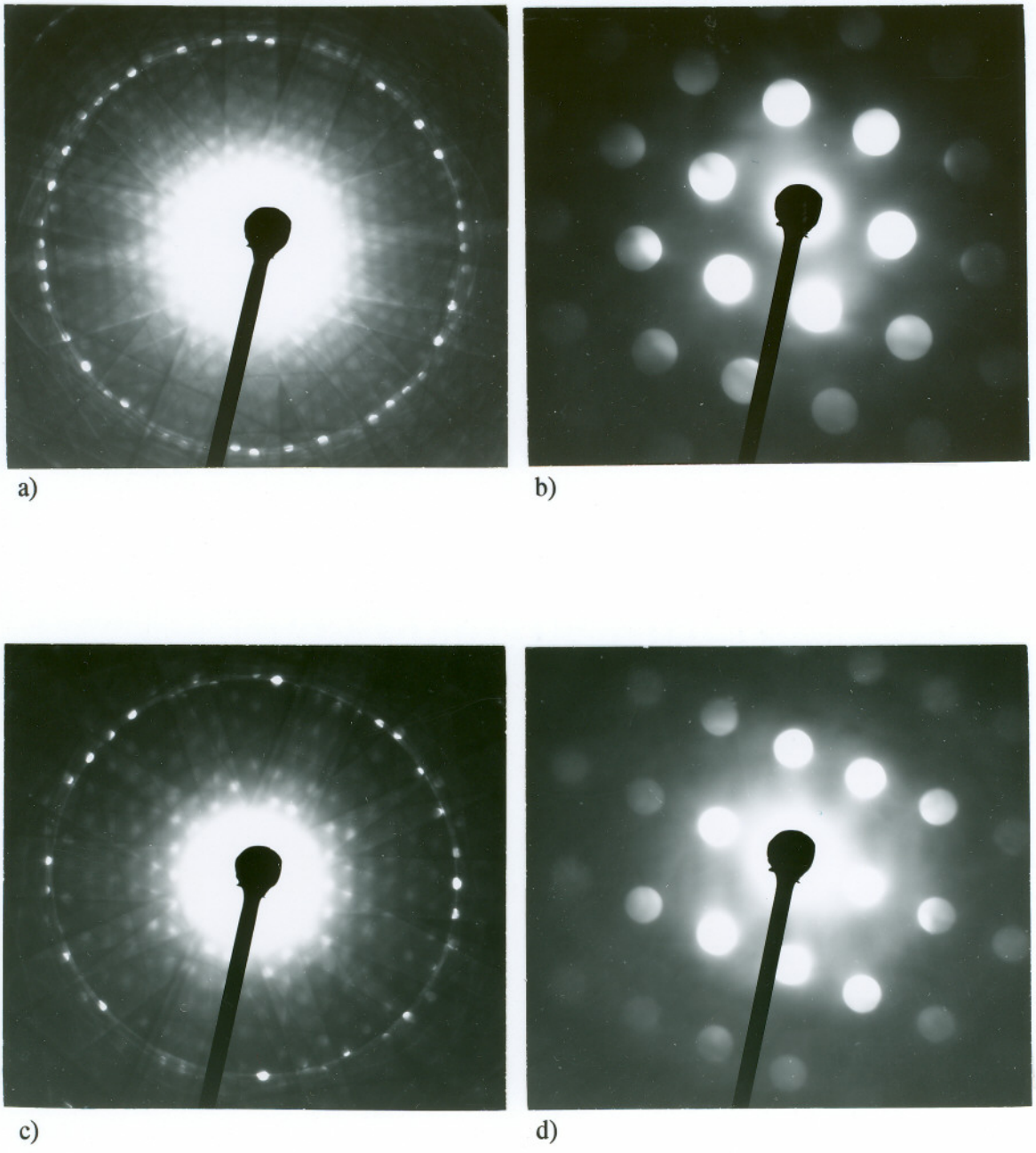

Figure 45

Electron diffraction patterns obtained from a Y_2O_2S particle found in the as-homogenized Ni-23Cr-650 ppm Y alloy dissolved in the iodine-methanol solution. a) $[\bar{1}\bar{1}23]$ holz pattern, b) $[\bar{1}\bar{1}23]$ zolz pattern c) $[\bar{2}\bar{2}43]$ holz pattern, d) $[\bar{2}\bar{2}43]$ zolz pattern

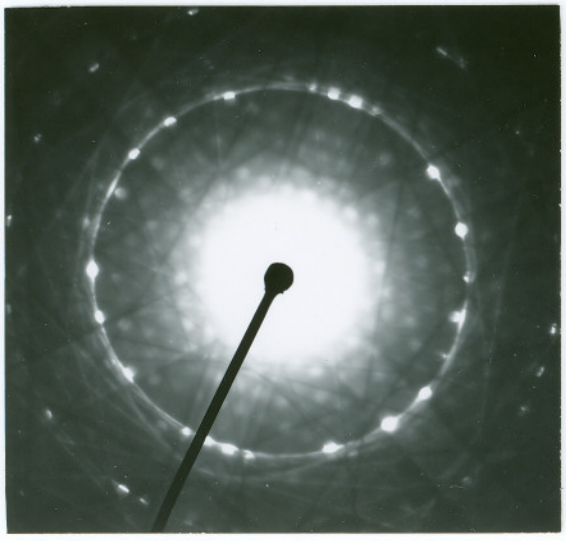

e)

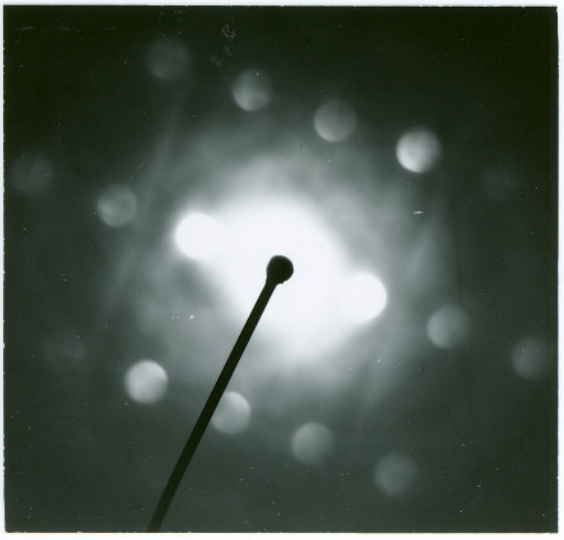

f)

g)

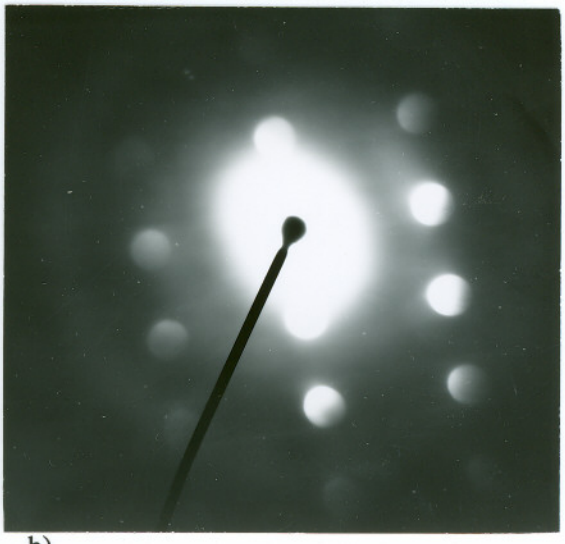

h)

Figure 45 (cont.)

Electron diffraction patterns obtained from a Y_2O_2S particle found in the as-homogenized Ni-23Cr-650 ppm Y alloy dissolved in the iodine-methanol solution. e) $[\bar{1}\bar{1}26]$ holz pattern, f) $[\bar{1}\bar{1}26]$ zolz pattern g) $[0\bar{1}12]$ holz pattern, h) $[0\bar{1}12]$ zolz pattern

Table 9a

Experimentally measured and theoretically calculated d-spacings and the reduced unit cell volume for the Y_2O_2S particle found in the as-homogenized Ni-23Cr-650 ppm Y alloy, dissolved in the iodine-methanol solution

zone axis	measured (theoretical) d-spacing, Å	measured (theoretical) reduced unit cell volume, Å^3
$[\bar{1}\bar{1}23]$	a) 1.63 (1.64) b) 2.93 (2.93) c) 3.28 (3.27)	82 (81.5)
$[\bar{2}\bar{2}43]$	a) 2.32 (2.26) b) 1.59 (1.64) c) 3.14 (3.27)	69 (81.55)
$[\bar{1}\bar{1}26]$	a) 1.76 (1.82) b) 1.51 (1.59) c) 3.14 (3.27)	82 (81.55)
$[0\bar{1}12]$	a) 1.91 (1.89) b) 1.64 (1.58) c) 2.97 (2.93)	83 (81.55)

Table 9b

Experimentally measured and theoretically calculated angles between the zone axes for the Y_2O_2S particle, found in the as-homogenized Ni-23Cr-650 ppm Y alloy, dissolved in the iodine-methanol solution. Figures in brackets are the theoretical values

zone axis	$[\bar{1}\bar{1}23]$	$[\bar{2}\bar{2}43]$	$[\bar{1}\bar{1}26]$	$[0\bar{1}12]$
$[\bar{1}\bar{1}23]$	0.0 (0.0)	21.37 (19.08)	12.58 (13.84)	15.11 (14.41)
$[\bar{2}\bar{2}43]$	21.37 (19.08)	0.0 (0.0)	33.93 (32.92)	31.15 (28.5)
$[\bar{1}\bar{1}26]$	12.58 (13.84)	33.93 (32.92)	0.0 (0.0)	13.63 (14.74)
$[0\bar{1}12]$	15.11 (14.41)	31.15 (28.5)	13.63 (14.74)	0.0 (0.0)

ii. Y_2O_3 Phase

The yttria phase, Y_2O_3, with a cubic crystal structure space group 206, $Ia\bar{3}$, lattice parameter a = 10.61Å was identified in the Ni-31Cr-900 ppm Y alloy (Figure 46), by matching the experimentally recorded diffraction patterns with the computer simulated diffraction patterns for the compound Y_2O_3.

The bright field image and the EDX spectrum obtained from a Y_2O_3 particle found in the Ni-31Cr-900 ppm Y alloy are shown in the Figures 46a and 46b. The Y_2O_3 particle was found to be in association with the Y and S rich particles. Figure 46c shows the EDX spectrum obtained from the Y-S rich particles found in association with the Y_2O_3 particle. The semi-quantitative analysis of the EDX spectrum obtained from the Y-S rich particles yielded 86.18 weight% Y and 13.82 weight% S.

The electron diffraction patterns taken from the Y_2O_3 particle, along with their attendant indexing, are shown in the Figures 47a to 47h. The experimentally measured and theoretically calculated d-spacings, the reduced unit cell volume and the angle between the zone axes are given in Table 10a and 10b. The experimentally determined values matched very well with the theoretical calculations.

The Wyckoff positions of the atoms in the Y_2O_3 crystal (8 Y on b sites at (1/4, 1/4, 1/4), 24 Y on d sites at (0.673, 0, 0.25) and 48 O on e sites at (0.3907, 0.152, 0.3804))[117], and the lattice parameters of the crystal required for simulating the crystal, the diffraction patterns, and for calculating the d-spacings, the reduced unit cell volume and the angles between the axes, using Desktop Microscopist™, were obtained from the data published in the literature [117].

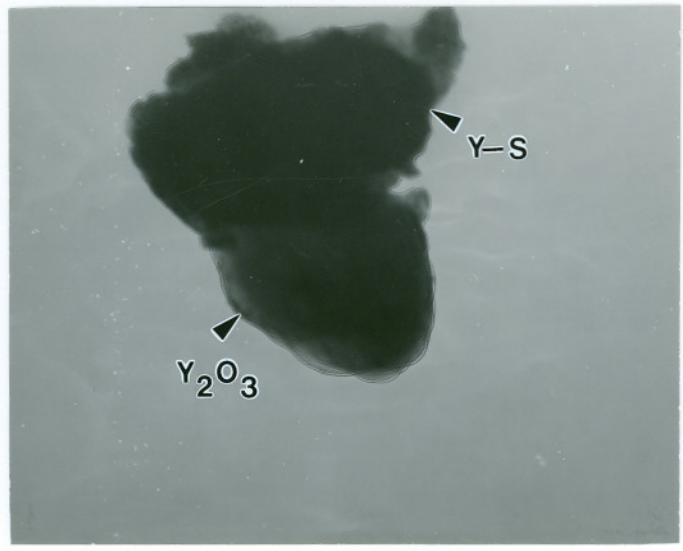

a) 200 nm

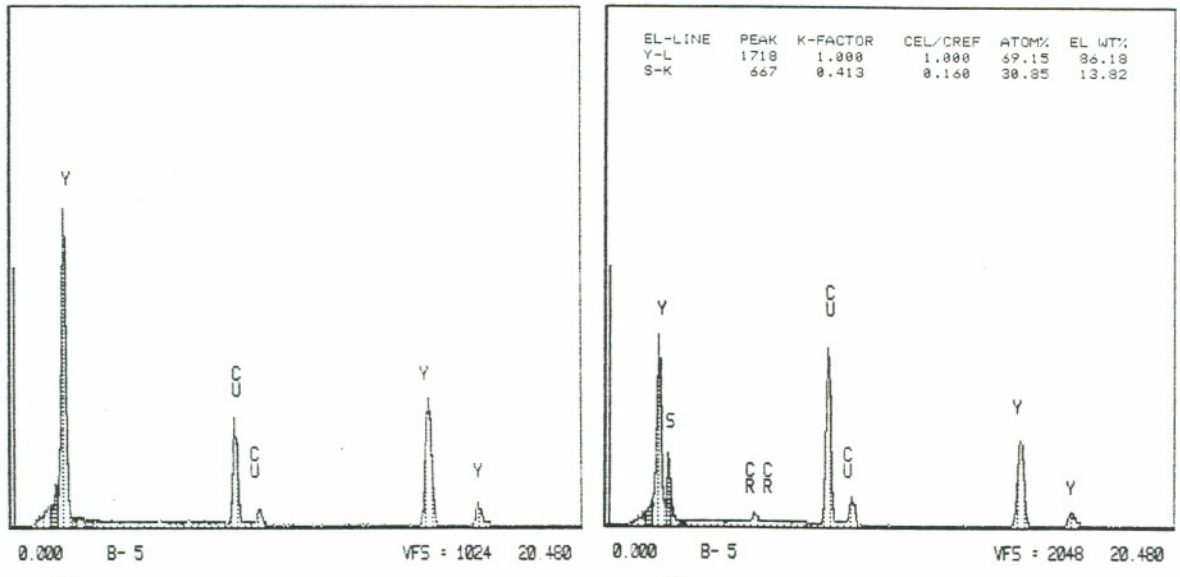

b) c)

Figure 46

a) Bright field image and b) EDX spectrum obtained from a Y_2O_3 particle, and c) EDX spectrum obtained from the Y-S rich paticles found in association with the Y_2O_3 particle found in the as-homogenized Ni-31Cr-900 ppm Y alloy dissolved in the iodine-methanol solution. The Cu peaks are from the Cu grid

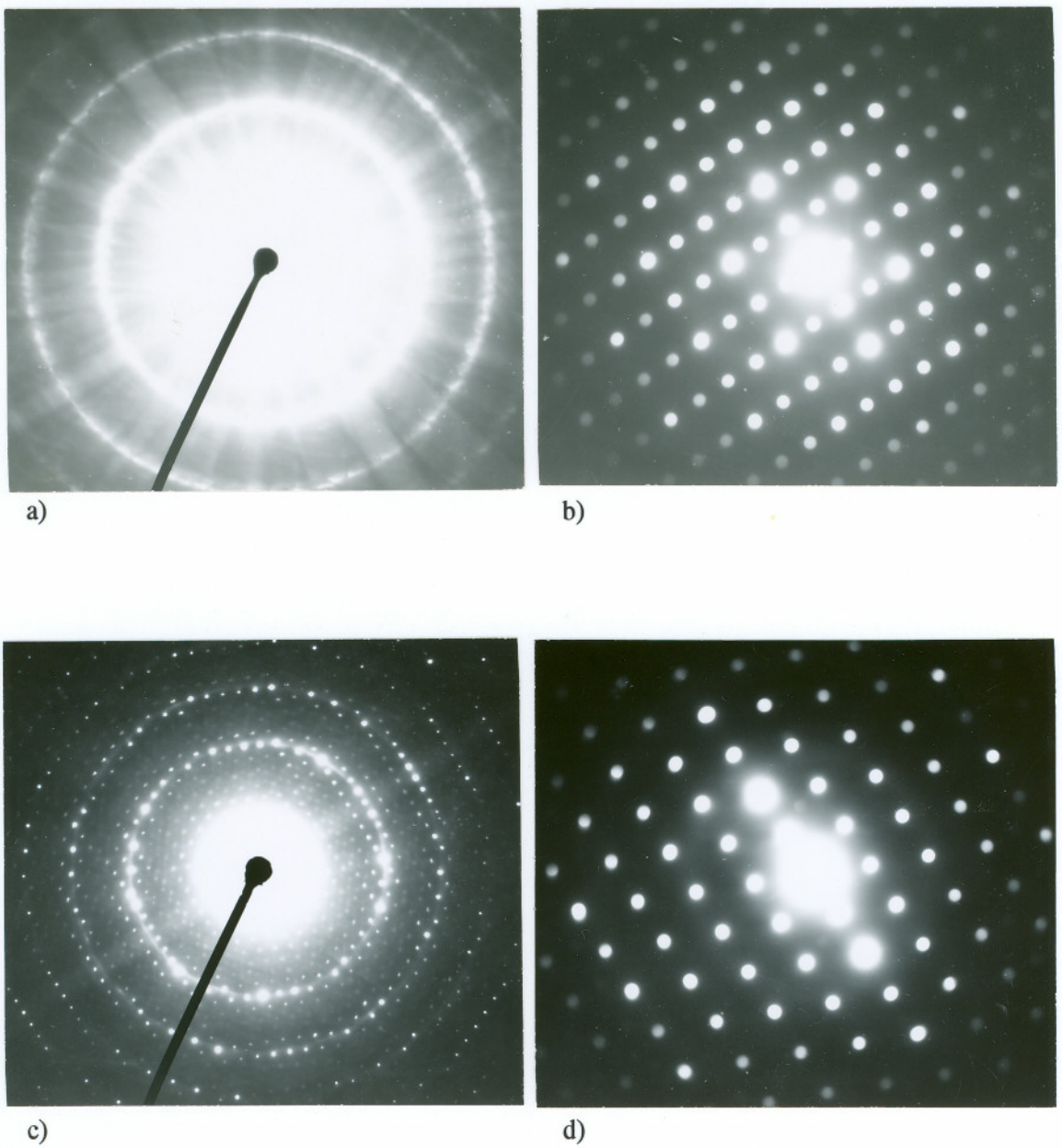

Figure 47

Electron diffraction patterns obtained from a Y_2O_3 particle found in the as-homogenized Ni-31Cr-900 ppm Y alloy dissolved in the iodine-methanol solution. a) [$10\bar{1}$] holz pattern, b) [$10\bar{1}$] zolz pattern, c) [$10\bar{2}$] holz pattern, d) [$10\bar{2}$] zolz pattern

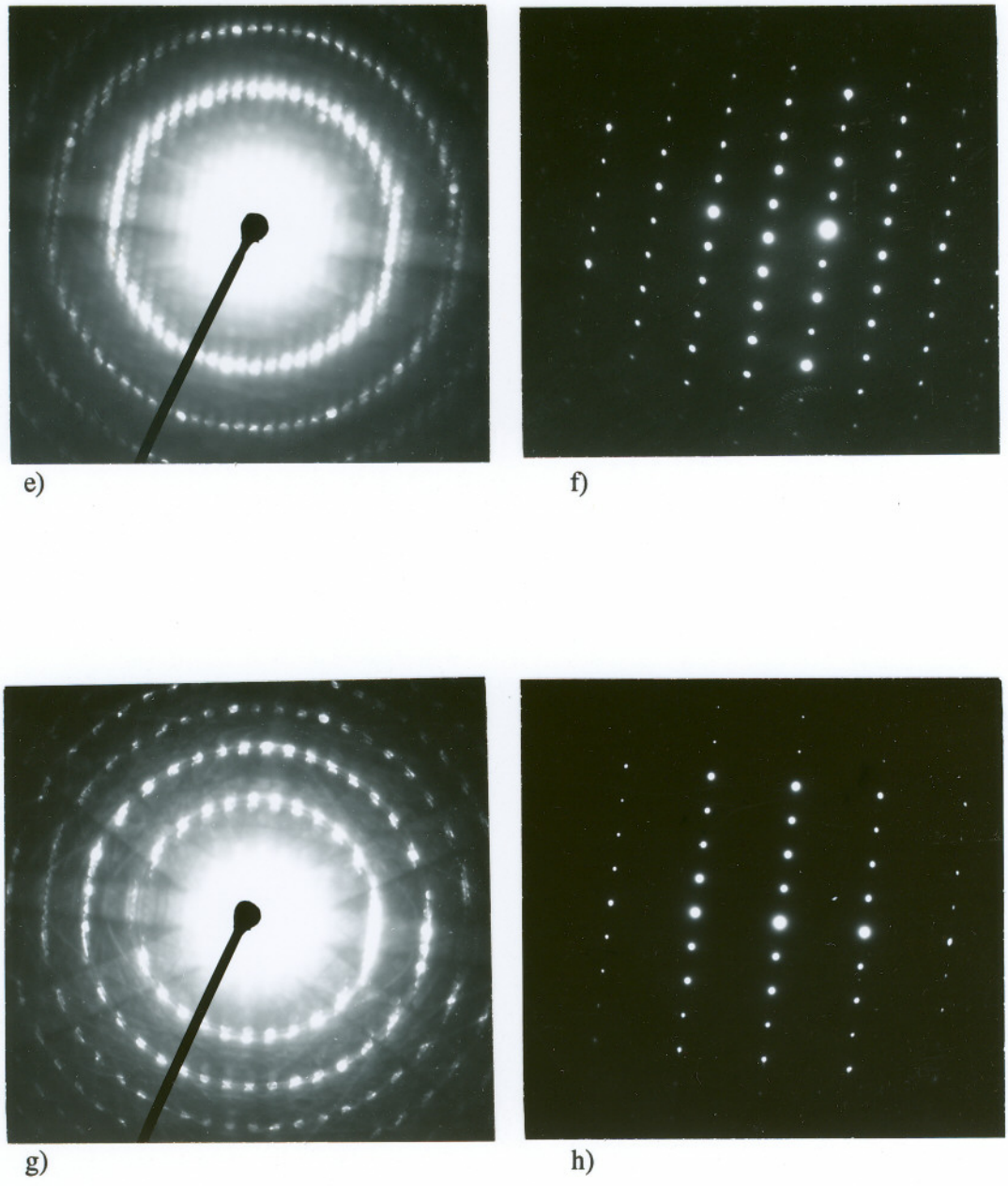

Figure 47 (cont.)

Electron diffraction patterns obtained from a Y_2O_3 particle found in the as-homogenized Ni-31Cr-900 ppm Y alloy dissolved in the iodine-methanol solution. e) $[11\bar{3}]$ holz pattern, f) $[11\bar{3}]$ zolz pattern, g) $[11\bar{2}]$ holz pattern, h) $[11\bar{2}]$ zolz pattern

Table 10a

Experimentally measured and theoretically calculated d-spacings and the reduced unit cell volume for a Y_2O_3 particle found in the as-homogenized Ni-31Cr-900 ppm Y alloy dissolved in the iodine-methanol solution

zone axis	$[10\bar{1}]$	$[10\bar{2}]$	$[11\bar{3}]$	$[11\bar{2}]$
measured (theoretical) d-spacing, Å	a) 5.26 (5.31) b) 2.48 (2.50) c) 4.31 (4.33)	a) 2.41 (2.37) b) 4.20 (4.33) c) 5.31 (5.33)	a) 2.26 (2.26) b) 4.29 (4.33) c) 3.79 (3.75)	a) 3.08 (3.06) b) 2.83 (2.83) c) 3.79 (3.79)
measured (theoretical) reduced unit cell volume, $Å^3$	524 (597.19)	507 (597.19)	553 (597.19)	591 (597.19)

Table 10b

Experimentally measured and theoretically calculated angles between the zone axes for a Y_2O_3 particle found in the as-homogenized Ni-31Cr-900 ppm Y alloy dissolved in the iodine-methanol solution. Figures in brackets are theoretical values

zone axis	$[10\bar{1}]$	$[10\bar{2}]$	$[11\bar{3}]$	$[11\bar{2}]$
$[10\bar{1}]$	0.0 (0.0)	21.6 (18.43)	35.03 (31.48)	31.39 (30.00)
$[10\bar{2}]$	21.6 (18.43)	0.0 (0.0)	18.25 (19.29)	21.11 (24.09)
$[11\bar{3}]$	35.03 (31.48)	18.25 (19.29)	0.0 (0.0)	9.68 (10.02)
$[11\bar{2}]$	31.39 (30.00)	21.11 (24.09)	9.68 (10.02)	0.0 (0.0)

4. OXIDIZED YTTRIUM CONTAINING ALLOYS

a. Alloy Dissolution

i. Y_2O_2S Phase

The phase yttrium oxysulfide, Y_2O_2S, with a trigonal crystal structure space group 164, $P\bar{3}m1$, lattice parameters of a = 3.79Å, and c = 6.59 Å, as reported in the literature[113,118], was found in the oxide scale grown on all the alloys exposed at 900°C and 1000°C in air for a period of 2-5 minutes (Figure 48a). The oxide scales were stripped from the alloys by dissolving the alloys in the iodine-methanol solution. The oxide scale stripped from the alloys exposed for longer time at temperature, was too thick for electron diffraction analysis in the TEM.

The bright field image and the EDX spectrum obtained from a Y_2O_2S particle are shown in the Figures 48a and 48b. The electron diffraction patterns obtained from this particle along with their attendant indexing, are shown in the Figures 49a to 49e. The experimentally determined and theoretically calculated d-spacings, the reduced unit cell volume and the angles between the zone axes are given in Table 11a and 11b. The experimentally measured d-spacings, reduced unit cell volume, and the angles between the zones, match well with the theoretically calculated values for Y_2O_2S.

The Wyckoff positions of the atoms in the Y_2O_2S crystal and the lattice parameters of the crystal, required for simulating the crystal, the diffraction patterns, and for calculating the d-spacings, the reduced unit cell volume and the angle between the axes, using Desktop Microscopist™, were obtained from the data published in the literature [113,118].

The analysis of the EDX spectrum shown in Figure 48b, yielded 86.06 weight% Y and 13.94 weight% S in Y_2O_2S.

a) 1 μm

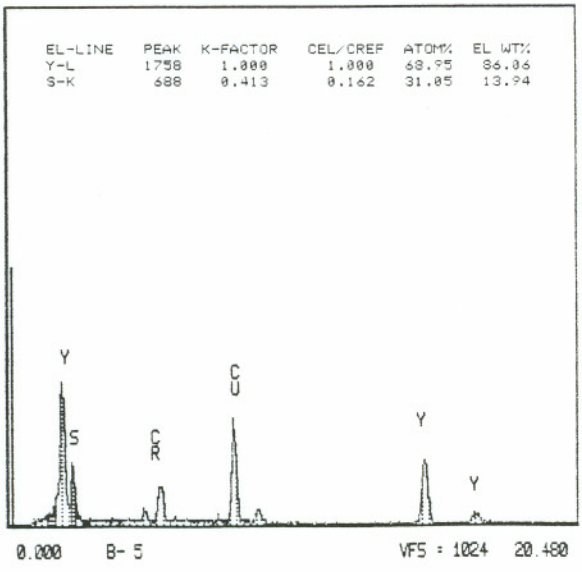

b)

Figure 48

a) Bright field image and b) EDX spectrum obtained from a Y_2O_2S particle found in the oxide scale grown on the Ni-22Cr-650 ppm Y alloy at 1000°C in air for 2 minutes. The Cu peaks are from the Cu grid

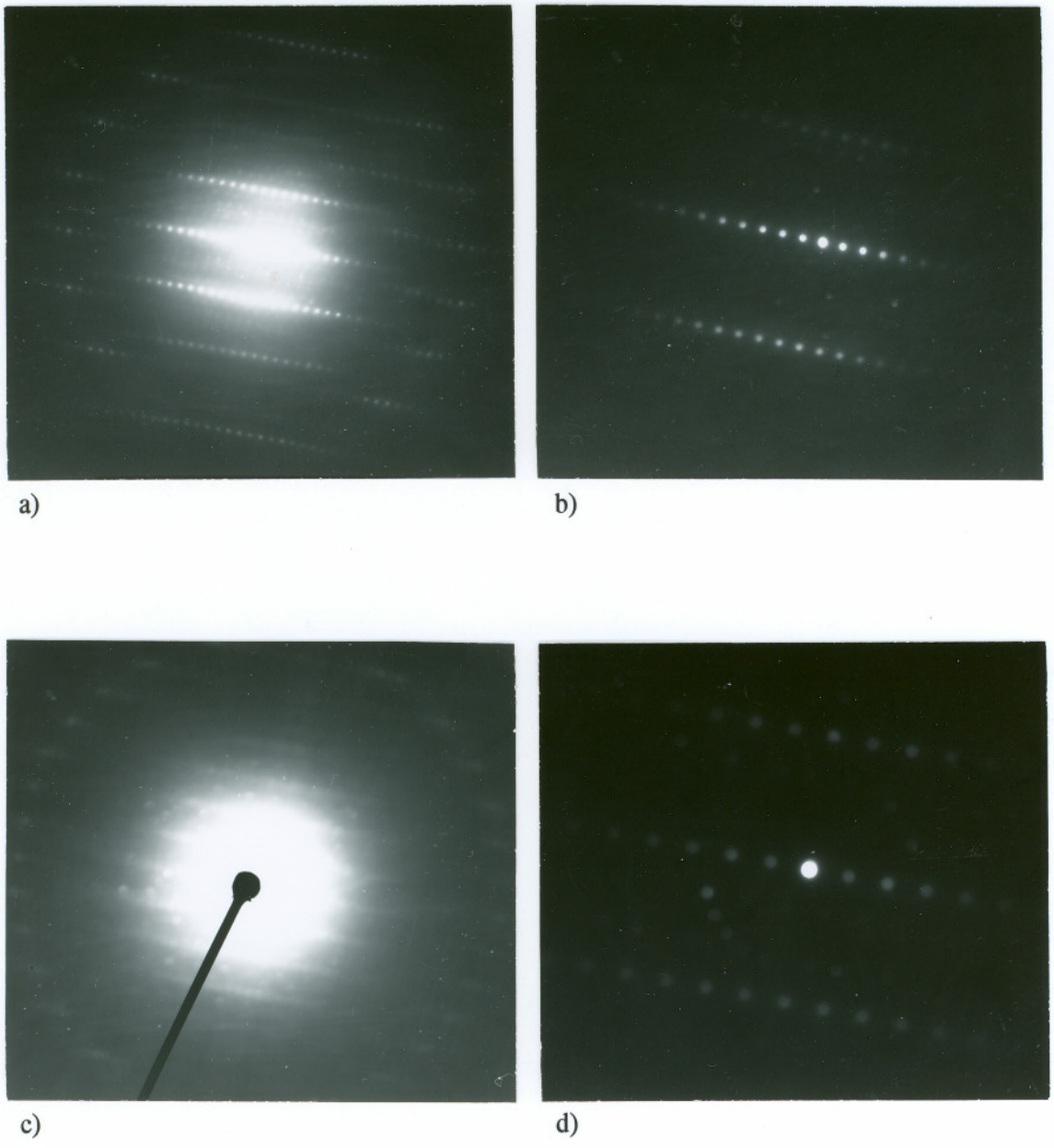

Figure 49

Electron diffraction patterns obtained from a Y_2O_2S particle found in the oxide scale grown on the Ni-22Cr-650 ppm Y alloy at 1000°C in air for 2 minutes. a) [4$\bar{5}$10] holz pattern, b) [4$\bar{5}$10] zolz pattern, c) [1$\bar{1}$00] holz pattern, d) [1$\bar{1}$00] zolz pattern

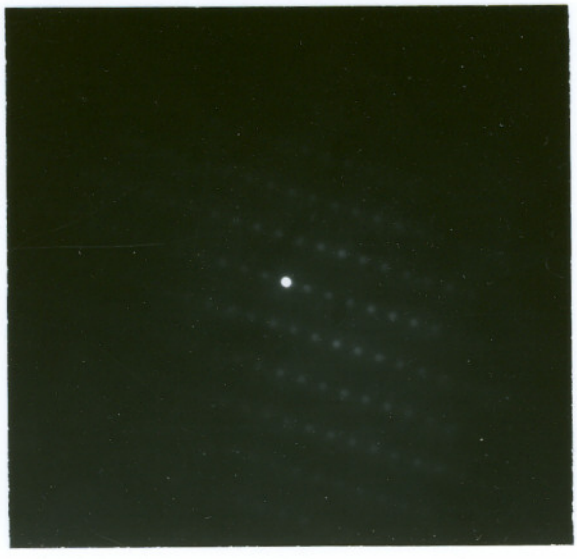

e)

Figure 49 (cont.)

Electron diffraction patterns obtained from a Y_2O_2S particle found in the oxide scale grown on the Ni-22Cr-650 ppm Y alloy at 1000°C in air for 2 minutes. e) $[2\bar{1}\bar{1}0]$ zolz pattern

Table 11a

Experimentally measured and theoretically calculated d-spacings and the reduced unit cell volume for a Y_2O_2S particle found in the oxide scale grown on the Ni-22Cr-650 ppm Y alloy at 1000°C in air for 2 minutes

zone axis	$[4\bar{3}10]$	$[1\bar{1}00]$	$[2\bar{1}\bar{1}0]$
measured (theoretical) d-spacing, Å	a) 1.21 (1.22) b) 1.19 (1.22) c) 6.45 (6.59)	a) 1.85 (1.89) b) 1.79 (1.82) c) 6.5 (6.59)	a) 3.21 (3.27) b) 2.88 (2.93) c) 6.45 (6.59)
measured (theoretical) reduced unit cell volume, $Å^3$	72 (81.55)	77 (81.55)	(81.55)

Table 11b

Experimentally measured and theoretically calculated angles between the zone axes for a Y_2O_2S particle found in the oxide scale grown on the Ni-31Cr-900 ppm Y alloy at 1000°C in air for 2 minutes. Figures in brackets are theoretical values

zone axis	$[4\bar{3}10]$	$[1\bar{1}00]$	$[2\bar{1}\bar{1}0]$
$[4\bar{3}10]$	0.0 (0.0)	10.47 (10.89)	44.31 (40.89)
$[1\bar{1}00]$	10.47 (10.89)	0.0 (0.0)	33.92 (30.00)
$[2\bar{1}\bar{1}0]$	44.31 (40.89)	33.92 (30.00)	0.0 (0.0)

ii. $Y_2O_2SO_4$ Phase

The yttrium oxysulfate phase, $Y_2O_2SO_4$, was found in the chromium oxide scale grown on the Ni-31Cr-900 ppm Y alloy oxidized at 1000°C in air for 2 minutes (Figure 51a). The crystal structure for this compound has been reported[119] to be I-centered orthorhombic, space group 71, Immm with the lattice parameters a = 4.15 Å, b = 4.01 Å, c = 12.68 Å. However, both the space group of the crystal and the Wyckoff positions of the atoms in the crystal, have not been unambiguously determined.

The bright field image and the EDX spectrum obtained from a $Y_2O_2SO_4$ particle are shown in the Figures 50a and 50b. The Y_2O_2S particles had a distinct lozenge shaped morphology, as shown in the Figure 50a. The electron diffraction patterns taken from this particle along with their attendant indexing, are shown in the Figures 51a and 51b. HOLZ patterns could not be obtained from the $Y_2O_2SO_4$ particles.

Shown in the Table 12a and 12b are the experimentally determined and theoretically calculated d-spacings and the angles between the zone axes are given in, and they compare well with each other. Since the Wyckoff positions of the atoms in the $Y_2O_2SO_4$ crystal are not known, the diffraction patterns were simulated by using the computer program Desktop Microscopist™, using only one atom of yttrium per cell.

Due to the very small size of the lozenge shaped crystal of $Y_2O_2SO_4$, not more than 2 ZOLZ patterns could be obtained from them. The crystals were also found to be beam unstable, which also restricted the number of zones from which electron diffraction patterns could be obtained.

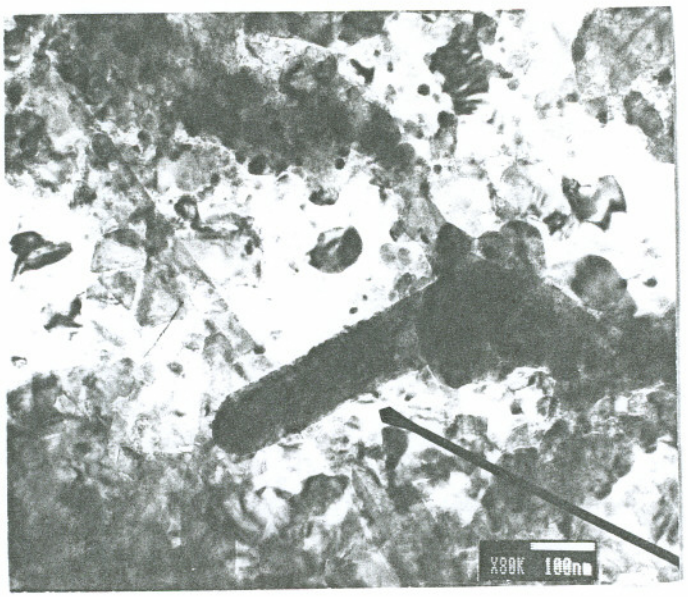

a)

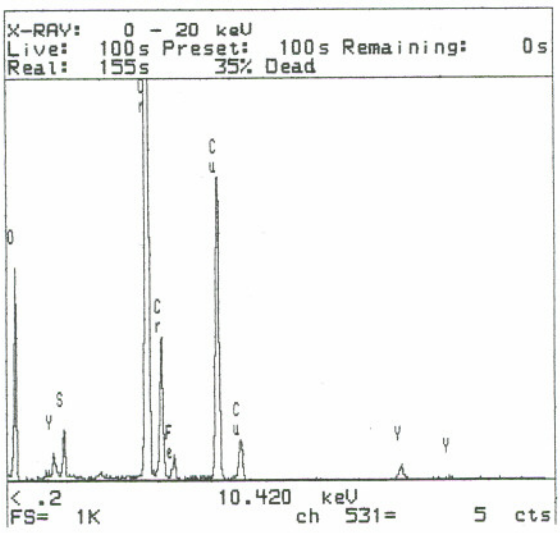

b)

Figure 50

a) Bright field image and b) EDX spectrum obtained from a $Y_2O_2SO_4$ particle found in the oxide scale grown on the Ni-31Cr-900 ppm Y alloy in air at 1000°C for 2 minutes. The Cu peaks are from the Cu grid

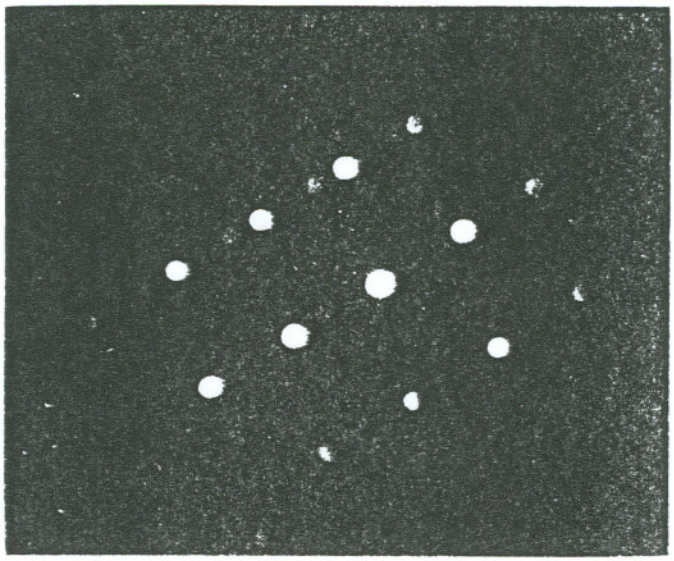

a)

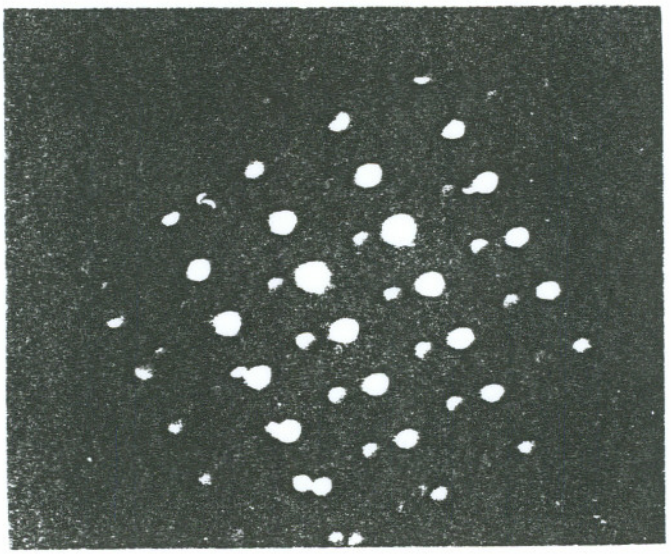

b)

Figure 51

Electron diffraction patterns obtained from a $Y_2O_2SO_4$ particle found in the oxide scale grown on the Ni-31Cr-900 ppm Y alloy at 1000°C in air for 2 minutes. a) $[3\bar{1}\bar{1}]$ zolz pattern, b) $[30\bar{1}]$ zolz pattern

Table 12a

Experimentally measured and theoretically calculated d-spacings for a $Y_2O_2SO_4$ particle found in the oxide scale grown on the Ni-31Cr-900 ppm Y alloy at 1000°C in air for 2 minutes

zone axis	$[3\bar{1}\bar{1}]$	$[30\bar{1}]$
measured (theoretical) d-spacing, Å	a) 1.93 (1.91) b) 1.43 (1.29) c) 1.56 (1.49)	a) 3.04 (2.96) b) 1.61 (1.66) c) 2.01 (2.00)

Table 12b

Experimentally measured and theoretically calculated angle between the zone axes for a $Y_2O_2SO_4$ particle found in the oxide scale grown on the Ni-31Cr-900 ppm Y alloy at 1000°C in air for 2 minutes. Figures in brackets are the theoretical values

zone axis	$[3\bar{1}\bar{1}]$	$[30\bar{1}]$
$[3\bar{1}\bar{1}]$	0.0 (0.0)	12.07 (12.72)
$[30\bar{1}]$	12.07 (12.72)	0.0 (0.0)

iii. $YCrO_3$ Phase

The yttrium orthochromite phase, $YCrO_3$, was identified in the oxide scale (Figure 52) grown on the Ni-31Cr-900 ppm Y alloy at 1000°C in air for 2 minutes, by matching the computer simulated diffraction patterns for $YCrO_3$ with those recorded experimentally (Figure 53). The crystal structure was found to be orthorhombic space group 62, Pnma, with the lattice parameters of a = 5.52 Å, b = 5.25 Å, c = 7.54 Å, as reported in the literature[120].

The bright field image and the EDX spectrum obtained from the $YCrO_3$ particle are shown in the Figures 52a and 52b. The electron diffraction patterns taken from this particle along with their attendant indexing, are shown in the Figures 53a to 53h. The experimentally determined and the theoretically calculated d-spacings, the reduced unit cell volume and the angles between the zone axes, are given in the Table 13a and 13b. The experimentally determined d-spacings, the reduced unit cell volume, and the angles between the zone axes match well with the theoretically calculated values for $YCrO_3$. The analysis of the EDX spectrum shown in the Figure 52b yielded 66.63 weight% Y and 33.37 weight% Cr. This is also shown in the Figure 52b.

The Wyckoff positions of the atoms in the $YCrO_3$ crystal (4 Gd on c sites at (0.982, 0.06, 0.25), 4 Fe on b sites at (1/2, 0, 0), 4 O on c sites at (0.05, 0.47, 0.25) and 8 O on d sites at (0.71, 0.27, 0.05))[121] and the lattice parameters required for simulating the crystal, the diffraction patterns, and for calculating the d-spacings, the reduced unit cell volume and the angles between the axes, using Desktop Microscopist™, were obtained from the work of Geller and Wood [121] and Geller[120].

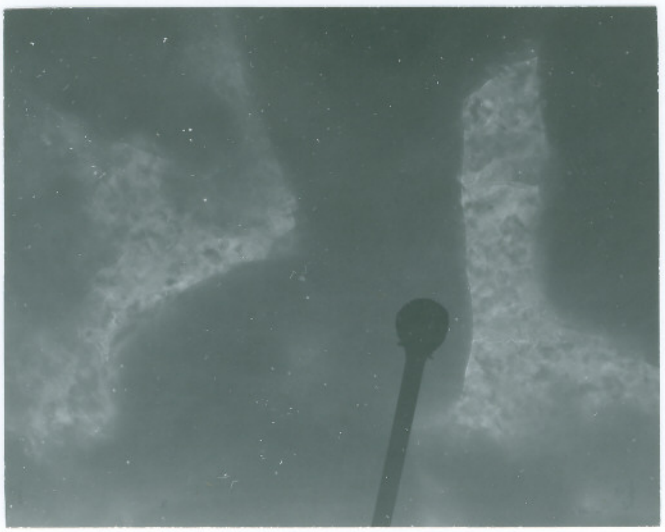

a) 400 nm

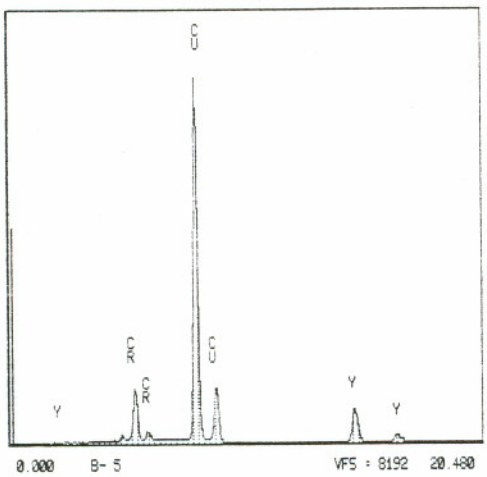

EL-LINE	PEAK	K-FACTOR	CEL/CREF	ATOM%	EL WT%
Y-K	6338	1.000	1.000	53.85	66.63
CR-K	8210	0.386	0.501	46.15	33.37

b)

Figure 52

a) Bright field image and b) EDX spectrum obtained from a $YCrO_3$ particle found in the oxide scale grown on the Ni-31Cr-900 ppm Y alloy at 1000°C in air for 2 minutes. The Cu peaks are from the Cu grid

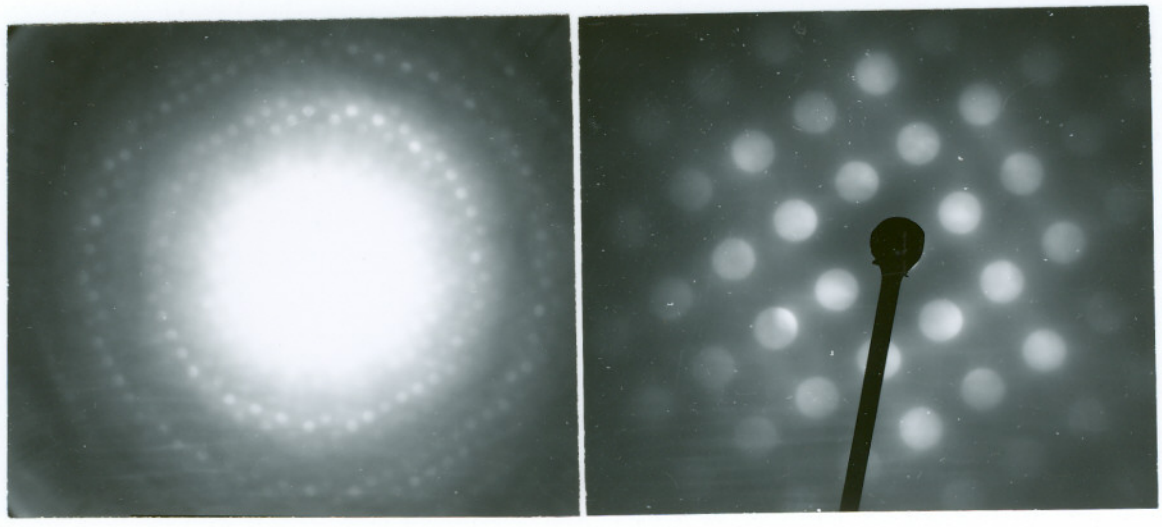

a) b)

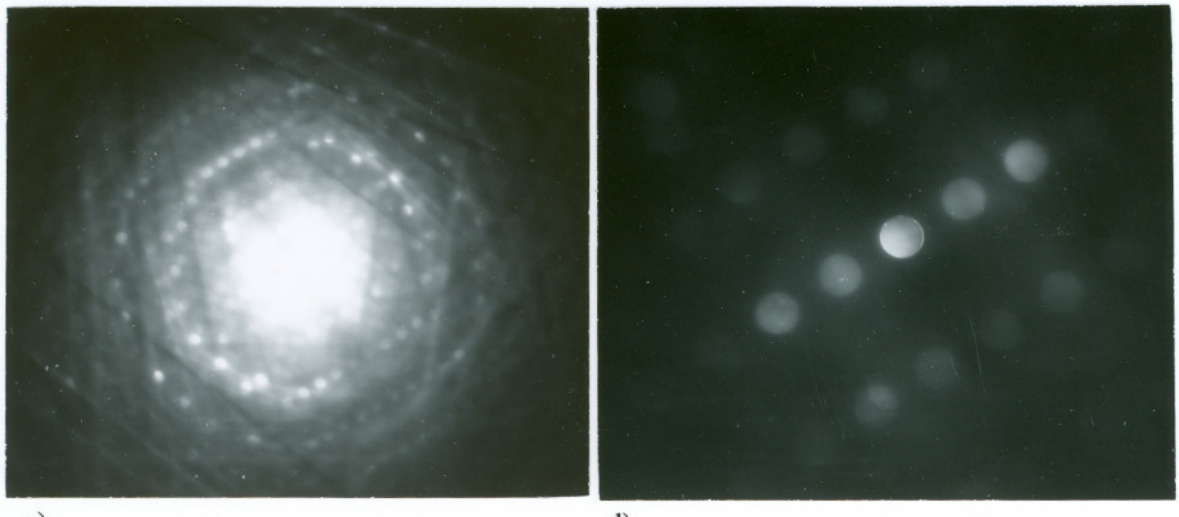

c) d)

Figure 53

Electron diffraction patterns obtained from a $YCrO_3$ particle found in the oxide scale grown on the Ni-31Cr-900 ppm Y alloy at 1000°C in air for 2 minutes. a) [$11\bar{2}$] holz pattern, b) [$11\bar{2}$] zolz pattern, c) [$22\bar{3}$] holz pattern, d) [$22\bar{3}$] zolz pattern

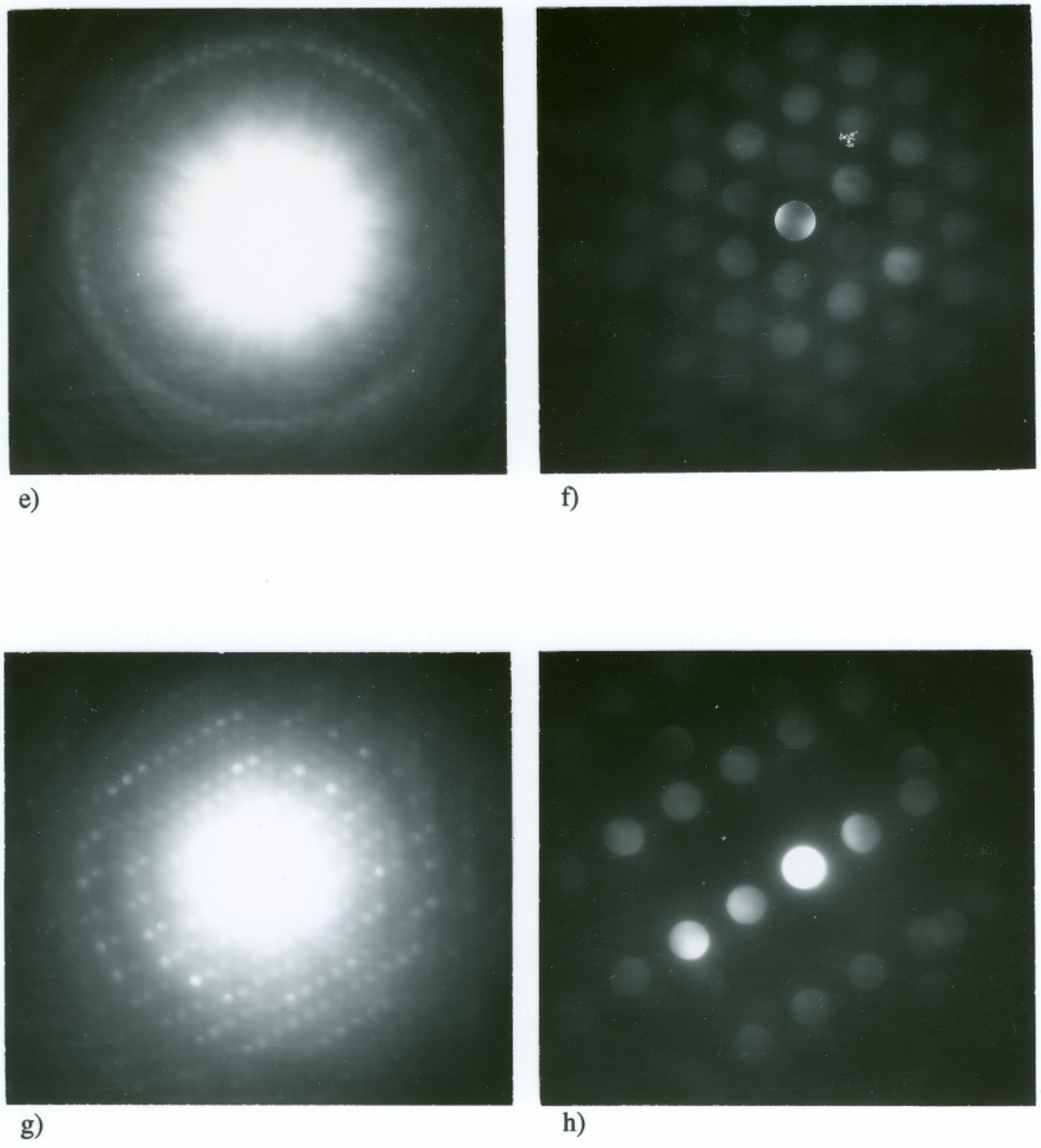

Figure 53 (cont.)

Electron diffraction patterns obtained from a $YCrO_3$ particle found in the oxide scale grown on the Ni-31Cr-900 ppm Y alloy at 1000°C in air for 2 minutes. e) [$11\bar{1}$] holz pattern, b) [$11\bar{1}$] zolz pattern, g) [$33\bar{2}$] holz pattern, h) [$33\bar{2}$] zolz pattern

Table 13a

Experimentally measured and theoretically calculated d-spacings and the reduced unit cell volume for a $YCrO_3$ particle found in the oxide scale grown on the Ni-31Cr-900 ppm Y alloy at 1000°C in air for 2 minutes

zone axis	$[11\bar{2}]$	$[22\bar{3}]$	$[11\bar{1}]$	$[33\bar{2}]$
measured (theoretical) d-spacing, Å	a) 1.9 (1.9) b) 2.59 (2.58) c) 3.39 (3.37)	a) 2.05 (2.05) b) 2.005 (2.006) c) 1.9 (1.9)	a) 4.37 (4.31) b) 1.85 (1.9) c) 4.38 (4.45)	a) 1.85 (1.86) b) 2.09 (2.09) c) 1.9 (1.9)
measured (theoretical) reduced unit cell volume, $Å^3$	214 (218)	215 (218)	207 (218)	

Table 13b

Experimentally measured and theoretically calculated angles between the zone axes for a $YCrO_3$ particle found in the oxide scale grown on the Ni-31Cr-900 ppm Y alloy at 1000°C in air for 2 minutes. Figures in brackets are the theoretical values

zone axis	$[11\bar{2}]$	$[22\bar{3}]$	$[11\bar{1}]$	$[33\bar{2}]$
$[11\bar{2}]$	0.0 (0.0)	7.06 (7.16)	18.02 (18.49)	29.19 (29.78)
$[22\bar{3}]$	7.06(7.16)	0.0 (0.0)	11.21 (11.33)	22.36 (22.62)
$[11\bar{1}]$	18.02 (18.49)	11.21 (11.33)	0.0 (0.0)	11.18 (11.29)
$[33\bar{2}]$	29.19 (29.78)	22.36 (22.62)	11.18 (11.29)	0.0 (0.0)

5. SIMULATION EXPERIMENTS

a. CeO_2 Phase

The phase ceria, CeO_2, was identified in the mixture of Cr_2O_3 + 1wt% Ce_2O_2S, Cr + 1wt% Ce_2O_2S and Cr_2O_3 + 10wt% Cr + 1wt% Ce_2O_2S, heated in air and vacuum at 900°C and 1000°C (Figures 54 and 55). The CeO_2 phase had a cubic crystal structure space group 225, $Fm\bar{3}m$, as reported in the literature[115]. The lattice parameter was found to be a = b = c = 5.42 Å, as reported in the literature[115]

The bright field image and the EDX spectrum obtained from a CeO_2 particle are shown in the Figures 54a and 54b. The electron diffraction patterns obtained from this particle along with their attendant indexing, are shown in the Figures 55a to 55h. The experimentally determined and theoretically calculated d-spacings, the reduced unit cell volume, and the angles between the zone axes are given in Table 14a and 14b. These values matched well with each other.

The Wyckoff positions of the atoms in the CeO_2 crystal (4 Ce on a sites at (0, 0, 0) and 8 O on c sites at (1/4, 1/4, 1/4))[115] and the lattice parameters of the crystal required for simulating the crystal, the diffraction patterns, and for calculating the d-spacings, the reduced unit cell volume and the angles between the zone axes, using Desktop Microscopist™, were obtained from the data published in the literature [115].

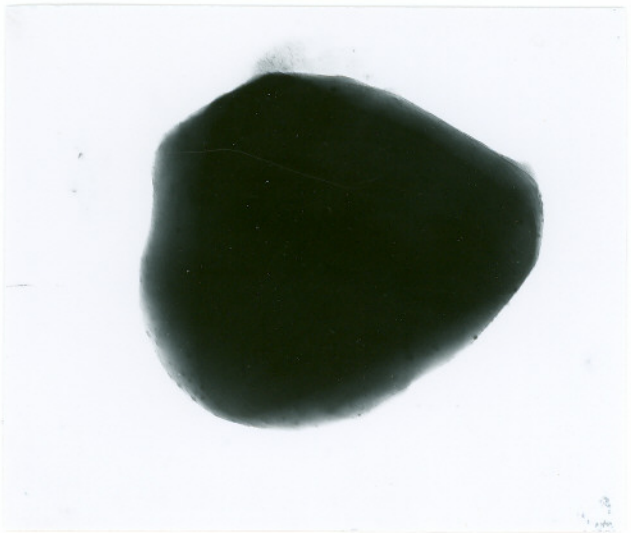

a) 200nm

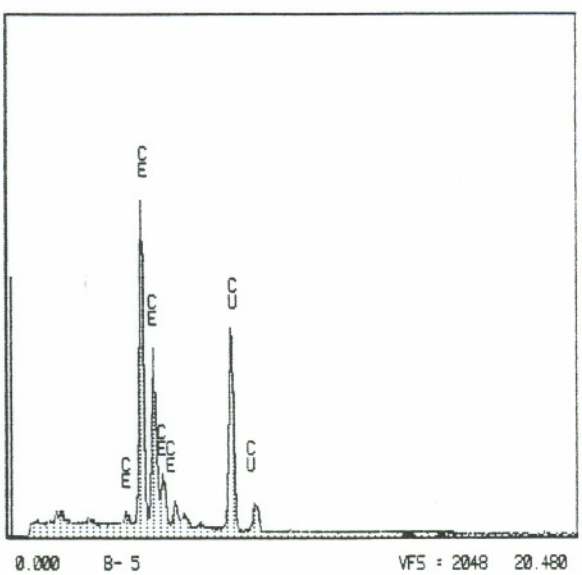

b)

Figure 54

a) Bright field image and b) EDX spectrum obtained from a CeO_2 particle. The Cu peaks are from the Cu grid

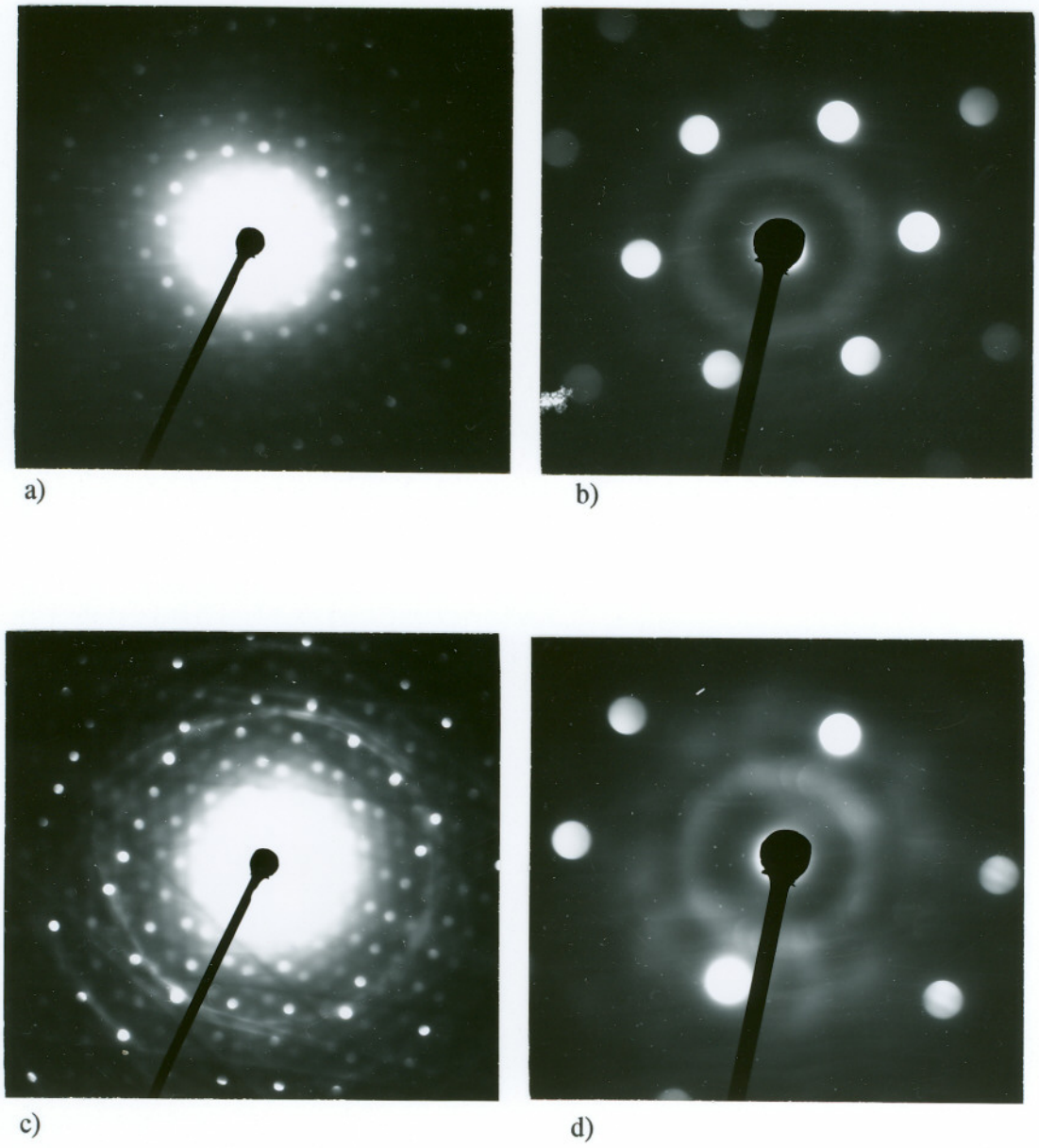

Figure 55

Electron diffraction patterns obtained from a CeO_2 particle. a) $[\bar{1}1\bar{1}]$ holz pattern, b) $[\bar{1}1\bar{1}]$ zolz pattern, c) $[\bar{3}4\bar{3}]$ holz pattern, d) $[\bar{3}4\bar{3}]$ zolz pattern

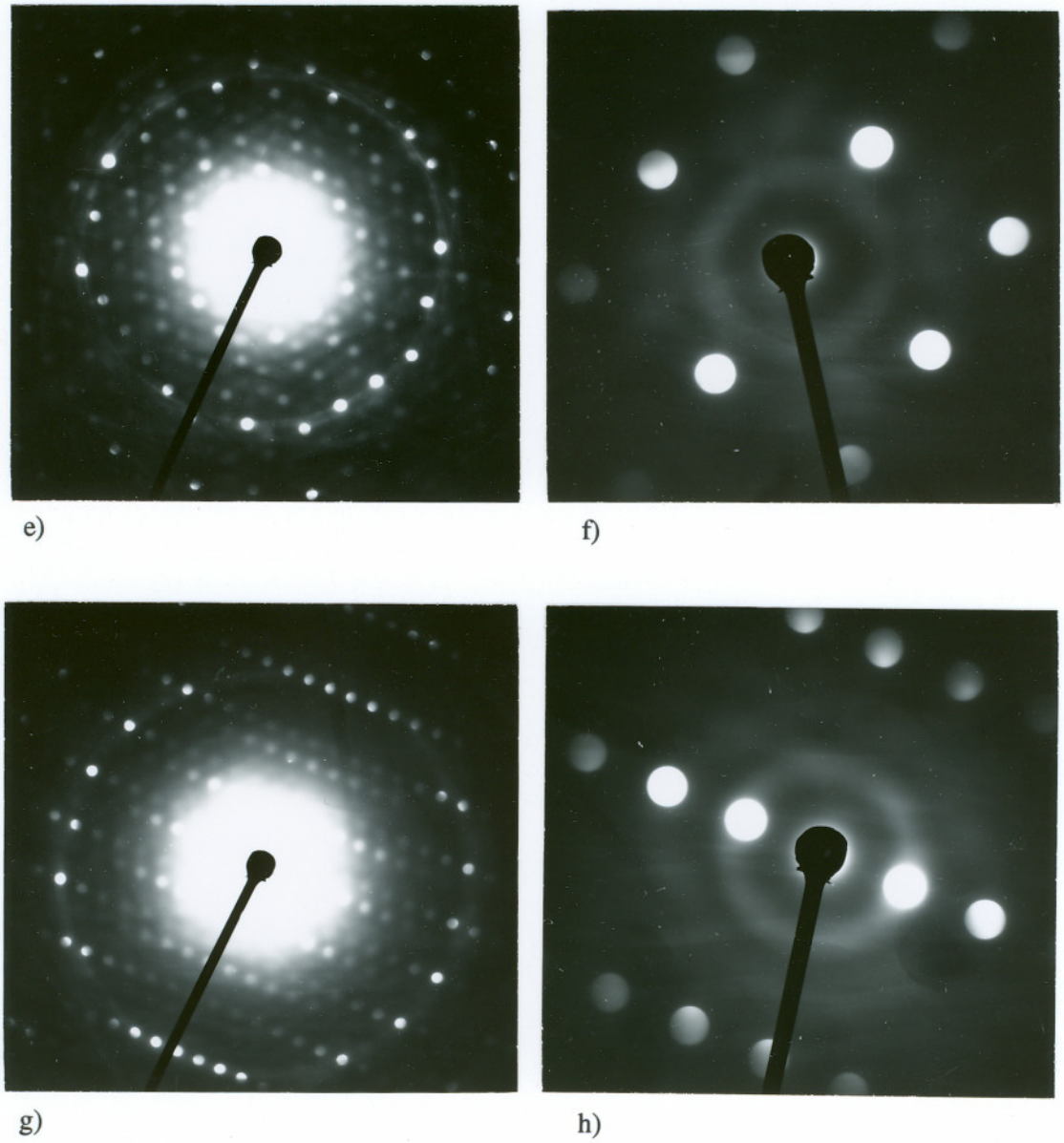

Figure 55 (cont.)

Electron diffraction patterns obtained from a CeO_2 particle. e) $[\bar{2}3\bar{3}]$ holz pattern, f) $[\bar{2}3\bar{3}]$ zolz pattern, g) $[\bar{1}3\bar{2}]$ holz pattern, h) $[\bar{1}3\bar{2}]$ zolz pattern

Table 14a

Experimentally measured and theoretically calculate d-spacings and the reduced unit cell volume for a CeO_2 particle

zone axis	$[\bar{1}1\bar{1}]$	$[\bar{3}4\bar{3}]$	$[\bar{2}3\bar{3}]$	$[\bar{1}3\bar{2}]$	$[\bar{1}2\bar{1}]$
measured (theoretical) d-spacing, Å	a) 1.09 (1.10) b) 1.89 (1.91) c) 1.09 (1.10)	a) 1.89 (1.91) b) 0.90 (0.91) c) 1.23 (1.24)	a) 1.90 (1.91) b) 1.22 (1.24) c) 1.62 (1.63)	a) 1.18 (1.21) b) 1.03 (1.04) c) 3.11 (3.12)	a) 1.90 (1.91) b) 1.61 (1.63) c) 3.11 (3.12)
measured (theoretical) reduced unit cell volume, $Å^3$	35 (39.56)	40 (39.56)	38 (39.56)	38 (39.56)	37 (39.56)

Table 14b

Experimentally measured and theoretically calculated angles between the zone axes for a CeO_2 particle. Figures in brackets are theoretical values

zone axis	$[\bar{1}1\bar{1}]$	$[\bar{3}4\bar{3}]$	$[\bar{2}3\bar{3}]$	$[\bar{1}3\bar{2}]$	$[\bar{1}2\bar{1}]$
$[\bar{1}1\bar{1}]$	0.0 (0.0)	7.60 (8.05)	10.08 (10.02)	18.80 (22.21)	18.66 (19.47)
$[\bar{3}4\bar{3}]$	7.60 (8.05)	0.0 (0.0)	8.42 (9.17)	13.67 (15.73)	11.23 (11.42)
$[\bar{2}3\bar{3}]$	10.08 (10.02)	8.42 (9.17)	0.0 (0.0)	9.55 (14.38)	16.86 (16.78)
$[\bar{1}3\bar{2}]$	18.80 (22.21)	13.67 (15.73)	9.55 (14.38)	0.0 (0.0)	15.02 (10.89)
$[\bar{1}2\bar{1}]$	18.66 (19.47)	11.23 (11.42)	16.86 (16.78)	15.02 (10.89)	0.0 (0.0)

b. $CeCrO_3$ Phase

The phase cerium orthochromite, $CeCrO_3$, was identified in the Cr + 1% Ce_2O_2S, Cr_2O_3 + 1% Ce_2O_2S and Cr_2O_3 + 10wt% Cr + 1wt% Ce_2O_2S mixture heated in vacuum at 900°C and 1000°C (Figures 56 and 57). The phase identification was carried out by matching the electron diffraction patterns with the computer simulated patterns for the compound $CeCrO_3$.

The bright field image and the EDX spectrum obtained from a $CeCrO_3$ particle are shown in the Figures 56a and 56b. The electron diffraction patterns taken from this particle along with their attendant indexing, are shown in the Figures 57a to 57h. Shown in the Table 15a and 15b are the experimentally determined and theoretically calculated d-spacings, the reduced unit cell volume, and the angles between the zone axes. The analysis of the EDX spectrum shown in Figure 56b yielded 66.96 weight% Ce and 33.04 weight% Cr.

The crystal structure of $CeCrO_3$ was found to be orthorhombic space group 62, Pnma, with the lattice parameters of a = 5.47 Å, b = 5.47 Å and c = 7.74 Å, as reported in the literature[121,122]. Geller and Wood[121] had determined the Wyckoff positions of the atoms in the $GdFeO_3$ crystal, which was also shown to be isostructural with $LaCrO_3$ and $CeCrO_3$.

The Wyckoff positions of the atoms in the $CeCrO_3$ crystal and the lattice parameters of the crystal required for simulating the crystal, were obtained from the work of Geller and Wood[121] and, Quezel-Ambrunaz and Mareschal [122]. The Wyckoff positions of the atoms in the $CeCrO_3$ crystal were assumed to be the same as those for $GdFeO_3$ crystal. The diffraction patterns, d-spacings, the reduced unit cell volume and the angles between the zone axes, were then theoretically calculated.

a) 200 nm

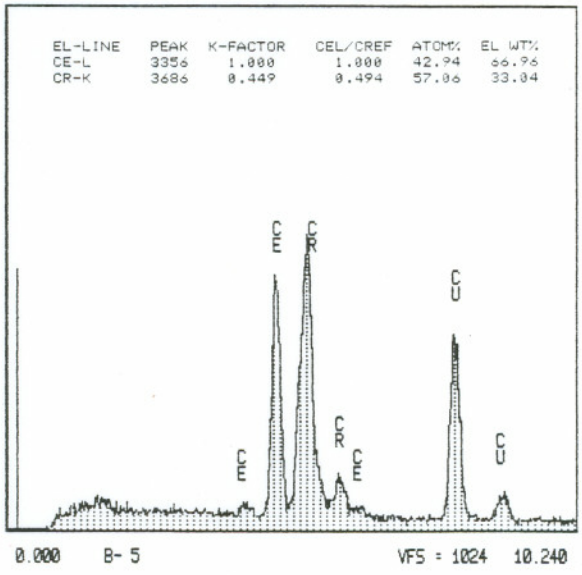

b)

Figure 56

a) Bright field image and b) EDX spectrum obtained from $CeCrO_3$ particles. The Cu peaks are from the Cu grid

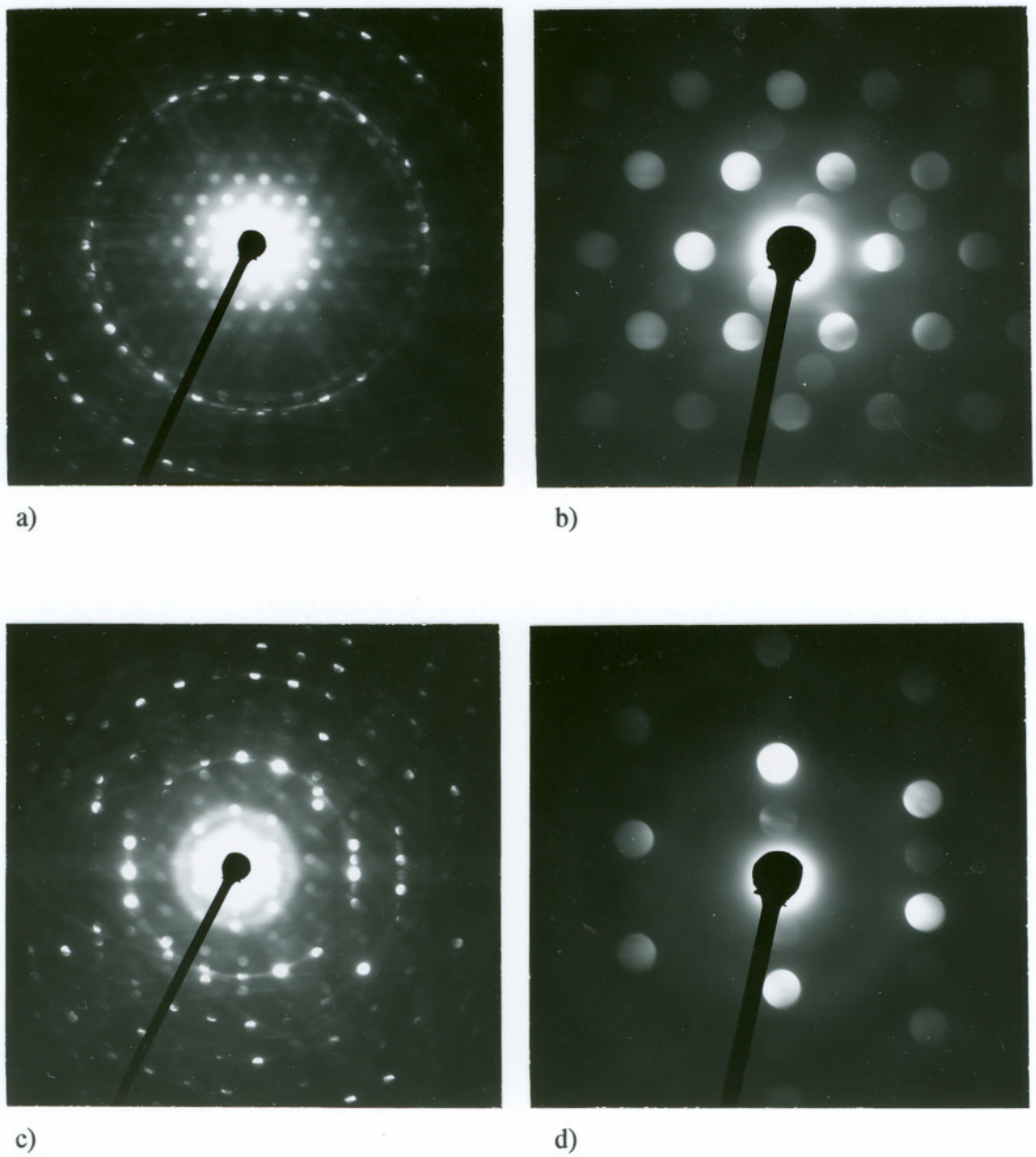

Figure 57

Electron diffraction patterns obtained from a $CeCrO_3$ particle. a) $[0\bar{2}1]$ holz pattern, b) $[0\bar{2}1]$ zolz pattern, c) $[\bar{1}\bar{3}3]$ holz pattern, d) $[\bar{1}\bar{3}3]$ zolz pattern

e)

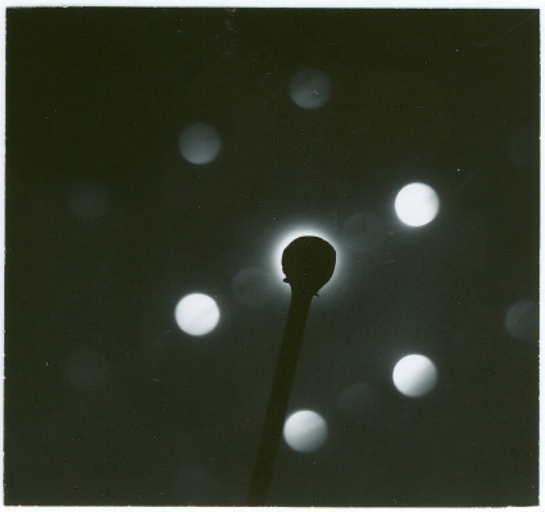

f)

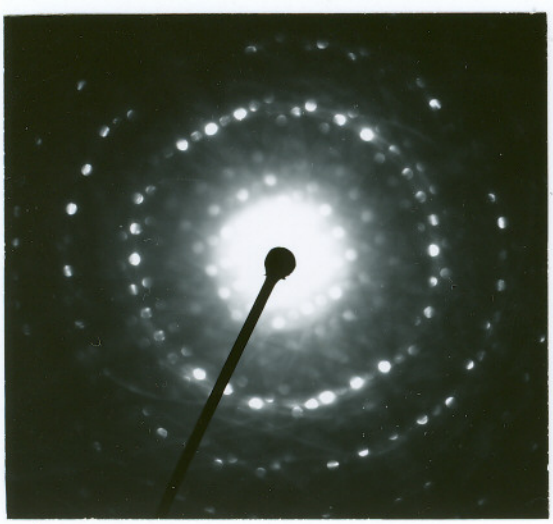

g)

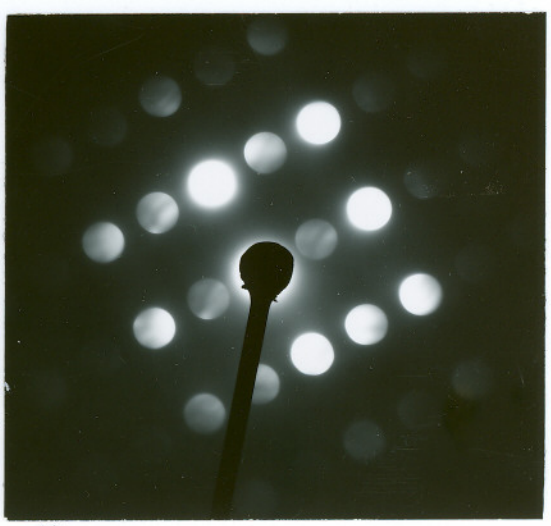

h)

Figure 57 (cont.)

Electron diffraction patterns obtained from a $CeCrO_3$ particle. e) $[1\bar{3}3]$ holz pattern, f) $[1\bar{3}3]$ zolz pattern, g) $[\bar{1}\bar{3}1]$ holz pattern, h) $[\bar{1}\bar{3}1]$ zolz pattern

Table 15a

Experimentally measured and theoretically calculated d-spacings and the reduced unit cell volume for a $CeCrO_3$ particle

zone axis	$[0\bar{2}1]$	$[\bar{1}\bar{3}3]$	$[1\bar{3}3]$	$[\bar{1}\bar{3}1]$
measured (theoretical) d-spacing, Å	a) 2.67 (2.74) b) 2.03 (2.07) c) 5.45 (5.47)	a) 1.77 (1.78) b) 1.71 (1.73) c) 4.46 (4.47)	a) 1.78 (1.78) b) 1.58 (1.58) c) 4.46 (4.47)	a) 2.73 (2.73) b) 2.33 (2.33) c) 4.45 (4.47)
measured (theoretical) reduced unit cell volume, $Å^3$	226 (232)	227 (232)	230 (232)	236 (232)

Table 15b

Experimentally measured and theoretically calculated angles between the zone axes for a $CeCrO_3$ particle. Figures in brackets are the theoretical values

zone axis	$[0\bar{2}1]$	$[\bar{1}\bar{3}3]$	$[1\bar{3}3]$	$[\bar{1}\bar{3}1]$
$[0\bar{2}1]$	0.0 (0.0)	22.34 (22.21)	23.80 (22.21)	21.32 (19.47)
$[\bar{1}\bar{3}3]$	22.34 (22.21)	0.0 (0.0)	23.50 (21.79)	30.60 (29.20)
$[1\bar{3}3]$	23.80 (22.21)	23.50 (21.79)	0.0 (0.0)	10.87 (12.00)
$[\bar{1}\bar{3}1]$	21.32 (19.47)	30.60 (29.20)	10.87 (12.00)	0.0 (0.0)

c. $La_2O_2SO_4$ Phase

The phase lanthanum oxysulfate, $La_2O_2SO_4$, was found in the La_2O_2S powder heated in air at 900°C and 1000°C for a period of 10 - 30 minutes (Figure 58a). The crystal structure was found to be I-centered orthorhombic space group 71, Immm with the lattice parameters of a = 4.29 Å, b = 13.72 Å, c = 4.19 Å, as reported in the literature[119].

The bright field image and the EDX spectrum obtained from a cluster $La_2O_2SO_4$ particles identified in the La_2O_2S powder heated at 1000°C in air for a period of 30 minutes, are shown in the Figures 58a and 58b. Since the lanthanum oxysulfate particles were highly beam unstable, diffraction patterns from only one zone form various particles could be obtained. The electron diffraction patterns taken from various particles along with their attendant indexing, are shown in the Figures 59a to 59j.

Shown in the Table 16 are the experimentally determined and theoretically calculated d-spacings and the reduced unit cell volume. These figures match well with each other. The semiquantitative analysis of the EDX spectrum shown in the Figure 58b yielded 89.01 weight% La and 10.99 weight% S.

The lattice parameters of the $La_2O_2SO_4$ crystal required for simulating the crystal, were obtained from the work of Ballestracii and Mareschal[119]. Since both the space group of the crystal and the Wyckoff positions of the atoms in the crystal are not unambiguously determined, only one atom of La was considered for simulating the crystal in the program Desktop Microscopist™, using the reported space group 71, Immm. The diffraction patterns, d-spacings, the reduced unit cell volume and the angle between the axes, were then calculated using Desktop Microscopist™.

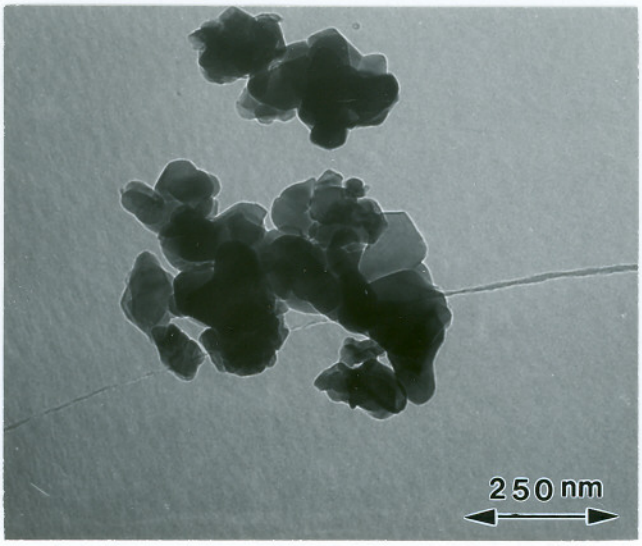

a)

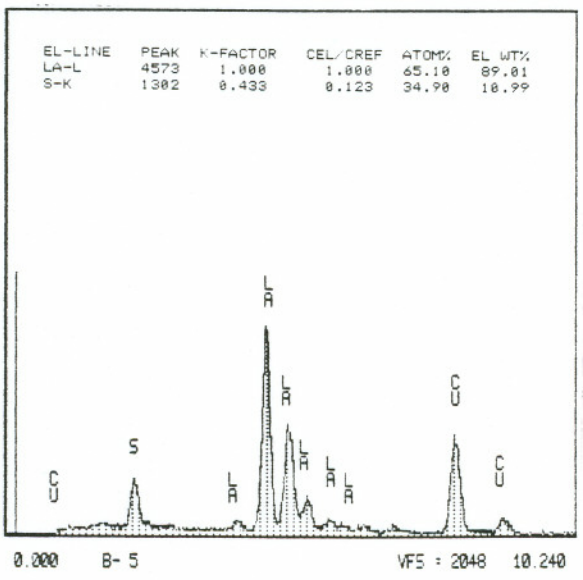

b)

Figure 58

a) Bright field image and b) EDX spectrum obtained from a cluster of $La_2O_2SO_4$ particles. The Cu peaks are from the Cu grid

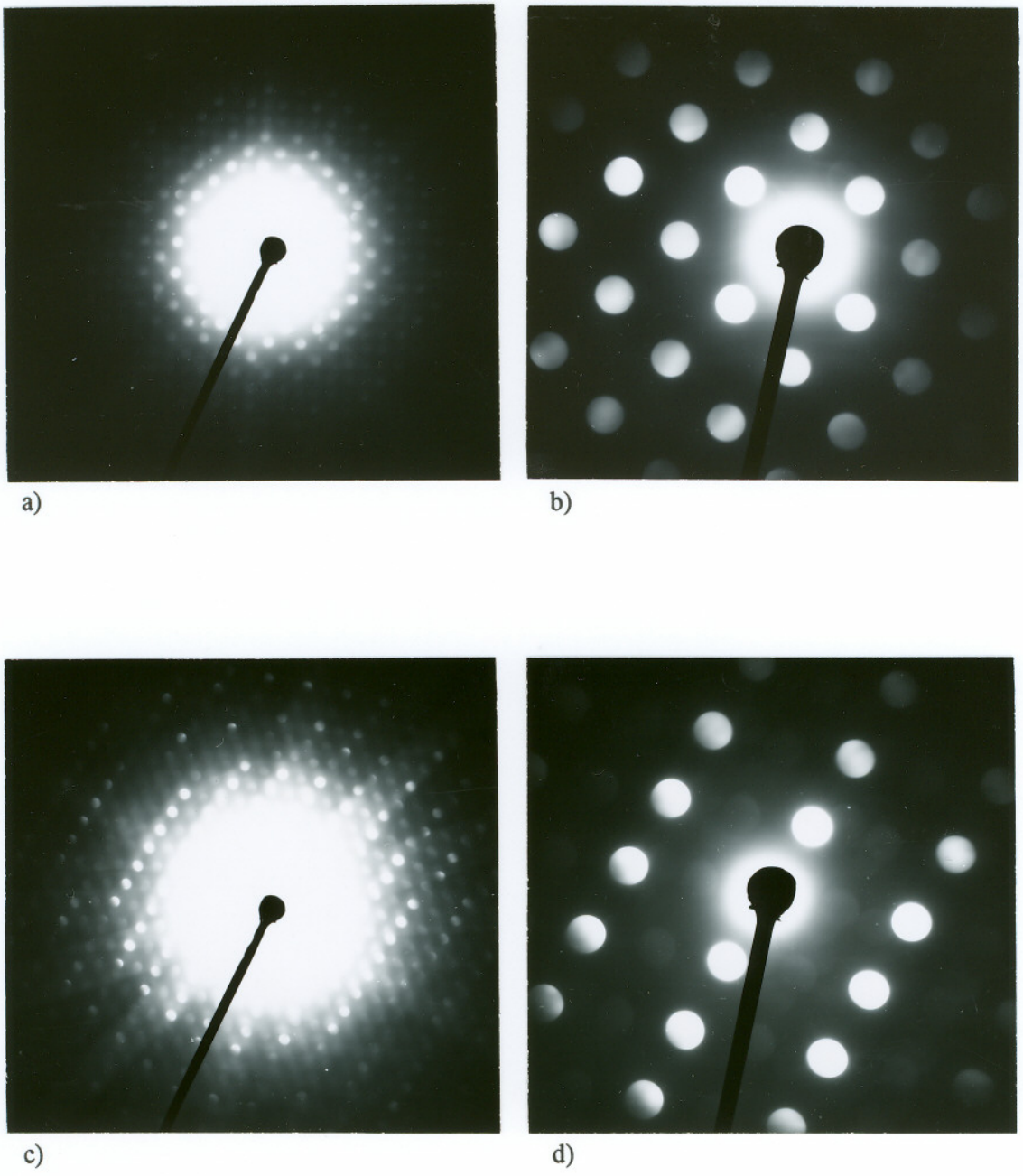

Figure 59

Electron diffraction patterns obtained from $La_2O_2SO_4$ particles. a) [001] holz pattern, b) [001] zolz pattern, c) [771] holz pattern, d) [771] zolz pattern

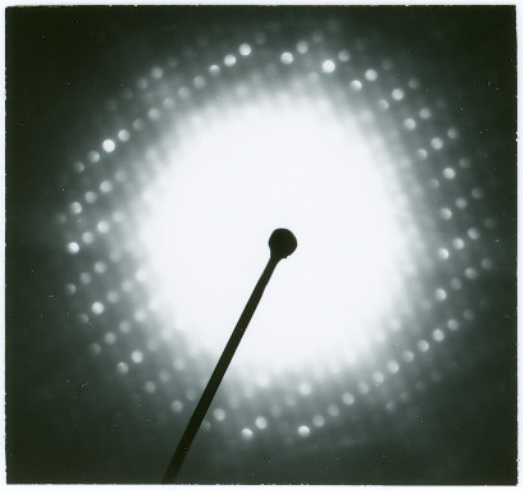

e)

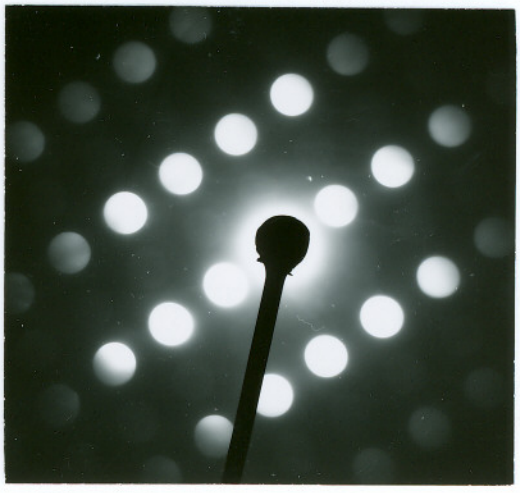

f)

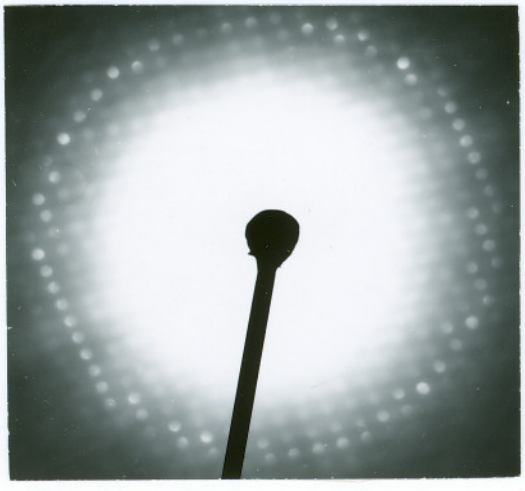

g)

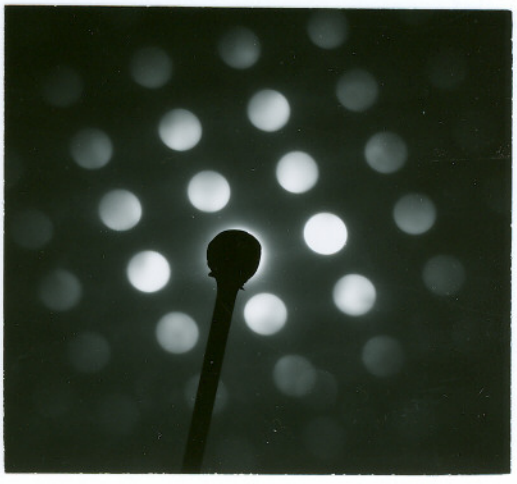

h)

Figure 59 (cont.)

Electron diffraction patterns obtained from $La_2O_2SO_4$ particles. e) [511] holz pattern, f) [511] zolz pattern, g) [131] holz pattern, h) [131] zolz pattern

Table 16

Experimentally measured and theoretically calculated d-spacings and the reduced unit cell volume for the phase $La_2O_2SO_4$

zone axis	[001]	[771]	[511]	[131]
measured (theoretical) d-spacing, Å	a) 2.89 (2.98) b) 2.08 (2.10) c) 2.89 (2.98)	a) 1.81 (1.78) b) 2.83 (2.83) c) 3.10 (3.09)	a) 2.28 (2.30) b) 1.81 (1.79) c) 4.05 (4.07)	a) 1.86 (1.89) b) 2.73 (2.75) c) 3.07 (3.09)
measured (theoretical) unit cell volume, Å	124 (123.3)	135 (123.3)	125 (123.3)	120 (123.3)

d. $LaCrO_3$ Phase

Lanthanum orthochromite, $LaCrO_3$, was identified in the mixtures of Cr_2O_3 + 1 wt% La_2O_2S, Cr + 1wt% La_2O_2S, and Cr_2O_3 + 10wt%Cr + 1wt% La_2O_2S heated in vacuum at 900°C and 1000°C for 1 hour. $LaCrO_3$ could not be found in the mixtures heated in air. The identification of the phase was carried out by matching the electron experimentally recorded diffraction patterns with those simulated by the program Desktop Microscopist™ for the compound $LaCrO_3$. The crystal structure of the $LaCrO_3$ phase was found to be orthorhombic space group 62, Pnma, with the lattice parameters of a = 5.47 Å, b = 5.51Å, c = 7.76 Å, as reported in the literature[121].

The diffraction patterns, d-spacings, the reduced unit cell volume and the angles between the zone axes, were then calculated using Desktop Microscopist™. The bright field image and the EDX spectrum of a $LaCrO_3$ particle are shown in the Figures 60a and 60b. The $LaCrO_3$ phase had a distinct lozenge shaped morphology, as is evident from Figure 60a. The electron diffraction patterns taken from this particle along with their attendant indexing, are shown in the Figures 61a to 61h. The experimentally determined and theoretically calculated d-spacings, the reduced unit cell volume and the angles between the zone axes are given in Table 17a and 17b. These figures match well with each other.

The Wyckoff positions of the atoms in the $LaCrO_3$ crystal and the lattice parameters of the crystal required for simulating the crystal, were obtained from the work of Geller and Wood[121]. Geller and Wood[121] had determined the Wyckoff positions for the atoms in gadolinium orthoferrite, $GdFeO_3$, which was shown to be isostructural with $LaCrO_3$ and $CeCrO_3$. The Wyckoff positions required for simulating the electron diffraction patterns for $LaCrO_3$ were assumed to be the same as those for $GdFeO_3$.

The semi-quantitative analysis of the EDX spectrum shown in the Figure 60b yielded 63.25 weight% La and 36.75 weight% Cr.

a) 400 nm

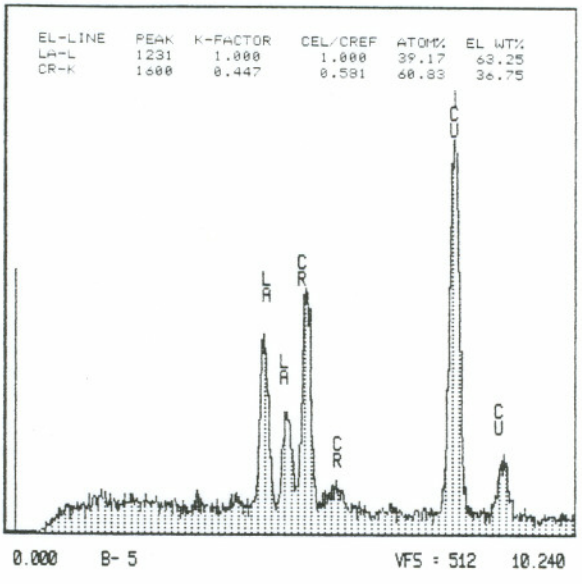

b)

Figure 60

a) Bright field image and b) EDX spectrum obtained from a $LaCrO_3$ particle. Seen in a) is a cluster of particles. The Cu peaks are from the Cu grid

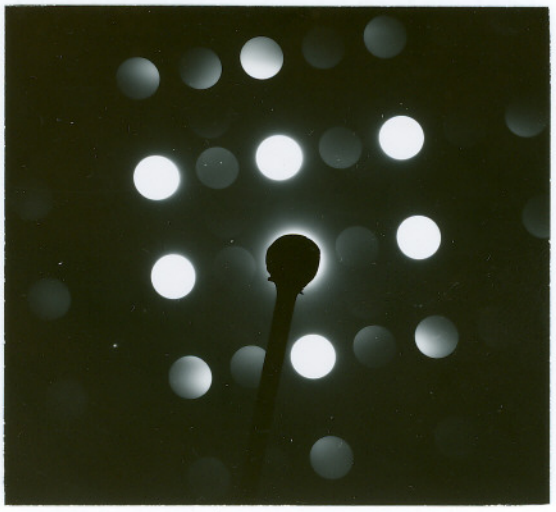

a)

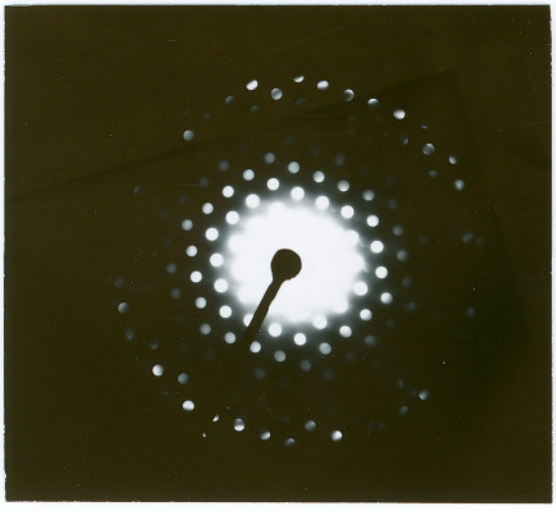

b)

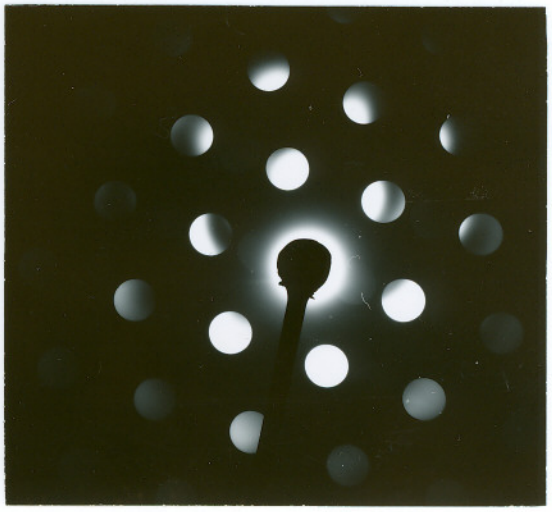

c)

Figure 61

Electron diffraction patterns obtained from a $LaCrO_3$ particle. a) $[10\bar{1}]$ zolz pattern, b) $[20\bar{1}]$ holz pattern, c) $[20\bar{1}]$ zolz pattern

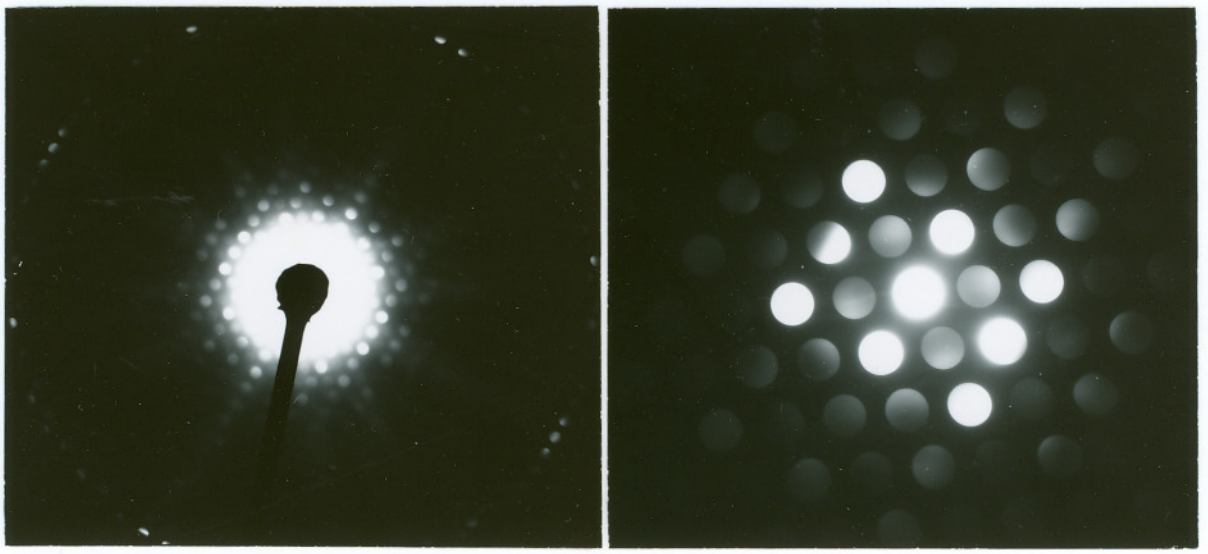

d) e)

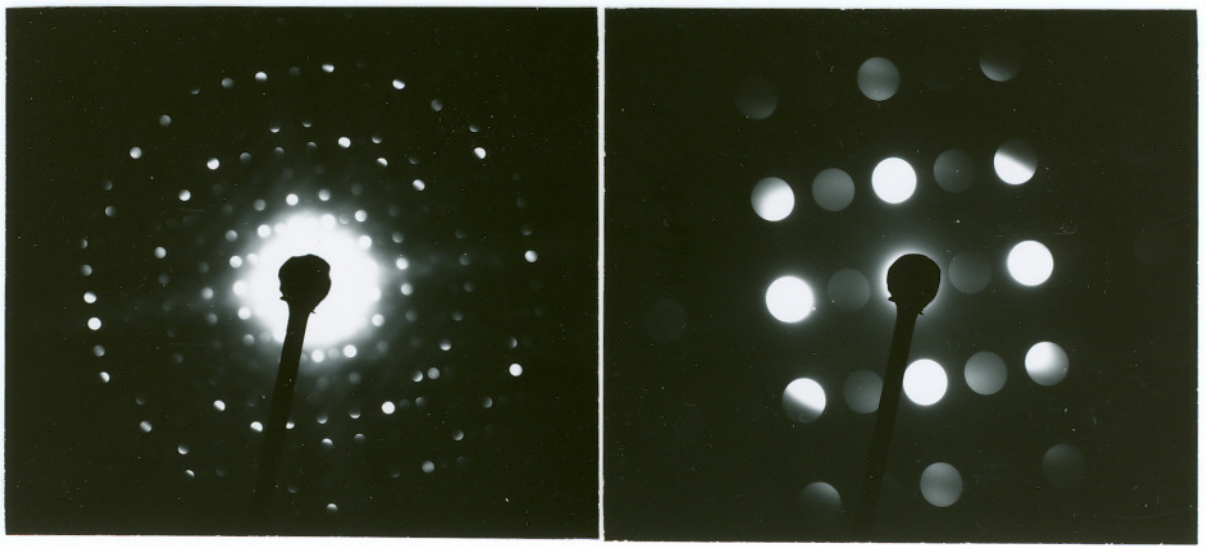

f) g)

Figure 61 (cont.)

Electron diffraction patterns obtained from a $LaCrO_3$ particle. d) $[11\bar{1}]$ holz pattern, e) $[11\bar{1}]$ zolz pattern, f) $[31\bar{1}]$ holz pattern, g) $[31\bar{1}]$ zolz pattern

Table 17a

Experimentally measured and theoretically calculated d-spacings and the reduced unit cell volume for a $LaCrO_3$ particle

zone axis	[10$\bar{1}$]	[20$\bar{1}$]	[11$\bar{1}$]	[31$\bar{1}$]
measured (theoretical) d-spacing, Å	a) 2.68 (2.74) b) 2.34 (2.29) c) 4.44 (4.49)	a) 2.71 (2.74) b) 2.06 (2.07) c) 2.74 (2.74)	a) 4.48 (4.49) b) 2.72 (2.74) c) 4.48 (4.49)	a) 2.69 (2.74) b) 2.30 (2.34) c) 4.44 (4.47)
measured (theoretical) reduced unit cell volume, $Å^3$	(234.27)	239 (234.27)	(234.27)	221 (234.27)

Table 17b

Experimentally measured and theoretically calculated angles between the zone axes for a $LaCrO_3$ particle. Figures in brackets are theoretical values

zone axis	[10$\bar{1}$]	[20$\bar{1}$]	[11$\bar{1}$]	[31$\bar{1}$]
[10$\bar{1}$]	0.0 (0.0)	22.06 (19.47)	29.60 (29.94)	33.54 (33.49)
[20$\bar{1}$]	22.06 (19.47)	0.0 (0.0)	39.80 (35.10)	19.09 (19.38)
[11$\bar{1}$]	29.60 (29.94)	39.80 (35.10)	0.0 (0.0)	32.06 (29.85)
[31$\bar{1}$]	33.54 (33.49)	19.09 (19.38)	32.06 (29.85)	0.0 (0.0)

e. La_2O_3 Phase

The lanthana phase, La_2O_3, with a trigonal crystal structure space group 164 $P\bar{3}m1$, with lattice parameters of a = 3.93 Å and c = 6.14 Å was identified when the La_2O_2S powder was heated in air for a period of 2 hours at 900°C and 1000°C (Figures 62 and 63)[117].

The bright field image and the EDX spectrum obtained from a La_2O_3 particle are shown in the Figures 62a and 62b. The electron diffraction patterns taken from this particle along with their attendant indexing, are shown in the Figures 63a to 63h. The experimentally determined and theoretically calculated d-spacings, the reduced unit cell volume, and the angles between the zone axes are given in Table 18a and 18b. These figures are in good agreement with each other.

The Wyckoff positions of the atoms in the La_2O_3 crystal, and the lattice parameters of the crystal required for simulating the crystal, were obtained from the Pearsons Handbook of Crystallographic Data for Intermetallic Phases, Volume 3[117]. The reported Wyckoff positions are - 2 La on d sites at (0.333, 0.667, 0.2467), 1 O on a site at (0, 0, 0) and 2 O on d sites at (0.333, 0.667 and 0.647)[117]. The diffraction patterns, d-spacings, the reduced unit cell volume and the angles between the zone axes, were then calculated using Desktop Microscopist™.

a)

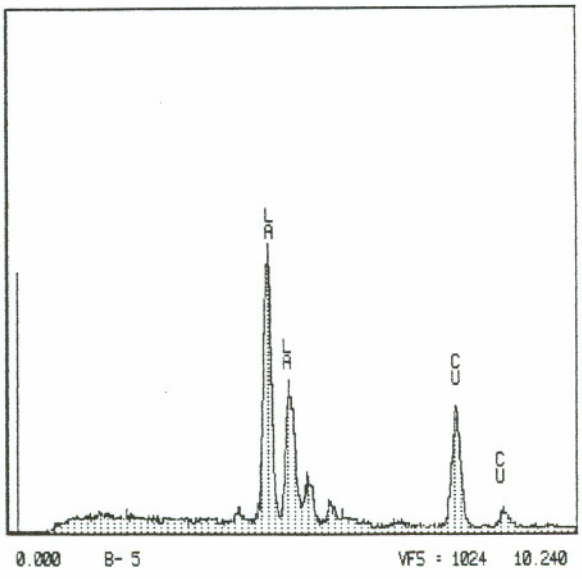

b)

Figure 62

a) Bright field image and b) EDX spectrum obtained from a La_2O_3 particle. The Cu peaks are from the Cu grid

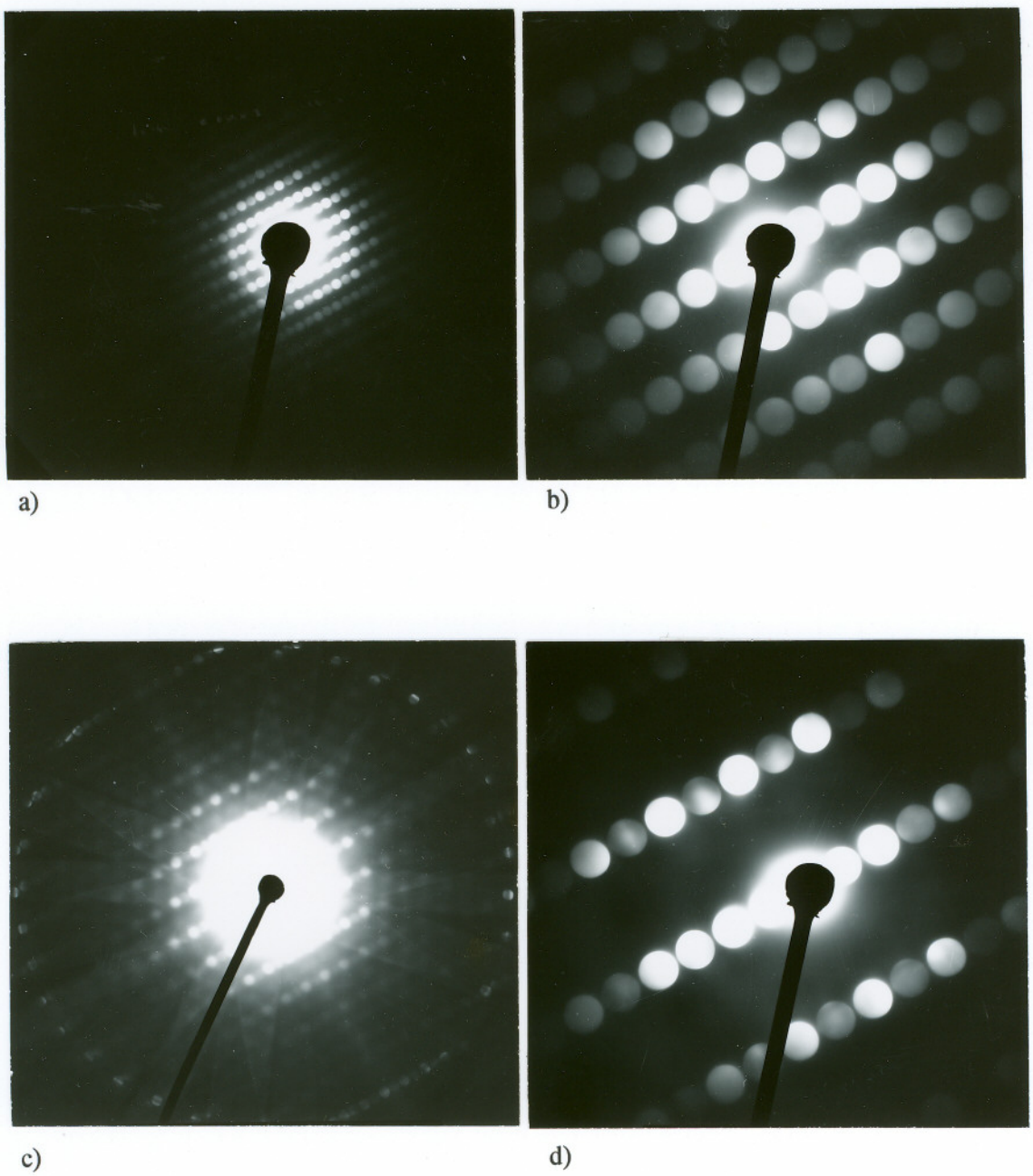

Figure 63

Electron diffraction patterns obtained from a La_2O_3 particle. a) $[2\bar{1}\bar{1}0]$ holz pattern, b) $[2\bar{1}\bar{1}0]$ zolz pattern, c) $[1\bar{1}00]$ holz pattern, d) $[1\bar{1}00]$ zolz pattern

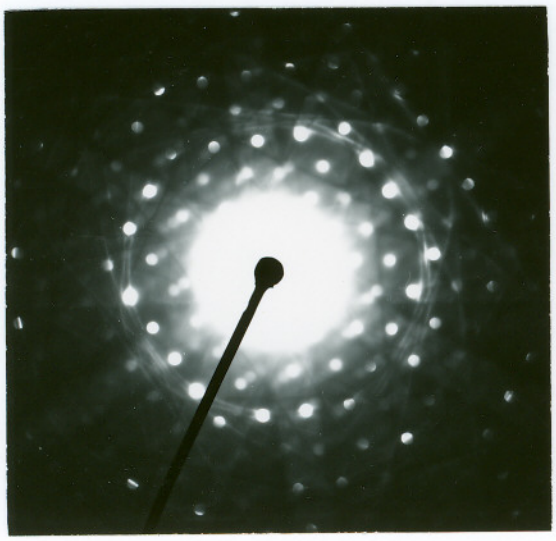

e)

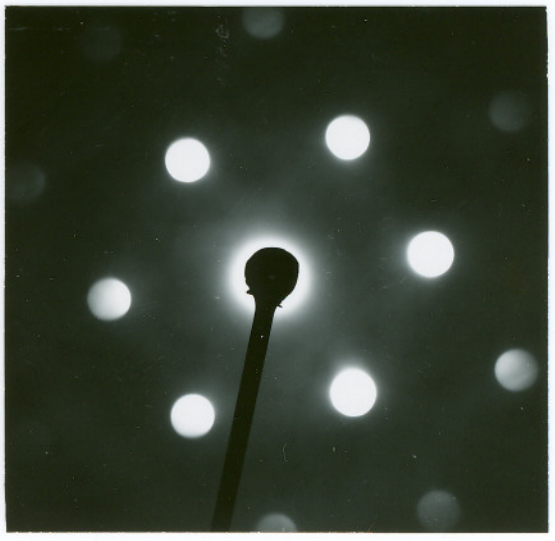

f)

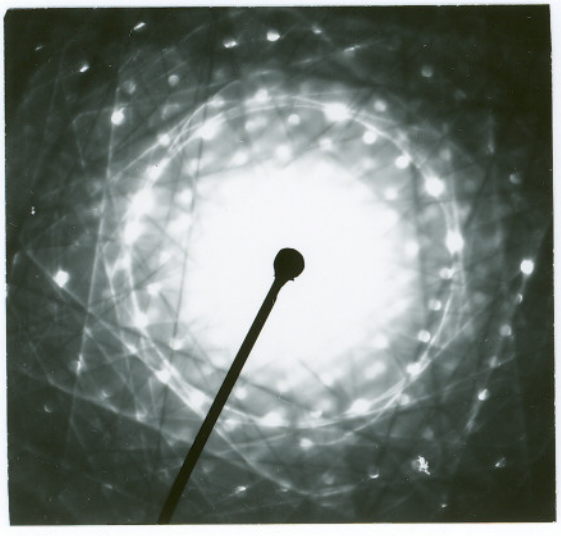

g)

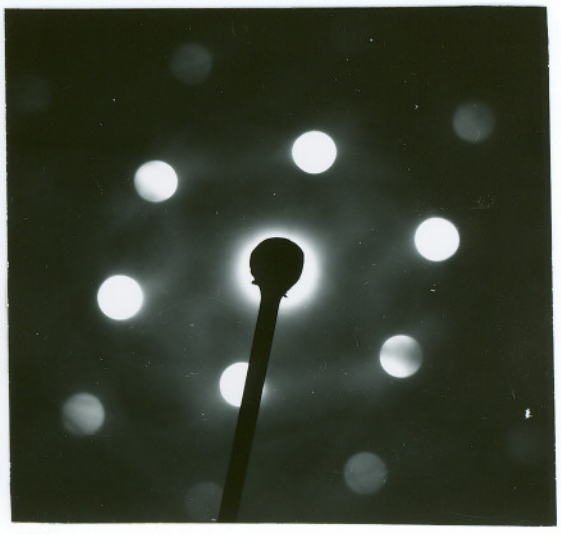

h)

Figure 63 (cont.)

Electron diffraction patterns obtained from a La_2O_3 particle. e) $[3\bar{3}01]$ holz pattern, f) $[3\bar{3}01]$ zolz pattern, g) $[8\bar{7}\bar{1}\bar{3}]$ holz pattern, h) $[8\bar{7}\bar{1}\bar{3}]$ zolz pattern

Table 18a

Experimentally measured and theoretically calculated d-spacings and the reduced unit cell volume for a La_2O_3 particle

zone axis	$[2\bar{1}\bar{1}0]$	$[1\bar{1}00]$	$[3\bar{3}01]$	$[8\bar{7}\bar{1}\bar{3}]$
measured (theoretical) d-spacing, Å	a) 3.37 (3.41) b) 2.95 (2.98) c) 6.15 (6.13)	a) 1.98 (1.97) b) 1.88 (1.87) c) 6.13 (6.13)	a) 1.75 (1.75) b) 0.98 (0.98) c) 1.94 (1.97)	a) 2.28 (2.28) b) 1.15 (1.15) c) 1.75 (1.75)
measured (theoretical) reduced unit cell volume, $Å^3$	(82.28)	78 (82.28)	80 (82.28)	74 (82.28)

Table 18b

Experimentally measured and theoretically calculated angles between the zone axes for a La_2O_3 particle. Figures in brackets are theoretical values

zone axis	$[2\bar{1}\bar{1}0]$	$[1\bar{1}00]$	$[3\bar{3}01]$	$[8\bar{7}\bar{1}\bar{3}]$
$[2\bar{1}\bar{1}0]$	0.0 (0.0)	31.52 (30.00)	33.85 (33.94)	29.98 (30.21)
$[1\bar{1}00]$	31.52 (30.00)	0.0 (0.0)	18.83 (16.68)	23.63 (20.69)
$[3\bar{3}01]$	33.85 (33.94)	18.83 (16.68)	0.0 (0.0)	7.47 (6.93)
$[8\bar{7}\bar{1}\bar{3}]$	29.98 (30.21)	23.63 (20.69)	7.47 (6.93)	0.0 (0.0)

CHAPTER 4

DISCUSSION OF RESULTS

A. OXIDATION KINETICS

In the initial stages of oxidation, all the alloys showed a very steep increase in the oxide growth rate and then the growth rate tapered off and followed the parabolic rate law (Figures 12 and 13). This initial stage of oxidation is termed as the "transient oxidation"[9,16,47]. During the transient stage of oxidation, the oxide growth rate controlling step is the size of the surface area of the alloy on which an oxide can grow. Since prior to oxidation, the entire surface of the alloy is available for the oxide growth, a steep increase is observed in the weight gain/area, during this period of oxidation.

It was postulated that during the transient stage of oxidation, the oxides of both Ni and Cr are formed on the alloy surface[3,47]. Chattopadhyay and Wood[16] had reported the formation of $NiCr_2O_4$ layer on Ni-30Cr alloy in the transient stage of oxidation at 800°C. However, they found that after extended exposure at temperature, a healing layer of Cr_2O_3 had formed over the alloy surface just beneath the transient oxides. Wood[19] had also reported similar results for Ni-27%Cr alloy oxidized at 1200°C.

Although oxides such as NiO and $NiCr_2O_4$ initially form on the alloy surface, eventually, after extended period of time at temperature, the growth rate of the thermodynamically more stable oxide, Cr_2O_3, exceeds the growth rate of the other oxides and becomes the oxide growth rate controlling species[9,16]. In this study, the $NiCr_2O_4$ oxide was also found in the oxide scale grown at 900°C in air for 24 hours, on all the yttrium free alloys (Figures 34-37). A similar observation was reported by Davis et al.[52] in their study on Ni-22.6Cr-1ThO_2 alloy oxidized at 1000°C for 30 hours. This result may be of significance in explaining the higher rate of oxide growth in the case of yttrium free alloys, compared with the yttrium containing alloys.

A larger area of the oxide surface, in the case of yttrium free alloys (Figure 21), was found to be rich in Ni, Cr and O, compared to the oxide grown on the yttrium containing alloys (Figure 27). These Ni, Cr and O rich oxides with a floret type of morphology, were found to be of the type $NiCr_2O_4$ (Figures 34 and 35). Observation of this phase in the oxide scale may qualitatively explain the increased weight gain/area observed in the yttrium free alloys compared with the yttrium containing alloys. It may be noted that an exact corelation between the amount of $NiCr_2O_4$ oxides formed on the alloy surface, and the oxide growth rate was not attempted in this study.

Since weight gained by an alloy during oxidation is essentially the weight increase due to the oxide formation, higher the amount of $NiCr_2O_4$ in the oxide scale, larger would be the weight gain. Since 4 atoms of O are required to form $NiCr_2O_4$ compared with 3 atoms for the formation of Cr_2O_3, larger amount of $NiCr_2O_4$ in the oxide scale would translate into a higher weight gain/area by the alloy.

The amount of sulfur in the alloys did not affect both the weight gain/area and the parabolic rate contant. Both the yttrium free alloys containing high and low sulfur, exhibited similar weight gain/area and the parabolic rate constant. Rhys-Jones and Grabke[41] in their studies on Fe-20Cr-0.02S and Fe-20Cr-0.0055S at 1000°C in 13.33 kPa oxygen had found that the weight gain of both the alloys at the end of 25 hours of oxidation was approximately the same i. e. about 6 mg/cm^2, although the parabolic rate constants were different. However, both the weight gain/area and the parabolic rate constant were significantly higher for the Fe-20Cr-0.02 S alloy compared to the Fe-20Cr-0.0055 S alloy[41].

In the case of yttrium containing alloys, higher amount of yttrium in the alloys, resulted in the decrease in the weight gain/area and the parabolic rate constant, irrespective of the alloy sulfur content (Figure 13). A similar result was reported by Rhys-Jones and Grabke[41] in the Fe-20Cr alloy containing 0-0.9% Ce.

The Ni-31Cr-900 ppm Y alloy had 220 ppm S, almost 4.5 times the sulfur content of the Ni-23Cr-650 ppm Y alloy, but the oxide growth rate of the former alloy was lower than that of the latter alloy. The Ni-22Cr-0.62Y alloy had 29 ppm S, which is somewhat comparable to the

47 ppm S in the Ni-23Cr-650 ppm Y alloy; however, the weight gain/area rate and the parabolic rate constant of the former alloy was significantly lower than that of the latter alloy (Figures 14 and 15). These results indicate that a higher amount of yttrium in the alloy would decrease the oxide growth rate of the alloy, and that the sulfur content of the alloy may not significantly affect the oxide growth rate, for an oxidation period of 24 hours at 900°C in air.

B. THERMAL CYCLING OF THE OXIDIZED ALLOYS

1. YTTRIUM FREE ALLOYS

Both the yttrium free alloys containing high and low sulfur exhibited oxide scale spallation when the oxidized specimens were removed from the furnace, at the end of 24 hours of exposure at 900°C in air. Figure 20-24 show the SEM micrographs of the spalled regions observed on both the yttrium free alloys studied. The EDX analysis of the spalled regions, (Figures 23, 24), did not indicate presence of any elements other than Ni and Cr.

Segregation of sulfur to the alloy/oxide interface has been shown by SIMS depth profiling by Hussey et al.[67] in the Fe-20Cr alloy coated with 40 Å of CeO_2 prior to oxidation. A similar observation was also reported by Graham et al.[68] on Fe-20Cr alloy coated with 40 Å layer of CeO_2. The alloy studied by both Hussey et al.[67] and Graham et al.[68] had low sulfur content, ~ 55 ppm. Walker and El Gomati[90] had also shown by using a Scanning Auger Microsope that sulfur segregated to the alloy surface in a Ni-15Cr-24Al alloy. They had shown that the sulfur segregation was only a monolayer thick. These studies showed that even when the alloy contained only a few ppm sulfur, it segregated to the alloy/oxide interface when exposed to high temperature.

In the Ni-25Cr-4.8 ppm S alloy oxidized at 900°C in air for 24 hours, it is possible that sulfur may have segregated to the alloy/oxide interface, but the quantity may not be detectable by the method employed i. e. EDX analysis. However, it is clear that reduction in the sulfur content of the alloy did not improve its spalling resistance; this is a significantly different result than that reported in the literature.

Melas and Lees[78] had shown that the reduction in the indigenous sulfur content of reactive element free chromium metal by annealing it in hydrogen prior to oxidation, resulted in an adherent oxide scale. The results of this study do not appear to be in agreement with those reported by these authors and others[77,79-83,94]. Melas and Lees[78] argued that the reduction in the sulfur content of the alloy was responsible for the improvement in the oxide adherence. They had however, not reported the composition of the chromium metal after hydrogen annealing. If the Cr_2O_3/metal interface was indeed as strong as suggested by these authors, the Ni-25Cr alloy containing 4.8 ppm S should not have spalled since the sulfur content of the alloy was comparable to that reported by Melas and Lees[78].

Smeggil[94] had also reported an improvement in the adherence of the oxide scale grown on Ni-40Cr alloy containing less than 2 ppm sulfur. The conclusion that the oxide scale adherence had improved was based on the measurement of the mass of the spalled oxide scale. Since a lesser mass of the spalled scale was detected in the low ppm sulfur alloy compared to the normal purity ($\sim$ 50 ppm S) sulfur alloy when the oxidized alloys were thermally cycled, it was concluded that the oxide scale on the low sulfur ($<$ 2 ppm) was more adherent. Here again it is not clear if the threshold limit on the amount of sulfur necessary to promote adherent oxide scale was 2 ppm.

In view of the results found in this study, spallation of the oxide scale from the 4.8 ppm S containing alloy at the temperature of 900°C may suggest that the oxide/metal interface may not be as strong as that suggested by the researchers[76-79, 81-83, 93-94] who claim it to be so.

The appearance of the spalled oxide surface indicated that the oxide scale was in contact with the substrate alloy before it had spalled (Figures 20-24). The thermally ethched appearance of the spalled surface indicated that the oxide scale was in contact with the alloy substrate prior to the spallation of the scale[42, 47]. Voids along the alloy grain boundaries (Figures 23,24) have been thought to be the result of coalescence of vacancies[42], caused by the faster diffusion of Cr^{3+} cations to the alloy/scale interface, than the diffusion of oxygen anions to the alloy/scale interface.

Observation of voids along the alloy grain/dendrite boundaries (Figures 23,24) lends support to the theory suggested by some researchers[29,31,60] that a larger number of voids form in the case of reactive element free alloys compared to the reactive element containing alloys. In this study, voids were not found on the spalled oxide regions of the yttrium containing alloys (Figure 30). It is possible that yttrium may have reduced the diffusion of Cr^{3+} cations to the alloy/scale interface, and this may have reduced the number of voids which may have formed at the alloy/scale interface.

2. YTTRIUM CONTAINING ALLOYS

Spalling was not observed in any of the yttrium containing alloys when they were removed from the furnace after exposure at 900°C in air for a period of 24 hours. However, the alloys containing 650 ppm Y and 900 ppm Y exhibited spallation of the scale after thermally cycling the oxidized alloys for 2 times at 900°C in air (Figure 30). The EDX spectra obtained from the spalled regions did not indicate presence of any element other than Ni and Cr (Figure 30). Sulfur, which is believed to segregate to the oxide/alloy interface and result in the spallation of the oxide scale, was not detected in the EDX spectra (Figures 30b and 30d).

It is possible that, sulfur segregation at the alloy/oxide interface may be only a few monolayers thick as reported by Walker and El Gomati[90] in a Ni-15Cr-24Al alloy heated in-situ at 700°C for 15 hours in a Scanning Auger Microscope. In the alloys investigated in this study, if the sulfur segregation was only a few monolayers thick, it is possible that it may not have been detected by the EDX analysis carried out on the alloy.

The sulfur content of both the 650 ppm Y and 900 ppm Y containing alloys was significantly different (Table 1). Based on the sulfur content of the alloys alone, it may be conjectured that the oxide scale grown on the 900 ppm Y alloy which contained 220 ppm sulfur, should have spalled even before the oxide scale on the 650 ppm Y had spalled, if sulfur segregation at the alloy/oxide interface was responsible for the spallation of the oxide scale.

Consider the following situation. Yttrium oxysulfide, Y_2O_2S, was found in all the as-homogenized yttrium containing alloys (Figures 42-45). From the stoichiometry of Y_2O_2S one can determine that 177.82 g of yttrium would be required to combine with 32.06 g of sulfur, to form Y_2O_2S. If it was assumed that all the yttrium in the alloy was tied up with sulfur in the alloy in the form of Y_2O_2S, the 650 ppm Y alloy would still be left with 389 ppm of Y, with no sulfur to combine and form Y_2O_2S.

On the other hand, in the case of 900 ppm Y alloy, all the yttrium in the alloy would be tied up with 162 ppm of S in the alloy, leaving 58 ppm of S, free to spall the oxide scale. One would then expect the oxide scale grown on the 900 ppm Y alloy to spall even before the oxide scale on the 650 ppm Y alloy had spalled. However, since this was not found to be the case, it may be argued that, a mere reduction in the sulfur content of the alloy, may not necessarily improve the oxide scale adherence in the chromia forming alloys.

The Ni-22Cr-0.62Y alloy did not exhibit oxide scale spallation even after the oxidized alloy was thermally cycled 10 times at 900°C in air (Figures 31a-c). Comparing the sulfur content of this alloy with the 4.8 ppm S in the Ni-25Cr alloy, one may expect the oxide scale on the 0.62%Y alloy to spall, since this alloy had almost 6 times the sulfur content compared to the yttrium free Ni-25Cr alloy. Since spallation of the scale was not observed in the Ni-22Cr-0.62Y alloy even after thermally cycling the oxidized alloy, it may be concluded that presence of yttrium in the alloy was necessary to prevent oxide spalling, contrary to the results reported by Smeggil[94]. The question remains whether there was a threshold limit on the amount of yttrium in the alloy, necessary to produce an adherent oxide scale, since lower yttrium containing alloys exhibited spallation of the oxide scale upon thermal cycling (Figure 30).

C. SCANNING ELECTRON MICROSCOPY

1. HOMOGENIZED YTTRIUM CONTAINING ALLOYS

In all the as-homogenized yttrium containing alloys, Ni and Y were found to be segregated along the grain/dendrite boundaries (Figures 16b and 16d). Solubility of yttrium in nickel is very small, ~ 0.1 atomic% at 1250°C and it is not known to form a solid solution with

Ni as seen from the Ni-Y phase diagram[123] shown in Figure 64. Yttrium however, forms several intermetallic compounds with Ni (Figure 64). It is thus possible that the Ni-Y rich grain/dendrite boundary regions may be some intermetallic compound of Ni and Y.

In this study, the compound Ni_5Y was found along the alloy grain/dendrite boundaries in the yttrium containing alloys (Figures 40 and 41). It may be possible that the Ni-Y rich phase observed along the grain boundary/dendrite boundary may have consisted of the Ni_5Y phase.

In some areas of the grain/dendrite boundary, yttrium was found in association with sulfur and oxygen (Figures 18a and 18b). These Y-S-O rich regions of the grain/dendrite boundary may be the Y_2O_2S phase, which was found in all the yttrium containing alloys by electron diffraction analysis in this study (Figures 42-45). This demonstrated that yttrium content as low as 650 ppm in the alloy was capable of gettering trace quantities of sulfur in the alloy.

Specimens obtained by the dissolution of the as-homogenized yttrium containing alloys in the iodine-methanol solution, were observed in the SEM (Figure 19a). The EDX spectrum obtained from such a specimen (Figure 19b) showed that the yttrium containing alloys contained yttrium, sulfur and oxygen rich particles . In this study, these particles were found to be particles of the Y_2O_2S phase and their morphology was found to be globular (Figures 19, 42 and 44). This observation suggested that these particles may have formed during the melting of the alloys.

2. OXIDIZED ALLOYS

In the case of yttrium free alloys, large areas of the oxide grown at the temperature of 900°C and 1000°C, were found to be Ni-Cr-O rich areas (Figures 20-22), as compared to the yttrium containing alloys (Figures 25, 27 and 28). The Ni-Cr-O rich areas of the oxide had a floret morphology (Figure 34a and 34b). Further, it may also be noted that the regions of the oxide scale rich in Ni-Cr-O, were larger in the case of yttrium free alloys compared to the yttrium containing alloys.

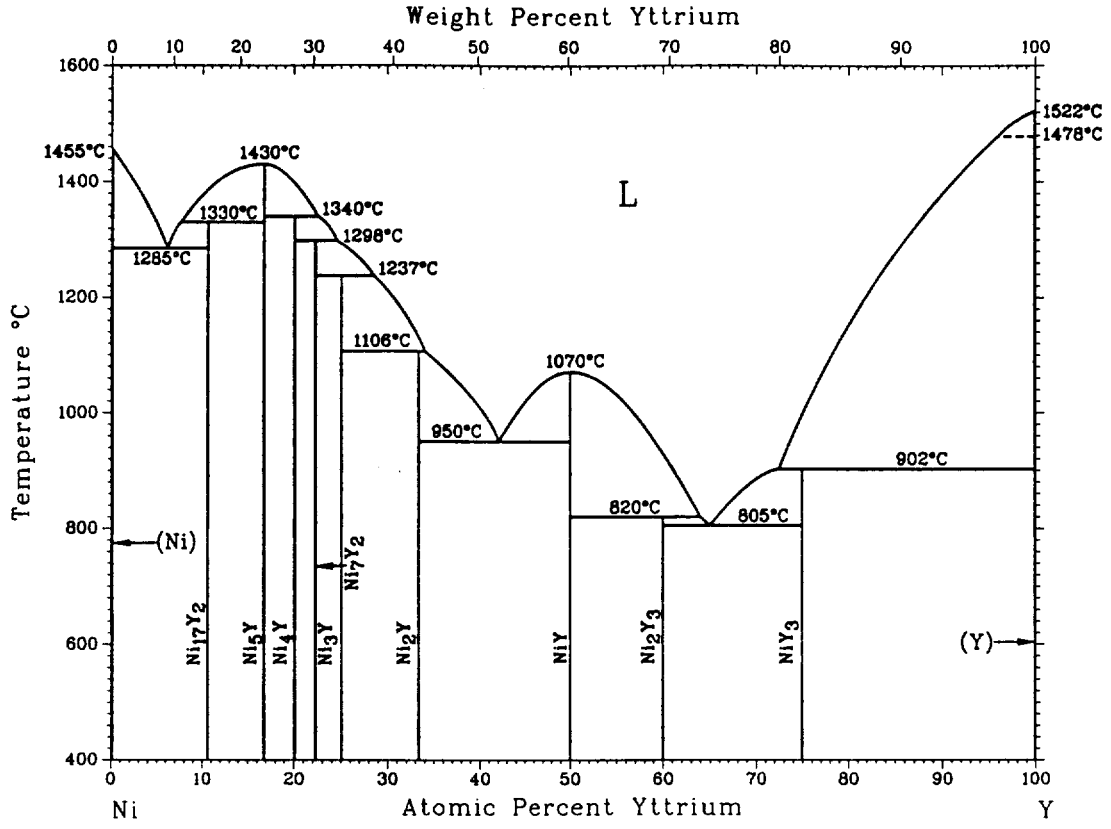

Figure 64

Nickel-Yttrium binary phase diagram[123]

The formation of $NiCr_2O_4$ on the surface of the Ni-Cr alloys when exposed to higher temperatures was found in this study by electron diffraction (Figures 35 and 37). It may thus be possible that the Ni-Cr-O rich oxides observed on the oxide surface consisted of $NiCr_2O_4$. From the chemical formula of $NiCr_2O_4$ and Cr_2O_3 it can be seen that the amount of oxygen required to form $NiCr_2O_4$ was higher compared to the amount of oxygen required to form Cr_2O_3. On this basis, the formation of $NiCr_2O_4$ may also explain the higher weight gain of the yttrium free alloys compared to the yttrium containing alloys at 900°C at the end of 24 hours of exposure (Figure 15).

Yttrium was found in association with Ni, Cr and O along the grain/dendrite boundary regions of the yttrium containing alloys which were exposed to both 900°C and 1000°C in air for short periods of time. It is possible that Ni-Y rich phase formed at the grain/dendrite boundaries during alloy melting or the homogenization treatment (Figure 16), may have reacted with oxygen giving rise to an oxide of yttrium, or a complex compound consisting of Y, Ni, Cr and O. It is more likely that the Ni, Cr and O found in the EDX spectrum, were detected from the surrounding $NiCr_2O_4/Cr_2O_3$ oxides (Figure 28). Yttrium was however not detected in the oxide grown on the alloys oxidized at 900°C in air for 24 hours (Figure 27). This may be due to the reason that the oxide grown at shorter time interval is much too thin compared to the thickness of the oxide formed after 24 hours of exposure. Hence yttrium which may have been present under the oxide scale could not be detected in the SEM.

As shown in the Figure 29, yttrium was not found to be segregated along the oxide/alloy interface. It was found to be distributed along the alloy grain boundary and the alloy interdendritic regions, as shown in the x-ray map of yttrium (Figure 29). It thus seems that yttrium remains at the alloy grain/dendrite boundaries, at least at the end of 24 hours at 900°C. It was argued by some investigators[48] that the reactive elements such as yttrium, segregate to the alloy/scale interface, and reduce the diffusion of chromium cations from the alloy substrate towards the oxide. This was suggested as a possible reason for the reduction observed in the oxidation rate of the reactive element containing alloys. This however, does not seem to be the case, at least for the oxidation period of 24 hours at 900°C, although the oxide growth rate was significantly reduced.

D. TRANSMISSION ELECTRON MICROSCOPY

1. YTTRIUM FREE ALLOYS

a. CrS Phase

In the case of yttrium free alloys, ion-milled specimens did not reveal any phase other than the matrix phase consisting of Cr in solid solution in Ni. The specimens prepared by dissolving the specimens in iodine-methanol however revealed the chromium sulfide phase, CrS, which has a hexagonal crystal structure space group 194 $P6_3/mmc$ (Figure 33)[115].

From the literature it is known that CrS is the thermodynamically most stable sulfide of Cr[112]. Hence, in the presence of excess chromium in the metal substrate, reaction of chromium and sulfur may be expected to give rise to the formation of CrS. In the low sulfur (4.8 ppm S) alloy however, CrS was not identified. This may be due to the very small concentration of sulfur which may not be sufficient for the formation of CrS. It is also possible that due to the very small concentration of sulfur in the alloy matrix, only a very small amount of CrS may have formed which may not be detectable by the alloy dissolution method employed.

Since there is significantly more chromium in the yttrium free alloys studied compared to their sulfur content, sulfur would be expected to form a stable compound CrS, than stay as free sulfur in solution, in the Ni-Cr matrix. The standard free energy change at 1200 K for the solution of sulfur in iron is -105.3 kJ/mole of sulfur[124]. If it was assumed that the standard free energy change at 1200 K associated with the solution of sulfur in Ni-25Cr alloys was of a similar magnitude, sulfur in the alloy may not remain as free sulfur but instead may be tied up with Cr in the form CrS, since the driving force for the formation of CrS is greater (at 1200 K, ΔG° for the formation of CrS is -133.76 kJ/mole of sulfur)[112].

Rhys-Jones and Grabke[41] in their study on the Fe-20Cr alloys containing 55 ppm S had observed the segregation of sulfur to the alloy/oxide interface when the alloy was exposed at 1000°C in 13.33 kPa oxygen. These studies indicate that sulfur, even when present in the alloy in very small quantities does segregate to the alloy/oxide interface. However, Rhys-Jones and

Grabke[41] did not provide the Auger spectra obtained from the Fe-20Cr-0.02 S alloy, and hence it is not clear if sulfur had segregated as free sulfur and remained as free sulfur, or whether it was trapped in the form of some compound, such as CrS. From the thermodynamic considerations stated above it seems likely that it may be tied up in the form of chromium sulfide.

A clearer evidence that sulfur may be tied up in the form of CrS at the alloy/oxide interface was reported by Grabke et al.[89] in their studies on Fe-15Cr-160 ppm S. They found that sulfur saturated as a monolayer on the metal surface after a few minutes of heating at 900°C in vacuum (10^{-8} mbar). They also found that chromium co-segregated to the alloy surface along with sulfur. It is possible that sulfur may have been tied up as CrS, which resulted in the strong sulfur and chromium Auger spectra.

Grabke et al.[89] aslo found that when the Fe-15Cr-160 ppm S alloy was oxidized for 3 hours at 900°C in 10^{-2} mbar O_2, sulfur segregated along with chromium at the spalled oxide surface. However, when the spalled oxide surface was sputtered with Ar ions, in the Auger electron microscope, both sulfur and chromium peaks disappeared after a few minutes of sputtering. This result indicated that sulfur had segregated only in a monolayer and that co-segregation with chromium had taken place. This result also indicates that sulfur may not have been present as free sulfur on the spalled oxide surface, but may have been tied up in the form of chromium sulfide, possibly CrS.

The above analysis poses a question - why does sulfur segregate to the alloy/scale interface when it can be tied up in the form of a stable compound such as CrS ? Certainly, more extensive study is needed to conclusively determine the answer to this question.

b. $NiCr_2O_4$ PHASE

In the oxidized yttrium free alloys, the phase $NiCr_2O_4$ with a cubic crystal structure[116,117] was observed in this study (Figures 35 and 37). The analysis of the EDX spectrum obtained from the floret type of oxide found in the oxide scale (Figure 34) compared well with the analysis of the EDX spectrum obtained from the $NiCr_2O_4$ particles (Figures 34d and 36a). This suggests that the Ni-Cr-O rich floret type of oxides found in the oxide grown on the yttrium free and

yttrium containing alloys, may be the $NiCr_2O_4$ phase. As suggested above, observation of $NiCr_2O_4$ (Figures 20-22) in the oxide scale in the yttrium free alloys, may partly explain the increased oxide growth rate found in the yttrium free alloys compared to the yttrium containing alloys.

2. YTTRIUM CONTAINING ALLOYS

a. Ni_5Y Phase

The phase Ni_5Y was identified in the ion-milled as-homogenized yttrium containing alloys (Figures 40 and 41). The experimentally calculated d-spacings, reduced unit cell volume and the angles between the zone axes match very well with the theoretical values of the d-spacings, unit cell volume and the angles between the zones for the phase Ni_5Y. This confirmed the presence of Ni_5Y phase in the yttrium containing alloys.

Theoretical calculations show that Ni_5Y contains 23.25 wt% Y and 76.75 wt% Ni. The semi-quantitative analysis of the EDX spectra (Figures 40b and 40d) also showed comparable Ni and Y content. This confirmed the presence of Ni_5Y along the grain/dendrite boundaries. The x-ray map of yttrium taken from the ion-milled as-homogenized Ni-22Cr-0.62Y alloy (Figure 17) clearly showed that yttrium had segregated to the alloy grain boundaries and the interdendritic regions in the alloy.

Formation of Ni_5Ce phase along the grain boundaries in the Ni-19Cr-3Al-3Ti-0.2Ce alloy was reported by Seybolt[112]. The Ni-rare earth systems show similar behavior in terms of formation of intermetallic compounds, and thus the Ni_5Y phase may also be expected to form along the grain/dendrite boundaries in the alloys studied in this investigation. From Figure 64 it can be seen that the Ni_5Y is expected to form in the Ni-Y system. In the SEM micrographs (Figures 16a and 16c) Ni-Y rich regions were found along the alloy grain/dendrite boundaries, of the alloy. Hence the Ni-Y rich grain boundary/dendritic boundaries may consist of Ni_5Y. Both the SEM and TEM results suggest that the phase Ni_5Y may have formed at the alloy grain/dendrite boundaries and the interdendritic regions in the yttrium containing alloys.

Observation of the Ni-Y rich regions along the alloy grain/dendritic boundaries may have a significant relevance in explaining the phenomenon of reactive element effect. Grain boundaries are believed to provide short circuit diffusion paths for the transport of Cr^{3+} cations from the alloy substrate to the alloy/oxide interface. Since the Ni_5Y phase has a different crystal structure (hexagonal space group 191, P6/mmm)[117] than that of the matrix (cubic space group 225 $Fm\bar{3}m$)[117] it may retard the diffusion of Cr^{3+} ions from the alloy substrate toward the alloy/scale interface. This may partly explain the reduction in the oxide growth rate of the yttrium containing alloys compared to the yttrium free alloys.

Decrease in the number of voids at the alloy/scale interface has also been suggested as a possible reason for the improvement in the oxide scale adherence of the reactive element containing alloys[29,31,60]. It is possible that formation of Ni_5Y along the grain/dendritic boundaries, which are thought to act as short circuit diffusion paths for the diffusion of Cr^{3+} cations, may have retarded the diffusion of Cr^{3+} cations. This may have resulted in a reduction in the formation of voids at the alloy/scale interface in the yttrium containing alloys, thereby improving the oxide scale adherence. It may be of significance to note that, no voids were found in the spalled oxide areas on the yttrium containing alloys (Figure 30), as opposed to the observation of voids in the spalled regions of the oxide grown on the yttrium free alloys (Figures 23 and 24).

b. Y_2O_2S Phase

The yttrium oxysulfide phase, Y_2O_2S, was found in the as-homogenized yttrium containing alloys (Figures 42-45) and also in the oxide scale grown on these alloys (Figures 48 and 49). The yttrium and sulfur content of the Y_2O_2S phase, found from the EDX analysis of all the particles determined to be Y_2O_2S (Figures 42b, 44b and 48b) also compared well with the theoretically calculated yttrium and sulfur content in Y_2O_2S. Theoretical calculations, without considering oxygen, show that Y_2O_2S contains 86.78 wt% Y and 13.22 wt% S. Thus, both the EDX analysis and the electron diffraction analysis, confirmed that the phase identified was Y_2O_2S.

It is for the first time, that a conclusive evidence of the formation of the yttrium oxysulfide phase, Y_2O_2S, in the yttrium containing Ni-25wt%Cr alloys, was found in this study. A similar observation was also made by Shendye and Downham[125] in the lanthanun and cerium

containing Ni-25Cr alloys, containing comparable sulfur and lanthanum (or cerium) content.

Several studies reported in the literature[20,56,72,86-90], had suggested that the reactive elements improved the oxidation resistance of the chromia and alumina forming alloys, by tying up sulfur in the alloy. However, conclusive evidence of the Y-S species which may be responsible for imparting an improvement in the oxidation resistance, was not reported so far.

The thermodynamic stability of the rare-earth oxysulfides has been studied in detail by Gschneidner, Jr. et al.[126]. The oxysulfide species was shown to be thermodynamically more stable than the rare-earth sulfide species. Shown in the Figure 65, taken from the work of Gschneidner, Jr. et al.[126], is the thermodynamic stability of the oxides of various elements. From this figure, it can be seen that the rare-earth oxides are more stable than most other metal oxides. Shown in the Figure 66 is the standard free energy change associated with the formation of oxysulfides of yttrium, lanthanum and cerium. Figure 67 shows a comparison of the standard free energy change of formation associated with the oxides, oxysulfides and the sulfides of the rare-earth elements and yttrium.

Figure 67 shows that the rare-earth oxysulfides are more stable than the rare-earth sulfides, and that the rare-earth oxides are only marginally more stable than the rare-earth oxysulfides. Shown in the Table 19 is the standard free energy change associated with the formation of of Y, La and Ce oxide, oxysulfide and sulfide, at 1273 K and 2000 K. Since the oxysulfide species is thermodynamically more stable compared to the sulfide species, it would be expected to form, in the presence of sufficient amount of sulfur and oxygen in the alloy.

The formation of the yttrium oxysulfide in the yttrium containing alloys may also be explained on the basis of thermodynamic calculations suggested by Seybolt[112]. Consider the reaction involving Y given below. The oxygen in the reaction may be the residual amount of oxygen present in the furnace during the melting operation.

$$Y_{(\text{in alloy})} + 1/2\ CrS + 1/6\ Cr_{(\text{1in alloy})} + O_2 \rightarrow 1/2\ Y_2O_2S + 1/3\ Cr_2O_3 \quad \text{-------} \quad (5)$$

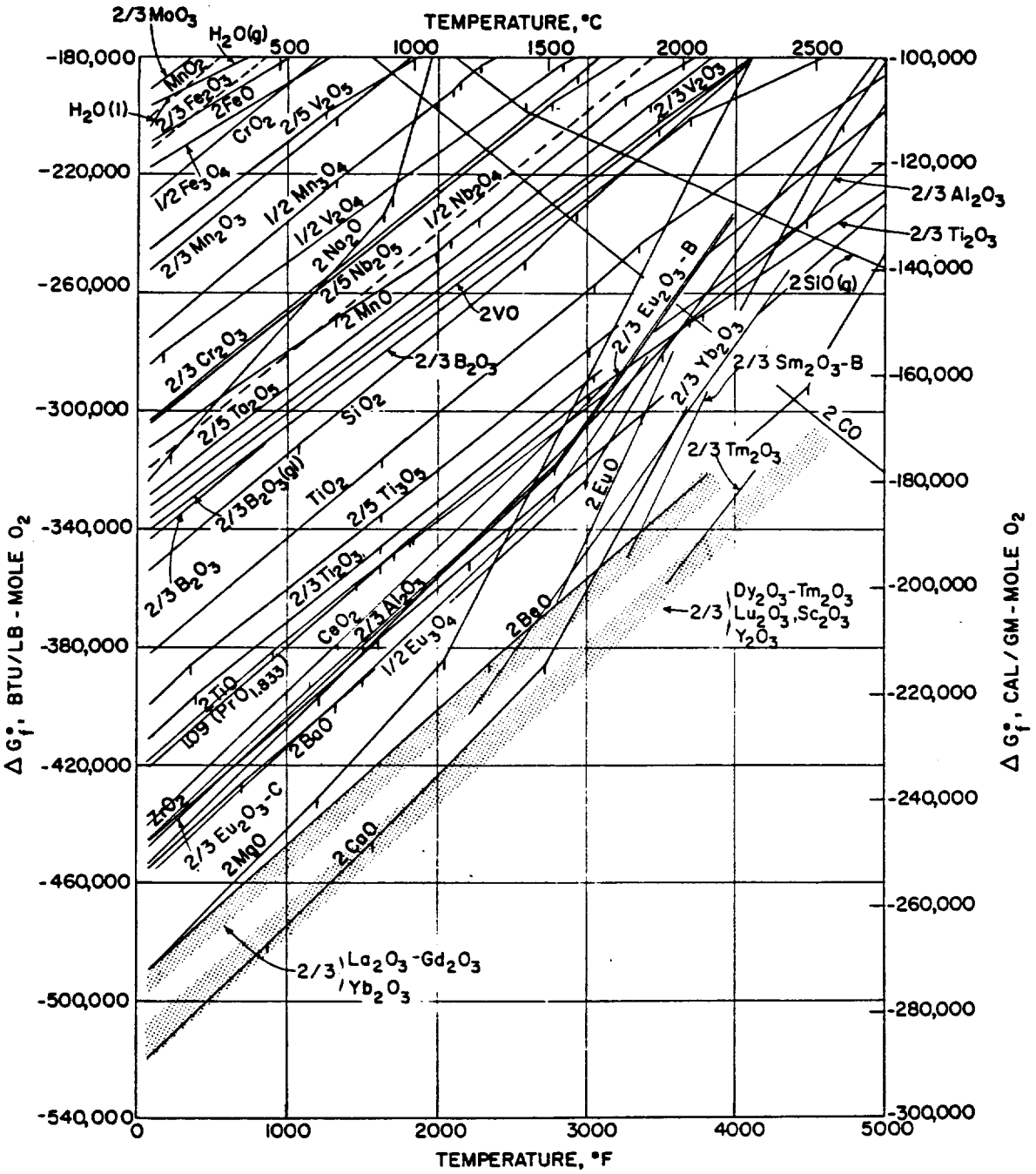

Figure 65

The standard free energy change of formation of the oxides, as a function of temperature. The notation "La_2O_3 - Gd_2O_3" means that the oxides of La, Ce, Pr, Nd, Sm and Gd lie in the band indicated, and the notation "Dy_2O_3" - Tm_2O_3" means that the oxides of Dy, Ho, Er and Tm lie in the band indicated (Reference Gschneidner, Jr. et al.[126])

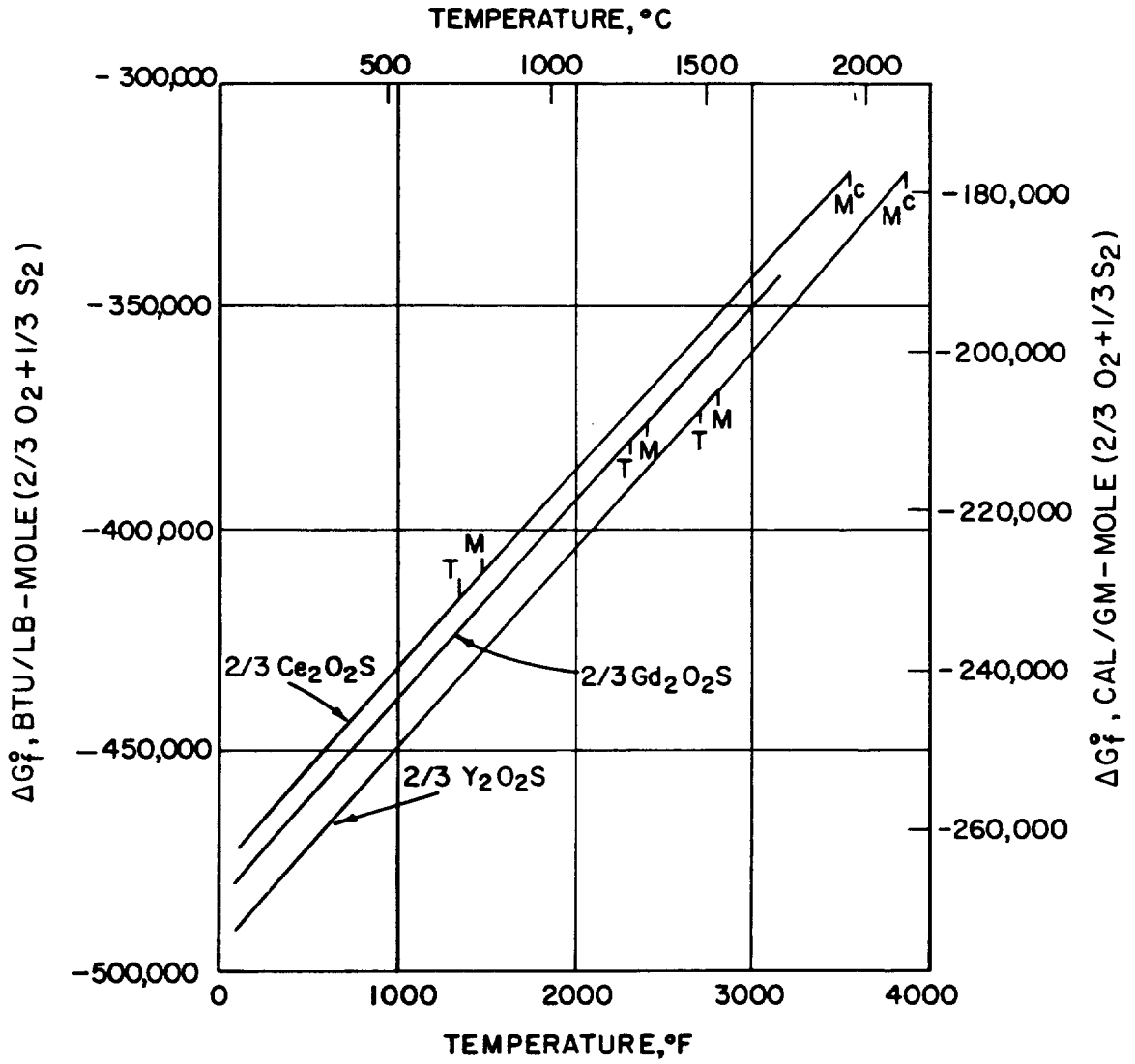

Figure 66

The standard free energy change of formation of three rare-earth oxysulfides for the reaction $2R(s,l) + 1/2\ S_2(g) \rightarrow R_2O_2S(s)$ as a function of temperature. T refers to the transformation of the metal, M refers to the melting of the metal, and M^C refers to the melting of the oxysulfide (Ref. Gschneidner, Jr. et al.[126])

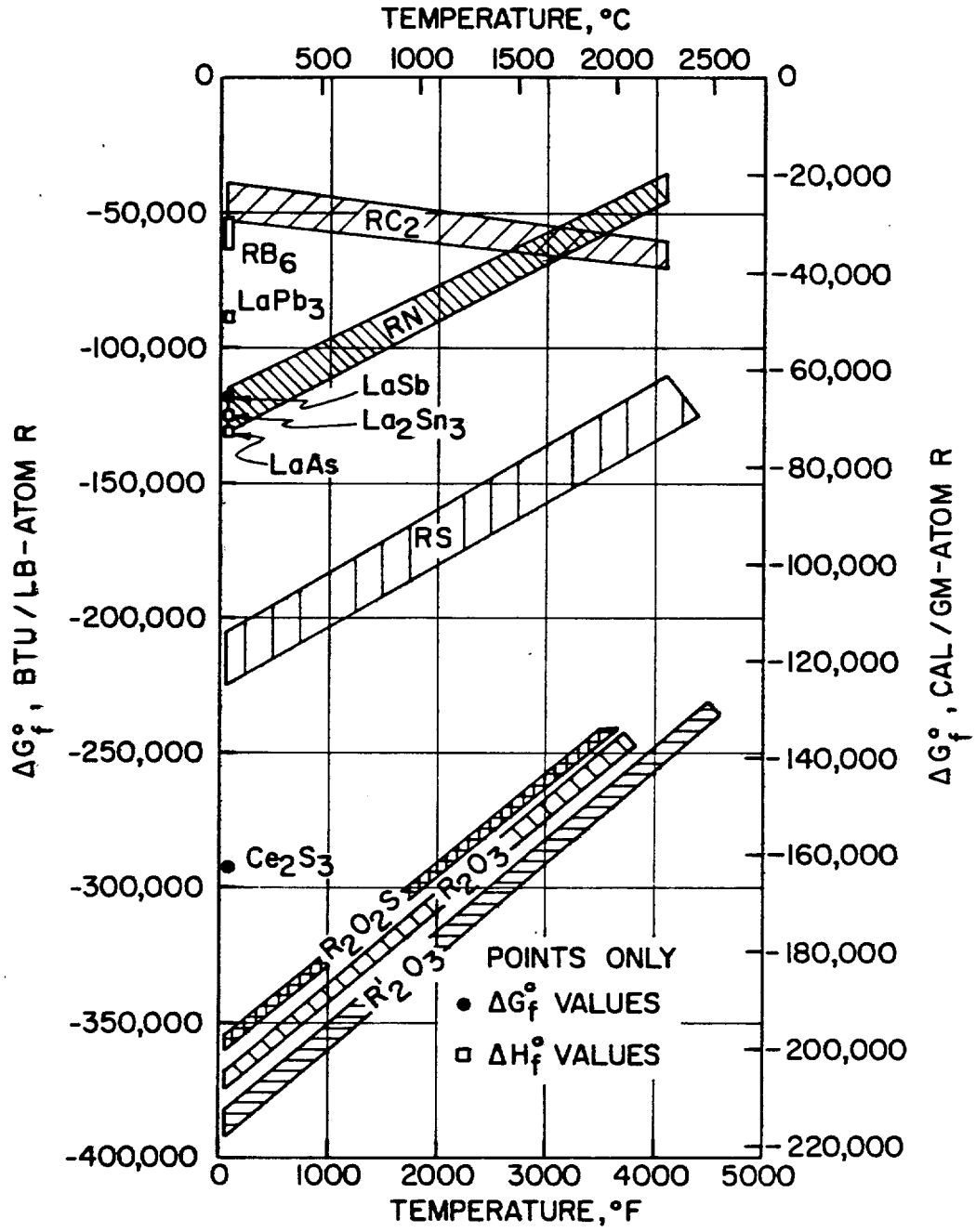

Figure 67

The standard free energy change of formation of some rare-earth compounds as a function of temperature for the reaction $R(s,l) + y/x\ X(s) \longrightarrow 1/x\ R_xX_y\ (s)$, where X = B, C, As, Sn, Sb and Pb, or for the general reaction $R(s,l) + y/2x\ Y_2\ (g) \longrightarrow 1/x\ R_xY_y\ (s)$, where Y = N, O and S. R represents the light lanthanide metals, while R' represents yttrium and heavy lanthanide elements (Ref. Gschneidner, Jr. et al.[126])

Table 19

The standard free energy change of formation of oxides, oxysulfides and sulfides of cerium, lanthanum and yttrium at 1273 K and 2000 K[126]

Compound	ΔG° at 1273K, (cal/mole)	ΔG° at 2000K, (cal/mole)	ΔG° at 1273K (J/mole)	ΔG° at 2000K (J/mole)
Ce_2O_3(s)	-341,603	-293,621	-1,430,223	-1,229,332
Ce_2O_2S(s)	-327,985	-280,730	-1,373,208	-1,175,360
La_2O_3(s)	-342,091	-292,655	-1,432,267	-1,225,288
La_2O_2S(s)	-324,955	-277,700	-1,360,522	-1,162,674
Y_2O_3 (s)	-372,582	-318,760	-1559,926	-1334,584
Y_2O_2S (s)	-349,909	-279,800	-1465,001	-1171,466
CeS (s)	-100,782	-82,680	-421,954	-346,165
Ce_2S_3(s)	-254,412	-199,160	-1,065,172	-833,843
LaS(s)	-91,043	-72,650	-381,179	-304,171
YS (s)	-94,840	-75,320	-397,076	-315,349

Consider the Gibb's standard free energy change at 1200 K given in Table 20 for the species involved in the reactions listed above. The standard free energy change values nearest 5 kJ have been taken from the work of Seybolt[112] and Gschneidner, Jr. et al.[126].

Consider equation (5) above. In order for the reaction to proceed in the direction shown, the value of the Gibb's standard free energy change at 1200 K for $Y_{(in\ alloy)}$ will have to be larger than -934.8 kJ per mole of Y, i.e. $|\Delta G^\circ| < 934.8$. The standard free energy change associated with the solution of cerium in Ni-19Cr alloys was reported to be -41.8 kJ/mole of cerium[112]. Since yttrium and cerium are known to have many identical properties[126], it may be conjectured that the free energy change associated with the solution of yttrium in the Ni-25Cr alloys would also be of a similar magnitude as that of cerium. By substituting the ΔG° values for the reactants and the products, reaction (5) would be expected to proceed in the forward direction.

The phase Y_2O_2S was also found in the oxide scale (Figures 48 and 49). The morphology of the Y_2O_2S phase in the oxide scale and in the alloy was found to be globular, which suggests that the oxysulfide particles present on the surface of the alloy prior to oxidation, may have integrated into the oxide scale. The other possible route by which the Y_2O_2S phase was incorporated into the oxide scale may be due to the reaction of the Ni_5Y phase with the oxygen to form Y_2O_3, which in turn may have reacted with the sulfur in the alloy to give rise to the Y_2O_2S phase, in accordance with the theory suggested by Seybolt[112].

Seybolt [112] had reported the formation of the Ce_2O_2S phase in the Ni-19Cr-3Al-3Ti-0.2Ce alloy which was heated at 1000°C in liquid Na_2SO_4 in still air for 24 hours. He had postulated that the phase Ni_5Ce which formed at the alloy grain boundaries during alloy preparation, may have reacted with oxygen to form a more stable compound CeO_2. This compound in turn, may have acted as a sink for the sulfur diffusing in from the oxide scale toward the alloy/scale interface, giving rise to yet another more stable compound Ce_2O_2S. In the present study, observation of Ni_5Y, Y_2O_3 and Y_2O_2S in the yttrium containing alloys supports the theory suggested by Seybolt[112].

Table 20

The standard free energy change of formation at 1200 K for various compounds of Cr and Y[112,126]

compound	CrS	$Cr_{(in\ alloy)}$	Y_2O_3	Cr_2O_3	Y_2O_2S
ΔG°, kJ/mole	-133.76	-16.13	-1585	-827.64	-1480

Yttrium, when present in the alloy in the form of an oxide dispersion, is also known to produce the reactive element effect[31,41,46,49,50,64,70,72,86]. Ikeda et al.[72] in their study on the Y_2O_3 dispersed alumina forming alloys had shown that Y_2O_3 dispersions were effective in trapping sulfur in the alloy. They had predicted that yttrium may trap sulfur in the form of yttrium sulfide, and had discounted the formation of yttrium oxysulfide. Contrary to their predictions, Shendye and Downham[127] had shown that even if yttrium was present as an oxide dispersion in the alloy, it was still effective in trapping sulfur in the alloy and forming the oxysulfide.

Consider the following reactions :

$$2\ Y_{(in\ alloy)} + 3/2\ O_2 \rightarrow Y_2O_3 \quad \text{---------- (6a)}$$

$$Y_2O_3 + S_{(in\ alloy)} + 2/3\ Cr_{(in\ alloy)} \rightarrow Y_2O_2S + 1/3\ Cr_2O_3 \quad \text{--- (6b)}$$

Since ΔG° for the formation of Y_2O_3 at 1200 K is a significantly large negative value, -1585 kJ per mole of Y_2O_3, reaction (6a) may be expected to proceed spontaneously.

Now consider reaction (6b). In this reaction the standard free energy change associated with the solution of S in the alloy, $S_{(in\ alloy)}$ is not known. However ΔG° for the formation of the other compounds in the reaction is known, as shown in the Table 20. In order for the reaction (6b) to proceed as written, the standard free enrgy change associated with the solution of S in alloy, $S_{(in\ alloy)}$ will have to be -160 kJ per mole S, or greater i.e. $|\Delta G^\circ| < 160$ kJ/mole S. The standard free energy change associated with the solution of sulfur in iron is reported[124] to be of the form $\Delta G^\circ = -131.75 + 22.03T$ kJ per mole S, where T is in K. At 1200 K, the standard free energy change associated with the solution of sulfur in iron equals -105.3 kJ per mole S. If it was assumed that the standard free energy change associated with the solution of sulfur in Ni-25Cr alloys was of a similar magnitude, reaction (6b) would be expected to proceed as written above.

Figure 67 taken from the work of Gschneidner, Jr. et al.[126] shows that the standard free energy change associated with the formation of rare-earth oxides is only slightly more negative compared with the standard free energy change associated with the formation of reactive element

oxysulfides. It is thus possible that, in the presence of sulfur in the alloys, formation of Y_2O_2S may be feasible compared to the formation of Y_2O_3.

The observation of the oxysulfide species in the alloy may be used to qualitatively explain the results of several other researchers[31,46,49,69,72,86]. Nagai[31] had demonstrated that at 1000°C and 1100°C in air, 0.7 wt% addition of Y, La and Gd to a Ni-20Cr alloy reduced the mass gain/area significantly, compared to the Ni-20Cr alloy without Y, La or Gd additions (Figure 3). It was however not clear why the order of effectiveness was in the order Y > Gd > La. This trend may be explained on the basis of the standard free energy change of formation of the oxysulfides of Y, La and Gd.

From the work of Gschneidner, Jr. et al.[126] it can be seen that the standard free energy change of formation of the oxysulfides was in the order $Y_2O_2S > Gd_2O_2S > La_2O_2S$. For comparison purposes, consider the standard free energy change of formation at 1100 K ($\Delta G°_{Y2O2S}$ = -1479.7 kJ/mole Y_2O_2S, $\Delta G°_{Gd2O2S}$ = -1446.3 kJ/mole Gd_2O_2S, $\Delta G°_{La2O2S}$ = -1408.6 kJ/mole La_2O_2S). Since the standard free energy change of formation of Y_2O_2S is more negative than that of Gd_2O_2S and La_2O_2S, yttrium additions may have resulted in lower weight gain/area than that of gadolinium or lanthanum additions.

Nagai[31] had also reported the relative effectiveness of the reactive elements when added as an oxide dispersion to the Ni-20Cr alloy. In this case, La_2O_3 dispersions were found to be more effective than Y_2O_3 dispersions in providing the oxidation resistance at 1100°C in air. These results concur with those of Michels[49] who reported the same result at 1100°C and 1200°C. However, Michels[49] observed a reverse order i. e. Y_2O_3 more effective than La_2O_3, when the same experiments were carried out at 1000°C.

A qualitative explanation of why lanthana dispersions were found to be more effective than yttria dispersions, may be attempted on the basis of reaction (6b) as follows. Assuming $\Delta G°$ for all the other species such as $S_{(\text{in alloy})}$, $Cr_{(\text{in alloy})}$, and Cr_2O_3 remain same irrespective of whether Y_2O_3 or La_2O_3 was added to the alloy, reaction (6b) above would have a greater tendency to go forward if the alloy contained La_2O_3 dispersions as opposed to the alloy containing Y_2O_3 dispersions.

This may be explained on the basis of the standard free energy change of formation at 1100 K of the oxide and the oxysulfide of Y and La ($\Delta G°_{Y2O3}$ = - 1585.3 kJ/mole, $\Delta G°_{Y2O2S}$ = - 1479.7 kJ/mole, $\Delta G°_{La2O3}$ = -1479 kJ/mole, $\Delta G°_{La2O2S}$ = -1408.6 kJ/mole)[126]. Since the difference in the standard free energy change of formation of the oxide and the oxysulfide of yttrium is more than that for lanthnaum, reaction (6b) would have a greater tendency to go in the forward direction in the case of La_2O_3 than in the case of Y_2O_3. Hou and Stringer[69] had reported similar results in the case of a Ni-25wt%Cr alloy coated with 0.2 mg/cm^2 La_2O_3 and 0.4 mg/cm^2 Y_2O_3 oxidized at 1000°C in 1 atm O_2 for 45 hours.

By the same argument, reaction (6b) would be expected to have a greater driving force in the case of Gd_2O_3 dispersed alloy compared to La_2O_3 dispersed alloy ($\Delta G°_{Gd2O3}$ = -1504 kJ/mole, $\Delta G°_{Gd2O2S}$ = -1446.3 kJ/mole, $\Delta G°_{La2O3}$ = -1479 kJ/mole, $\Delta G°_{La2O2S}$ = -1408.6 kJ/mole 1100 K). Furthermore, the above argument would predict that Y_2O_3 dispersions would be less effective than Gd_2O_3 dispersions. Exactly the same results have been reported by Nagai[31] in the case of Y, La and Gd oxide containing Ni-20Cr alloy oxidized at 1200°C in air. The same trend was reported by Nagai et al.[46] in their studies on La and Y oxide dispersed Fe-20Cr alloy oxidized in the range of 1000°C to 1100°C.

In the case of Co-25wt%Cr alloy coated with oxides of Y (0.4 mg/cm^2), La (0.2 mg/cm^2) and Ce (0.4 mg/cm^2) oxidized at 1000°C and 1100°C in 1 atm. oxygen, Hou and Stringer[69] had reported that the effectiveness of the oxide coating was in the order of $La_2O_3 > Y_2O_3 > CeO_2$ at the end of 24 hours at 1000°C. This trend may be explained on the basis of the analysis suggested above. However, at the end of 45 hours at 1100°C the trend was $Y_2O_3 > La_2O_3 > CeO_2$. A possible reason for this observation may be the fact that the coating thickness of Y_2O_3 was twice that of La_2O_3.

The difference in the standard free energy change of formation of the oxide and the oxysulfide per mole of the reactive element is the largest in the case of Ce ($\Delta G°_{CeO2}$ = -859.3 kJ/mole Ce, $\Delta G°_{Ce2O2S}$ = -708.5 kJ/mole Ce at 1100 K) compared to Y and La. Thus coatings of CeO_2 on the alloy surface would be expected to be least effective compared to the oxide coating of Y or La. The same trend was reported by Hou and Stringer[69] in the case of Ni-25wt%Cr alloy coated with oxides of Ce (0.6 mg/cm^2), Y (0.4 mg/cm^2) and La (0.2 mg/cm^2)

oxidized at 1100°C for 100 hour in 1 atm oxygen. Nagai[31] had also reported that ceria containing Fe-20Cr alloys were the least effective in terms of mass gain/area compared to the lanthana, yttria or gadolinia coated Fe-20Cr alloy when oxidized at 1100°C for 72 ks in air.

Rhys-Jones and Grabke[41] had reported that addition of 0.9 wt%Ce rather than 0.9 wt%CeO_2 was more effective in reducing the weight gain of the Fe-20Cr alloy oxidized at 1000°C in 13.33 kPa O_2 for 70 hours. The reactions (5) and (6b) may be used to explain this behavior. According to the reactions (5) and (6b), the driving force for the formation of the oxysulfide would be greater when cerium is added as a metallic addition rather than as an oxide. This may result in a greater reduction in the oxide growth rate when a reactive element is added as a metallic addition rather than as an oxide dispersion.

The above analysis may explain why the reactive elements such as Y, La, Ce or Gd when added as a metallic addition or as an oxide dispersion (or surface oxide coating) to the high temperature alloys improve their oxidation resistance. It also explains to some extent, why a variation is observed in the oxidation resistance imparted by the addition of different reactive elements or their oxides. The other significant finding is that sulfur although did not seem to contribute to the improvement in the oxide scale adherence of the yttrium free alloys investigated in this study, it appears to play an important role in improving the oxide scale adherence and decreasing the oxide growth rate of the rare-earth containing alloys.

c. $Y_2O_2SO_4$ Phase

The yttrium oxysulfate phase, $Y_2O_2SO_4$, was found in the oxide scale as shown in the Figures 50 and 51. It is known that the Y_2O_2S phase when oxidized in air at a high temperature, forms $Y_2O_2SO_4$; however, this compound is reported to be very unstable at higher temperature[108,110]. Observation of $Y_2O_2SO_4$ in the oxide scale, after 2 minutes of oxidation at 1000°C in air, suggests that this species does not necessarily decompose further, in the early stages of oxidation. The oxysulfates of the rare-earth elements and yttrium, are also known to decompose further into the rare-earth oxide, and the decomposition temperature is known to decrease as the atomic number of the constituent rare-earth increases[108,110]. Thus one may expect to find $Y_2O_2SO_4$ in the Y_2O_2S containing oxide scale.

It is also known form the literature[108] that Ce_2O_2S when heated in air at a high temperature does not form an oxysulfate, but directly transforms to CeO_2. This result was confirmed in this study (Figures 54 and 55). Cerium is the only element in the rare-earth series of elements which does not form an oxysulfate, but directly transforms to its oxide, CeO_2[108]. This observation and the fact that the stability of the oxysulfate species decreases with increasing atomic number of the rare-earth element may explain the difference in the effectiveness of different elements in imparting the reactive element effect.

The results reported by Hou and Stringer[69] may be explained on the observations noted above. Hou and Stringer[69] had reported that a coating of CeO_2 (0.6 mg/cm^2) resulted in a lesser mass gain compared to a coating of Y_2O_3 (0.4 mg/cm^2) and La_2O_3 (0.2 mg/cm^2) in the case of a Ni-25wt%Cr alloy oxidized in 1 atm oxygen for 45 hours. The mass gain was 0.26 mg/cm^2, 0.36 mg/cm^2, and 0.35 mg/cm^2 respectively. However, when the same alloy with the same oxide coatings and coating thicknesses was oxidized at 1100°C for 100 hours, CeO_2 coated alloy resulted in the largest mass gain/area (0.94 mg/cm^2) than the La_2O_3 coated (0.63 mg/cm^2) or the Y_2O_3 (0.60 mg/cm^2) coated alloy.

Hussey et al.[67] in their studies on 4 nm thick CeO_2 coated Fe-25Cr alloy containing 55 ppm S, had shown by SIMS depth profiling that sulfur segregated along with Ce near the alloy/oxide interface after 0.017 hours at 900°C in 1 torr oxygen. However, after 19 hours of oxidation under the same conditions, the Ce peak was found to have moved away from the alloy/oxide interface towards the oxide/gas interface, while the sulfur peak remained near the alloy/scale interface. It is possible that the simultaneous observation of the Ce and S peaks after 0.017 hours of oxidation may have been due to the cerium oxysulfide phase present on the alloy surface prior to oxidation. As the alloy was exposed for a longer time at 900°C, the Ce_2O_2S phase may have decomposed into CeO_2, which resulted in a Ce peak away from the S peak.

These observations, apart from the thermodynamic considerations, may have some relationship to the fact that cerium oxysulfide does not form an oxysulfate but directly transforms to ceria. However, further work will be needed to determine the extent of the stability of the various rare-earth species in the oxide scale, and the relationship of these phases to the other species found in the oxide scale.

One other fact which may be of significance is that Ce is the only element other than Pr in the rare earth series of elements which exhibits a valency of +3 and +4. All the other elements exhibit a valency of either +3 or, +2 and +3. This may also affect the mechanism by which cerium imparts improved oxidation resistance to the high temperature alloys.

Lanthanum oxysulfide - La_2O_2S - however, is known to form the oxysulfate[106,110] and the same was confirmed by the electron diffraction analysis in this study (Figure 59). Diffraction patterns from more than 2 poles from a particle could not be taken because the $La_2O_2SO_4$ particles were found to be beam unstable. Hence diffraction patterns had to be taken from several particles. This finding also confirms that the oxysulfates of the rare-earth elements are unstable at higher temperatures. The yttrium oxysulfate particles found in the oxide scale were also highly beam unstable, and hence not more than two diffraction patterns could be obtained from a single particle.

A large part of the problem with the indexing of the diffraction patterns obtained from the $Y_2O_2SO_4$ and $La_2O_2SO_4$ particles was the fact that the structure of the rare-earth oxysulfates has not been adequately determined. Ballastracci and Mareschal[119] had indicated an I-centered orthorhombic lattice for $Y_2O_2SO_4$ and $La_2O_2SO_4$. But review of the original paper indicated that the space group of the oxysulfate was not unambiguously determined by these authors. However, the d-spacings and the reduced unit cell volume calculated for the phase $La_2O_2SO_4$ on the basis of the holz and the zolz pattrens (Figure 59) confirm that the identified phase was $La_2O_2SO_4$. Table 16 shows the experimentally measured and theoretically calculated d-spacings and the reduced unit cell volume for the phase $La_2O_2SO_4$, which match very well.

d. Y_2O_3 Phase

The phase Y_2O_3 was observed in the as-homogenized Ni-31Cr-900 ppm Y alloy (Figure 47). As seen from the Table 10a and 10b the experimentally measured d-spacings, reduced unit cell volume and the angles between the zone axes compared very well with the theoretical calculations.

The formation of the Y_2O_3 phase may be explained on the basis of reaction (6a). The standard free energy change of formation of this phase is a very large negative value over the temperature range of 1000 K to 2500 K (-1613.3 kJ/mole to -1103 kJ/mole) and hence its formation would be expected to occur spontaneously. The other route by which this phase may form is by the decomposition of Y_2O_2S formed in the alloy, to $Y_2O_2SO_4$ during the melting operation or during homogenization treatment. The phase $Y_2O_2SO_4$ may in turn have decomposed further to form Y_2O_3.

Observation of Y-S rich particles in association with the Y_2O_3 particle (Figure 46a) is quite significant. The EDX analysis of the Y-S rich particles showed that their yttrium and sulfur content was 86.18 wt% and 13.82 wt%, respectively (Figure 46c). Theoretical calculations show that yttrium and sulfur content in both Y_2O_2S and $Y_2O_2SO_4$ would be 86.78 weight% and 13.22 weight%, respectively, without considering oxygen. Thus, analysis of the EDX spectrum, indicates that the Y-S rich particles found in association with Y_2O_3 may consist of Y_2O_2S or $Y_2O_2SO_4$, or a combination of both the phases.

Two possible explanations may be given for the above observation. One is that Y_2O_2S which may have formed in the alloy during the melting/homogenizing operation, may have decomposed partly to $Y_2O_2SO_4$ and partly to Y_2O_3. The other possibility is that Y_2O_3 may have trapped the sulfur in the alloy and may have formed Y_2O_2S. The latter explanation would support the hypothesis that yttria dispersions in the alloy may also getter sulfur in the alloy. Ikeda et al.[72] had reported similar observations.

The observation of $La_2O_2SO_4$ (Figure 59) by heating the La_2O_2S powder for 30 minutes in air at 900°C and 1000°C, clearly confirmed that the rare-earth oxysulfides were unstable at higher temperature. The observation of La_2O_3 (Figure 62 and 63) by heating the La_2O_2S powder for 2 hours at 900°C also confirmd that, when La_2O_2S was heated for an extended period of time, it may transform to La_2O_3. Both these observations, support the results reported in the lierature[108,110] that La_2O_2S tranforms to $La_2O_2SO_4$ which further transforms to La_2O_3, when heated at higher temperatures for an extended period of time. Since yttrium is known to have identical properties as that of the rare-earth elements, a similar result would be expected when Y_2O_2S was heated at high temperatures.

e. $YCrO_3$ Phase

The phase yttrium orthochromite, $YCrO_3$, was observed in the oxide scale grown on the Ni-31Cr-900 ppm Y alloy at 1000°C in air for 2 minutes (Figures 52 and 53). It has been argued by some researchers[56,58,64,71] that the formation of the reactive element orthochromite phase in the oxide scale was a reason for the improved oxidation resistance of reactive element containing compounds. Downham et al.[64] had reported the observation of the phase $CeCrO_3$ in the oxide scale grown on a Fe-26Cr alloy implanted with a 40 Å layer of CeO_2 prior to oxidation. Pryzybylski and Yurek[56] and Patibandla et al.[58] had reported the observation of the orthochromite phase in the oxide scale and claimed that this phase was responsible for the improvement in the oxidation resistance of the Y and Ce containing alloys. Seybolt[71] had also attributed the improved oxidation resistance of yttrium containing alloys to the formation of $YCrO_3$. It was however, not clear as to how this phase may have formed in the first place.

The results of the simulation experiments carried out with the mixtures of Cr_2O_3, Ce_2O_2S, and Cr and, Cr_2O_3, La_2O_2S and Cr in vacuum (2×10^{-5} torr) may be able to explain the formation of this phase. In both the cases, heating the mixtures in vacuum at 900°C and 1000°C, resulted in the formation of the cerium orthochromite, $CeCrO_3$, (Figures 56 and 57) and lanthanum orthochromite, $LaCrO_3$ (Figures 60 and 61). Heating the mixtures in air for 1 hour however, did not result in the formation of the orthochromite species. This suggests that, depending upon the partial pressure of oxygen used during the oxidation of an alloy, a difference in the oxide scale growth rate and the oxide scale adherence may be expected, since a different set of species may be involved in imparting improved oxidation resistance. There are however, no data in the literature to support this hypothesis.

Shendye and Downham[125] had identified the compound $CeCrO_3$ in the as-homogenized Ni-23Cr-390 ppm Ce alloy, but not in the yttrium and lanthanum containing alloys. It may be noted that the alloys were melted in vacuum (10^{-4} torr) under argon atmosphere. The results of the simulation experiments carried out with Ce_2O_2S in vacuum explain why $CeCrO_3$ was observed in the Ce containing alloy, by Shendye and Downham [125].

Downham et al.[64] had reported the formation of $CeCrO_3$ in the oxide scale grown on a Fe-26Cr alloy sputter coated with 4 nm of CeO_2 and oxidized at 900°C in 5 x 10^{-3} torr O_2. Patibandla et al.[58] had also observed the formation of $CeCrO_3$ in a Ce implanted Ni-30Cr alloy oxidized at low oxygen partial pressures in the temperature range 900-1000°C. It is possible that the low oxygen partial pressure of oxygen may have resulted in the formation of the orthochromite species.

Data on the thermodynamic stability of the orthochromite species at higher temperatures is not known. In the absence of such data, one might estimate that the free energy of formation of the orthochromite species would be somewhat greater than Cr_2O_3 and Ce_2O_3 for $CeCrO_3$, and greater than that of Cr_2O_3 and La_2O_3 for $LaCrO_3$.

Seybolt[71] in his work on the oxidation in air of Cr + 5 volume % Y_2O_3 alloy prepared by powder metallurgy method, had also observed the formation of the $YCrO_3$ phase. This result indicates that in the chromia forming yttria containing alloys, $YCrO_3$ may be expected to form by the reaction of Cr (or Cr_2O_3) with Y_2O_3 in air. He had attributed the observed reduction in the oxidation kinetics to the formation of this phase. He argued that the $YCrO_3$ barrier which formed at the oxide/metal interface increasingly became effective with time at temperature, and it resulted in blocking the transfer of Cr into the oxide, thus reducing the oxide growth rate.

Seybolt[71] had also further argued that, since each mole of Y_2O_3 consumed formed two moles of $YCrO_3$, there was an appreciable increase with time in the $YCrO_3$ content at the interface. Since the $YCrO_3$ is depleted in Cr with respect to the pure Cr matrix, it would continuously reduce the diffusion flux of Cr^{3+} through Cr_2O_3, because the concentration gradient of the migrating Cr^{3+} ions was reduced. Therefore the slowly accumulating $YCrO_3$ at the Cr_2O_3/matrix interface, may tend to choke off the Cr_2O_3 growth rate.

CHAPTER 5

CONCLUSIONS

1. A reduction in the growth rate of the oxide and the parabolic rate constant was observed in the yttrium containing alloys compared to the yttrium free alloys. Alloy containing 0.62 wt% Y, exhibited the largest reduction in the weight gain.

2. Reduction in the sulfur content of the yttrium free alloys did not improve the oxide scale adherence. Addition of yttrium to the alloys improved the oxide scale adherence, irrespective of their sulfur content. This suggested that it was necessary to add reactive elements to the chromia forming alloys to achieve improved oxidation resistance, and that a mere reduction in the sulfur content of the alloy may not improve the oxide scale adherence.

3. Chromium sulfide, CrS, with a hexagonal crystal structure space group 194, $P6_3/mmc$ ($a = 3.46$ Å, $c = 5.78$ Å) was observed in the yttrium free alloys in the as-homogenized condition. This observation indicated that, in the absence of reactive elements in the alloy, sulfur in the alloy may be tied up in the form of chromium sulfide, and thus it may not diffuse to the oxide/alloy interface as free sulfur.

4. The phase $NiCr_2O_4$ with a floret-like morphology and with a cubic crystal structure space group 227, $Fd\bar{3}m$ was found in the oxide scale grown on all the alloys when they were oxidized at 900°C in air. The oxide Cr_2O_3 with a rhombohedral crystal structure space group 167 $R\bar{3}c$ ($a = 4.96$ Å, $c = 13.59$ Å) was observed in the oxide scale grown on all the alloys.

5. The phase Ni_5Y with a hexagonal crystal structure space group 191 P6/mmm ($a = 4.89$Å, $c = 3.96$ Å) was observed along the grain/dendritic boundaries of the yttrium

containing alloys. Since Ni_5Y has a different crystal structure than that of the matrix (cubic) it is suggested that it may act as a barrier for the diffusion of chromium cations along the short circuit diffusion paths such as alloy grain/dendrite boundaries. This may partly explain the improved oxidation resistance of the yttrium containing alloys compared to the yttrium free alloys.

6. The yttrium oxysulfide phase, Y_2O_2S, with a trigonal crystal structure space group 164, $P\bar{3}m1$ (a =3.79 Å, c = 6.59 Å) was observed in the yttrium containing alloys and in the oxide scales grown on them. Observation of this phase demonstrated that yttrium was capable of trapping the sulfur in the alloy in the form of an oxysulfide species. Since the rare-earth elements are also known to form the oxysulfide phase, it may explain why a similarity is observed in the oxidation resistance of yttrium and the rare-earth element containing alloys.

The thermodynamic calculations involving yttrium metal, yttrium oxysulfide and yttria indicated that the driving force for the formation of the oxyslfide species was sufficiently large to produce the reactive element effect in the high temperature alloys, irrespective of the manner in which the element was added to the alloy.

The differences in the free energy of formation of the oxides and the oxysulfides of yttrium and the rare-earth elements also clearly indicated why different reactive elements impart a slightly different oxidation resistance to the oxidation resistant chromia forming alloys.

7. In the absence of yttrium in the alloy, sulfur did not seem to play any role in the oxidation behavior of the alloys. However, in the presence of yttrium, it appeared to have an important role, since it lead to the formation of the oxysulfide species.

8. The yttrium oxysulfate phase, $Y_2O_2SO_4$, with a crystal structure space group 71, Immm (a = 4.15 Å, b = 4.01 Å, c = 12.68 Å) was found in the oxide scale grown on the yttrium containing alloy. Oxysulfides of the rare-earth elements are also known to form the oxysulfate species when oxidized, with the exception of Ce which directly forms

ceria, CeO_2. Stability of the oxysulfate species is known to be different for different rare-earth elements and yttrium, and this may have an effect on the oxidation behavior of the alloys containing these elements.

9. The yttria phase, Y_2O_3, with a cubic crystal structure space group 206, $Ia\bar{3}$ (a = 10.63 Å) was found in the as-homogenized yttrium containing alloy, in association with $Y_2O_2S/Y_2O_2SO_4$ particles. This observation suggested two different possibilities : 1) yttria may have formed by the decomposition of the oxysulfide species and 2) yttria may have been responsible for gettering sulfur in the alloy and may have resulted in the formation of the oxysulfide/oxysulfate species. The latter explanation supports the hypothesis that yttria dispersions in the alloy may also getter sulfur in the alloy and thus impart improved oxidation resistance.

10. The yttrium orthochromite phase, $YCrO_3$, with a orthorhombic crystal structure space group 62, Pnma (a = 5.52 Å, b = 5.25 Å, c = 7.54 Å) was found in the oxide scale grown on the yttrium containing alloy. The improvement in the oxidation resistance of yttrium and the rare-earth containing alloys has also been attributed to the formation of their respective orthochromite species.

11. Partial pressure of oxygen involved in the oxidation process may affect the oxidation behavior of the high temperature alloys. Simulation experiments with the oxysulfide of La and Ce indicated that oxidation under low partial pressure of oxygen would result in the formation of the orthochromite species, while oxidation in air may not result in the formation of this species, at least in the initail stages of oxidation. Thus depending upon the partial pressure of oxygen used during oxidation experiments, the oxide scale adherence and the oxide scale growth rate of the high temperature alloys may be different.

REFERENCES

1. Stoloff, N.S., "Wrought and P/M Superalloys", *Met. Handbook*, **1**, 10th ed., 950-977 (1990)

2. Klarstrom, D.L., "Corrosion of Nickel-base Alloys", *Met. Handbook*, **13**, 9th ed., 641-643 (1987)

3. Whittle, D.P. and Stringer, J., "Improvements in Properties: Additives in Oxidation Resistance", *Phil. Trans. R.. Soc. Lond.*, **A 295**, 309-329 (1980)

4. Stringer, J., "The Reactive Element Effect in High Temeperature Corrosion", *Mat. Sci. Eng.*, **A 120**, 129-137 (1989)

5. Jones, D.A., *Principles and Prevention of Corrosion*, Macmillan Publishing Company, New York (1992)

6. Fontana, M.G., *Corrosion Engineering Principles*, 3rd ed., McGraw-Hill Publishing Company, New York (1986)

7. Uhlig, H.H. and Rievie, R.W., *Corrosion and Corrosion Control: An Introduction to Corrosion Science and Engineering*, 3rd ed., John Wiley & Sons, New York (1985)

8. Stott, F.H., "Methods of Improving Adherence", *Matl. Sci. Technol.*, **4**, 431-438 (1988)

9. Wood, G.C. and Stott, F.H., "Oxidation of Alloys", *Matl. Sci. Technol.*, **3**, 519-530 (1987)

10. Mevrel, R., "Cyclic Oxidation of High Temperature Alloys", *Matl. Sci. Technol.*, **3**, 531-535 (1987)

11. Moon, D.P., "Role of Reactive Elements in Alloy Protection", *Matl. Sci. Technol.*, **5**, 754-764 (1989)

12. Wallwork, G.R. and Hed, A.Z., "Some Limiting Factors in the Use of Alloys at High Temperatures", *Oxid. Met.*, **3(2)**, 171-184 (1971)

13. Gulbransen, E.A. and Jansson, S.A., *Thermochemistry of Gas-Metal Reactions*, American Society for Metals, Metals Park, Ohio (1971)

14. Lillerud, K.P. and Kofstad, P., "On High Temperature Oxidation of Chromium", *J. Electrochem. Soc*, **127(11)**, 2397-2419 (1980)

15. Ellingham, H.J.T, "Reducibility of Oxides and Sulfides in Metallurgical Processes", *J. Soc. Chem. Industry*, **63**, 125-133 (1944)

16. Chattopadhyay, B. and Wood, G.C., "The Transient Oxidation of Alloys", *Oxid. Met.*, **2(4)**, 373-399 (1970)

17. Hauffe, K., *Progress in Materials Science, Volume 4: The Mechanism of Oxidation of Metals and Alloys at High Temperature*, Pergamon Press, Great Britain (1953)

18. Kofstad, P., *Non Stoichiometry, Diffusion and Electrical Conductivity in Binary Metal Oxides*, John Wiley & Sons, New York (1972)

19. Wood, G.C., "High Temperature Oxidation of Alloys", *Oxid. Met.*, **2(1)**, 11-57 (1970)

20. Stott, F.H., "Developments in Understanding the Mechanisms of Growth of Protective Scales on High Temperature Alloys", *Mat. Char.*, **28(4)**, 311-325 (1992)

21. Croll, J.E. and Wallwork, G.R., "The Design of Iron-Chromium-Nickel Alloys for use at High Temperatures", *Oxid. Met.*, **1(1)**, 55-71 (1969)

22. Croll, J.E. and Wallwork, G.R., "The High Temperature Oxidation of Iron-Chromium-Nickel Alloys Containing 0-30% Chromium", *Oxid. Met.*, **4(3)**, 121-140 (1972)

23. Pilling, N.B. and Bedworth, R.E., "The Oxidation of Metals at High Temperatures", *J Inst. Met.*, **29**, 529-582 (1923)

24. Hou, P.Y. and Stringer, J., "The Influence of Ion-implanted Yttrium on the Selective Oxidation of Chromium in Co-25wt%Cr", *Oxid. Met.*, **29(1/2)**, 45-74 (1988)

25. Francis, J.M. and Whitlow, W.H., "High Temperature Oxidation Resistance of an Yttrium-bearing 20%Cr/25%Ni/Nb Stabilized Austenitic Steel in Carbon-dioxide", *J. Iron Steel Inst.*, **204**, 355-359 (1966)

26. Nagai, H., Murai, T. and Mitani, H., "The Role of Rare Earths and Reactive Elements in High Temperature Oxidation Behavior of Fe-20Cr Alloy", *Trans. Jap. Inst. Met.*, **20**, 299-310 (1979)

27. Nakamura, Y., "The Oxidation Behavior of an Iron-Chromium Alloy Containing Yttrium or Rare Earth Elements Between 900°C and 1200°C", *Metall. Trans.*, **5**, 909-913 (1974)

28. Antill, J.E. and Peakall, K.A., "Influence of an Alloy Addition of Yttrium on the Oxidation Behavior of an Austenitic and Ferritic Stainless Steel", *J. Iron Steel Inst.*, **205**, 1136-1142 (1967)

29. Tsuzi, E., "The Role of Yttrium on the Oxide Adherence of Fe-24Cr Base Alloys", *Metall. Trans. A*, **11A**, 1965-1972 (1980)

30. Strafford, K.N., "High Temperature Corrosion of Alloys Containing Rare Earth or Refractory Elements: A Review of Current Knowledge and Possible Future Developments", *High Temp. Technol.*, **6**, 307-318 (1983)

31. Nagai, H., "Effect of Rare Earth Metals and Oxides Addition on the High Temperature Oxidation of Ni-Cr and Fe-Cr Alloys", *Mat. Sci. Forum*, **43**, 75-130 (1989)

32. Wei, F.I. and Stott, F.H., "The Development of Cr_2O_3 Scales on Iron-Chromium Alloys Containing Reactive Elements", *Corr. Sci.*, **29(7)**, 839-861 (1989)

33. Hou, P.Y. and Stringer, J., "Room Temperature Strains in Cr_2O_3 Scales Formed at Elevated Temperatures on Ni-25wt%Cr and Y and Al Doped Ni-25wt%Cr", *Acta Metall. Mater.*, **39(5)**, 841-849 (1991)

34. Kumar, A., Nasrallah, M. and Douglass, D.L., "The Effect of Yttrium and Thorium on the Oxidation Behavior of Ni-Cr-Al Alloys", *Oxid. Met.*, **8(4)**, 227-263 (1974)

35. Strafford, K.N. and Harrison, J.M., "Observations on the Oxidation Behavior of Ni-Cr Alloys Containing Minor Additions of Group III, IV or V Elements", *Oxid. Met.*, **10(6)**, 347-359 (1976)

36. Wood, G.C. and Boustead, J., "The Influence of Group III A Metals on the Oxidation of Fe-Cr Alloys", *Corr. Sci.*, **8**, 719-723 (1968)

37. Beltran, A.M., "The Oxidation and Hot Corrosion Resistance of Cobalt-base Superalloys", *Cobalt*, **46**, 3-14 (1970)

38. Saito, Y., Murayama, T. and Amano, T., "Adherence of Oxide Scale Formed on Ni-20Cr-1Si Alloys with Small Additions of Rare Earth Elements", *Mat. Sci. Eng.*, **8**, 275-280 (1987)

39. Wright, I.G. and Wilcox, B.A., "The Oxidation of Fe-Cr Alloys Containing an Oxide Dispersion of Reactive Metal Additions", *Oxid. Met.*, **8(5)**, 283-301 (1974)

40. Rundell, G. and McConnell, J., "Oxidation Resistance of Eight Heat Resistant Alloys at 870°, 980°, 1095°, and 1150°C", *Oxid. Met.*, **36(3/4)**, 253-263 (1991)

41. Rhys-Jones, T.N. and Grabke, H.J., "Use of Cerium and Cerium Oxide Additions to Improve High Temperature Oxidation Behavior of Fe-Cr Alloys", *Matl. Sci. Technol.*, **4**, 446-454 (1988)

42. Ecer, G.M. and Meier, G.H., "The Effect of Cerium on the Oxidation of Ni-50Cr Alloys", *Oxid. Met.*, **13(2)**, 159-180 (1979)

43. Wright, I.G. and Wilcox, B.A., "Observations on Strengthening and Oxidation Behavior of a Dispersion Hardened Fe-Cr-base Alloy Prepared by Mechanical Alloying", *Metall. Trans.*, **5**, 957-960 (1974)

44. Ramanarayanan, T.A. and Petkovic-Luton, R., "Investigations on the Growth Mechanisms of alpha Cr_2O_3 on Ni-base Alloys With and Without Y_2O_3 Dispersions", *Ber. Bunsenges. Phy. Chem.*, **89**, 402-409 (1985)

45. Yurek, G.J., Pryzybylski, K. and Garratt-Reed, A.J., "Segregation of Y to Grain Boundaries in Cr_2O_3 and NiO Scales Formed on an ODS Alloy", *J. Electrochem. Soc.*, **134**, 2643-2644 (1987)

46. Nagai, H., Takebayashi, Y. and Mitani, H., "Effect of Dispersed Oxides of Rare Earths and Other Reactive Elements on the High Temperature Oxidation Resistance of Fe-20Cr Alloy", *Metall. Trans. A*, **12A**, 435-442 (1981)

47. Whittle, D.P. and Hindam, H., "Microstructure and Growth of Protective Cr_2O_3 and Al_2O_3 Scales at High Temperature", U.S. Department of Energy Contract No. DE-AC03-76SF00098, National Association of Corrosion Engineers, Houston, Texas

77084, 54-99 (1982)

48. Giggins, C.S. and Pettit, F.S., "The Oxidation of TD NiC (Ni-20Cr-2 vol. pct. ThO_2) Between 900°C and 1200°C", *Metall. Trans.*, **2**, 1071-1078 (1971)

49. Michels, H.T., "The Effect of Dispersed Reactive Metal Oxides on the Oxidation Resistance of Nickel-20wt percent Chromium Alloys", *Metall. Trans. A*, **7A**, 379-386 (1976)

50. Stringer, J., Wilcox, B.A. and Jaffee, R.I., "The High Temperature Oxidation of Nickel-20wt% Chromium Alloys Containing Dispersoid Oxide Phases", *Oxid. Met.*, **5(1)**, 11-36 (1972)

51. Stringer, J. and Wright, I.G., "The High Temperature Oxidation of Cobalt-21wt% Chromium-3 vol.% Y_2O_3 Alloys", *Oxid. Met.*, **5(1)**, 59-84 (1972)

52. Davis, H.H., Graham, H.C. and Kvernas, I.A., "Oxidation Behavior of Ni-Cr-1ThO_2 Alloys at 1000°C and 1200°C", *Oxid. Met.*, **3(5)**, 431-451 (1971)

53. Angerman, C.L., "Long Term Oxidation of Superalloys", *Oxid. Met.*, **5(2)**, 149-167 (1972)

54. Yang, C.H., Labun, P.A., Welsch, G.H., Mitchell, T.E. and Bennett, M.J., "Influence of Ion-implantation on the Microstructure of Oxide Scales Formed on a 20Cr/25Ni Nb-Stabilized Stainless Steel in Carbon-dioxide at 825°C", *J. Mater. Sci.*, **22(2)**, 449-458 (1987)

55. Mrowec, S., Jedlinski, J. and Gill, A., "The Influence of Certain Reactive Elements on the Oxidation Behavior of Chromia and Alumina Forming Alloys", *Mat. Sci. engg.*, **A120**, 169-173 (1989)

56. Pryzybylski, K. and Yurek, G.J., "The Influence of Implanted Yttrium on the Mechanisms of Growth of Chromia Scales", *Mat. Sci. Forum*, **43**, 1-74 (1989)

57. Cotell, C.M., Yurek, G.J., Hussey, R.J., Mitchell, D.F. and Graham, M.J., "Growth Mechanism of Cr_2O_3 Scales on Cr and Cr Implanted With Y", *Proceedings of the Symposium on High Temperature Material Chemistry*, The Electrochemical Society, High Temperature Materials Division, **88-5**, 268-276 (1988)

58. Patibandla, N., Ramanarayanan, T.A. and Cosandy, F., "Effect of Ion-implantated Cerium on the Growth Rate of Chromia Scales on Ni-Cr Alloys", *J. Electrochem. Soc*, **138(7)**, 2176-2184 (1991)

59. Cotell, C.M., Yurek, G.J., Hussey, R.J., Mitchell, D.F. and Graham, M.J., "The Influence of Implanted Yttrium on the Mechanism of Growth of Cr_2O_3 on Cr", *J. Electrochem. Soc*, **134(7)**, 1871-1872 (1987)

60. Yang, C.H., Welsch, G.H. and Mitchell, T.E., "Analytical Electron Microscopy Investigation of the Oxide Scale on a Yttrium Implanted Ni-20wt%Cr Alloy", *Mat. Sci. Eng.*, **5(2)**, 149-167 (1985)

61. Pryzybylski, K. and Yurek, G.J., "The Influence of Implanted Yttrium on the Microstructures of Chromia Scales Formed on a Co-45 Weight Percent Cr Alloy", *J. Electrochem. Soc.*, **135(2)**, 517-523 (1988)

62. Pryzybylski, K., Garratt-Reed, A.J. and Yurek, G.J., "Grain Boundary Segregation of Yttrium in Chromia Scales", *J. Electrochem. Soc.*, **135(2)**, 509-517 (1988)

63. Pivin, J.C., Roques-Carmes, C., Chaumont, J. and Bernas, H., "The Influence of Yttrium Implantation on the Oxidation Behavior of 67Ni-33Cr, Fe-43Ni-27Cr and Fe-41Ni-25Cr-10Al Refractory Alloys", *Corr. Sci.*, **20**, 947-962 (1980)

64. Downham, D.A., Hussey, R.J., Mitchell, D.F. and Graham, M.J., "Segregation of Cerium in Chromia Scales", *Proc. 29th Conf. Metall. Met. Soc. of C.I.M.*, Hamilton,Ontario, Canada, (1990)

65. Hussey, R.J., Papaiacovou, P., Shen, J., Mitchell, D.F. and Graham, M.J., "The Effect of Ceria Coatings on the High Temperature Oxidation of Iron-Chromium Alloys", *Mat. Sci. Eng.*, **A120**, 147-151 (1989)

66. Moon, D.P. and Bennet, M.J., "The Effects of Reactive Element Oxide Coatings on the Oxidation Behavior of Metals and Alloys at High Temperatures", *Mat. Sci. Forum*, **43**, 269-298 (1989)

67. Hussey, R.J., Papaiacovou, P., Shen, J., Mitchell, D.F. and Graham, M.J., "The High Temperature Oxidation of Iron-Chromium Alloys Sputter Coated with Ceria", *Proc. Symp. Corr. and Particle Erosion at High Temp.*, The Minerals, Metals & Materials Society, 567-584 (1989)

68. Graham, M.J., Downham, D.A., Hussey, R.J., Mitchell, D.F. and Sproule, G.I., "Chemical Microanalysis of Oxide Scales", *Proc.Corrosion-Erosion Wear of Matls. at Elevated Temperatures*, Berkeley, California, 4-1-4-21 (1990)

69. Hou, P.Y. and Stringer, J., "The Effect of Surface Applied Reactive Metal Oxides on the High Temperature Oxidation of Alloys", *Mat. Sci. Eng.*, **87**, 295-302 (1987)

70. Landkof, M., Levy, A.V., Boone, D.H., Gray, R. and Yaniv, E., "The Effect of Surface Additives on the Oxidation of Chromia Forming Alloys", *Corr.*, **41(6)**, 344-357 (1985)

71. Seybolt, A.U., "High Temperature Oxidation of Chromium Containing Y_2O_3", *Corr. Sci.*, **6**, 263-269 (1966)

72. Ikeda, Y., Nii, K. and Yata, M., "Y_2O_3 Dispersion Effect on Al_2O_3 Protective Coating Examined on the Basis of Five Models", *ISIJ International*, **33(2)**, 298-306 (1993)

73. Allam, I.A., Whittle, D.P. and Stringer, J., "The Oxidation Behavior of CoCrAl Systems Containing Active Element Additions", *Oxid. Met.*, **12(1)**, 35-66 (1978)

74. Delauny, D. and Huntz, A.M., "Mechanisms of Adherence of Alumina Scale Developed During High Temperature Oxidation of Fe-Ni-Cr-Al-Y Alloys", *J. Mater. Sci.*, **17**, 2027-2036 (1982)

75. Smigelskas, A.D. and Kirkendall, E.O, "Zinc Diffusion in Alpha Brass", *Trans. AIME*, **171**, 130-142 (1947)

76. Smeggil, J.G., "Some Comments on the Role of Yttrium in Protective Oxide Scale Adherence", *Mat. Sci. Eng.*, **87**, 261-265 (1987)

77. Lees, D.G., "On the Reasons for the Effects of Dispersions of Stable Oxides and Additions of Reactive Elements on the Adhesion and Growth Mechanisms of Chromia and Alumina Scales - The 'Sulfur Effect'", *Oxid. Met.*, **27(1/2)**, 75-81 (1987)

78. Melas, I. and Lees, D.G., "Factors Affecting Adhesion of Chromia Scales on Chromium", *Matl. Sci. Technol.*, **4**, 455-456 (1988)

79. Smialek, J.L., "Effect of Sulfur Removal on Al_2O_3 Scale Adhesion", *Metall. Trans. A*, **22A**, 739-752 (1991)

80. Fox, P., Lees, D.G. and Lorimer, G.W., "Sulfur Segregation During the High Temperature Oxidation of Chromium", *Oxid. Met.*, **36(5/6)**, 491-503 (1991)

81. Funkenbusch, A.W., Smeggil, J.G. and Bornstein, N.S., "Reactive Element-Sulfur Interaction and Oxide Scale Adherence", *Metall. Trans. A*, **16A**, 1164-1166 (1985)

82. Smialek, J.L., "Adherent Al_2O_3 Scales Formed on Undoped NiCrAl Alloys", *Metall. Trans. A*, **18A**, 164-167 (1987)

83. Smeggil, J.G., Funkenbusch, A.W. and Bornstein, N.S., "A Relationship Between Indigenous Impurity Elements and Protective Oxide Scale Adherence Characteristics", *Metall. Trans. A*, **17A**, 923-932 (1986)

84. Anderson, A.B., Mahendru, S.P. and Smialek, J.L., "Dopant Effect of Yttrium and the Growth and Adherence of Alumina on Nickel-Aluminum Alloys", *J. Electrochem. Soc.*, **132(7)**, 1695-1701 (1985)

85. Bornstein, N.S., DaCrescente, M.A. and Smeggil, J.G., "The Influence of Sulfur on the Oxidation of Coatings", *Mat. Sci. Eng.*, **A120**, 175-178 (1989)

86. Ikeda, Y., Tosa, M., Yoshihara, K. and Nii, K., "Adherence of Al_2O_3 Coating Layers to Steels: The Detrimental Effect of Sulfur and the Beneficial Effect of Rare Earth Metals", *Matl. Sci. Technol.*, **A120**, 179-184 (1989)

87. Khanna, A.S., Wasserfuhr, C., Quaddakkers, W.J. and Nickel, H., "Addition of Yttrium, Cerium and Hafnium to Combat the Deleterious Effect of Sulfur Impurity During Oxidation of an Ni-Cr-Al Alloy", *Mat. Sci. Eng.*, **A120**, 185-191 (1989)

88. Huntz, A.M., "French Research on the 'Effect of Reactive Elements on the Oxidation Behavior'", *Mat. Sci. Forum*, **43**, 131-206 (1989)

89. Grabke, H.J., Weimer, D. and Viefhaus, H., "Segregation of Sulfur During Growth of Oxide Scales", *Appl. Surf. Sci.*, **47**, 243-250 (1991)

90. Walker, C.G.H. and El Gomati, M.M., "The Role of Zirconium and Sulfur in the Adherence of Oxides on Superalloys", *Appl. Surf. Sci.*, **35**, 164-172 (1988)

91. Stott, F.H. and Wood, G.C., "Growth and Adhesion of Oxide Scales on Al_2O_3-forming Alloys and Coatings", *Mat. Sci. Eng.*, **87**, 267-274 (1987)

92. Hong, S.Y., Anderson, A.B. and Smialek, J.L., "Sulfur at Nickel-Alumina Interfaces", *Surf. Sci.*,**230**, 175-183 (1990)

93. Smeggil, J.G., Bornstein, N.S. and DaCrescente, M.A., "The Importance of Interfacial Chemistry in Protective Oxide Scale Adherence", *Oxid. Met.*, **30(3/4)**, 259-266 (1988)

94. Smeggil, J.G., "The Effect of Indigenous Sulfur on the High Temperature Oxidation Performance of the Chromia-Forming Alloy Ni-40wt%Cr", *Proceedings of the Symposium on Corrosion and Particle Erosion at High Temperatures*, The Minerals, Metals & Materials Society, 403-424 (1989)

95. Papaiacovou, P., Hussey, R.J., Mitchell, D.F. and Graham, M.J., "Interfacial Segregation During Oxidation in O_2 at 1173 K of CeO_2-Coated Fe-20Cr Alloys", *Oxid. Met.*, **33**, 19-30 (1990)

96. Bennett, M.J., "New Coatings for High Temperature Materials Protection", *J. Vac. Sci. Technol. B*, **2(4)**, 800-805 (1984)

97. LePage, Y. and Downham, D.A., "Primitive Unit Cell Volumes Obtained From Unindexed Convergent-Beam Electron Diffraction Patterns", *J., Electron Microscopy Technique*, **18**, 437-439 (1991)

98. Thomas, G. and Goringe, M.J., *Transmission Electron Microscopy of Materials*, John Wiley & Sons, New York (1979)

99. Burns, G. and Glazer, A.M., *Space Groups for Solid State Scientists*, 2nd ed., Academic Press, Inc., San Diego, California (1990)

100. Czerwinski, F. and Smeltzer, W.W., "The Early Stage Oxidation of CeO_2 Sol-Coated Nickel", *J. Electrochem. Soc.*, **140(9)**, 2606-2615 (1993)

101. Rooney, T.E. and Stapleton, A.G., "The Iodine Method for the Determination of Oxides in Steel", *J. Iron Steel Inst.*, **131**, 249-254 (1935)

102. Evans, U.R., "The Passivity of Metals. Part I. The Isolation of the Protective Film", *J Chem. Soc.*, 1020-1040 (1927)

103. Vernon, W.H.J., Wormwell, F. and Nurse, T.J., "The Thickness of Air-Formed Oxide Films on Iron", *J. Chem. Soc.*, 621-632 (1939)

104. Gulbransen, E.A., Phelps, R.T. and Hickman, J.W., "Oxide Films Formed on Alloys at Moderate Temperatures", *Indus. Eng. Chem.*, **18**, 640-652 (1946)

105. Phelps, R.T., Gulbransen, E.A. and Hickman, J.W., "Electron Diffraction and Electron Microscope Study of Oxide Films Formed on Metals and Alloys at Moderate Temperatures", *Indus. Eng. Chem.*, **18**, 391-400 (1946)

106. Schneider, S.J., Roth, R.S. and Waring, J.L., "Solid State Reactions Involving Oxides of Trivalent Cations", *J. Res. Natl. Bureau Stds. A*, **65A**, 345-374 (1961)

107. Wilson, W.G., Kay, D.A.R. and Vahed, A., "The Use of Thermodynamics and Phase Equilibria to Predict the Behavior of the Rare Earth Elements in Steel", *J. Metals*, **26**, 14-23 (1974)

108. Dwivedi, R.K. and Kay, D.A.R., "Thermodynamics of the Oxidation of Rare Earth Oxysulfides at High Temperatures", *Metall. Trans. B*, **15B**, 523-528 (1984)

109. Vahed, A. and Kay, D.A.R., "Thermodynamics of Rare Earths in Steel Making", *Metall. Trans. B*, **7B**, 375-383 (1976)

110. Dwivedi, R.K. and Kay, D.A.R., "Thermodynamics of High Temperature Oxidation of La_2O_2S and Nd_2O_2S at High Sulfur Partial Pressure", *J. Mater. Sci. Lett.*, **3**, 983-986 (1984)

111. Leskelä, M. and NiiNistö, L., "Solid Solutions in the Rare-Earth Oxysulfide Series", *J Solid State Chem.*, **19**, 245-250 (1976)

112. Seybolt, A.U., "Role of Rare Earth Additions in the Phenomenon of Hot Corrosion", *Corr. Sci.*, **11**, 751-761 (1971)

113. Zachariasen, W.H., "Crystal Chemical Studies of the 5f-series of Elements. VII. The Crystal Structure of Ce_2O_2S, La_2O_2S and Pu_2O_2S", *Acta Cryst.*, **2**, 60-62 (1949)

114. Seybolt, A.U., "High Temperature Oxidation of Chromium Containing Y_2O_3", *Corr. Sci.*, **6**, 263-269 (1966)

115. Villars, P. and Calvert, L.D., *Pearson's Handbook of Crystallographic Data for Intermetallic Phases*, 3rd ed., **2**, American Society for Metals, Metals Park, Ohio (1985)

116. Wyckoff, R.W.G, *Inrorganic Compounds, Hydrates and Ammoniates*, 2nd ed., **3**, Interscience Publishers, New York (1965)

117. Villars, P. and Calvert, L.D., *Pearson's Handbook of Crystallographic Data for Intermetallic Phases*, 3rd ed., **3**, American Society for Metals, Metals Park, Ohio (1985)

118. Flahaut, J. and Guittard, M., "Sur les oxysulfures de cerium et d'yttrium", *C. R. Seances Acad. Sci. (Paris)*, **241**, 1775-1778 (1955)

119. Ballestracci, R. and Mareschal, J., "Etude Structurale Des Sulfates Basiques De Terres Rares Et d'Yttrium", *Mat. Res. Bull.*, **2**, 993-998 (1967)

120. Geller, S., "Crystallographic Studies of Perovskite-like Compounds. IV . Rare Earth Scandates, Vanadates, Galliates, Orthochromites", *Acta Cryst.*, **10**, 243-248 (1957)

121. Geller, S. and Wood, E.A., "Crystallographic Studies of Perovskite-Like Compounds. I. Rare Earth Orthoferrites and $YFeO_3$, $YCrO_3$, $YAlO_3$", *Acta Cryst.*, **9**, 563-568 (1956)

122. Quezel-Ambrunaz, S. and Mareschal, M., "Parametres Cristallins des Chromites de Terres Rares", *Bull. Soc. Franc. Miner. Crist.*, **86**, 204-205 (1963)

123. Nash, P., *Binary Alloy Phase Diagrams*, 2nd ed., **3**, ASM International, The Materials Information Society, Metals Park, Ohio (1990)

124. Elliott, J.F., Gleiser, M. and Ramakrishna, V., *Thermochemistry for Steel Making: Thermodynamic and Transport Properties*, **II**, Addison-Wesley Publishing Company, Inc., Reading (1963)

125. Shendye, S.B. and Downham, D.A., "Characterization of Reactive Element Containing Ni-25wt%Cr Alloys and the Oxide Scales Grown on Them at High Temperatures Using Transmission Electron Microscopy", submitted for publication in Oct. 1993 to *Oxid. Met.*

126. Gschneidner Jr., K.A., Kippenhan, N. and McMasters, O.D., "Thermochemistry of the Rare Earths", Rare-Earth Information Center, Institute for Atomic Research, Iowa State University, Ames, Iowa 50010, **Report No. IS-RIC-6** (1973)

127. Shendye, S.B. and Downham, D.A., "Comments on the Role of Yttria in Gettering Sulfur in the "Y_2O_3 Dispersion Effect on Al_2O_3 Protective Coating Examined on the Basis of Five Models"", *ISIJ International*, **34**, 704-706 (1994)

BIOGRAPHICAL NOTE

The author was born at Murud-Janjira, Maharashtra State, India, on March 28, 1960. He went to school in Bombay and Thane. After completing the requirements for the higher secondary school certificate examination (XII grade) from the Ramnarain Ruia College of Science and Arts, Matunga, Bombay, he enrolled in the Indian Institute of Technology, Bombay, in 1978 from where he graduated with a Bachelor of Technology (B. Tech.) in Metallurgical Engineering, in 1983. He then came to the Oregon Graduate Institute of Science & Technology (it was then called Oregon Graduate Center) in fall 1983 and graduated in fall 1985, with a Master's degree in Materials Science and Engineering.

After completion of the requirements for the Master's degree the author went back to Bombay, India in fall 1985 and worked in the metals and steel industry. He was working as an Assistant Manager (Marketing) in Nippon Denro Ispat Ltd., Bombay, untill December 1991. He then came to the Oregon Graduate Institute in the beginning of January 1992 and completed the requirements for Ph. D in Materials Science and Engineering in July 1994.

He now plans to go back again to the real world and continue to work in the field of Materials Science and Engineering.